Fakultät für Chemie
Technische Universität München

Technische Universität München
Lehrstuhl für Organische Chemie

Wigner representation, its reconstruction, and optimal control of spin systems with applications in NMR spectroscopy, quantum technology, and beyond

David Leiner

Vollständiger Abdruck der von der Fakultät für Chemie der Technischen Universität München zur Erlangung des akademischen Grades eines

Doktors der Naturwissenschaften (Dr. rer. nat.)

genehmigten Dissertation.

Vorsitzender:
Prof. Dr. Klaus Köhler

Prüfende der Dissertation:
1. Prof. Dr. Steffen J. Glaser
2. Prof. Dr. Bernd Reif

Die Dissertation wurde am 08.10.2018 bei der Technischen Universität München eingereicht und durch die Fakultät für Chemie am 03.12.2018 angenommen.

Faculty of Chemistry
Technical Univeristy of Munich

Technical University of Munich
Chair of Organic Chemistry

Wigner representation, its reconstruction, and optimal control of spin systems with applications in NMR spectroscopy, quantum technology, and beyond

David Leiner

Full imprint of the dissertation approved by the Faculty of Informatics of the Technical University of Munich to obtain the academic degree of

Doctor of Natural Sciences (Dr. rer. nat.)

Chairman:
Prof. Dr. Klaus Köhler

Examiners of the dissertation:
1. Prof. Dr. Steffen J. Glaser
2. Prof. Dr. Bernd Reif

The dissertation was submitted to the Technical University of Munich on 08.10.2018 and was accepted by the Faculty of Chemistry on 03.12.2018.

Abstract

In this thesis, we introduce new methodologies for the visualization, evaluation, and optimal control of spin systems based on four publications appended in Appendix A - D. Essential parts are established on the DROPS representation, a phase-space method which exploits generalized Wigner functions, denoted as droplets, to represent and visualize quantum systems.
In the first publication "Wigner tomography of multispin quantum states" in Appendix A, a general sampling theorem for spherical functions is derived. This is evolved to a novel Wigner quantum state tomography: A technique to reconstruct the surface of the droplets representing quantum states by measuring expectation values of rotated axial tensor operators.
This concept is extended in the second publication "Wigner process tomography: Visualization of spin propagators and their spinor properties" in Appendix B to experimentally recover the phase space representation of propagators by mapping these operators to density matrices of an augmented system with an additional ancillar qubit and by applying a modified form of the Wigner quantum state tomography. Both techniques are experimentally demonstrated for quantum states of systems up to three qubits and for standard 1 qubit gates using nuclear magnetic resonance spectroscopy. In doing so, the droplets are associated to measurable quantities, which were originally the mere result of an abstract mathematical mapping, and an interpretation in form of multipoles is provided. Those tomography schemes can be regarded as universally applicable validation methods for quantum systems. They are particularly well suited for the characterization of spin operators, pulse sequence elements, or entire pulse sequences in spectroscopy and in quantum information processing.
In a third publication "Symmetry-adapted decomposition of tensor operators and the visualization of coupled spin systems" in Appendix C, the concept of the DROPS representation, which is in its original form restricted to systems of up to four spins 1/2 due to computational challenges, is generalized to any number of coupled spins 1/2 and to two coupled spins with arbitrary spin numbers. These obstacles are circumvented by extending and introducing two different approaches based on explicit projection operators and coefficients of fractional parentage. This results in a powerful and versatilely applicable visualization tool for the analysis of highly diverse spin topologies and paves the way for the Wigner tomography schemes in such quantum systems.
This thesis is complemented by proposing novel optimal control strategies, which, combined with the previous techniques, provide a rich toolbox for the control, analysis, and verification of spin systems. In a last publication "Linking the rotation of a rigid body to the Schrödinger equation: The quantum tennis racket effect and beyond" in Appendix D, efficient and robust control strategies are introduced by linking the free rotation of a classical rigid body to the control of two-level quantum systems using external electromagnetic fields. In the case of state to state transfer and gate implementation, a new class of optimal controls is derived. This relies on two free parameters and allows for a variable efficiency, time, and robustness of the transfer process. An experimental demonstration is presented using techniques of nuclear magnetic resonance.

Zusammenfassung

In dieser Arbeit werden aufbauend auf vier Publikationen im Anhang A - D neue Methodiken für die Visualisierung, Evaluation und optimale Kontrolle von quantenmechanischen Systemen entwickelt. Im Kern steht dabei die DROPS Darstellung, eine Technik um Spinoperatoren im Phasenraum mittels generalisierten spährischen Wignerfunktionen, sogenannte Droplets, zu repräsentieren und zu visualisieren.
In der ersten Veröffentlichung "Wigner tomography of multispin quantum states" in Anhang A wird ein allgemeines Abtasttheorem für Kugelflächenfunktionen hergeleitet, auf dessen Basis eine neuartige Wigner Quantentomographie entsprungen ist: ein Verfahren für die Rekonstruktion von Quantenzuständen in Form von Wigner Funktionen. Dabei kann die Oberfläche dieser sphärischen Funktionen mittels Erwartungswerte von rotierten axialen Tensoroperatoren abgetastet und wiederhergestellt werden.
Dieses Konzept wurde in der zweiten Publikation "Wigner process tomography: Visualization of spin propagators and their spinor properties" in Anhang B auf die Ebene der Prozesstomographie erweitert. In dieser wird die Wignerdarstellung von Zeitentwicklungsoperatoren rekuperiert, die die dynamischen Prozesse in einem geschlossenen Quantensystem diktieren. Hierzu werden die Propagatoren eines Systems auf den Zustand eines mit einem zusätzlichen Qubit expandierten Systems aufgeprägt und eine variierte Form der Wigner Quantentomographie angewandt. Die experimentelle Realisierbarkeit wurde für beide Tomographietypen mittels Methoden der Kernspinresonanzspektroskopie demonstriert, indem die Wignerfunktionen von einer Reihe von Quantenzuständen von Systemen mit bis zu drei Qubits und standard 1-Qubit Quantengattern rekonstruiert wurden. In diesem Zusammenhang konnte die physikalische Existenz der Droplets bewiesen werden, die bis dahin nur die Konsequenz einer mathematisch-abstrakten Abbildung waren. Jene Techniken können als universell, funktionale Validierungsmethoden für Quantensysteme im Allgemeinen betrachtet werden, um Prozesse und Zustände in quanteninformationsverarbeitende Systemen zu verifizieren. Insbesondere für die Analyse von Spinoperatoren oder Pulssequenzen z.B. in der Kernspinresonanz sind diese geeignet.
In einer weiteren Publikation "Symmetry-adapted decomposition of tensor operators and the visualization of coupled spin systems" in Anhang C wird die DROPS Darstellung, die ursprünglich aufgrund von gruppentheoretischen Problemen nur auf bis zu vier gekoppelten Qubits anwendbar war, auf Systeme mit beliebiger Anzahl an Qubits und Systemen aus zwei gekoppelten Spins mit belibieger Spinzahl generalisiert. Dies wurde ermöglicht, indem ein Algorithmus aufbauend auf Projektionsoperatoren erweitert wurde und ein neuartiges Berechnungsverfahren innoviert wurde, das auf den coefficients of fractional parentage basiert. Dieses erweiterte Visualisierungsframework dient nicht nur als mächtiges Analysewerkzeug, sondern ebnet auch den Weg für die Anwendung obiger Wigner Tomographiemethoden auf einer größeren Variation an Quantensysteme.
Diese Arbeit wird durch die Einführung neuartiger optimaler Steuerstrategien für Spinsysteme komplementiert, die mit den vorgenannte Methodiken einen mächtigen Werkzeugkasten für die Steuerung, Analyse, und Verifikation von Quantensystemen zur Verfügung stellt. In einer letzten Veröffentlichung "Linking the rotation of a rigid body to the Schrödinger equation: The quantum tennis racket effect and beyond" in Anhang D wird eine neue Familie von Steuerungspulsen eingeführt, die auf dem Übertragen von der formalen Beschreibung der freien

Zusammenfassung

Drehung eines starren Körpers auf die Ebene der Spinsysteme basiert und in optimale Lösungen für die Probleme einer Zustandsüberführung und Implementierung von unitären Transformationen resultiert. Demonstrationsexperimente für diese Klasse von Pulsen wurden mit Techniken der Kernspinresonanz durchgeführt und deren Funktionalität gezeigt.

List of publications

This thesis is established on four publications given in Appendix A - D:

1. L. Van Damme, D. Leiner, P. Mardešić, S. J. Glaser, and D. Sugny. Linking the rotation of a rigid body to the schrödinger equation: The quantum tennis racket effect and beyond. *Sci. Rep.*, 7(3998), 2017

2. D. Leiner, R. Zeier, and S. J. Glaser. Wigner tomography of multispin quantum states. *Phys. Rev. A*, 96, 063413 (2017)

3. D. Leiner and S. Glaser. Wigner process tomography: Visualization of spin propagators and their spinor properties. *Phys. Rev. A*, 98, 012112 (2018)

4. D. Leiner, R. Zeier, and S. J. Glaser. Symmetry-adapted decomposition of tensor operators and the visualization of coupled spin systems. arXiv:1809.09006 (2018)

To fulfill the formal criteria for the thesis as a collection of articles, publications 2 and 3 are used.

Contents

List of Figures

List of Tables

1 Introduction

The first quantum revolution emerged in the last century [3], which primordially arose from the fundamental concept of wave-particle duality. In the peak of this stage, quantum mechanics matured to a sophisticated framework which gave birth to rules that govern modern physics and paved the way for novel applications that follow these principles. By the end of the 20th century, the first quantum revolution evolved into abundant scientific and technological breakthroughs including transistor, lasers, MRI, and GPS already integrated into society. Today, we are in the advent of a second quantum revolution, which is defined by the engineering of the quantum systems at the individual levels. Since quantum effects are inherently fragile, there is an immense necessity of experimental and theoretical frameworks to validate and precisely control individual atoms, electrons, and other particles. This includes the process of creation, manipulation, and the read-out of their quantum states.

In this context, visualization techniques are of great assistance to respond to these challenges. Various methods are known: Bloch vectors introduced by Feynman et al. [4], bar charts representing individual matrix elements, energy level diagrams [5], non-classical vector representation based on single-transition operators [6, 7, 8], and many more [9, 10, 11, 12, 13, 14]. In particular phase space representations [15, 16, 17, 18], as an alternative description for quantum mechanics, provide both, theoretically and experimentally powerful tools for the characterization and visualization of quantum systems. The most prominent candidates are the Wigner functions, quasiprobability distributions introduced by Eugene Wigner in 1932 [19]. However, all these techniques are not feasible or inconvenient for finite-dimensional systems containing several spins and a general methodology was still missing until recently.

A novel visualization approach was proposed in 2015 by Garon et al. denoted as the DROPS representation, an acronym for discrete representation of operators for spin systems [1]. It describes the high-dimensional structure of quantum systems by multiple three-dimensional generalized Wigner functions, called droplets, assembled from spherical harmonics resulting in a beneficial partitioning of the information of operators. Crucial features of the represented system are directly observable including symmetry properties and transformation behavior under the effect of specific external controls. This provides a general framework for the systematic analysis of such systems and their time evolution.

This thesis builds on the DROPS foundation and bridges the gap between the modern challenges in quantum information processing and the often purely conceptually applied visualization of such systems. The first publication "Wigner tomography of multispin quantum states" in Appendix A is dedicated to the read-out of the state, referred to as quantum state tomography [20], i.e., the process in which the state of the system is reconstructed by applying measurements on the system. In particular Wigner functions are frequently exploited in optical homodyne tomography for the determination of the quantum state of light [21, 22, 23, 24, 25]. By incorporating the DROPS representation into this concept, a new form of Wigner function based quantum state tomography, or short Wigner tomography, is evolved for (finite-dimensional) coupled multi-spin systems. In this context, a sampling theorem for spherical functions in general and in particular for the finite dimensional Wigner functions was developed. It establishes a correspondence between droplets, being initially mere results of an abstract mathematical mapping, and experimentally measurable quantities by measuring points on the surface of the droplets to eventually reconstructing the shapes.

A full characterization of a system requires not only the read-out of specific states, but also the determination of the dynamical process itself, referred to as system identification in classical systems [26]. Thus, in the second publication "Wigner process tomography: Visualization of spin propagators and their spinor properties" of this thesis in Appendix B, a quantum mechanical analog to system identification is established on this new Wigner tomography, the so-called process tomography [27, 28, 29, 30, 31, 32]. Its purpose is the entire determination of a quantum process which is described in the case of closed systems by unitary operators, the propagators, governing the time evolution of states. In its most elementary form [20], an ensemble of varying and well-defined input states are prepared, which are then evolved by the unknown quantum process. The output states are eventually measured providing full information of the propagator. Our method relies on the mapping of a propagator onto a quantum state of an enhanced system by ancilla qubits which is then reconstructed exploiting a modified version of the Wigner tomography. Direct applications would be the facilitation of quantum system identification processes in general and in particular the characterization of operators, pulse sequences and elements in spectroscopy and quantum information processing.

The original DROPS representation in [1] is explicitly elaborated for up to three spin 1/2 particles. Unfortunately, its primal computation algorithm is restricted to systems containing at maximum four spins 1/2, which is attributed to properties of the underlying mathematical group structure [33, 34, 35, 36, 37, 38]. Abundant practical applications in spectroscopy and quantum information processing, however, include systems with more particles and possibly with spin numbers unequal to 1/2 constituting a substantial restriction in the utilization of the DROPS representation and the associated tomography schemes. In order to circumvent these limitations, in the third publication "Symmetry-adapted decomposition of tensor operators and the visualization of coupled spin systems" of this thesis in Appendix C, the original computational method is extended and a new algorithm is introduced which is exclusively established on the framework of linear algebra by exploiting so-called coefficients of fractional parentage (CFP) [39]. They typically arise in the anti-symmetrization of many-body states. This considerably increases the range of application of the DROPS representation to any spin-1/2 system and to two coupled spins with arbitrary spin numbers.

In contrast to the first three publications, which introduce new concepts in tomography and visualizations of operators playing an essential role in the characterization and validation in spectroscopy and quantum information processing in general, the last publication "Linking the rotation of a rigid body to the Schrödinger equation: The quantum tennis racket effect and beyond" in Appendix D engages the challenge of the optimal control of such systems to complement the established toolbox of this thesis. Typically, the goal here is to externally influence a system to steer a given initial state to a desired target state while fulfilling certain constraints. The theory of classical optimal control peaked in the Pontryagin maximum principle [40] and in the Hamilton–Jacobi–Bellman equation in the framework of dynamic programming [41] which both give conditions for an optimal solution. It was introduced in the late 80s [42, 43] to the field of quantum mechanics for finding robust solutions for the control of such systems, i.e., robust against experimental uncertainties. Numerical techniques such as Krotov [44], GRAPE [45], and CRAB [46, 47] provide powerful frameworks for solving such quantum control problems. Unfortunately, purely numerical methods suffer from a lack of insight into the robustness nature of the optimal solution and are system-dependent. On the other hand, complementary geometric and analytic approaches [48, 49, 50, 51, 52, 53, 54], for the case of low dimensional systems, support a physical understanding of the control process resulting in optimization strategies resilient to experimental imperfections. In this last publication, new optimal control protocols are established by transferring a formal geometric description of a free rotation of a rigid body [55, 56, 57] to quantum systems. A prominent candidate for such geometric properties is known as the tennis racket effect [58, 59].

The remainder of this work is structured as follows. We start by introducing essential concepts on which the DROPS representation and its associated tomography approach are established. In chapter 2, multiple foundations are briefly summarized, including the time evolution of quantum mechanical systems, spherical tensors and harmonics, phase space representations and quantum tomography basics. We continue in chapter 3 with a short overview in group theory with the focus on the symmetric group and its representation. After these fundamentals, the original DROPS representation is eventually presented in chapter 4. NMR basics, its quantum mechanical description, and the connection to quantum information are outlined in chapter 5 to convey an in-depth understanding of the experimental implementation of the Wigner tomography schemes with NMR. In chapter 6, a concise introduction to optimal control is then given providing a brief survey on the typical statement of the problem in this field. The thesis is concluded in chapter 7 by summarizing the results, embedding them into existing literature and giving an outlook for future work. The publications on which this thesis is established are appended in Appendix A - D.

2 Foundations

We start by recalling some key aspects from quantum physics. A brief summary of the dynamics of closed quantum systems is given in Sec. 2.1. We move on and define irreducible tensors in Sec. 2.2, which prove to be a convenient basis for spin systems. In Sec. 2.3 we introduce spherical harmonics, functions which form a complete basis on the sphere, and its correspondance to irreducible tensors. The concept of a phase space is outlined in Sec. 2.4 and this chapter is concluded with a brief overview of quantum tomography in Sec. 2.5.

2.1 Quantum Mechanics

We will briefly summarize the main concepts in particular for closed systems. A plethora of textbooks can be found in literature [60, 61, 62, 63, 64]. Quantum mechanics is a fundamental theory in physics describing the smallest scales in nature. Its most prominent formulation is rooted in linear algebra. In this framework, a (quantum) system is associated with a complex vector space with inner product known as the Hilbert space or state space. The system is completely characterized by its state vector $|\psi\rangle$. If the state corresponds to a vector in a Hilbert space with unit length $\langle\psi|\psi\rangle = 1$, we call this state a pure quantum state. Otherwise it is a mixed quantum state corresponding to a probabilistic mixture of pure states. Mixed states are represented by the so-called density matrices

$$\rho = \sum_{k=1}^{N} p_k |\psi_k\rangle\langle\psi_k| \tag{2.1}$$

where $|\psi_k\rangle$ are pure states and N can be arbitrary and is not necessarily limited by the dimension of the state space. We can interpret the weights p_k as probabilities with $0 \leq p_k \leq 1$ and $\sum_k^N p_k = 1$ or analogously $\mathrm{tr}\{\rho\} = 1$. Note that we will also use the expression density operators interchangeably for the density matrix. Strictly, the density matrix is a matrix representation of the density operator and is obtained from it by a choice of a particular basis. Further, note that the framework of mixed states is a more general concept, since pure states can also be described by density matrices ρ.

The time evolution of a closed (statistical) quantum system is governed by the Liouville–von Neumann equation

$$i\hbar\frac{\partial\rho}{\partial t} = [H, \rho] \tag{2.2}$$

in the Schrödinger picture and with the commutator of two matrices A and B given by $[A, B] = AB - BA$. We do only consider closed systems throughout this thesis. There is no interchange of information (i.e. energy and/or matter) with the surroundings and consequently decoherence and dissipation is neglectable. A more general type of time evolution for open quantum system is given by the Gorini – Kossakowski – Sudarshan – Lindblad equation [65, 66, 67]. The Hamiltonian operator H corresponds to the energy of the system and generates the time evolution of the quantum states. This operator is particularly important since its eigenvalues define the energy levels of the quantum system, and transitions between these levels give rise to detectable signals in spectroscopy. If H is time-independent, a closed-form

solution of Eq. (2.2) can be found via

$$\rho(t) = U\rho_0 U^\dagger \tag{2.3}$$

with $\rho(t)$ being the density matrix at time t, ρ_0 the initial density matrix and U a unitary time evolution operator denoted as the propagator. If H is constant during the time interval, we find

$$U = \exp\left(\frac{-iHt}{\hbar}\right). \tag{2.4}$$

The knowledge of the quantum state ρ together with the Hamiltonian H for the time evolution of the system suffice to predict the system's behavior for future points in time t.

After a system evolved in time, one usually wants to measure this system. In quantum mechanics, the state ρ is not directly detectable, only the expectation values of some observables A are accessible

$$\langle A\rangle_\rho = \mathrm{tr}(A\rho). \tag{2.5}$$

The expectation value can be interpreted as the probabilistic expected value of a measurement on a system.

2.2 Irreducible Spherical Tensor Operators

An irreducible spherical tensor operator T_j [68, 69, 70, 71, 72, 73] with rank j is a mathematical object consisting of a set of $2j+1$ components T_{jm} with the order $m \in \{-j, \ldots, j\}$, which can be represented as matrices. Classically, they can be defined by their transformation under rotation [63]

$$\mathcal{R}_{\alpha,\beta,\gamma} T_{jm} = \sum_{m'=-j}^{j} D^j_{m'm}(\alpha,\beta,\gamma) T_{jm'} \tag{2.6}$$

with $\mathcal{R}_{\alpha,\beta,\gamma}$ being the rotation operator with its action on a matrix C given by $\mathcal{R}_{\alpha,\beta,\gamma} C := \mathfrak{R}_{\alpha,\beta,\gamma} C \mathfrak{R}^{-1}_{\alpha,\beta,\gamma}$ and with $\mathfrak{R}_{\alpha,\beta,\gamma} := \exp(-i\alpha F_z)\exp(-i\beta F_y)\exp(-i\gamma F_z)$. $F_y = \sum_{k=1}^N I_{ky}$ and $F_z = \sum_{k=1}^N I_{kz}$ are the total spin operators [6], I_{ka} with $a \in \{x, y, z\}$ are the Cartesian product operators [6] which are for a single spin 1/2 system described by the Pauli matrices σ_a with $I_a = 1/2\sigma_a$ for $a \in \{x, y, z\}$. The angles α, β, and γ are the Euler angles. Finally, $D^j_{m'm}(\alpha,\beta,\gamma)$ are the elements of the Wigner-D-Matrix [71, 74]. Eq. (2.6) defines a rotation on the spherical tensors as a linear combination of tensor components T_{jm} of the same rank which transform analogously as the angular momentum eigenstates (and thus like spherical harmonics) under an analogous rotation. In this context, irreducibility means that the components of a tensor transform linearly under rotation in a way that all components of the tensor enter the linear combination (although some coefficients can be zero). Thus, irreducible tensors are defined with respect to a basis in a j-dimensional space which is invariant and does not contain an invariant subspace in itself [73].

Alternatively, the following commutation relations may be used to defined the spherical tensor operators [63, 75, 70]:

$$[\mathcal{J}_z, T_{jm}] = mT_{jm} \tag{2.7}$$

$$[\mathcal{J}_+, T_{jm}] = \sqrt{j(j+1) - m(m+1)}\, T_{jm+1} \tag{2.8}$$

$$[\mathcal{J}_-, T_{jm}] = \sqrt{j(j+1) - m(m-1)}\, T_{jm-1} \tag{2.9}$$

with the raising and lowering operators defined as $\mathcal{J}_\pm = \mathcal{J}_x \pm i\mathcal{J}_y$ and where $\mathcal{J}_a$ with $a \in \{x, y, z\}$ are the infinitesimal rotation operators. For the most prominent case of an isolated single spin 1/2, the infinitesimal rotation operators are described by the Pauli matrices [6]

$$\mathcal{J}_x = \frac{1}{2}\sigma_x = \frac{1}{2}\begin{pmatrix} 0 & 1 \\ 1 & 0 \end{pmatrix}, \quad \mathcal{J}_y = \frac{1}{2}\sigma_y = \frac{1}{2}\begin{pmatrix} 0 & -i \\ i & 0 \end{pmatrix}, \quad \mathcal{J}_z = \frac{1}{2}\sigma_z = \frac{1}{2}\begin{pmatrix} 1 & 0 \\ 0 & -1 \end{pmatrix}. \tag{2.10}$$

The only component of the spherical tensor T_0 of rank $j = 0$ is then

$$T_{00} = \frac{1}{\sqrt{2}}\begin{pmatrix} 1 & 0 \\ 0 & 1 \end{pmatrix} \tag{2.11}$$

and the 3 components of the spherical tensor T_1 of rank $j = 1$ are

$$T_{1,-1} = \begin{pmatrix} 0 & 0 \\ 1 & 0 \end{pmatrix}, \quad T_{10} = \frac{1}{\sqrt{2}}\begin{pmatrix} 1 & 0 \\ 0 & -1 \end{pmatrix}, \quad T_{11} = \begin{pmatrix} 0 & -1 \\ 0 & 0 \end{pmatrix}. \tag{2.12}$$

These spherical tensor operators have been defined in this particular way to mimic the properties and behaviour of spherical harmonics [76], which will be introduced in the next section.

2.3 Spherical Harmonics and the Correspondence to Spherical Tensor Operators

Spherical harmonics $Y_{lm}(\theta, \phi)$ are special functions defined on the surface of the unit sphere and on which they form a complete set of orthogonal functions in the index l and m [76]. They can be defined as the angular part of the solutions to Laplace's equation in three dimensions. More explicitly, a spherical harmonic of rank j and order m is given by [76]

$$Y_{lm}(\theta, \phi) = \sqrt{\frac{2l+1}{4\pi}\frac{(l-m)!}{(l+m)!}} P_l^m[\cos(\theta)] \exp(im\phi) \tag{2.13}$$

with $P_l^m(x)$ being the associated Legendre function and which can be explicitly stated using the Rodrigues' formula

$$P_l^m(x) = \frac{-1^m}{2^l l!}(1-x^2)^{m/2}\frac{d^{l+m}}{dx^{l+m}}(x^2-1)^l. \tag{2.14}$$

The spherical harmonics are orthonormal $\int_0^{2\pi} d\phi \int_0^{\pi} \sin(\theta) d\theta Y^*_{l'm'}(\theta, \phi) Y_{lm}(\theta, \phi) = \delta_{l'l}\delta_{m'm}$, complete $\sum_{l=0}^{\infty}\sum_{m=-l}^{l} Y^*_{lm}(\theta', \phi') Y_{lm}(\theta, \phi) = \delta(\phi - \phi')\delta[\cos(\theta) - \cos(\theta')]$, and have the useful property $Y_{l,-m}(\theta, \phi) = (-1)^m Y^*_{lm}(\theta, \phi)$. The spherical harmonics obey the equivalent transformation rule in Eq. (2.6), i.e.,

$$R_{\alpha,\beta,\gamma} Y_{jm}(\theta, \phi) = \sum_{m'=-j}^{j} D^j_{m'm}(\alpha, \beta, \gamma) Y_{jm'}(\theta, \phi) \tag{2.15}$$

which is, of course not surprising, since spherical tensors are defined to mimic these properties. The action of rotation operator $R_{\alpha,\beta,\gamma}$ on $Y_{jm}(\theta, \phi)$ is defined by first rotating $Y_{jm}(\theta, \phi)$ around the z-axis by an azimuthal angle γ, followed by a rotation around the y-axis by a polar angle β and then rotating the result again around the z-axis by an azimuthal angle α.

This equivalence of the transformation in Eq. (2.6) and Eq. (2.15) can be exploited to find a direct and unique mapping between $Y_{jm}(\theta, \phi)$ and T_{jm}

$$Y_{jm}(\theta, \phi) \quad \longleftrightarrow \quad T_{jm}, \tag{2.16}$$

which allows for the application of methods and tools of angular momentum theory to tensor algebra and vice versa [73, 72]. Spherical harmonics $Y_{jm}(\theta,\phi) = r(\theta,\phi)\exp[\eta(\theta,\phi)]$ can be visualized using polar plots by mapping their spherical coordinates θ and ϕ to the radial part $r(\theta,\phi)$ and phase $\eta(\theta,\phi)$. Note that the spherical harmonics (and also the irreducible tensors operators in Sec. 2.2) are defined up to an algebraic sign. We will adopt the convention of Condon and Shortley [77, 78] throughout this work.

2.4 Phase Space and Wigner Functions

A phase space is a space originated from classical physics in which states of a system are represented as unique points. Since quantum mechanics is governed by the fundamental limit of the uncertainty principle, states are here represented by quasiprobability distributions or functions and not just points. Every quantum mechanical observable, which is a Hermitian operator in a Hilbert space, corresponds to a unique function or quasiprobability distribution in the phase space and vice versa [79, 80, 19, 81, 82].

The representation in phase space is not unique. In fact, there are different ways to define the functions which are interrelated [83, 84, 85]. The most prominent distribution is the Wigner representation [19], which is a special representation of the density matrix. Hilbert space expressions, observables, and operations can be correspondingly stated in this framework. For example, expectation values in phase-space are obtained isomorphically to the Hilbert space, which traces (observable) operators with the density matrix. Here, expectation values are obtained by integrals of observables with the Wigner quasi-probability distribution.

In particular we want to introduce a family of generalized Wigner functions. A set of spherical functions $\{f_A^{(\ell)}(\theta,\phi)\}$ on the sphere which is distinguished by the label $\ell \in L$ from a finite set L, can be interpreted as Wigner functions representing an operator A by satisfying the generalized conditions of Stratonovich [1, 86, 87, 88]

1. Linearity: $A \mapsto f_A^{(\ell)}(\theta,\phi)$ is linear for each $\ell \in L$
2. Reality: $f_{A^\dagger}^{(\ell)}(\theta,\phi) = [f_A^{(\ell)}(\theta,\phi)]^*$ for each $\ell \in L$
3. Norm: $\sum_{\ell\in L}\int_{S^2} f_A^{(\ell)}(\theta,\phi) f_{\mathrm{Id}}^{(\ell)}(\theta,\phi)\mathrm{d}\mu = \mathrm{tr}(A)$
4. Covariance: $f_{R(A)}^{(\ell)}(\theta,\phi) = f_A^{(\ell)}(R^{-1}(\theta,\phi))$ holds for all non-selective rotations $R \in \mathrm{SU}(2)$
5. Trace: $\sum_{\ell\in L}\int_{S^2} f_A^{(\ell)}(\theta,\phi) f_B^{(\ell)}(\theta,\phi)\mathrm{d}\mu = \mathrm{tr}(AB)$.

These type of Wigner functions arise in the DROPS representation introduced in chapter 4. Such phase-space representations provide a valuable framework for the analysis, characterization, and visualization of quantum systems [15, 89, 90].

2.5 Quantum Tomography

Tomography is the process of obtaining an image of a slice through a three dimensional object. Analogously, quantum tomography is the reconstruction process applied on systems in the quantum regime. One distinguishes between quantum state and quantum process tomography.

Quantum state tomography [20] is the procedure of experimentally reconstructing the quantum state given in form of the density matrix or its phase space representation e.g. the Wigner function, by measurements on the systems. It is not possible to obtain the state just from a single copy (or experiment) of the system since there are no measurements available which

distinguish between non-orthogonal states and in addition, measurements also alter the state. However, the state can be estimated if the measurements are applied on an ensemble of copies of the desired state or repeatedly conduct the identical experiment (and generate the same state). Moreover, the measurements on the system require to be tomographically complete, i.e., all experimentally obtained operators form a basis on the Hilbert space to retrieve the complete information of the state. For example, for a single spin, we have to measure the three operators given in Eq. (2.10) together with identity.

Quantum process tomography [20], being the quantum analogue to system identification for classical systems, is the process of characterizing unknown dynamics of a system, i.e., time evolution operators or propagators. In its most basic form [27], a certain number of different and well-defined quantum states are prepared. They are then evolved, governed by the unknown dynamics, and eventually the outcome states are measured using quantum state tomography. This information is then used to identify the unknown propagator. More sophisticated techniques are available including ancilla-assisted process tomography [31], tomography with compressed sensing [91], and approaches without the necessity for applying quantum state tomography [92]. In Appendix A and B we will show how the generalized Wigner functions (of the previous section) representing states and propagators can be obtained by applying a sequence of measurements on the system.

3 Introduction to Group Theory

Groups are algebraic structures which are omnipresent in science and have notable applications in physics, chemistry, materials science, and cryptography. They are dated back to Cauchy and Lagrange. Many important contributions were made in the course of the 19th and 20th century in particular by French mathematicians including Galois, Serret, Jordan, Sylow, and Poincare [93] but also by many more scientists such as Kummer, Klein, and Lie. Still today group theory is a frequently studied discipline. In Sec. 3.1, we introduce and define the term groups in a formal way. A prominent class of groups, the symmetric groups, are then presented in Sec. 3.2 and the action of elements of this group on tensors are summarized in Sec. 3.3. Groups can be represented in certain ways, which will be shown in Sec. 3.4 and an important representation of the symmetric group is described in Sec. 3.5. An illustrative example is then given in Sec. 3.6.

3.1 Definition

A group $(G, \bullet)$ is a mathematical structure which consists of an underlying set G of elements on which an operation $\bullet$ is defined [94]. A set can be for example the integer numbers $\mathbb{Z}$ which, when equipped with an operation such as addition, form a group. This operation, which combines two elements of the set to a third element again in the set, has to satisfy the four group axioms

1. Associativity: for every $a_1, a_2, a_3 \in G$, the associative property is fulfilled, i.e., $(a_1 \bullet a_2) \bullet a_3 = a_1 \bullet (a_2 \bullet a_3)$.

2. Identity: there exists an unique element $e \in G$, the identity, such that the relation $e \bullet a = a \bullet e = a$ holds for every $a \in G$.

3. Invertibility: for every element $a \in G$, there exists an element $\overline{a} \in G$, such that the relation $a \bullet \overline{a} = \overline{a} \bullet a = e$ is satisfied.

4. Closure: for all elements $a_1, a_2 \in G$, the result of the operation is also in G, i.e., $a_1 \bullet a_2 \in G$.

If also the commutativity propertiy $a_1 \bullet a_2 = a_2 \bullet a_1$ is satisfied, then the group is called abelian. If the underlying set G of a group is finite, then the group is also denoted finite with its cardinality $|G|$ given by the number of elements in G. More details can be found in literature [95, 96, 97, 98, 69, 99, 100, 35, 101]. A non-abelian and finite group will be introduced in the next section, the so called symmetric group.

3.2 Symmetric Group

Let $G = \{1, 2, \ldots, g\}$ be a finite set with g symbols. We introduce a permutation σ which is a bijective mapping from G to itself

$$\sigma : G \longmapsto G. \tag{3.1}$$

The action of σ onto G is the rearrangement of the elements $a \in G$ by replacing each a by the corresponding $\sigma(a)$. Permutations can be conveniently specified as disjoint cycles $c =$

Table 3.1: The multiplication table between two elements $\sigma_1, \sigma_2 \in S_3$ of the symmetric group S_3

$\sigma_1\sigma_2$	$()$	$(1,2)$	$(2,3)$	$(1,3)$	$(1,2,3)$	$(1,3,2)$
$()$	$()$	$(1,2)$	$(2,3)$	$(1,3)$	$(1,2,3)$	$(1,3,2)$
$(1,2)$	$(1,2)$	$()$	$(1,2,3)$	$(1,3,2)$	$(2,3)$	$(1,3)$
$(2,3)$	$(2,3)$	$(1,3,2)$	$()$	$(1,2,3)$	$(1,3)$	$(1,2)$
$(1,3)$	$(1,3)$	$(1,2,3)$	$(1,3,2)$	$()$	$(1,2)$	$(2,3)$
$(1,2,3)$	$(1,2,3)$	$(1,3)$	$(1,2)$	$(2,3)$	$(1,3,2)$	$()$
$(1,3,2)$	$(1,3,2)$	$(2,3)$	$(1,3)$	$(1,2)$	$()$	$(1,2,3)$

$(a_1, a_2, \ldots, a_n)$ meaning that each a_i is mapped to a_{i+1} and a_n to a_1. Two cycles c and $\tilde{c}$ are said to be disjoint if they do not share any element, i.e., if $a_i \neq \tilde{a}_j$ for all i and j. For example the cyclic decomposed permutation $\sigma = (1,2)(3,5)$ on the set $G = \{1,2,3,4,5\}$ results in $\{2,1,5,4,3\}$. The collection or set of all permutations σ on G forms a group and is denoted the symmetric group S_g [96, 97]. The symmetric group S_g has cardinality $g!$ since we find $g!$ permutations on a tuple out of g symbols. Its group operation is multiplication and is defined by the composition

$$(\sigma_2\sigma_1)(a) := (\sigma_2 \circ \sigma_1)(a) = \sigma_2(\sigma_1(a)) \tag{3.2}$$

for permutations $\sigma_1, \sigma_2 \in S_g$. Thus, a permutation $\sigma \in S_g$ maps $a \in G$ to $\sigma(a)$ such that $\sigma(a_1) \neq \sigma(a_2)$ for two elements $a_1 \neq a_2$. Note that in general permutations do not commute. That is $\sigma_1\sigma_2 \neq \sigma_2\sigma_1$. For example for $g = 3$, we obtain $G = \{1,2,3\}$ and $S_3 = \{(), (1,2), (2,3), (1,3), (1,2,3), (1,3,2)\}$ with the multiplication operations given in Table 3.1.

3.3 Action of Permutations on Tensors

Permutations are elements of the symmetric group S_g. They act naturally on tensor components which are composed of g elements

$$T = T_1 \otimes \cdots \otimes T_k \otimes \cdots \otimes T_l \otimes \cdots \otimes T_g \tag{3.3}$$

by permuting the indices. That is, a permutation $\sigma = (k,l)$ on T is defined as

$$\tilde{T} = T_1 \otimes \cdots \otimes T_l \otimes \ldots T_k \otimes \cdots \otimes T_N = (k,l)[T_1 \otimes \cdots \otimes T_k \otimes \ldots T_l \otimes \cdots \otimes T_N], \tag{3.4}$$

i.e., interchanging the kth and lth component. Note that σ can also be expressed as a superoperator represented by a matrix σ_M acting on the vectorized tensor components $\mathrm{vec}\,(T)$

$$\mathrm{vec}(\tilde{T}) = \sigma_M\,[\mathrm{vec}\,(T)]\,. \tag{3.5}$$

3.4 Representation of a Group

Groups are closely related to representations [36, 102, 97]. Loosely speaking, a representation [of a finite group $(G, \bullet)$] is a relationship between the elements $b \in (G, \bullet)$ and another set of elements or objects while conserving and transforming the group's properties and rules to the new set of objects. More formally, a representation is a homomorphism from $(G, \bullet)$ to the automorphism group of an object. A prominent candidate for representations are matrix representations. Here the group elements can be modeled by matrices and the group operation is

then given by matrix multiplication. By using representations in general, group-theoretic problems can be reduced to problems in for example linear algebra, for which powerful frameworks exist.

In this context, it is important to differentiate between reducible and irreducible representations. If a representation cannot be broken up into smaller ones, this representation is called irreducible. That is, if $\Gamma : (G, \bullet) \mapsto \mathrm{Aut}(V)$ is a representation, then Γ is irreducible, if and only if V is not the zero vector space and the subspaces of V are mapped to themselves under the action of every $b \in (G, \bullet)$. Assume we have two different representations Γ_1 and Γ_2 of $(G, \bullet)$, for which all elements $b \in (G, \bullet)$ are represented as matrices on the vector spaces V_1 and V_2, respectively. The action is given by matrix multiplications. Then a "combined" representation Γ composed of Γ_1 and Γ_2 can be constructed, that is a bigger matrix in the space of $V = V_1 \oplus V_2$. By using Γ, we do not get more insight in $(G, \bullet)$ compared to by using both representations Γ_1 and Γ_2. Conversely, if we have a (reducible) representation Γ, which can be decomposed into Γ_1 and Γ_2 with the respective spaces V_1 and V_2 in a way, that the action of every $b \in (G, \bullet)$ on V maps V_1 (and V_2 respectively) to itself. Then, all information can be obtained by restricting the action of $(G, \bullet)$ on V_1 and on V_2. In general, it is beneficial to work on smaller subspaces V_1 and V_2 instead of work on V. Γ_1 and Γ_2 are then called irreducible (if no proper subspace in V_1 and V_2 exists). Note that each (reducible) representation can be decomposed into a direct sum of irreducible representations. We will use this concept of irreducible representations in the next section for describing the symmetric group S_g in a convenient way.

3.5 Representation of the Symmetric Group and Young Projectors

We start by summarizing the theory of Young tableaux $\tau_i^{[g]}$ which are combinatorial objects providing us with a systematic way to construct the irreducible representation of the symmetric group S_g. That is the construction of the so called Young symmetrizers $e_{\tau_i^{[g]}}$ [94, 95, 97, 103, 35, 104, 96, 105], projectors which built such irreducible representations. An illustrative example for the methodology introduced here will be given in Sec. 3.6. A standard Young tableau of size g is a left-justified arrangement of g boxes with the number of boxes in each row and each column is non-increasing. A number of a set $G \in \{1, 2, \ldots, g\}$ is assigned to each box in a strictly increasing pattern from left to right and top to bottom. For example, for $g = 1$ we have $G \in \{1\}$ and for $g = 2$ we find $G \in \{1, 2\}$ and thus have the tableaux

$$\tau_1^{[1]} = \begin{array}{|c|}\hline 1 \\ \hline \end{array}, \quad \tau_1^{[2]} = \begin{array}{|c|c|}\hline 1 & 2 \\ \hline \end{array}, \quad \text{and} \quad \tau_2^{[2]} = \begin{array}{|c|}\hline 1 \\ \hline 2 \\ \hline \end{array}. \tag{3.6}$$

The four possibilities of standard Young tableau for $g = 3$ and $G \in \{1, 2, 3\}$ are given by

$$\tau_1^{[3]} = \begin{array}{|c|c|c|}\hline 1 & 2 & 3 \\ \hline \end{array}, \quad \tau_2^{[3]} = \begin{array}{|c|c|}\hline 1 & 2 \\ \hline 3 \\ \cline{1-1} \end{array}, \quad \tau_3^{[3]} = \begin{array}{|c|c|}\hline 1 & 3 \\ \hline 2 \\ \cline{1-1} \end{array}, \quad \text{and} \quad \tau_4^{[3]} = \begin{array}{|c|}\hline 1 \\ \hline 2 \\ \hline 3 \\ \hline \end{array}. \tag{3.7}$$

The shape of $\tau_i^{[g]}$ is described by its partition $\lambda(\tau_i^{[g]}) = [\lambda_1, \lambda_2, \ldots, \lambda_{\kappa(\tau_i^{[g]})}]$, where $\kappa(\tau_i^{[g]})$ is the number of rows of $\tau_i^{[g]}$ and λ_i with $i \in \{1, 2, \ldots \kappa\}$ is the number of boxes of row i. The filling pattern $\omega(\tau_i^{[g]}) = [\omega_1, \omega_2, \ldots, \omega_g]$ of a tableau are all entries of $\tau_i^{[g]}$ strung together from left to right in each row and from the first to the last row. For example $\lambda(\tau_3^{[3]}) = [2, 1]$ and $\omega(\tau_3^{[3]}) = [132]$. A total order on the set of the g-sized standard Young tableau can be defined in the following way: A tablau $\tau_i^{[g]} > \tau_j^{[g]}$, if $\lambda(\tau_i^{[g]}) < \lambda(\tau_j^{[g]})$ or if $\lambda(\tau_i^{[g]}) = \lambda(\tau_j^{[g]})$ and

$\omega(\tau_i^{[g]}) > \omega(\tau_j^{[g]})$. By applying these rules, the order $\tau_1^{[3]} < \tau_2^{[3]} < \tau_3^{[3]} < \tau_4^{[3]}$ in Eq. (3.7) is obtained.

Now, we have all ingredients to construct the Young symmetrizers $e_{\tau_i^{[g]}}$, which build an irreducible representation of the symmetric group S_g. These are elements of the group algebra $e_{\tau_i^{[g]}} \in \mathbb{R}[S_g]$ of S_g, i.e., they are elements of an algebraic structure consisting of a set given by the symmetric group and on which the operation of addition, multiplication, and scalar multiplication of the underlying field $\mathbb{R}$ are defined:

$$x = \sum_{\sigma \in S_g} x_\sigma \sigma \tag{3.8}$$

$$x + y = \sum_{\sigma \in S_g} (x_\sigma y_\sigma)\sigma \tag{3.9}$$

$$xy = \sum_{\sigma, \tilde{\sigma} \in S_g} (x_\sigma y_\sigma)(\sigma\tilde{\sigma}). \tag{3.10}$$

Here $x, y \in \mathbb{R}[S_g]$, $\sigma, \tilde{\sigma} \in S_g$, and $x_\sigma, y_\sigma \in \mathbb{R}$. We can now define the set of row-wise permutations $R(\tau_i^{[g]})$ and column-wise permutations $C(\tau_i^{[g]})$ for a given standard Young tableau $\tau_i^{[g]}$ by

$$R(\tau_i^{[g]}) = \prod_{i=j}^{\kappa(\tau_i^{[g]})} \sigma_j \text{ for all possibilities of } \sigma_j \in S_{R(\tau_i^{[g]},j)} \tag{3.11}$$

$$C(\tau_i^{[g]}) = \prod_{j=1}^{\lambda_1} \sigma_j \text{ for all possibilities of } \sigma_j \in S_{C(\tau_i^{[g]},j)}. \tag{3.12}$$

The order of the multiplication is irrelevant here since the different permutations σ_i act on distinct subsets of $G = \{1, \ldots, g\}$. $R(\tau_i^{[g]}, j)$ is the set of all entries and $S_{R(\tau_i^{[g]},j)}$ are all permutations of $R(\tau_i^{[g]}, j)$ in the jth row of $\tau_i^{[g]}$ with $1 \leq j \leq \kappa(\tau_i^{[g]})$. Similarly, $C(\tau_i^{[g]}, j)$ is the set of all entries and $S_{C(\tau_i^{[g]},j)}$ are all permutations of $C(\tau_i^{[g]}, j)$ in the jth column with $1 \leq j \leq \lambda_1$.

Next, the elements in $R(\tau_i^{[g]})$ and $C(\tau_i^{[g]})$ are summed up to define $H_{\tau_i^{[g]}}$ and $V_{\tau_i^{[g]}}$

$$H_{\tau_i^{[g]}} := \sum_{\sigma \in R(\tau_i^{[g]})} \sigma \tag{3.13}$$

$$V_{\tau_i^{[g]}} := \sum_{\sigma \in C(\tau_i^{[g]})} (-1)^{|\sigma|}\sigma. \tag{3.14}$$

Here σ can be decomposed in a product of a minimal number $|\sigma|$ of transpositions (p, q). The Young symmetrizers are eventually obtained by

$$e_i^{[g]} := e_{\tau_i^{[g]}} = f_{\tau_i^{[g]}} H_{\tau_i^{[g]}} V_{\tau_i^{[g]}}. \tag{3.15}$$

The normalization factor $f_{\tau_i^{[g]}}$ guarantees that $e_i^{[g]} e_i^{[g]} = e_i^{[g]}$ and is given by

$$f_{\tau_i^{[g]}} = \frac{\#\text{ standard Young tableaux of shape } \tau_i^{[g]}}{g!}. \tag{3.16}$$

Each irreducible representation is associated with an invariant subspace. A map (or projection) into one of these subspaces suffices to uniquely define the irreducible representation. As a consequence, the Young symmetrizers $e_i^{[g]}$ for every $\tau_i^{[g]}$, which are orthogonal projectors, corresponds to an irreducible representation of S_g and each of such can be constructed from the associated $e_i^{[g]}$. Note that the number of irreducible representations of S_g is given by the number of partitions with g boxes.

In a final step, we determine the Young projectors $P_i^{[g]}$ [96], which can be interpreted as orthogonalized versions of the symmetrizers $e_i^{[g]}$, with respect to tensor operators on which they can be applied. They model permutation symmetries for a given standard Young tableau $\tau_i^{[g]}$ and will be used in Sec. 4.4.2 to obtain permutational symmetrized orthogonal tensors which are invariant under their action $P_i^{[g]} T_{jm} = T_{jm}$ with $m \in \{-j, \dots, j\}$. Our approach is based on the methodology given in [96], but can also be inferred from [94, 95, 106, 98]. We start by considering the ordered sequence

$$\tau_r^{[g]} < \tau_{r+1}^{[g]} < \cdots < \tau_s^{[g]} \tag{3.17}$$

of all standard Young tableaux of a given shape λ. Here r is the index of the first and s the index of the last element. The Young projectors $P_i^{[g]}$ are recursively defined based on the symmetrizers $e_i^{[g]}$ by

$$P_i^{[g]} = \begin{cases} e_i^{[g]}, & \text{if } i = r, \\ f[d(a,b) + e] P_q^{[g]}, & \text{if } r < i \leq s. \end{cases} \tag{3.18}$$

$P_q^{[g]}$ with $q \in \{r, \dots, i-1\}$ is the projector that corresponds to the tableau $\tau_q^{[g]}$ which differs from $\tau_i^{[g]}$ only by the position of two boxes $\boxed{a}$ and $\boxed{b}$ with the consecutive labels $a \in \{1, 2, \dots, g-1\}$ and $b = a + 1 \in \{2, 3, \dots, g\}$. The (signed) axial distance $d \in \mathbb{Z}$ of box $\boxed{a}$ to box $\boxed{b}$ is the required number of steps from $\boxed{a}$ to $\boxed{b}$. Steps down or to the left are counted positively whereas steps up or to the right are counted negatively. $f \in \mathbb{R}$ is a scalar normalization factor which is chosen such as that $P_i^{[g]} P_i^{[g]} = P_i^{[g]}$. By recursively executing Eq. (3.18), the Young projectors $P_i^{[g]}$, corresponding to all standard tableaux $\tau_i^{[g]}$ and partitions $\lambda(\tau_i^{[g]})$ of a given size g, can be obtained. In the following section, an illustrative example for this methodology is presented.

3.6 Example: Young Projectors for $g = 3$

The methodology of Sec. 3.5 to obtain a (orthogonalized) Young projector is illustrated for a simple example for $g = 3$ and more explicitly for $\tau_3^{[3]}$

$$\tau_3^{[3]} = \begin{array}{|c|c|} \hline 1 & 3 \\ \hline 2 \\ \cline{1-1} \end{array} \tag{3.19}$$

as already given in Eq. (3.7). The length of $\tau_3^{[3]}$ is given by $\kappa(\tau_3^{[3]}) = 2$ and its shape (or partition) is $\lambda(\tau_3^{[3]}) = [2, 1]$ with the filling pattern $\omega(\tau_3^{[3]}) = [132]$. We find for $R(\tau_3^{[3]}, 1) = \{1, 3\}$, $R(\tau_3^{[3]}, 2) = \{2\}$, $S_{R(\tau_3^{[3]},1)} = \{(), (1,3)\}$, $S_{R(\tau_3^{[3]},2)} = \{()\}$, and as a result the row-wise permutations $R(\tau_3^{[3]}) = \{(), (1,3)\}$. Analogously, we get $C(\tau_3^{[3]}, 1) = \{1, 2\}$, $C(\tau_3^{[3]}, 2) = \{3\}$, $S_{C(\tau_3^{[3]},1)} = \{(), (1,2)\}$, $S_{C(\tau_3^{[3]},2)} = \{()\}$, and thus for the column-wise permutations $C(\tau_3^{[3]}) = \{(), (1,2)\}$. In the next step, we compute $H_{\tau_3^{[3]}}$ and $V_{\tau_3^{[3]}}$ and we obtain $H_{\tau_3^{[3]}} = () + (1,3)$,

$V_{\tau_3^{[3]}} = () - (1,2)$, and $f = 1/3$. This can be done for all tableaux in Eq. (3.7) and we get for the symmetrizers in Eq. (3.15)

$$e_1^{[2]} = e_{\tau_1^{[3]}} = \tfrac{1}{6}[() + (1,2) + (1,3) + (2,3) + (1,2,3) + (1,3,2)] \tag{3.20}$$

$$e_2^{[2]} = e_{\tau_2^{[3]}} = \tfrac{1}{3}[() + (1,2) - (1,3) - (1,3,2)] \tag{3.21}$$

$$e_3^{[2]} = e_{\tau_3^{[3]}} = \tfrac{1}{3}[() - (1,2) + (1,3) - (1,2,3)] \tag{3.22}$$

$$e_4^{[2]} = e_{\tau_4^{[3]}} = \tfrac{1}{6}[() - (1,2) - (1,3) - (2,3) + (1,2,3) + (1,3,2)]. \tag{3.23}$$

Now the Young projectors $P_i^{[3]}$ can be computed. We find for $\lambda(\tau_1^{[3]}) = [3]$ the indices $r = s = 1$, for $\lambda(\tau_2^{[3]}) = \lambda(\tau_3^{[3]}) = [2,1]$ the indices $r = 2$ and $s = 3$, and for $\lambda(\tau_4^{[3]}) = [1,1,1]$ the values $r = s = 4$. According to Eq. (3.18), it directly follows that

$$P_1^{[3]} = e_1^{[3]} \tag{3.24}$$

$$P_2^{[3]} = e_2^{[3]} \tag{3.25}$$

$$P_4^{[3]} = e_4^{[3]}. \tag{3.26}$$

To obtain $P_3^{[3]}$, we have to find q. We see that $\tau_3^{[3]}$ differs from $\tau_2^{[3]}$ only by the two boxes $\boxed{2}$ and $\boxed{3}$ with $a = 2$ and $b = 3$. Thus, we get $q = 2$. Furthermore, $d = 2$ and we eventually obtain

$$P_3^{[3]} = [2(2,3) + ()]P_2^{[3]} \tag{3.27}$$

$$= [() - (1,2) - (1,3) + 2(2,3) - 2(1,2,3) + (1,3,2)]/3. \tag{3.28}$$

4 The DROPS Representation

We already introduced Wigner functions in Sec. 2.4. In this section, we establish a particular species of generalized and continuous Wigner functions occurring in the DROPS representation, which is an acronym for discrete representation of operators for spin systems [1]. It is an intuitive representation of spin operators of coupled spin systems using multiple shapes assembled from linear combinations of spherical harmonics and conserves physically crucial properties, such as rotations under the influence of non-selective pulses and symmetries with respect to permutations of spins. The individual spherical functions or generalized Wigner functions are called droplets. It is important to mention that the methodology which will be presented in the following sections, is only valid for up to four spins 1/2. A generalization approach is, however, introduced in the appended publication in Appendix C. In Sec. 4.1 we give an overview on the DROPS representation and in Sec. 4.2 a particular choice of basis, the so called LISA basis, for this representation is shown and an example is illustrated in Sec. 4.3. Eventually, the Sec. 4.4 is dedicated to the computational details of the LISA basis.

4.1 Mapping Spin Operators to Spherical Functions

In single spin systems with $N = 1$, any spin operator A can be represented bijectively by an in general complex spherical function using the framework of Wigner functions. In doing so, the operator can be decomposed into spherical tensor operators and mapped to the corresponding spherical harmonics [86, 1]. For $N \geq 2$, this approach is, however, in general not bijective and consequently not suited for a representation since two different operators may be represented by the same shape. This restriction can be resolved by mapping the operator A not to a single but to a discrete set of spherical functions or droplets $f^{(\ell)}(\theta, \phi)$, which is called the DROPS representation [1].

An operator A can always be decomposed into a sum of droplet operators $A^{(\ell)}$

$$A = \sum_{\ell \in L} A^{(\ell)} \tag{4.1}$$

according to a suitable set L of labels or quantum numbers ℓ. Various different choices for ℓ are possible [1] but in this work, we focus on one particular decomposition which is induced by the so-called LISA basis and will be introduced in Sec. 4.2. We call $A^{(\ell)}$ the droplet operators. These can be further split up into their multipole components $A_j^{(\ell)}$

$$A^{(\ell)} = \sum_{j \in J(\ell)} A_j^{(\ell)}. \tag{4.2}$$

The occurring ranks $j \in J(\ell)$ are given by the finite set of all possible ranks $J(\ell)$ which depends on the label ℓ and is in general different for each $A^{(\ell)}$ [1]. Finally, the rank-j multipole contributions $A_j^{(\ell)}$ can be decomposed into a linear combination of irreducible spherical tensor operators $T_{jm}^{(\ell)}$ [68, 69, 70, 71, 72, 73]

$$A_j^{(\ell)} = \sum_{m=-j}^{j} c_{jm}^{(\ell)} T_{jm}^{(\ell)} \tag{4.3}$$

with the in general complex expansion coefficients $c_{jm}^{(\ell)}$. The original computation scheme (for up to four spins 1/2) for $T_{jm}^{(\ell)}$ is presented in Sec 4.4 and a generalized technique is elaborated on the appended publication in Appendix C.

On this level, the well-known mathematical correspondence between irreducible tensor operators and spherical harmonics [72, 73]

$$T_{jm}^{(\ell)} \quad \longleftrightarrow \quad Y_{jm}(\theta, \phi) \tag{4.4}$$

is exploited which maps $T_{jm}^{(\ell)}$ to $Y_{jm}(\theta, \phi)$. Eq. (4.4) directly induces a dualism between the rank-j component $A_j^{(\ell)}$ of the operator $A^{(\ell)}$ and the rank-j spherical components $f_j^{(\ell)}(\theta, \phi)$ of the droplet function $f^{(\ell)}(\theta, \phi)$

$$A_j^{(\ell)} = \sum_{m=-j}^{j} c_{jm}^{(\ell)} T_{jm}^{(\ell)} \quad \longleftrightarrow \quad f_j^{(\ell)}(\theta, \phi) = \sum_{m=-j}^{j} c_{jm}^{(\ell)} Y_{jm}(\theta, \phi). \tag{4.5}$$

Note the identical expansion coefficients $c_{jm}^{(\ell)}$. By applying Eq (4.5) to Eq. (4.2), the duality between the droplets $f^{(\ell)}(\theta, \phi)$ and the droplet operators $A^{(\ell)}$ is straightforwardly evoked via

$$A^{(\ell)} = \sum_{j \in J(\ell)} A_j^{(\ell)} \quad \longleftrightarrow \quad f^{(\ell)}(\theta, \phi) = \sum_{j \in J(\ell)} f_j^{(\ell)}(\theta, \phi), \tag{4.6}$$

which eventually results with Eq. (4.1) in the representation of an operator A by a discrete set of spherical functions $f^{(\ell)}(\theta, \phi)$

$$A = \sum_{\ell \in L} A^{(\ell)} \quad \longleftrightarrow \quad \bigcup_{\ell \in L} f^{(\ell)}(\theta, \phi). \tag{4.7}$$

In summary, an operator A is mapped to a discrete set of spherical functions $f^{(\ell)}(\theta, \phi)$ which are identified by the labels ℓ and denoted as droplets. The whole representation in Eqs. (4.5) - (4.7) is referred to as the DROPS representation.

4.2 The LISA Tensor Basis

The set L introduced in Sec. 4.1 induces a grouping of irreducible tensor operators into non-overlapping classes which are identified by the label ℓ. This guarantees the bijectivity of the mapping between operators A and spherical functions $f^{(\ell)}(\theta, \phi)$, i.e., no tensorrank j occurs more than once in each group ℓ and $J(\ell)$, respectively. There are different choices avaiable for this partitioning [1]. Here, we will focus on the partition which is generated using the so called LISA tensor basis that characterizes each droplet operator using the criteria linearity, subsystem, and further auxiliary criteria such as permutation symmetry. The irreducible tensor operators can be sorted in distinct groups ℓ, which corresponds to the decomposition of the space spanned by T_j into (irreducible) subspaces, using these criteria by proceeding in three steps:

1. The tensor operators T_j are divided according to their g-linearity, i.e., the number g of spins on which T_j acts.

2. T_j with identical g are further grouped with respect to the set G of involved spins, i.e., the spin's identities, and where the cardinality of G is given by $|G| = g$.

3. For subsystems with three or more spins ($g \geq 3$), irreducible tensor operators with indistinguishable values of g and G can be further partitioned by using the symmetry type under permutations of the set G. These permutations of set G with $|G| = g$ are characterized by a Young tableau $\tau_i^{[g]}$ and are given by the symmetric group S_g.

This scheme is exemplified with a coupled 3 spin 1/2 system in Fig 4.1. Note that the third step can be omitted if $g \leq 2$ since no rank j occurs more than once for a given set G [1]. Following the above three steps, a complete and unique label ℓ is defined by

$$\ell = (G, \tau_i^{[g]}) \tag{4.8}$$

for systems of up to five spins 1/2 and we use the notation $T_j^{(\ell)}$ for an irreducible spherical tensor which is identified by ℓ. Note that g is not required in Eq. (4.8) since g is specified by the cardinality of $|G| = g$. To further simplify the notation, compressed labels can be used for $g = 0$

$$\ell = (G, \tau_i^{[0]}) := \mathrm{Id}, \tag{4.9}$$

for $0 < g \leq 2$

$$\ell = (G, \tau_i^{[g]}) := G, \tag{4.10}$$

and for $2 < g \leq 5$

$$\ell = (G, \tau_i^{[g]}) := (G, \tau_i), \tag{4.11}$$

since these shorthand labels are still unique. Note, that for $g = N$ with N being the number of spins in the system, the labels could even be more reduced since there exists only one $G = \{1, 2, \ldots, N\}$ and thus

$$\ell = (g = N, G, \tau_i^{[g]}) := \tau_i. \tag{4.12}$$

For operators involving six or more spins ($g \geq 6$), further ad hoc labels are required to uniquely characterize the T_j, which is, however, part of the publication in Appendix C.

4.3 Example: Visualization of Three Spin 1/2 System

We present an example of the visualization of a coupled three spin 1/2 system which can be completely represented according to the partition scheme from the LISA basis as shown in Fig. 4.2 (compare also Fig. 4.1). We assume, that we have already computed the LISA-tensor basis $\{T_{jm}^{(\ell)}\}$, which is presented in detail in Sec 4.4. For a three spin 1/2 system ($N = 3$), we find $0 \leq g \leq 3$, since operators can at least act on no spins and at maximum act on all $N = 3$ spins simultaneously. We follow the scheme from Sec. 4.2 and partition tensors (and the spherical functions) according to g, G, and $\tau_i^{[g]}$:

$\underline{g = 0}$**:** In this case, we find only one subsystem with no spins, i.e., $G = \emptyset$ with the only occurring rank $j = 0$. The corresponding label is $\ell = \mathrm{Id}$ as given in Eq. (4.9) for the identity part of the operator A which is mapped to the identity droplet $f^{\{\mathrm{Id}\}}(\theta, \phi)$ and which is plotted in the middle of the triangle in Fig. 4.2 (a).

$\underline{g = 1}$**:** The three subsystems $G \in \{\{1\}, \{2\}, \{3\}\}$ exist and contain only the first, the second, or the third spin, respectively. They are described by the three (linear) droplet operators $A^{(\ell)}$ with the label ℓ given by G [see Eq. (4.10)] and consist of a single rank-1 component $A_1^{(\ell)}$. The corresponding linear droplets $f^{(\ell)}(\theta, \phi)$ are plotted at the vertices of the triangle in Fig. 4.2 (a).

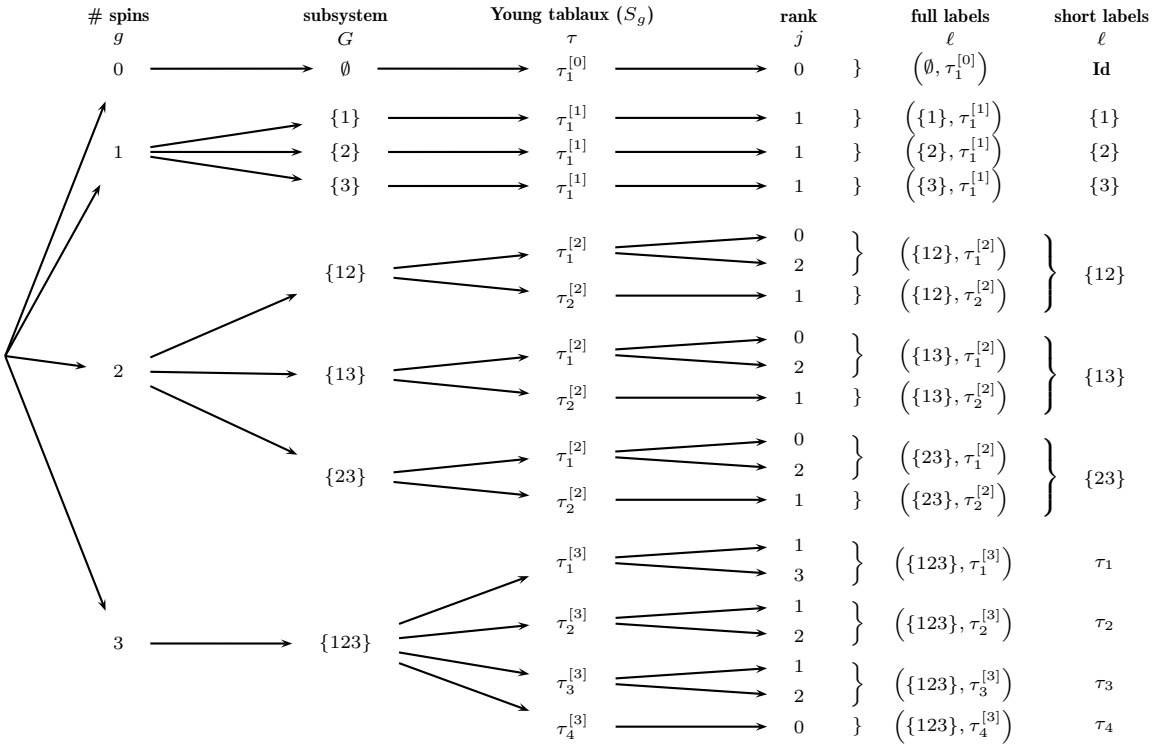

Figure 4.1: Labeling scheme for the irreducible tensor operators $T_j^{(\ell)}$ corresponding to the LISA basis for a system consisting of three coupled spins 1/2. The tensors can be partitioned first, according to their g-linearity (the number of spins involved), second, according to their subsystem G (the identity of the spins involved), and third, according to their permutation symmetry $\tau_i^{[g]}$. Since some information are redundant, compressed labels can also be used to simplify the notation in the last column. Note that for $g = 2$, both droplets for each G can be added while preserving the bijectivity, i.e., no tensors of the same rank are grouped together. This figure is an adpated version from Table 1 in [1].

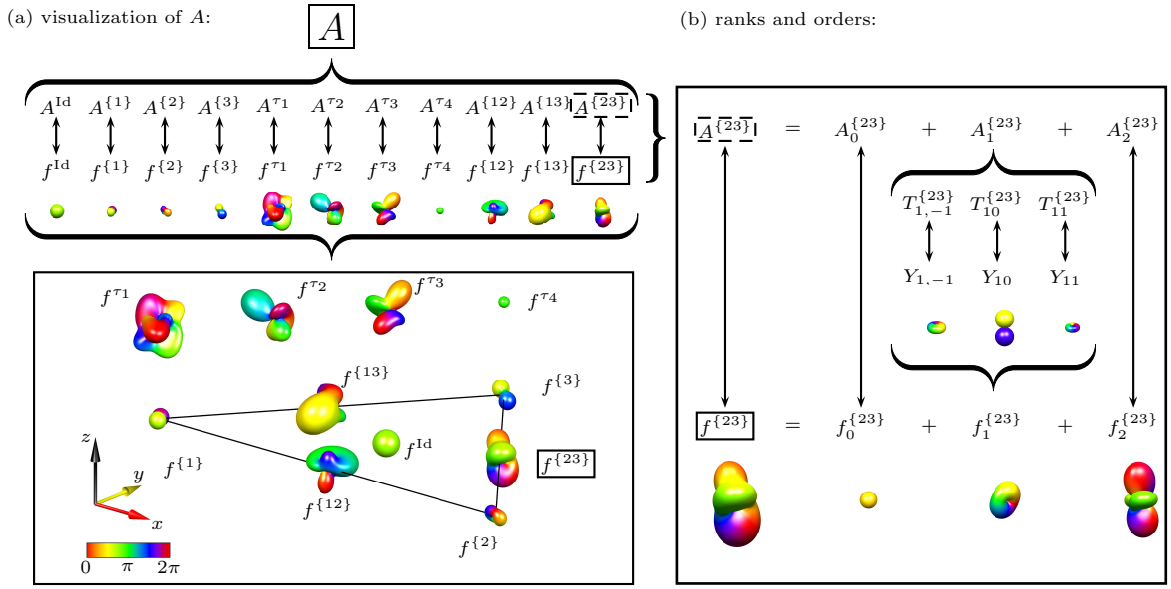

Figure 4.2: Representation of a random three-spin 1/2 operator. In (a), the operator A is decomposed into 11 droplet operators $A^{(\ell)}$ with the labels $\ell \in L$ given from the set $L = \{\mathrm{Id}, \{1\}, \{2\}, \{3\}, \{12\}, \{13\}, \{23\}, \tau_1, \tau_2, \tau_3, \tau_4\}$ which are mapped to the spherical functions $f^{(\ell)} := f^{(\ell)}(\theta, \phi)$. These can be arranged as shown in the lower panel in (a), where the nodes are associated with the particles and the edges symbolize couplings between the spins. The droplet corresponding to the identity part is placed in the middle of the triangle, the linear droplets ($g = 1$) with $\ell \in \{\{1\}, \{2\}, \{3\}\}$ are plotted on the corresponding node for each spin, the bilinear doplets ($g = 2$) with $\ell \in \{\{12\}, \{13\}, \{23\}\}$ are placed on the edges between the corresponding spins, and the trilinear droplets ($g = 3$) with $\ell \in \{\tau_1, \tau_2, \tau_3, \tau_4\}$ are plotted above the triangle. In (b), the mapping from the droplet operator $A^{\{23\}}$ to the droplet $f^{\{23\}}$ is highlighted by decomposing $A^{\{23\}}$ into its rank-j components with $j \in \{0, 1, 2\}$ and where each $A_j^{\{23\}}$ can be further split up into its orders m (tenors components $T_{jm}^{\{23\}}$) with $m \in \{-j, \ldots, j\}$. This is exemplified for $A_1^{\{23\}}$ into its three parts with $m \in \{-1, 0, 1\}$. These are then mapped to the corresponding spherical harmonics $Y_{jm} := Y_{jm}(\theta, \phi)$, which can analogously be synthesized to the rank-j parts $f_j^{\{23\}}$ and eventually to the droplet $f_j^{\{23\}}$.

$g = 2$: We also find three subsystems $G \in \{\{12\}, \{13\}, \{23\}\}$ which contain exactly two spins. The labels ℓ are also directly given by G as stated in Eq. (4.10). The three bilinear droplet operators $A^{(\ell)}$ exhibit three rank-j parts $A_j^{(\ell)}$, with $j \in 0, 1, 2$. The corresponding (bilinear) droplets $f^{(\ell)}$ are plotted on the edges of the triangle in Fig. 4.2 (a).

$g = 3$: Finally, for $g = N = 3$, the only subsystem which contains all spins is $G = \{123\}$. Since tensor operators in this group with ranks $j = 1$ and $j = 2$ occur more than once, symmetry types are used in the LISA basis reflecting permutation symmetries of the elements in the set G, to obtain finer decomposition and thus a complete labeling. For $|G| = 3$, there are four types characterized by the standard Young tableaux $\tau_i^{[3]}$ [see Eq. (3.7)] and the labels are given by $\ell \in \{\tau_1, \tau_2, \tau_3, \tau_4\}$. The four trilinear droplet operators $A^{(\ell)}$ (each with different rank-j components) are mapped to the corresponding four droplets which are located above the triangle in Fig. 4.2 (a).

Each rank-j droplet operator $A_j^{(\ell)}$ and spherical function $f_j^{(\ell)}(\theta, \phi)$ consists of $2j + 1$ orders with $m \in \{-j, \ldots, j\}$ given by the spherical tensors $T_{jm}^{(\ell)}$ and spherical harmonics $Y_{jm}(\theta, \phi)$, respectively. Note that the symmetry type can also be specified for $g \leq 2$ (see Fig. 4.1). It is trivial for $g \in \{0, 1\}$, since the set G only contains zero or one element. For $g = 2$, there are two symmetry types $\tau_1^{[2]}$ (defining the irreducible tensors of rank $j = 0$ and $j = 2$) and $\tau_2^{[2]}$ (characterizing the irreducible tensor of rank $j = 1$). See also Eq. (3.6). As a consequence, we would have two droplet operators for each bilinear subsystem $G =\in \{\{12\}, \{13\}, \{23\}\}$. However, since in each G, there are only tensors of different ranks $j \in \{0, 1, 2\}$, the corresponding two droplets can be summed up and the labels $\tau_1^{[2]}$ and $\tau_2^{[2]}$ can be suppressed in ℓ. In general, different symmetry types are grouped to different droplets. Here, the bilinear operators are an exception which combines the two dissimilar symmetry types in a single droplet.

The droplets $f^{(\ell)}(\theta, \phi)$ can be plotted using three-dimensional polar plots where the distance from the origin to a point on the surface is given by the absolute value $|f^{(\ell)}(\theta, \phi)|$ and the color is given by phase $\vartheta = \arg[f^{(\ell)}(\theta, \phi)]$ and is defined by the color bar in Fig. 4.2 (a).

4.4 Construction Details of the LISA Tensor Basis

We start with a brief repetition of the Clebsch-Gordon decomposition in Sec. 4.4.1. Then, the LISA tensor basis $\{T_{jm}^{(\ell)}\}$ can be iteratively constructed in three consecutive steps: First, in Sec. 4.4.2, the g-linear tensor operators of a g-spin system for $g \in \{0, 1, \ldots, N\}$ are built by repeatedly applying the Clebsch-Gordon decomposition and subsequently exploiting the projection operators from Sec 3.5 to symmetrize the tensors. Second, these symmetrized g-linear tensors are phase and sign corrected, which is described in Sec. 4.4.3. Third, the g-linear tensors for $g \in \{0, 1, \ldots N\}$ are embedded into the full N-spin system presented in Sec. 4.4.4.

4.4.1 Clebsch-Gordon Decomposition

The Clebsch-Gordon decomposition [69, 71, 107, 108] decomposes an inner product of two irreducible (symmetric group) representations which form a reducible representation into a direct sum of irreducible representations

$$T_{j_1} \otimes T_{j_2} = \bigoplus_{|j_1 - j_2|}^{j_1 + j_2} T_j. \tag{4.13}$$

The tensor components T_{jm} for all $j \in \{|j_1 - j_2|, \ldots, j_1 + j_2\}$ and $m \in \{-j, \ldots, j\}$ are explicitly given by

$$T_{jm} = \sum_{m=m_1+m_2} C^{jm}_{j_1 j_2 m_1 m_2} T_{j_1 m_1} \otimes T_{j_2 m_2}, \tag{4.14}$$

where $C^{jm}_{j_1 j_2 m_1 m_2}$ are the so called Clebsch Gordon coefficients [69, 71, 107, 108] which depend on the ranks j, j_1, and j_2 and orders m, m_1, and m_2 of the tensors. They frequently appear in the coupling of spins and angular momenta as the expansion coefficients for an (uncoupled) tensor product basis into a (coupled) total angular momentum basis. Several techniques are available for the computation of the Clebsch-Gordan coefficients, which includes recursion relations and explicit formulas [109, 110, 111]. Tables of these coefficients can also be found for example in [108].

4.4.2 Construction of the g-linear Tensors

A single isolated spin 1/2 can be described by a rank $j = 0$ and $j = 1$ tensor as defined in Eq. (2.11) and Eq. (2.12). The g-linear tensors are iteratively constructed for each $g \in \{0, 1, \ldots, N\}$:

$\underline{g = 0}$: We start the construction process by computing the single tensor for a subsystem without any spins, i.e., $g = 0$. The only occurring tensor is of rank $j = 0$ and the symmetry with respect to particle permutation is trivial and is given by the empty tableau $\tau_1^{[0]} = \boxed{0}$, since there is no particle in $G = \emptyset$ and thus, no permutation possible. We find for $g = 0$

$$T_0(\tau_1^{[0]}) := T_0 \tag{4.15}$$

with its single component T_{00} defined in Eq. (2.11).

$\underline{g = 1}$: Next, we consider the subsystem with one particle $g = 1$. We have one rank $j = 1$ tensor with the trivial symmetry $\tau_1^{[1]} = \boxed{1}$

$$T_1(\tau_1^{[1]}) := T_1 \tag{4.16}$$

where the three components $m \in \{-1, 0, 1\}$ are given by Eq. (2.12).

$\underline{g \geq 2}$: In this case, the g-linear tensors $T_j(\tau_i^{[g]})$ can be iteratively determined in two steps:

1. First, the g-linear (unsymmetrized) tensors $T_p^{[g]}$ with $p \in \{|j-1|, \ldots, j+1\}$ can be iteratively constructed by coupling the tensor operator T_1 for one single spin to the $g-1$ tensors $T_j^{[g-1]}$ using the Clebsch-Gordan decomposition introduced in Sec 4.4.1

$$T_j^{[g-1]} \otimes T_1 = T_{j-1}^{[g]} \oplus T_j^{[g]} \oplus T_{j+1}^{[g]}, \tag{4.17}$$

and where the $2j + 1$ components of the g-linear tensor $T_j^{[g]}$ with $m \in \{-j, \ldots, j\}$ are given by the Clebsch-Gordan coefficients. For example, the three bilinear tensors $T_0^{[2]}$, $T_1^{[2]}$, and $T_2^{[2]}$ for $g = 2$ are obtained via

$$T_1^{[1]} \otimes T_1 = T_0^{[2]} \oplus T_1^{[2]} \oplus T_2^{[2]} \tag{4.18}$$

and for $g = 3$ the seven trilinear tensors are calculated by

$$T_0^{[2]} \otimes T_1 = \dot{T}_1^{[3]} \tag{4.19}$$

$$T_1^{[2]} \otimes T_1 = \ddot{T}_0^{[3]} \oplus \ddot{T}_1^{[3]} \oplus \ddot{T}_2^{[3]} \tag{4.20}$$

$$T_2^{[2]} \otimes T_1 = \dddot{T}_1^{[3]} \oplus \dddot{T}_2^{[3]} \oplus \dddot{T}_3^{[3]}. \tag{4.21}$$

where the dots over the T are only introduced here to help the reader to distinguish tensors of same rank j. Note, that $T_1^{[1]}$ is identical to T_1.

2. Second, the symmetrized g-linear tensors $T_j(\tau_i^{[g]})$ are obtained from their unsymmetrized versions $T_j^{[g]}$ by applying the projection operator $P_i^{[g]}$ on $T_j^{[g]}$ with its action described in Sec. 3.3. The symmetrized tensor components fulfill the following equation

$$P_i^{[g]} T_j(\tau_l^{[g]}) = \begin{cases} T_j(\tau_l^{[g]}) & \text{if } i = l, \\ 0 & \text{if } i \neq l. \end{cases} \tag{4.22}$$

Explicitly, we obtain for example for $g = 2$

$$T_0(\tau_1^{[2]}) = T_0^{[2]} \tag{4.23}$$
$$T_1(\tau_2^{[2]}) = T_1^{[2]} \tag{4.24}$$
$$T_2(\tau_1^{[2]}) = T_2^{[2]} \tag{4.25}$$

and for $g = 3$

$$T_{0m}(\tau_4^{[3]}) = \ddot{T}_{0m}^{[3]} \tag{4.26}$$
$$T_{1m}(\tau_1^{[3]}) = \tfrac{3}{\sqrt{5}} \dot{T}_{1m}^{[3]} + \tfrac{6}{5} \dddot{T}_{1m}^{[3]} \tag{4.27}$$
$$T_{1m}(\tau_2^{[3]}) = \tfrac{3}{2} \dot{T}_{1m}^{[3]} - \tfrac{3\sqrt{5}}{4} \ddot{T}_{1m}^{[3]} \tag{4.28}$$
$$T_{1m}(\tau_3^{[3]}) = \ddot{T}_{1m}^{[3]} \tag{4.29}$$
$$T_{2m}(\tau_2^{[3]}) = \dddot{T}_{2m}^{[3]} \tag{4.30}$$
$$T_{2m}(\tau_3^{[3]}) = \ddot{T}_{2m}^{[3]} \tag{4.31}$$
$$T_{3m}(\tau_3^{[3]}) = \dddot{T}_{3m}^{[3]} \tag{4.32}$$

4.4.3 Phase and Sign Convention

The irreducible spherical (and symmetrized) tensors $T_j(\tau_i^{[g]})$ are uniquely defined up to an algebraic sign [1, 78, 112]. To address this non-uniqueness, we apply conventions to define more precisely the shapes of the spherical functions $f^{(\ell)}(\theta, \phi)$:

1. The spherical functions representing Hermitian operators exhibit only the colors red and green corresponding to phases 0 and π.

2. The droplet visualizing the identity operator is a sphere and has a positive (red) value.

3. The Wigner functions for linear Cartesian operators $I_{k\eta}$ with $\eta \in \{x, y, z\}$ [6] consist of two spheres colored red and green and the positive lobe points in the direction of the η-axis.

4. The droplets for bilinear operators $2I_{1\eta}I_{2\eta}$ [6] consist of a positive and a negative part which is displaced in the η_3-direction with respect to the center of the droplet.

5. The spherical functions representing the fully symmetric Cartesian tensor $4I_{1\eta}I_{2\eta}I_{3\eta}$ is of an elongated shape where its positive lobe points in the direction of η-axis.

6. Raising and lowering operators are visualized by donut shapes with rainbow colors and where the number of rainbows are given by the coherence order. The sequence of the colors of the raising operator are inverse compared to the lowering operator.

Table 4.1: Algebraic sign convention for each g-linear spherical tensor operator $T_j(\tau_i^{[g]})$. The entries show with which sign and phase $T_j(\tau_i^{[g]})$ has to be multiplied to obtain the sign-corrected LISA basis.

g	T_0	T_1	T_2	T_3
0	$T_0(\tau_0^{[0]})$			
1		$T_1(\tau_1^{[1]})$		
2	$-T_0(\tau_1^{[2]})$	$-iT_1(\tau_2^{[2]})$	$T_2(\tau_1^{[2]})$	
3	$iT_0(\tau_4^{[3]})$	$-T_1(\tau_1^{[3]})$	$iT_2(\tau_2^{[3]})$	$T_3(\tau_1^{[3]})$
		$T_1(\tau_2^{[3]})$	$iT_2(\tau_3^{[3]})$	
		$T_1(\tau_3^{[3]})$		

7. The droplets of characteristic longitudinal and planar coupling Hamiltonians are of an elongated and disc shape.

Note that tensor components with $m = 0$ are always Hermitian. The choice of phase factor for each rank j tensor is completely arbitrary but the resulting representation can differ notably. The transformation table in Table 4.1 is used. To simplify notation, from here on, we denote the sign and phase corrected and permutatation symmetrical spherical tensors also by $T_j(\tau_i^{[g]})$.

4.4.4 Embedding

The construction of the LISA basis is completed by first embedding each g-linear (symmetrized and sign corrected) spherical tensors $T_j(\tau_i^{[g]})$ of the g-spin systems of Sec. 4.4.3, into the full N spin system with $N \geq g$ described in the case of spin 1/2 with matrices of dimension $2^N \times 2^N$. Second, we expand to the full basis with its 2^{2N} basis elements by generating all $\binom{N}{g}$ subsystems G for each g and assigning permuted versions of the embedded tensors. In this step, the labels are eventually attributed to the tensors. Explicitly, we obtain for each g:

$\underline{g = 0}$: This case is trivial since there is only one subsystem $G = \emptyset$ and the full embedded tensor is directly given by tensorizing Eq. (4.15) $N - 1$ times with T_{00} [see Eq. (2.11)]:

$$T_0^{\mathrm{Id}} := T_0^{\emptyset}(\tau_1^{[0]}) = T_0(\tau_1^{[0]}) \otimes \left(\bigotimes_n^{N-1} T_{00} \right) = \left(\tfrac{1}{\sqrt{2}} \right)^N \mathrm{id}_{2^N}. \tag{4.33}$$

id_q is the $q \times q$ identity matrix. We use the shortened label $\ell = \mathrm{Id}$ as stated in Eq. (4.9).

$\underline{g = 1}$: For $g = 1$, the components with $m \in \{-1, 0, 1\}$ of the linear tensor of Eq. (4.16) are first embedded by applying the tensor product $N - 1$ times with T_{00}:

$$T_{1,m}^{\{1\}} := T_{1,m}^{\{1\}}(\tau_1^{[1]}) = T_{1,m}(\tau_1^{[1]}) \otimes \left(\bigotimes_n^{N-1} T_{00} \right) \tag{4.34}$$

which corresponds to the linear rank $j = 1$ tensor of the group $G = \{1\}$ and where we use the combined label $\ell = \{1\}$ [see Eq. (4.10)]. Since for $g = 1$, we find $\binom{N}{1} = N$ sets of

$G \in \{\{1\},\{2\},\ldots,\{N\}\}$, the tensors for $G \in \{\{2\},\ldots,\{N\}\}$ are obtained by permuting $T^{\{1\}}_{1,m}(\tau^{[1]}_1)$ of Eq. (4.34)

$$T^{\{k\}}_{1,m} := T^{\{k\}}_{1,m}(\tau^{[1]}_1) = (1,k)T^{\{1\}}_{1,m}(\tau^{[1]}_1) \tag{4.35}$$

for $k \in \{2,3,\ldots N\}$ and where the action of the permutation $p = (k,l)$ is defined in Eq. (3.4) and Eq. (3.5), and the combined labels are used.

$\underline{g = 2}$: In this case, the bilinear tensors of Eqs. (4.23) - (4.25) are first embedded into the $G = \{12\}$ subsystem of the full system by tensorizing $T_{jm}(\tau^{[g]}_i)$ $N-2$ times with T_{00}

$$T^{\{12\}}_{jm} := T^{\{12\}}_{jm}(\tau^{[2]}_i) = T_{jm}(\tau^{[2]}_i) \otimes \left(\bigotimes_n^{N-2} T_{00} \right) \tag{4.36}$$

with $j \in \{0,1,2\}$ and $m \in \{-j,\ldots,j\}$. The bilinear tensors $T^{\{kl\}}_{jm}(\tau^{[g]}_i)$ for all $\binom{N}{2}$ bilinear subsystems $G \in \{\{12\},\{13\},\{23\}\}$ are then obtained by permuting $T^{\{12\}}_{jm}(\tau^{[g]}_i)$ in Eq. (4.36)

$$T^{\{kl\}}_{jm} := T^{\{kl\}}_{jm}(\tau^{[2]}_i) = \begin{cases} (2l)T^{\{12\}}_{jm}(\tau^{[2]}_i), & \text{if } k = 1 \ \wedge \ l > 2 \\ (1k)(2l)T^{\{12\}}_{jm}(\tau^{[2]}_i), & \text{if } l > k > 1. \end{cases} \tag{4.37}$$

with the labels ℓ directly given by G as stated in Eq (4.10).

$\underline{g \geq 3}$: This approach is generalized for $g \geq 3$. First, we embed the symmetrized tensors $T_{jm}(\tau^{[g]}_i)$ from Eq. (4.22) in the subsystem $G = \{12\ldots g\}$ by tensorizing $N-g$ times with T_{00} and obtain

$$T^{\{\{12\ldots g\},\tau^{[g]}_i\}}_{jm} := T^{\{12\ldots g\}}_{jm}(\tau^{[g]}_i) = T_{jm}(\tau^{[g]}_i) \otimes \left(\bigotimes_n^{N-g} T_{00} \right), \tag{4.38}$$

where the shorthand notation for the labels ℓ can be used for $N = g$ as introduced in Eq. (4.11). Then, the tensors for all remaining $\binom{N}{g} - 1$ subsystems are obtained by permutation of $T^{\{\{12\ldots g\},\tau^{[g]}_i\}}_{jm}$

$$T^{\{\{k_1 k_2 \ldots k_g\},\tau^{[g]}_i\}}_{jm} = \begin{cases} (gk_g)T^{\{\{12\ldots g\},\tau^{[g]}_i\}}_{jm}, & \text{if } k_n = 1 \ \forall n \in \{1,\ldots,g-1\} \\ & \wedge \ k_g > g \\ ([g-1]k_{g-1})(gk_g)T^{\{\{12\ldots g\},\tau^{[g]}_i\}}_{jm}, & \text{if } k_n = 1 \ \forall n \in \{1,\ldots,g-2\} \\ & \wedge \ k_g > k_{g-1} > g \\ \vdots & \vdots \\ (1k_1)\cdots(gk_g)T^{\{\{12\ldots g\},\tau^{[g]}_i\}}_{jm}, & \text{if } k_g > k_{g-1} > \cdots > k_1 > g. \end{cases} \tag{4.39}$$

After executing the above steps, the complete LISA basis $\{T^{(\ell)}_{jm}\}$ is eventually constructed and can be used in Eqs. (4.5) - (4.7) to first decompose an operator A into different groups ℓ of tensors operators and then establish the mapping to the set of spherical function $f^{(\ell)}(\theta,\phi)$.

5 NMR and Quantum Information

A nucleus in a magnetic field can absorb and reemit electromagnetic radiation. This physical phenomenon is called nuclear magnetic resonance (NMR). The energy of the radiation is given by a specific resonance frequency which depends on the magnetic properties of the particle in the field and on the magnetic field's strength. By exploiting the NMR effect, observation of particular quantum mechanical magnetic properties of nuclei can be made leading to applications in NMR spectroscopy, magnetic resonance imaging, and quantum information processing. This will be the focus on here. In Sec. 5.1, the NMR basics are briefly introduced, followed by the most prominent description of NMR, i.e., the product operators in Sec. 5.2. We then provide a quantum mechanical treatment of NMR in Sec. 5.3. We conclude this chapter by outlining connections to quantum information processing in Sec. 5.4. Note that we focus on liquid state NMR here, for which rich literature is available [6, 113, 114, 20].

5.1 NMR Basics

In this section, we will set up the physical stage of NMR. All nuclei that are composed by neutrons and protons have an intrinsic quantum property known as spin. Its value is given by the (total) spin quantum number I. In nuclei with an even number of both protons and neutrons, the nucleons pair up resulting in a zero overall spin, i.e, $I = 0$. On the other hand, odd numbers of nucleons in a nuclei give rise to a non-zero spin which is associated with a non-zero magnetic moment μ by

$$\mu = \gamma I \tag{5.1}$$

and where γ is a proportionality constant of a specific nucleus known as the gyromagnetic ratio. It defines the ratio between the magnetic moment and the angular momentum. Thus, such a nucleus behaves like a small magnet. A particle with spin I has $2I + 1$ energy levels characterized by the azimuthal quantum number $m \in \{-I, \ldots, I\}$ and which are in absence of an external magnetic field degenerated, i.e., they have the same energy.

However, in presence of a magnetic field B_0, the non-vanishing magnetic moment of a particle with $I \neq 0$ evokes an interaction with B_0 inducing shifts in the energy levels which have then slightly different energies. This is known as the Zeeman effect and the energy separation between the sublevels in a magnetic field is known as the Zeeman splitting. Only the application of a magnetic field breaks this degeneracy. Typically, the classical description of the magnetic field is an accurate estimation and is preferable in NMR. A particle with non-vanishing spin I responses to a magnetic field B_0 by moving its magnetic moment on a cone. This motion is called precession and its frequency ω_0, also denoted the Lamour frequency, is given by

$$\omega_0 = -\gamma B_0. \tag{5.2}$$

In NMR, the sample does not consist of a single particle, but contains a huge amount of nuclei. In the absence of the external magnetic field, the spin polarizations of all particles are uniformly distributed resulting in a total magnetic moment of the sample of approximately zero. If the field is switched on, all nuclei precess around the field with their Lamour frequency. This precession does not change the total magnetic moment.

However, the nuclei (or to be more precise the molecules which contain the nuclei) undergo constant vigorous motion and their local fields slightly influence each other since each molecule is full of sources of magnetic fields, i.e., the electrons and nuclei. As a consequence, the nuclei precess not only around the static external field B_0, but around the sum of B_0 and all the fast time- and direction-varying microscopic fields created by the particles. These small fluctuations brake down the isotropy of spin polarization and facilitate the development of a macroscopic nuclear magnetic moment or bulk magnetization. The orientation of the magnetic moment of each nuclear spin wanders around between different precession cones. Due to the magnetic field and the finite temperature, an orientation with low magnetic energy, i.e., the magnetic moments are parallel to the magnetic field, is preferable than towards an orientation with high magnetic energy, i.e., the magnetic moments are antiparallel to the magnetic field. This biased process eventually results in a stable anisotropic distribution of orientations of magnetic moments, which is then called thermal equilibrium. Consequently, this anisotropic magnetization distribution leads to a small net magnetic moment of the entire sample (along the magnetic field). The time needed for this process is called spin-lattice relaxation time or longitudinal relaxation time and the time constant T_1.

Unfortunately, this longitudinal spin magnetization is very small and almost undetectable. That's the reason why in NMR another path is followed. This is that the magnetization perpendicular to the field is measured. In thermal equilibrium, perpendicular net magnetization is zero since the individual magnet moments are distributed cylindrically symmetrical around the axis of the external magnetic field (usually denoted as the z-axis). However, by applying high frequency pulses, i.e., oscillating radio-frequency fields (rf fields), of appropriate frequency and duration, the net polarization can be rotated to the perpendicular plane (x-y-plane), since these rf fields rotate the magnet moment of each individual spin. As a consequence the total magnetization is transferred from the z-axis to the x-y-plane and is then called transverse magnetization. The single spins continue their precession and since the net magnetization is now perpenticular to the magnetic field B_0, the total magnetic moment also precesses with the Larmor frequency of the individual spins. This net magnetization slowly decays until it is zero. This process is described by the spin–spin relaxation characterized by the time constant T_2. Note that this description is oversimplified since in reality different spins experience slightly different magnetic fields and the interactions between the nuclear spins are not considered here.

Although the rotating transverse magnetization is also very small, it is detactable using a wire coil perpendicular to the external magnetic field and a sensitive rf detector. The net magnetization moment precesses at a defined frequency, which is associated with a rotating magnetic field which itself induces an electric field in the coil as described by the Maxwell's equations. This electric field generates an oscillating electric current in the wire that can eventually be detected and inferred on the precessing transverse magnetization. This oscillating current is called the free-induction decay (FID) and gives rise to the NMR signal. The FID can then be further processed using filter functions and Fourier transformation to obtain the spectrum of the sample.

5.2 Product Operator Basis in NMR

In this section, we will introduce product operators, the most prominent basis for describing NMR systems and experiments with quantum mechanical methods. We start by defining a basis for a single spin 1/2. We focus here on spins 1/2 since these nuclei are the most abundant in NMR spectroscopy although spin operators exist for particles with different spins. The four basis operators in this case are the matrix representations of the components of the spin angular

momentum operators together with the identity [114, 6]

$$I_x = \frac{1}{2}\begin{pmatrix} 0 & 1 \\ 1 & 0 \end{pmatrix}, \quad I_y = \frac{1}{2}\begin{pmatrix} 0 & -i \\ i & 0 \end{pmatrix}, \quad I_z = \frac{1}{2}\begin{pmatrix} 1 & 0 \\ 0 & -1 \end{pmatrix}, \quad I_0 = \frac{1}{2}\begin{pmatrix} 1 & 0 \\ 0 & 1 \end{pmatrix}. \tag{5.3}$$

They form a complete basis, i.e., the density matrix ρ of a spin system can be decomposed as a linear combination of these operators.

The product operators for a system containing N spins can be built up by tensorizing the single spin product operators of Eq. (5.3). We introduce the additional subscript $k \in \{1, 2, \dots N\}$ identifying the individual spins. We find in general

$$I_{1a_1} I_{2a_2} \cdots I_{Na_N} = \bigotimes_{k=1}^{N} I_{a_k} \tag{5.4}$$

with $a_k \in \{x, y, z, 0\}$. Since the norm of the product operators is not in general identical to 1, norm-preserving constants c_N are introduced, which are multiplied with the product operators $c_N I_{1a_1} I_{2a_2} \cdots I_{Na_N}$ and where $c_N = 2^{N-1}$. Note that I_{k0} is omitted in the left hand side notation in Eq. (5.4). For example, we write I_{2z} instead of $I_{10} I_{2z}$. These operators are also correlated to some physical properties. For example, if ρ has only the term I_{2z}, the net polarization of spin I_2 is then along the magnetic field, whereas the polarizations of I_1 is isotropically distributed.

The product operators and their evolution, which will be described in the next section, is a rigorous quantum mechanical description to compute the outcome of NMR experiments by predicting the evolution of the bulk magnetization over time under the action of different Hamiltonians. It is based on the formalism of density matrix theory introduced in Sec. 2.1

5.3 Quantum Mechanical Description of NMR Experiments

After the rather qualitative introduction to NMR in Secs. 5.1 and 5.2, we will now focus on a quantitative description here. Since classical models such as the vector model or energy levels fail to describe even the simplest NMR experiment with involved coupled spins, we will only focus on the quantum mechanical framework of NMR for coupled particles using the product operators from Sec 5.2.

We start the description of the NMR system in thermal equilibrium at typical settings. That is, after the sample, which contains the ensemble of molecules and thus the spin systems, is placed into an NMR spectrometer with constant magnetic field B_0 at approximately room temperature. Then the ensemble of the spin systems follows the Boltzmann distribution. In the high-temperature limit, the thermal equlibrium density operator reads as

$$\rho_{\text{th}} = \frac{\mathbf{1}}{2^N} + \sum_k \mathcal{B}_k I_{kz} \tag{5.5}$$

with the Boltzmann factors given by $\mathcal{B}_k = \hbar\gamma_k B_0 / k_b T$ and with k_B being the Boltzmann constant and T the temperature of the system.

Next, the typical Hamiltonians which govern the time evolution of states in NMR are summarized. The total Hamiltonian H_{tot} of the system is given by

$$H_{\text{tot}} = H_0 + H_{\text{rf}}. \tag{5.6}$$

H_0 includes the interaction with the magnetic field, magnetic dipole coupling, J-coupling (indirect coupling mediated between the electrons of the chemical bonds between spins), and interactions with the environment. Accordingly, H_{rf} is the Hamiltonian arising from rf pulses.

We focus on liquid state NMR, i.e., the sample consists of an isotropic liquid. As a consequence, the molecules can move and rotate independently from each other and hence intramolecular interactions average out except for the isotropic part. Typically when applying NMR techniques for quantum information processing, we have heteronuclear systems, i.e., systems consisting of different species of spins, to differentiate and address the single spins individually. The couplings in such molecules are almost always weak. That is $|\omega_{0j} - \omega_{0k}| >> |\pi J_{jk}|$, where J_{jk} is the coupling constant between nucleus k and j, and ω_{0k} and ω_{0j} are the Lamour frequencies of spin k and j respectively. In total, we get a good approximation for H_0

$$H_0 = \sum_k \omega_{0k} I_{kz} + \sum_{j<k} 2\pi J_{jk} I_{jz} I_{kz}. \tag{5.7}$$

The first part is associated with the precission of the spins and the second part with the scalar J-coupling between spins in the weak coupling regime. Next, we discuss the transformation of a product operator under an rf field. We assume that the pulse is strong and has a short duration so that resonance offsets and J-coupling effects are negligible in the presence of the pulse. Furthermore, we assume a constant pulse. The result of such a high frequency field is a rotation of the state. A pulse is described by a phase α_k and a frequency ω_{1k}. Because of the arrangement of the coils in a typical NMR spectrometer, the range of the pulse's phase is between 0 and 2π in the perpendicular plane. The Hamiltonian is therefore

$$H_{\mathrm{rf}} = \sum_k \omega_{1k} [\cos(\alpha_k) I_{kx} + \sin(\alpha_k) I_{ky}]. \tag{5.8}$$

As already discussed in Sec. 2.1, the time evolution of a system is governed by the Liouville–von Neumann equation in Eq. (2.2), for which solutions for a specific Hamiltonian are given in Eq. (2.3) and Eq. (2.4). Hence, we obtain for the propagator for the evolution under coupling, i.e., without applying a pulse, using Eq. (5.7)

$$U_0 = \exp\left(-i \left[\sum_k \omega_{0k} I_{kz} + \sum_{j<k} 2\pi J_{jk} I_{jz} I_{kz} \right] t \right). \tag{5.9}$$

Furthermore, the propagator for the evolution under the effect of H_{rf} is given by exploiting Eq. (5.8)

$$U_{\mathrm{rf}} = \exp\left(-i \left\{ \sum_k \omega_{1k} [\cos(\alpha_k) I_{kx} + \sin(\alpha_k) I_{ky}] \right\} t \right). \tag{5.10}$$

Note that $\hbar$ was set to 1 for simplicity and t is the duration of the evolution period under coupling or of the pulse, respectively. Alternatively, we can define a flip angle θ with

$$\theta_k = \omega_{1k} t \tag{5.11}$$

and Eq. (5.10) can be recast into

$$U_{\mathrm{rf}} = \exp\left(-i \sum_k \theta_k [\cos(\alpha_k) I_{kx} + \sin(\alpha_k) I_{ky}] \right) \tag{5.12}$$

For example, the propagator of a pulse with phase $\alpha = 0$ and flip angle $\theta = \pi$ that acts on spin $k = 2$ is given by $U_{\mathrm{rf}} = \exp(-i\pi I_{2x})$. With both, the propagators U_{rf} and U_0 given in Eq. (5.9) and Eq. (5.12), respectively, and the solution of the Liouville–von Neumann equation in Eq. (2.2)

$$\rho(t) = U \rho_0 U^\dagger, \tag{5.13}$$

the systems in NMR can be fully described and simulated for each point in time t by decomposing the entire NMR experiments in intervals with constants Hamiltonian H_0 and H_{rf}. Then, for each interval the corresponding propagator given in Eqs. (5.9) and (5.12) is computed, and eventually the density matrix for each interval is determined via Eq. (5.13). The above transformations are unitary since the inner products are preserved. In addition, in NMR sometimes pulsed field gradients with spatial-dependent field intensity are used, which dephases the magnetization.

5.4 Quantum Information Experiments with NMR

A quantum computer, or an apparatus which can process quantum information, must be isolated from the environment to prevent the decoherence of its quantum properties. Simultaneously, the qubits have to be accessible for transforming and reading out the information. It has to fulfill 4 criteria:

- A robust physical realization representing the quantum information described in Sec. 5.4.1
- Preparation of well-defined initial states given in Sec. 5.4.2
- Availability of a complete set of unitary transformations dictating the evolution of the system presented in Sec. 5.4.3
- Measurement of the output result shown in Sec. 5.4.4.

An NMR spectrometer, which evolved over the last decades to a an extremely sophisticated machine due to its frequent applications in chemistry, biology, and physics, can be a good candidate for such a machine and NMR spectroscopy is an ideal testbed for quantum information experiments as sketched in Sec. 5.4.5.

5.4.1 Qubits in NMR

Basically every two-level quantum system can represent a qubit. A single nuclear spin 1/2 acts as a natural and good qubit since they can have a long decoherence time and different spins are separately accessible due to their dissimilar gyromagnetic ratio and the different chemical environment shielding effects. Typically, we find in NMR ^{1}H, ^{13}C, ^{19}F, ^{31}P, and ^{35}Cl. Several admissible spins can be found on the same molecule, which then form a coupled spin system or multi-qubit processor. Fig. 5.1 shows a one qubit system (HDO) and a two-qubit system (chloroform).

5.4.2 Initialization

Each computation (or even experiment) requires to start from a well-defined prepared input. It suffices to be able to generate one specific quantum state with high accuracy since unitary operations can transform this input state into any other state. In NMR, it is practically impossible to prepare all qubits, i.e., all spins of each molecule in the ensemble, to be in the identical state since the energy difference between two levels of the qubits is much smaller than $k_B T$. However, a completely well-known and specific state can be obtained by just using the equilibrium state given in Eq. (5.5) as an initial input.

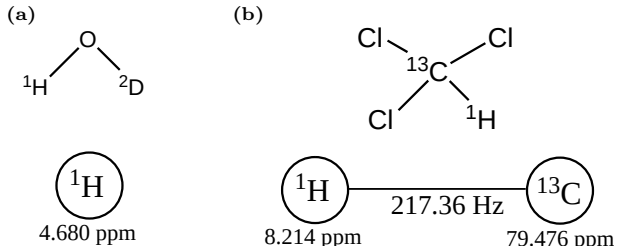

Figure 5.1: Molecules (a) HDO, (b) chloroform, with their schematic spin systems and coupling topologies; individual spins are labeled by chemical shifts (in parts per million); heteronuclear J couplings (lines) are labeled by coupling constants J_{kl} (in Hertz). The figure is in part from [2].

5.4.3 Universal Gates

The evolution of closed quantum systems in NMR is described by the propagators from Eq. (5.7) and Eq. (5.12). They can be created by evolution periods under the effect of couplings and frequency offsets and by rf pulses. Since qubits can be addressed individually and are connected via the J-coupling, both propagators can be used to generate the full range of single qubit gates and the cNOT two-qubit gate [115]. As a consequence, in NMR every (multiqubit) gate can be implemented, since each unitary transformation can be written as a decomposition of single spin operations and controlled-NOT gates. That means, universal unitary transformations can be created by a sequence of pulses and evolution periods under coupling. Nonunitary operations can be implemented by pulsed magnetic-field gradients.

5.4.4 Measurement

The measurement process is implemented with the rf coils. The computer switches to the pre-amplifier and the induced FID of the precessing spins can be detected, which is used to infer on the state of the spins. Thus, the classical measurement system is coupled to the quantum system and is only connected when desired. In NMR weak measurements are conducted since we have large ensembles of spins.

5.4.5 The Spectrometer and an NMR Experiment

The NMR system consists of two parts. First, the NMR sample is a glass tube which contains the molecules representing coupled qubits and which are typically dissolved in a solvent to reduce the inter-molecular interactions. In this state, the molecules can be described as an ensemble of identical coupled spin systems. Second, the spectrometer is a sophisticated apparatus for performing quantum information experiments. The sample is placed in a sample holder in a superconducting magnet. The generated strong static magnetic field B_0 from this magnet is per convention collinear to the z-axis. Coils are orthogonally arranged around the sample to form a tuned circuit with it. They consist of rf-electronics which allow for rapid on and off switching (pulsing). Its purpose is first to generate small, oscillating magnetic fields in the transverse x-y-plane to manipulate nuclear spin states. Second, they are used to detect the rf signal, i.e., free induction decay, generated by the precessing nuclei in the tube. This is achieved by switching between high power pulse amplifiers (for pulsing) and sensitive pre-amplifier (for acquisition) controlled by a computer. The procedure of a typical NMR experiment is then:

1. A relaxation period is used to obtain the thermal equilibrium

2. A single pulse or sequence of pulses can be applied using the rf coils and the high power pulse amplifiers to transform the states of the spins

3. After the pulse sequence, a computer switches to the sensitive pre-amplifier and the same coils detect the state of the spins by measuring the free induction decay current evoked by the precessing of spins.

4. The FID is then processed including Fourier transformations and filter functions to eventually obtain a frequency spectrum.

6 Optimal Control of Spin Systems

The optimal control of spins is an active field of research which is a combination of two disciplines: optimal control theory and spin physics. The latter one was already outlined in Sec. 2.1. This chapter gives a brief introduction to optimal control theory in quantum mechanics.

Optimal control theory is a framework for obtaining a control law for a given (dynamical) system with respect to certain optimality criteria. Such a dynamical system is described by n first order differential equations [116]

$$\dot{x}(t) = a(x[t], u[t], t) \tag{6.1}$$

and consists of (time dependent) state variables $x_i(t)$

$$x(t) = \begin{bmatrix} x_1(t) \\ x_2(t) \\ \vdots \\ x_n(t) \end{bmatrix}, \tag{6.2}$$

input variables or controls $u_i(t)$ to externally influence or steer the system

$$u(t) = \begin{bmatrix} u_1(t) \\ u_2(t) \\ \vdots \\ u_n(t) \end{bmatrix}, \tag{6.3}$$

and functions a_i depending on the states and controls

$$a(x[t], u[t], t) = \begin{bmatrix} a_1(x_1[t], x_2[t], \ldots, x_n[t], u_1[t], u_2[t], \ldots, u_n[t], t) \\ a_2(x_1[t], x_2[t], \ldots, x_n[t], u_1[t], u_2[t], \ldots, u_n[t], t) \\ \vdots \\ a_n(x_1[t], x_2[t], \ldots, x_n[t], u_1[t], u_2[t], \ldots, u_n[t], t) \end{bmatrix}. \tag{6.4}$$

The optimal control problem is then to find a set of admissible controls u^*, which minimizes a given cost function or performance measurement

$$J = h(x[t_f], t_f) + \int_{t_0}^{t_f} g(x[t], u[t], t)\mathrm{d}t \tag{6.5}$$

from the inital time t_0 to the final time t_f for given constraints on $x(t)$ and $u(t)$ stated as (in-)equalities. The set of input variables u^* that solves the optimal control problem are called optimal controls. The explicit forms of $u(t)$ and $a(t)$ depend on the modeling of the physical (or technical) system and the functions h and g on the constraints and problem-oriented cost. The greatest theoretical advances in finding optimal solutions for optimization problems are the Pontryagin maximum principle [40], which provides a necessary condition for an optimum, and the Hamilton–Jacobi–Bellman equation as a result of the framework of dynamic programming [41] supporting necessary and sufficient conditions.

Optimal control theory was introduced to quantum mechanics in the late 80s [42, 43] and is still an active research field nowadays [117]. The typical goal here is to find control fields which steer a given initial state to a desired target state in a fixed (minimum) amount of time. Constraints are then for example upper bounds for the amplitudes of the control fields. A general problem of directly applying optimal solution methods in this area is the absence of robustness against variations of the system parameters such as experimental imperfections of the control fields. However, this can be resolved by recasting the control problems into Hamiltonian problems using the Pontryagin maximum principle, i.e., finding a Hamiltonian trajectory which satisfies certain boundary conditions. Fortunately, such problems can then be solved by geometric and analytic tools [48, 49, 50, 51, 52, 53, 54] for low dimensional systems and by powerful complementary numerical frameworks such as Krotov [44], GRAPE [45], and CRAB [46, 47] in general. The latter ones can be interpreted as finding a path from the initial controls to the optimal controls in a quantum control landscape, i.e, a multidimensional hyperplane dependent on the cost functions and on the controls. However, purely numerical methods suffer from a lack of insight into the robust nature of the optimal solution and one may prefer geometrical approaches if feasible.

In non-relativistic, finite-dimensional, and closed systems the time evolution of a system is dictated by the Liouville–von Neumann equation in Eq. (2.2). The Hamiltonian, in this case, can be decomposed in

$$H = H_0 + \sum_{i=1}^{m} u_i(t) H_i \tag{6.6}$$

where H_0 is the drift or free Hamiltonian which cannot be controlled and $\sum_{i=1}^{m} u_i(t)H_i$ is the part which can be externally changed. For the case of NMR, H_0 is given by Eq. (5.7) and H_i are the radio frequency Hamiltonians given in Eq. (5.12). The control fields $u_i(t)$ are the amplitudes of the rf field that can be externally changed. A cost function can be defined as the overlap between the reached state $\rho(t_f)$ after time t_f and the desired state ρ_{target}

$$J = \langle \rho_{\text{target}} | \rho(t_f) \rangle = \text{tr}[\rho_{\text{target}}^{\dagger} \rho(t_f)]. \tag{6.7}$$

A typical constrain is t_f to be as minimal as possible while maxing J. In the appended paper "Linking the rotation of a rigid body to the Schrödinger equation: The quantum tennis racket effect and beyond" in Appendix D, a solution for such a problem is presented by exploiting a geometric framework which is established on geometric properties of the rotation of a rigid body known as the tennis raquet effect.

7 Discussion and Outlook

We conclude this thesis in Sec. 7.1 by giving a brief summary of the obtained results from the publications in Appendix A - D. A discussion in Sec.7.2 embeds these developments in existing literature. Eventually, in Sec. 7.3, future work and extensions which can be based on this thesis are discussed.

7.1 Summary

To summarize, we developed tools for the validation and optimal control of quantum systems. In the first publication "Wigner tomography of multispin quantum states" in Appendix A, a sampling scheme for the reconstruction of spherical functions was introduced. This was evolved to a Wigner tomography strategy for quantum states. It is based on measuring expectation values of rotated axial tensor operators. In the second publication "Wigner process tomography: Visualization of spin propagators and their spinor properties" in Appendix B, this concept was extended to process tomography by imprinting propagatos on the density matrix of an augmented system with an additional ancilla qubit. Both the Wigner state and the Wigner process tomography were demonstrated using NMR spectroscopy by reconstructing specific quantum states of systems of up to three qubits and typical single qubit gates. In doing so, the shapes of the droplets were experimentally recovered demonstrating their physical observability which were originally the result of a mere abstract mathematical mapping. Both methods are universally applicable and not restricted to the field of NMR and can be regarded as verification tools for quantum information processing in general but in particular for the analysis of pulse sequences in NMR spectroscopy. In the third publication "Symmetry-adapted decomposition of tensor operators and the visualization of coupled spin systems" in Appendix C, the DROPS representation, which both tomography methods build on, is generalized to systems of arbitrary spins 1/2 and to two-coupled spins with spin number $J > 1/2$. This is achieved by extending the original methodology and by introducing a novel computation approach for the LISA basis based on coefficients of fractional parentage. This paves the way for the expansion of the application areas of the Wigner (process) tomography. The thesis is complemented by presenting not only validation methods for quantum systems but also techniques to optimal control of such. In the last paper "Linking the rotation of a rigid body to the Schrödinger equation: The quantum tennis racket effect and beyond" in Appendix D, a new family of control fields is developed by transferring the description of a free rotation of a rigid body to quantum systems. This results in optimal and convenient solutions for state to state transfers and the implementation of unitary transformations, which is demonstrated with NMR techniques.

7.2 Discussion

In this section, we embed the results into existing literature. We start by having a closer look at the DROPS visualization approach, exploited throughout this thesis and which was extended in the paper "Symmetry-adapted decomposition of tensor operators and the visualization of coupled spin systems". Various visualization approaches for quantum systems are established in research and education. Threedimensional vectors such as Bloch vectors [4] are frequently used

to represent two-level systems in quantum physics, in particular magnetic resonance imaging [118, 6], spectroscopy [6], to quantum optics [15]. This technique however fails in the multi-spin case.

A prominent methodology for the visualization of multi-spin systems are bar charts, typically arising in illustrating experimental results of state tomography [20], where individual density matrix elements are represented by single bars. Alternatively, energy level diagrams [5] in the fields of quantum optics and magnetic resonance spectroscopy depicts populations by circles on energy levels and coherences by lines between energy levels. Density operators can also be visualized by non-classical vector representations build on single-transition operators [6, 7, 8] and spin dynamics can be portrayed with graphical shorthand notations [119]. However, such approaches are inconvenient for larger spin systems and important physical properties are not transferred to the visualization.

Further significant visualization approaches rely on phase space representations [15, 89, 18, 17], in particular Wigner functions [120, 15, 89]. For finite-dimensional systems, which are considered here, discrete Wigner functions [121, 122, 123, 124, 125, 126] are valuable tools for the representation, but also continuous Wigner functions for a single spin system are extensively studied in the literature [127, 88, 87, 128, 129, 130] since they naturally reflect the inherent rotational symmetries of spins. Extensions to multispin systems have been considered in [15, 12, 13, 131, 14]. But a general (continuous) Wigner representation was long time absent for arbitrary, coupled spins [131, 14] until the introduction of the DROPS representation by Garon et al [1] recently. Unfortunately, this approach is restricted to up to four coupled spins 1/2. By relying on coefficients of fractional parentage, the applicability of the DROPS visualization methodology can be considerably extended to various spin topologies, in particular to arbitrary number of coupled spins 1/2, but also to two-coupled spins with spin numbers larger than 1/2.

We move on to our novel introduced tomographic schemes established in the papers "Wigner tomography of multispin quantum states" and "Wigner process tomography: Visualization of spin propagators and their spinor properties". Tomography is substantial in almost every experiment in quantum information processing. Applications can be found in all fields of quantum physics. For example, the reconstruction of the quantum state of molecular systems can be done by calculating expansion coefficients of the decomposition of an excited state wave function via Fourier integrals from the detected signals [132, 133]. Another approach includes the computation of the overlap of the state with reference states for different time intervals to regain wave packets [134]. Tomographic schemes also exploiting Wigner functions can be frequently found in infinite-dimensional systems for which optical homodyne scheme belongs to the standard repertoire of techniques for scientists. Several demonstration experiments were conducted to reconstruct the Wigner representation of the quantum state of light [21, 22, 23, 24, 25].

In particular, our state tomography scheme shows similarities to a few other approaches in literature. In [135], Wigner functions, which are based on products of single-spin representations, are reconstructed. In [136], a comparable raster scanning approach is exploited to find the probability of the rotated quantum system being in each of the basis states by utilizing Stern-Gerlach-type experiments. Such experiments are also used in [137] to determine the Wigner function based on filtered back projections, which is closely related to planar inverse Radon transforms used e.g. in medical imaging. In contrast to our scheme, which is based on projections of operators onto rotated axial tensor operators and which is related to the measurement of spherical harmonics components of electromagnetic near-field radiation by loop antennas [138, 139, 140], their reconstruction schemes are established on Stern-Gerlach-type experiments.

Furthermore, our introduced sampling procedure for spherical functions is directly expandable to other spherical representations such as multipole operators [1] or the PROPS represen-

tation, based on compositions of single-spin representations [141]. A close resemblance can be found in the spherical tensor analysis (STA) approach, introduced by by Suter and Pearson [142] and van Beek et al. [143]. Both the STA and Wigner tomography feature a similar structure which can be attributed to characteristic properties of spherical tensor operators under rotations. That is, we find a preparation block, a rotation block, and a transformation block to convert to a detectable basis and signal, which is eventually detected during an acquisition period. However, both approaches are completely different, since first in STA the detectable signal is decomposed into individual components given by occurring ranks j and orders m of the density matrix, second a single reconversion sequence is used in the transformation block, third three Euler angles α, β, and γ are exploited in the rotation block, and fourth reconstruction is on the level of the density matrix and not Wigner functions.

In our works, experimental scanning schemes were demonstrated using a simple sampling procedure with equidistant steps of $\pi/12$ of the polar and azimuthal angles. This formed a reasonable compromise between the experiments duration and the resolution to capture all shapes in sufficient detail. However, more efficient sampling schemes are available in literature. The Wigner functions introduced here are band-limited. That is, the maximum rank of these functions is finite. For band-limited spherical functions, the minimal number of sampling points is characterized by the optimal dimensionality [144] for which various sampling strategies have been introduced approaching this limit. Methods based on an equiangular grid proposed by Driscoll & Healy [145, 146] and McEwen & Wiaux [147] exceed optimal dimensionality by factors of four and two, respectively. The Gauss-Legendre quadrature on the sphere [148] almost reaches the minimal number of sampling points. An optimal iso-latitude sampling strategy, recently introduced by Khalid et al. [144], is based on a fast and stable spherical harmonics transform. For large ranks, also the optimal dimensionality is approached by Lebedev grids [149, 150, 151].

We conclude this discussion by having a closer look on the last manuscript "Linking the rotation of a rigid body to the Schrödinger equation: The quantum tennis racket effect and beyond". The mathematical framework of the tennis racket effect has been studied in literature [58, 59, 55]. Jacobi elliptic functions [56] are used there to find the trajectories governing the dynamics of the integrable system describing the free rotation of a rigid body [55]. In our work, this concept was transfered to the quantum regime for the optimal control of two-level quantum systems [117, 152]. In general, such optimal control problems are either solved by powerful numerical frameworks such as Krotov [44], GRAPE [45], and CRAB [46, 47] or for low dimensional systems geometric and analytic tools [48, 49, 50, 51, 52, 53, 54] can be applied. Numerical methods may show a poor insight into the robustness nature of the optimal solution and the controls can exhibit complex structure. Thus, geometrical methodologies may be advantageous if they are feasible. Our approach belongs to the latter methods which results in a new family of control fields enabling the realization of either a state to state transfer or a specific unitary transformation. The interests of applications are beyond simple two-level quantum systems and range from chains of three coupled spins [153, 154], to implement a CNOT gate, to the integrable case of the Manakov top [155]. Our optimal controls are also used to realize geometric phase gates. Different techniques have been proposed in literature [156, 157]. They can be implemented either in the adiabatic regime [156] but also in the non-adiabatic domain using cyclic evolution [158, 159] to avoid decoherence effects. However, with these methods, applications are restricted to simple cases. By exploiting our approach, the range of usage can be considerably extended.

7.3 Future Work

Although this thesis is cohesive and completely closed, various interesting challenges are still unresolved. Both Wigner tomography schemes were introduced in an elementary form, i.e., with an equiangular sampling grid. An analysis of different sampling strategies was already given in the publication "Wigner process tomography: Visualization of spin propagators and their spinor properties" in Appendix B. However, experimental studies and implementations are still missing. Furthermore, experiments for four or five qubit quantum states and multi-qubit quantum gates need to be performed. The Wigner process tomography was established for known (controlled) propagators. A possible extension for unknown propagators was already proposed in the publication in Appendix B, an implementation is however still lacking. The DROPS representation (and hence the tomography schemes) was extended in Appendix C to systems containing an arbitrary number of spins 1/2 and to two-coupled spins with $J > 1/2$ by extending the original computation method and introducing a CFP-based new algorithm. Both schemes are generally applicable, still CFPs are yet only found for spins 1/2 and the projectors only feasible for up to four spins 1/2. Determination of CFPs for arbitrary spin numbers and generalized versions of projectors applicable for systems larger than four particles is still an open challenge. Finally, an experimental catalog presenting experimental imperfections and its effects on the outcome of the Wigner tomography could be extremely beneficial for a fast analysis of applied spectroscopy and quantum information processing in general.

Bibliography

[1] A. Garon, R. Zeier, and S. J. Glaser. Visualizing operators of coupled spin systems. *Phys. Rev. A*, 91:042122, Apr 2015. doi:10.1103/PhysRevA.91.042122.

[2] D. Leiner, R. Zeier, and S. J. Glaser. Wigner tomography of multispin quantum states. *Phys. Rev. A*, 96:063413, Dec 2017. URL: https://link.aps.org/doi/10.1103/PhysRevA.96.063413, doi:10.1103/PhysRevA.96.063413.

[3] J. P Dowling and G. J Milburn. Quantum technology: The second quantum revolution. 361:1655–74, 09 2003.

[4] R. P. Feynman, F. L. Vernon, Jr., and R. W. Hellwarth. Geometrical Representation of the Schrödinger Equation for Solving Maser Problems. *J. Appl. Phys.*, 28:49–52, 1957.

[5] O. W. Sørensen, G. W. Eich, M. H. Levitt, G. Bodenhausen, and R. R. Ernst. Product operator formalism for the description of nmr pulse experiments. *Progr. NMR Spectrosc.*, 16:163–192, 1983.

[6] R. R. Ernst, G. Bodenhausen, and A. Wokaun. *Principles of Nuclear Magnetic Resonance in One and Two Dimensions*. Clarendon Press, Oxford, 1987.

[7] D. G. Donne and D. G. Gorenstein. A Pictorial Representation of Product Operator Formalism: Nonclassical Vector Diagrams for Multidimensional NMR. *Concepts Magn. Reson.*, 9:95–111, 1997. doi:10.1002/(SICI)1099-0534(1997)9:2<95::AID-CMR4>3.0.CO;2-H.

[8] R. Freeman. *A Handbook of Nuclear Magnetic Resonance*. Addison Wesley Longman, Harlow, 2nd edition, 1997.

[9] U. Eggenberger and G. Bodenhausen. Moderne NMR-Pulsexperimente: eine graphische Beschreibung der Entwicklung von Spinsystemen. *Angew. Chem.*, 102:392–402, 1990. English translation in [119].

[10] T. K. Halstead and P. A. Osment. Multipole NMR. IX. Polar Graphical Representation of Nuclear Spin Polarizations. *J. Magn. Reson.*, 60:382–396, 1984.

[11] B. C. Sanctuary and T. K. Halstead. Multipole NMR. *Adv. Opt. NMR Reson.*, 15:97–161, 1991.

[12] J. P. Dowling, G. S. Agarwal, and W. P. Schleich. Wigner distribution of a general angular-momentum state: Applications to a collection of two-level atoms. *Phys. Rev. A*, 49(5):4101–4109, May 1994. doi:10.1103/PhysRevA.49.4101.

[13] P. S. Jessen, D. L. Haycock, G. Klose, G. A. Smith, I. H. Deutsch, and G. K. Brennen. Quantum control and information processing in optical lattices. *Quant. Inf. Computation*, 1:20–32, 2001.

[14] D. Harland, M. J. Everitt, K. Nemoto, T. Tilma, and T. P. Spiller. Towards a complete and continious Wigner function for an ensamble of spins or qubits. *Phys. Rev. A*, 86:062117, 2012. doi:10.1103/PhysRevA.86.062117.

[15] W. P. Schleich. *Quantum Optics in Phase Space*. Wiley-VCH, Weinheim, 2001.

[16] T. L. Curtright, D. B. Fairlie, and C. K. Zachos. *A concease treatise on quantum mechanics in phase space*. World Scientific Publishing UK, Sep 2013.

[17] F. E. Schroeck Jr. *Quantum Mechanics on Phase Space*. Springer, Dordrecht, 2013.

[18] C. K. Zachos, D. B. Fairlie, and T. L. Curtright. *Quantum Mechanics in Phase Space: An Overview with Selected Papers*. World Scientific, Singapore, 2005.

[19] E. Wigner. On the quantum correction for thermodynamic equilibrium. *Phys. Rev.*, 40:749–759, Jun 1932. doi:10.1103/PhysRev.40.749.

[20] M. A. Nielsen and I. L. Chuang. *Quantum Computation and Quantum Information*. Cambridge University Press, Cambridge (UK), 2000.

[21] D. T. Smithey, M. Beck, M. G. Raymer, and A. Faridani. Measurement of the wigner distribution and the density matrix of a light mode using optical homodyne tomography: Application to squeezed states and the vacuum. *Phys. Rev. Lett.*, 70:1244–1247, Mar 1993. doi:10.1103/PhysRevLett.70.1244.

[22] D. T. Smithey, M. Beck, J. Cooper, M. G. Raymer, and A. Faridani. Complete experimental characterization of the quantum state of a light mode via the wigner function and the density matrix: application to quantum phase distributions of vacuum and squeezed-vacuum states. *Phys. Scripta*, 1993(T48):35, 1993. doi:10.1088/0031-8949/1993/T48/005.

[23] D. T. Smithey, M. Beck, J. Cooper, and M. G. Raymer. Measurement of number-phase uncertainty relations of optical fields. *Phys. Rev. A*, 48:3159–3167, Oct 1993. doi:10.1103/PhysRevA.48.3159.

[24] U. Leonhardt. *Measuring the Quantum State of Light*. Cambridge University Press, Cambridge, 1997.

[25] M. Paris and J. Rehacek, editors. *Quantum State Estimation*. Springer, Berlin, 2004.

[26] T. Söderström and P. Stoica, editors. *System Identification*. Prentice-Hall, Inc., Upper Saddle River, NJ, USA, 1988.

[27] I. L. Chuang, N. Gershenfeld, M. G. Kubinec, and D. W. Leung. Bulk quantum computation with nuclear magnetic resonance: Theory and experiment. *Proceedings: Mathematical, Physical and Engineering Sciences*, 454(1969):447–467, 1998. URL: http://www.jstor.org/stable/53175.

[28] J. F. Poyatos, J. I. Cirac, and P. Zoller. Complete characterization of a quantum process: The two-bit quantum gate. *Phys. Rev. Lett.*, 78:390–393, Jan 1997. URL: https://link.aps.org/doi/10.1103/PhysRevLett.78.390, doi:10.1103/PhysRevLett.78.390.

[29] C. T. Schmiegelow, A. Bendersky, M. A. Larotonda, and J. P. Paz. Selective and efficient quantum process tomography without ancilla. *Phys. Rev. Lett.*, 107:100502, Sep 2011. URL: https://link.aps.org/doi/10.1103/PhysRevLett.107.100502, doi:10.1103/PhysRevLett.107.100502.

[30] A. M. Childs, I. L. Chuang, and D. W. Leung. Realization of quantum process tomography in nmr. *Phys. Rev. A*, 64:012314, Jun 2001. URL: https://link.aps.org/doi/10.1103/PhysRevA.64.012314, doi:10.1103/PhysRevA.64.012314.

[31] J. B. Altepeter, D. Branning, E. Jeffrey, T. C. Wei, P. G. Kwiat, R. T. Thew, J. L. O'Brien, M. A. Nielsen, and A. G. White. Ancilla-assisted quantum process tomography. *Phys. Rev. Lett.*, 90:193601, May 2003. URL: https://link.aps.org/doi/10.1103/PhysRevLett.90.193601, doi:10.1103/PhysRevLett.90.193601.

[32] A. Gaikwad, D. Rehal, A. Singh, Arvind, and K. Dorai. Experimental demonstration of selective quantum process tomography on an nmr quantum information processor. *Phys. Rev. A*, 97:022311, Feb 2018. URL: https://link.aps.org/doi/10.1103/PhysRevA.97.022311, doi:10.1103/PhysRevA.97.022311.

[33] J. Alcock-Zeilinger and H. Weigert. Compact hermitian young projection operators. *Journal of Mathematical Physics*, 58(5):051702, 2017. URL: https://doi.org/10.1063/1.4983478, arXiv:https://doi.org/10.1063/1.4983478, doi:10.1063/1.4983478.

[34] S. Keppeler and M. Sjödahl. Hermitian young operators. *Journal of Mathematical Physics*, 55(2):021702, 2014. URL: https://doi.org/10.1063/1.4865177, arXiv:https://doi.org/10.1063/1.4865177, doi:10.1063/1.4865177.

[35] W. K. Tung. *Group Theory in Physics*. World Scientific Publishing Company, Incorporated, 1985. URL: http://books.google.de/books?id=O89tgpOBO04C.

[36] W. Fulton and J. Harris. *Representation Theory: A First Course*. Springer, New York, 1991.

[37] D. E. Littlewood. *The Theory of Group Characters and Matrix Representations of Groups*. Clarendon Press, Oxford, 2nd edition, 1958.

[38] P. Cvitanovic. *Group Theory: Birdtracks, Lie's, and Exceptional Groups*. Princeton Univ Pr (1. Juli 2008), 2008.

[39] E. Feenberg and M. Phillips. On the Structure of Light Nuclei. *Phys. Rev.*, 51:597–608, 1937.

[40] L. Pontryagin, V. Boltyanskii, R. Gamkrelidze, and E. a. Mishchenko. *The Mathematical Theory of Optimal Processes*. Interscience Publishers, New York, 1962.

[41] R. E. Bellman. *Dynamic Programming*. Dover Publications Inc, Mineola, 2003.

[42] A. P. Peirce, M. A. Dahleh, and H. Rabitz. Optimal control of quantum-mechanical systems: Existence, numerical approximation, and applications. *Phys. Rev. A*, 37:4950–4964, Jun 1988. URL: https://link.aps.org/doi/10.1103/PhysRevA.37.4950, doi:10.1103/PhysRevA.37.4950.

[43] R. Kosloff, S. Rice, P. Gaspard, S. Tersigni, and D. Tannor. Wavepacket dancing: Achieving chemical selectivity by shaping light pulses. *Chemical Physics*, 139(1):201 – 220, 1989. URL: http://www.sciencedirect.com/science/article/pii/0301010489900128, doi:https://doi.org/10.1016/0301-0104(89)90012-8.

[44] A. I. Konnov and V. F. Krotov. On the Global Methods of Successive Improvement of Controllable Processes. *Autom. Remote Control*, 60:1427–, 1999. Russian original: *Avtom. Telemekh.* **1**999, 77–88.

[45] N. Khaneja, T. Reiss, C. Kehlet, T. Schulte-Herbrüggen, and S. J. Glaser. Optimal Control of Coupled Spin Dynamics: Design of NMR Pulse Sequences by Gradient Ascent Algorithms. *J. Magn. Reson.*, 172:296–305, 2005.

[46] P. Doria, T. Calarco, and S. Montangero. Optimal control technique for many-body quantum dynamics. *Phys. Rev. Lett.*, 106:190501, May 2011. URL: `https://link.aps.org/doi/10.1103/PhysRevLett.106.190501`, `doi:10.1103/PhysRevLett.106.190501`.

[47] T. Caneva, T. Calarco, and S. Montangero. Chopped random-basis quantum optimization. *Phys. Rev. A*, 84:022326, Aug 2011. URL: `https://link.aps.org/doi/10.1103/PhysRevA.84.022326`, `doi:10.1103/PhysRevA.84.022326`.

[48] U. Boscain, G. Charlot, J.-P. Gauthier, S. Guérin, and H.-R. Jauslin. Optimal control in laser-induced population transfer for two- and three-level quantum systems. *Journal of Mathematical Physics*, 43(5):2107–2132, 2002. URL: `https://aip.scitation.org/doi/abs/10.1063/1.1465516`, `arXiv:https://aip.scitation.org/doi/pdf/10.1063/1.1465516`, `doi:10.1063/1.1465516`.

[49] U. Boscain and P. Mason. Time minimal trajectories for a spin 1/2 particle in a magnetic field. *Journal of Mathematical Physics*, 47(6):062101, 2006. URL: `https://doi.org/10.1063/1.2203236`, `arXiv:https://doi.org/10.1063/1.2203236`, `doi:10.1063/1.2203236`.

[50] B. Bonnard and D. Sugny. Time-minimal control of dissipative two-level quantum systems: The integrable case. *SIAM Journal on Control and Optimization*, 48(3):1289–1308, 2009. URL: `https://doi.org/10.1137/080717043`, `arXiv:https://doi.org/10.1137/080717043`, `doi:10.1137/080717043`.

[51] B. Bonnard, M. Chyba, and D. Sugny. Time-minimal control of dissipative two-level quantum systems: The generic case. *IEEE Transactions on Automatic Control*, 54(11):2598–2610, Nov 2009. `doi:10.1109/TAC.2009.2031212`.

[52] N. Khaneja, R. Brockett, and S. J. Glaser. Time Optimal Control in Spin Systems. *Phys. Rev. A*, 63:032308, 2001.

[53] M. Lapert, Y. Zhang, M. Braun, S. J. Glaser, and D. Sugny. Singular Extremals for the Time-Optimal Control of Dissipative Spin 1/2 Particles. *Phys. Rev. Lett.*, 104:083001, 2010.

[54] V. Jurdjevic. *Geometric Control Theory*. Cambridge University Press, Cambridge, 2008.

[55] R. H. Cushman and L. M. Bates. *Global Aspects of Classical Integrable Systems*. Birkhäuser, Berlin, 1997.

[56] H. Goldstein, C. P. Poole Jr, and J. L. Safko. *Classical Mechanics*. Pearson, London, 2001.

[57] V. I. Arnold. *Mathematical Methods of Classical Mechanics*. Springer Verlag, New York, 1978.

[58] M. S. Ashbaugh, C. C. Chicone, and R. H. Cushman. The twisting tennis racket. *Journal of Dynamics and Differential Equations*, 3(1):67–85, Jan 1991. URL: `https://doi.org/10.1007/BF01049489`, `doi:10.1007/BF01049489`.

[59] L. V. Damme, P. Mardešić, and D. Sugny. The tennis racket effect in a three-dimensional rigid body. *Physica D: Nonlinear Phenomena*, 338:17 – 25, 2017. URL: `http://www.sciencedirect.com/science/article/pii/S0167278915301093`, `doi:https://doi.org/10.1016/j.physd.2016.07.010`.

[60] E. Merzbacher. *Quantum Mechanics*. John Wiley & Sons, New York, third edition, 1998.

[61] J. J. Sakurai. *Modern quantum mechanics*. Addison-Wesley, Reading, rev. auflage edition, 1994.

[62] A. Messiah. *Quantum mechanics*, volume I. North-Holland, Amsterdam, 1961.

[63] L. E. Ballentine. *Quantum Mechanics: A Modern Development*. World Scientific Publishing Company, Singapur, 1998.

[64] C. Cohen-Tannoudji, B. Diu, and F. Laloe. *Quantum Mechanics, Vol. 1*. Wiley-VCH, Weinheim, 1977.

[65] H. P. Breuer and F. Petruccione. *The Theory of Open Quantum Systems*. Oxford University Press, Oxford, 2002.

[66] S. Attal, A. Joye, and C.-A. Pillet, editors. *Open Quantum Systems I–III*. Lecture Notes in Mathematics Vols. 1880,1881,1882. Springer, Berlin, 2006.

[67] U. Weiss. *Quantum Dissipative Systems*. World Scientific, Singapore, 1999.

[68] E. Wigner. *Gruppentheorie und ihre Anwendung auf die Quantenmechanik der Atomspektren*. Friedrich Vieweg & Sohn, Braunschweig, 1931. (English translation in [69]).

[69] E. P. Wigner. *Group Theory and its Application to the Quantum Mechanics of Atomic Spectra*. Academic Press, London, 1959.

[70] G. Racah. Theory of Complex Spectra II. *Phys. Rev.*, 62:438–462, 1942. `doi:10.1103/PhysRev.62.438`.

[71] L. C. Biedenharn and J. D. Louck. *Angular Momentum in Quantum Physics*. Addison-Wesley, Reading, MA, 1981.

[72] B. L. Silver. *Irreducible Tensor Methods*. Academic Press, New York, 1976.

[73] M. Chaichian and R. Hagedorn. *Symmetries in Quantum Mechanics: From Angular Momentum to Supersymmetry*. Institute of Physics Publ., Bristol, 1998.

[74] E. Steinborn and K. Ruedenberg. Rotation and translation of regular and irregular solid spherical harmonics. volume 7 of *Advances in Quantum Chemistry*, pages 1 – 81. Academic Press, 1973. URL: `http://www.sciencedirect.com/science/article/pii/S0065327608605584`, `doi:https://doi.org/10.1016/S0065-3276(08)60558-4`.

[75] N. Zettili. *Quantum Mechanics: Concepts and Applications*. Wiley-VCH, Weinheim, 2009.

[76] J. D. Jackson. *Classical Electrodynamics*. John Wiley & Sons, New York, third edition, 1999.

[77] W. Magnus, F. Oberhettinger, and R. P. Soni. *Formulas and Theorems for the Special Functions of Mathematical Physics*. SPRINGER-VERLAG, Berlin, 1966.

[78] E. U. Condon and G. H. Shortley. *The Theory of Atomic Spectra*. Cambridge University Press, Cambridge, 1935.

[79] H. Weyl. Quantenmechanik und Gruppentheorie. *Z. Phys.*, 46:1–33, 1927.

[80] J. v. Neumann. Die eindeutigkeit der schrödingerschen operatoren. *Mathematische Annalen*, 104(1):570–578, Dec 1931. URL: https://doi.org/10.1007/BF01457956, doi:10.1007/BF01457956.

[81] H. Groenewold. On the Principles of Elementary Quantum Mechanics. *Physica*, 12:405–460, 1946.

[82] J. E. Moyal. Quantum Mechanics as a Statistical Theory. *Proc. Camb. Phil. Soc.*, 45:99–124, 1949.

[83] L. Cohen. Generalized phase-space distribution functions. *Journal of Mathematical Physics*, 7(5):781–786, 1966. URL: https://doi.org/10.1063/1.1931206, arXiv:https://doi.org/10.1063/1.1931206, doi:10.1063/1.1931206.

[84] G. S. Agarwal and E. Wolf. Calculus for functions of noncommuting operators and general phase-space methods in quantum mechanics. ii. quantum mechanics in phase space. *Phys. Rev. D*, 2:2187–2205, Nov 1970. URL: https://link.aps.org/doi/10.1103/PhysRevD.2.2187, doi:10.1103/PhysRevD.2.2187.

[85] B. Koczor, R. Zeier, and S. J. Glaser. Continuous phase-space representations for finite-dimensional quantum states and their tomography. arXiv:1711.07994.

[86] R. L. Stratonovich. On distributions in Representation Space. *JETP. (U.S.S.R.)*, 31:1012–1020, December 1956.

[87] C. Brif and A. Mann. A general theory of phase-space quasiprobability distributions. *J. Phys. A: Math. Gen.*, 31:L9–L17, 1997. doi:10.1088/0305-4470/31/1/002.

[88] C. Brif and A. Mann. Phase-space formulation of quantum mechanics and quantum-state reconstruction for physical systems with Lie-group symmetries. *Phys. Rev. A*, 59(2):971, 1999. doi:10.1103/PhysRevA.59.971.

[89] T. L. Curtright, D. B. Fairlie, and C. K. Zachos. *A Concise Treatise on Quantum Mechanics in Phase Space*. World Scientific, Singapore, 2014.

[90] M. A. De Gosson. *The Wigner Transform*. World Scientific Publishing Europe, UK, 2017.

[91] A. Shabani, R. L. Kosut, M. Mohseni, H. Rabitz, M. A. Broome, M. P. Almeida, A. Fedrizzi, and A. G. White. Efficient measurement of quantum dynamics via compressive sensing. *Phys. Rev. Lett.*, 106:100401, Mar 2011. URL: https://link.aps.org/doi/10.1103/PhysRevLett.106.100401, doi:10.1103/PhysRevLett.106.100401.

[92] M. Mohseni, A. T. Rezakhani, and D. A. Lidar. Quantum-process tomography: Resource analysis of different strategies. *Phys. Rev. A*, 77:032322, Mar 2008. URL: https://link.aps.org/doi/10.1103/PhysRevA.77.032322, doi:10.1103/PhysRevA.77.032322.

[93] W. Burnside. *Theory of groups of finite order*. Cambridge University press, Cambridge, 1911.

[94] H. Boerner. *Darstellungen von Gruppen*. Springer, Berlin, 2nd edition, 1967.

[95] M. Hamermesh. *Group Theory*. Addison-Wesley, Reading, MA, 1962.

[96] G. D. James. *The Representation Theory of the Symmetric Group*. Springer, Berlin, 1978.

[97] B. E. Sagan. *The Symmetric Group*. Springer, New York, 2nd edition, 2001.

[98] T. Ceccherini-Silberstein, F. Scarabotti, and F. Tolli. *Representation Theory of the Symmetric Groups*. Cambridge University Press, Cambridge, 2010.

[99] G. Racah. Group Theory and Spectroscopy. In *Ergebnisse der exakten Naturwissenschaften, 37. Band*, pages 28–84. Springer, Berlin, 1965.

[100] C. D. H. Chisholm. *Group Theoretical Techniques in Quantum Chemistry*. Academic Press, London, 1976.

[101] J. F. Cornwell. *Group Theory in Physics*, volume 2. Academic Press, London, 1984.

[102] W. Fulton. *Young Tableaux: With Applications to Representation Theory and Geometry*. Cambridge University Press, 1996.

[103] B. C. Sanctuary and F. P. Temme. Multipole N.M.R. XIII. multispin interactions and symmetry in Liouville space. *Mol. Phys.*, 55:1049–1062, 1985.

[104] R. Goodman and N. R. Wallach. *Symmetry, Representations, and Invariants*. Springer, Dordrecht, 2009.

[105] P. L. Corio. *Structure of High-Resolution NMR Spectra*. Academic Press, London, 1966.

[106] G. James and A. Kerber. *The Representation Theory of the Symmetric Group*. Addison-Wesley, Reading, MA, 1981.

[107] R. N. Zare. *Angular Momentum*. John Wiley & Sons, New York, 1988.

[108] Beringer, J. et al. (Particle Data Group). The Review of Particle Physics. *Phys. Rev. D*, 86:010001, 2012.

[109] A. Messiah. *Quantum mechanics*, volume II. North-Holland, Amsterdam, 1962.

[110] L. D. Landau and E. M. Lifshitz. *Quantum mechanics*, volume 3. Pergamon Press, Oxford, 1977.

[111] A. R. Edmonds. *Angular momentum in quantum mechanics*. Princeton University Press, Princeton, 1957.

[112] J. Schwinger. On Angular Momentum. Technical Report NYO-3071, U.S. Atomic Energy Commission, 1952.

[113] M. H. Levitt. *Spin Dynamics: Basics of Nuclear Magnetic Resonance*. Wiley, New York, 2008.

[114] J. Keeler. *Understanding NMR Spectroscopy*. John Wiley & Sons, Chichester, United Kingdom, 2nd edition, 2010.

[115] D. Leiner and S. J. Glaser. Wigner process tomography: Visualization of spin propagators and their spinor properties. *Phys. Rev. A*, 98:012112, Jul 2018. URL: https://link.aps.org/doi/10.1103/PhysRevA.98.012112, doi:10.1103/PhysRevA.98.012112.

[116] J. E. Kirk. *Optimal Control Theory: An Introduction*. Dover Publications Inc., Mineola, 2004.

[117] Glaser, Steffen J., Boscain, Ugo, Calarco, Tommaso, Koch, Christiane P., Köckenberger, Walter, Kosloff, Ronnie, Kuprov, Ilya, Luy, Burkhard, Schirmer, Sophie, Schulte-Herbrüggen, Thomas, Sugny, Dominique, and Wilhelm, Frank K. Training schrödinger´s cat: quantum optimal control - strategic report on current status, visions and goals for research in europe. *Eur. Phys. J. D*, 69(12):279, 2015. URL: https://doi.org/10.1140/epjd/e2015-60464-1, doi:10.1140/epjd/e2015-60464-1.

[118] M. A. Bernstein, K. F. King, and X. J. Zhou. *Handbook of MRI Pulse Sequences*. Elsevier, Burlington-San Diego-London, 2004.

[119] U. Eggenberger and G. Bodenhausen. Modern NMR Pulse Experiments: A Graphical Description of the Evolution of Spin Systems. *Angew. Chem. Int. Ed. Engl.*, 29:374–383, 1990.

[120] E. Wigner. On the Quantum Correction For Thermodynamic Equilibrium. *Phys. Rev.*, 40:749–759, 1932.

[121] W. K. Wooters. A Wigner-Function Formulation of Finite-State Quantum Mechanics. *Ann. Phys.*, 176:1–21, 1987. doi:10.1016/0003-4916(87)90176-X.

[122] U. Leonhardt. Discrete wigner function and quantum-state tomography. *Phys. Rev. A*, 53(5):2998, 1996. doi:10.1103/PhysRevA.53.2998.

[123] C. Miquel, J. P. Paz, and M. Saraceno. Quantum computers in phase space. *Phys. Rev. A*, 65:062309, Jun 2002. doi:10.1103/PhysRevA.65.062309.

[124] C. Miquel, J. P. Paz, M. Saraceno, E. Knill, R. Laflamme, and C. Negrevergne. Interpretation of tomography and spectroscopy as dual forms of quantum computation. *Nature*, 418:59–62, May 2002. doi:10.1038/nature00801.

[125] K. S. Gibbons, M. J. Hoffman, and W. K. Wootters. Discrete phase space based on finite fields. *Phys. Rev. A*, 70(6):062101, 2004. doi:10.1103/PhysRevA.70.062101.

[126] C. Ferrie and J. Emerson. Framed Hilbert space: hanging the quasi-probability pictures of quantum theory. *New J. Phys.*, 11:063040, 2009. doi:10.1088/1367-2630/11/6/063040.

[127] J. C. Várrily and J. M. Garcia-Bondía. The Moyal Representation for Spin. *Ann. Phys.*, 190:107–148, 1989. doi:10.1016/0003-4916(89)90262-5.

[128] A. Klimov. Exact evolution equations for SU(2) quasidistribution functions. *J. Math. Phys.*, 43(5):2202–2213, 2002. doi:10.1063/1.1463711.

[129] A. Klimov and P. Espinoza. Classical evolution of quantum fluctuations in spin-like systems: squeezing and entanglement. *J. Opt. B*, 7(6):183, 2005. doi:10.1088/1464-4266/7/6/004.

[130] A. B. Klimov and P. Espinoza. Moyal-like form of the star product for generalized SU(2) Stratonovich-Weyl symbols. *J. Phys. A*, 35:8435, 2002. doi:10.1088/0305-4470/35/40/305.

[131] D. J. Philp and P. W. Kuchel. A Way of Visualizing NMR Experiments on Quadrupolar Nuclei. *Concepts Magn. Reson. A*, 25A:40–52, 2005. doi:10.1002/cmr.a.20029.

[132] D. Avisar and D. J. Tannor. Complete reconstruction of the wave function of a reacting molecule by four-wave mixing spectroscopy. *Phys. Rev. Lett.*, 106:170405, Apr 2011. doi:10.1103/PhysRevLett.106.170405.

[133] C. Menzel-Jones and M. Shapiro. Complex wave function reconstruction and direct electromagnetic field determination from time-resolved intensity data. *J. Phys. Chem. Lett.*, 3(22):3353–3359, 2012. doi:10.1021/jz3015327.

[134] T. S. Humble and J. A. Cina. Molecular state reconstruction by nonlinear wave packet interferometry. *Phys. Rev. Lett.*, 93:060402, Aug 2004. doi:10.1103/PhysRevLett.93.060402.

[135] T. Tilma, M. J. Everitt, J. H. Samson, W. J. Munro, and K. Nemoto. Wigner functions for arbitrary quantum systems. *Phys. Rev. Lett.*, 117(18):180401, 2016. doi:10.1103/PhysRevLett.117.180401.

[136] R. P. Rundle, P. W. Mills, T. Tilma, J. H. Samson, and M. J. Everitt. Simple procedure for phase-space measurement and entanglement validation. *Phys. Rev. A*, 96(2):022117, 2017. doi:10.1103/PhysRevA.96.022117.

[137] R. Schmied and P. Treutlein. Tomographic reconstruction of the Wigner function on the Bloch sphere. *New J. Phys.*, 13:065019, 2011. doi:10.1088/1367-2630/13/6/065019.

[138] B. Vincent, O. Chadebec, J.-L. Schanen, C. A. F. Sartori, L. Krähenbühl, R. Perrussel, and K. Berger. New robust coil sensors for near field characterization. *J. Microw. Optoelectron. Electromagn. Appl.*, 8(1):64S–77S, 2009.

[139] B. Vincent, O. Chadebec, J. L. Schanen, and K. Berger. Loop antennas for near-field multipolar-expansion identification: First experimental validations. *IEEE Trans. Instrum. Meas.*, 59(12):3086–3092, Dec 2010. doi:10.1109/TIM.2010.2063052.

[140] A. Bréard, F. Tavernier, Z. Li, and L. Krähenbühl. New measurement system of magnetic near-field with multipolar expansion approach. *IEEE Trans. Magn.*, 52(3):1–4, March 2016. doi:10.1109/TMAG.2015.2501024.

[141] B. Koczor, R. Zeier, and S. J. Glaser. Time evolution of spin systems in a generalized Wigner representation. 2016. arXiv:1612.06777.

[142] D. Suter and J. Pearson. Experimental classification of multi-spin coherence under the full rotation group. *Chem. Phys. Lett.*, 144(4):328 – 332, 1988. doi:10.1016/0009-2614(88)87123-9.

[143] J. D. van Beek, M. Carravetta, G. C. Antonioli, and M. H. Levitt. Spherical tensor analysis of nuclear magnetic resonance signals. *J. Chem. Phys.*, 122(24):244510, 2005. doi:10.1063/1.1943947.

[144] Z. Khalid, R. A. Kennedy, and J. D. McEwen. An optimal-dimensionality sampling scheme on the sphere with fast spherical harmonic transforms. *IEEE Transactions on Signal Processing*, 62(17):4597–4610, Sept 2014. doi:10.1109/TSP.2014.2337278.

[145] J. Driscoll and D. Healy. Computing fourier transforms and convolutions on the 2-sphere. *Advances in Applied Mathematics*, 15(2):202 – 250, 1994. URL: http://www.sciencedirect.com/science/article/pii/S0196885884710086, doi:https://doi.org/10.1006/aama.1994.1008.

[146] R. A. Kennedy and P. Sadeghi. *Hilbert Space Methods in Signal Processing*. Cambridge University Press, Cambridge, 2013.

[147] J. D. McEwen and Y. Wiaux. A novel sampling theorem on the sphere. *IEEE Transactions on Signal Processing*, 59(12):5876–5887, Dec 2011. doi:10.1109/TSP.2011.2166394.

[148] A quadrature formula over the sphere with application to high resolution spherical harmonic analysis. *Bulletin géodésique*, 60(1):1–14, Mar 1986. URL: https://doi.org/10.1007/BF02519350, doi:10.1007/BF02519350.

[149] V. I. Lebedev. Values of the nodes and weights of ninth to seventeenth order gauss-markov quadrature formulae invariant under the octahedron group with inversion. *USSR Comput. Math. & Math. Phys.*, 15:44–51, 1975. doi:10.1016/0041-5553(75)90133-0.

[150] V. I. Lebedev. Quadratures on a sphere. *USSR Comput. Math. & Math. Phys.*, 16:10–24, 1976. doi:10.1016/0041-5553(76)90100-2.

[151] V. I. Lebedev and D. N. Laikov. A quadrature formula for the sphere of the 131st algebraic order of accuracy. *Russian Acad. Sci. Dokl. Math.*, 59:477–481, 1999.

[152] C. Brif, R. Chakrabarti, and H. Rabitz. Control of quantum phenomena: past, present and future. *New Journal of Physics*, 12(7):075008, 2010. URL: http://stacks.iop.org/1367-2630/12/i=7/a=075008.

[153] N. Khaneja, B. Heitmann, A. Spörl, H. Yuan, T. Schulte-Herbrüggen, and S. J. Glaser. Shortest paths for efficient control of indirectly coupled qubits. *Phys. Rev. A*, 75:012322, Jan 2007. URL: https://link.aps.org/doi/10.1103/PhysRevA.75.012322, doi:10.1103/PhysRevA.75.012322.

[154] L. Van Damme, R. Zeier, S. J. Glaser, and D. Sugny. Application of the pontryagin maximum principle to the time-optimal control in a chain of three spins with unequal couplings. *Phys. Rev. A*, 90:013409, Jul 2014. URL: https://link.aps.org/doi/10.1103/PhysRevA.90.013409, doi:10.1103/PhysRevA.90.013409.

[155] A. M. Perelomov. Motion of four-dimensional rigid body around a fixed point: an elementary approach i. *Journal of Physics A: Mathematical and General*, 38(47):L801, 2005. URL: http://stacks.iop.org/0305-4470/38/i=47/a=L03.

[156] J. A. Jones, V. Vedral, A. Ekert, and G. Castagnoli. Geometric quantum computation using nuclear magnetic resonance. *Nature*, 403:869 EP –, Feb 2000. URL: http://dx.doi.org/10.1038/35002528.

[157] E. Sjöqvist. A new phase in quantum computation. *Physics Online Journal*, 1:35, November 2008. doi:10.1103/Physics.1.35.

[158] W. Xiang-Bin and M. Keiji. Nonadiabatic conditional geometric phase shift with nmr. *Phys. Rev. Lett.*, 87:097901, Aug 2001. URL: https://link.aps.org/doi/10.1103/PhysRevLett.87.097901, doi:10.1103/PhysRevLett.87.097901.

[159] S.-L. Zhu and Z. D. Wang. Implementation of universal quantum gates based on nonadiabatic geometric phases. *Phys. Rev. Lett.*, 89:097902, Aug 2002. URL: `https://link.aps.org/doi/10.1103/PhysRevLett.89.097902`, `doi:10.1103/PhysRevLett.89.097902`.

A Wigner tomography of multispin quantum states

Bibliography:

Title: Wigner tomography of multispin quantum states

Authors: D. Leiner, R. Zeier, and S. J. Glaser

Journal: Physical Review A

Volume: 96

Issue: 6

Page: 063413

Published: 18.12.2017

DOI: 10.1103/PhysRevA.96.063413

URL: `https://link.aps.org/doi/10.1103/PhysRevA.96.063413`

Summary and contribution to this manuscript:
In this work, a novel (quantum) state tomography was introduced which reconstructs generalized Wigner functions representing the density matrix of coupled spin systems. It is based on the DROPS representation [1], which completely characterizes and visualizes an arbitrary operator using multiple shapes assembled from linear combinations of spherical harmonics. We develop a new sampling and reconstruction theorem, which gives a protocol how in general such spherical functions can be obtained by sampling points on the sphere (Result 1). The value of the functions at a given polar angle and azimuthal angle is proportional to the scalar product of these functions with zero-ranked spherical harmonics, which are rotated around these angles. The proof relies on the framework of Wigner D-matrices and was worked out by David Leiner, but refined by Robert Zeier and Steffen Glaser. This theorem was evolved to an experimental measurement scheme for the Wigner function representation of quantum states in general (Result 2): The spherical functions can be recovered by measuring expectation values of rotated axial spherical tensor operators. Eventually, an explicit protocol for NMR (Result 3) was derived. That is, points on the surface of the functions can be acquired by measuring a set of expectation values of (product) operators of the corresponding rotated state, which has to be repeated for different polar and azimuthal angles. Both Results 2 and 3 were elaborated by David Leiner and details were incorporated by Steffen Glaser and Robert Zeier. To prove its feasibility, NMR techniques were applied to experimentally reconstruct the Wigner functions representing various quantum states including fully symmetric operators, raising operators, double quantum operators, and triple quantum operators in systems of up to three coupled spins. As model systems, we used HDO for one-spin experiments, chloroform for two-spin experiments, and 2-^{13}C-2-fluoromalonic-acid-diethyl-ester for three-spin experiments. A simple

rectangular grid of sampling points in the space of polar and azimuthal angles is explicitly used to recover the shapes in sufficient detail. Simulations were carried out to compare the experimental data to the expected theory. Both experiments and simulations were done by David Leiner. A reasonable match between the theoretical predicted and the experimentally reconstructed spherical functions is found. Deviations are attributed to experimental imperfections including finite accuracy of pulse calibration, B_0 and B_1 inhomogeneity, and relaxation losses. The manuscript in its first form was written by David Leiner. Steffen Glaser extended the paper by chapter IV "Droplets as multipole potentials" which introduces a formal interpretation of this sampling methodology which connects the spherical functions to multipole potentials. Both, Robert Zeier and Steffen Glaser optimized the paper with respect to notation and language. The figures were also done by David Leiner and Robert Zeier occasionally revised them.

PHYSICAL REVIEW A **96**, 063413 (2017)

Wigner tomography of multispin quantum states

David Leiner,[*] Robert Zeier,[†] and Steffen J. Glaser[‡]
Technische Universität München, Department Chemie, Lichtenbergstrasse 4, 85747 Garching, Germany
(Received 26 July 2017; published 18 December 2017)

We study the tomography of multispin quantum states in the context of finite-dimensional Wigner representations. An arbitrary operator can be completely characterized and visualized using multiple shapes assembled from linear combinations of spherical harmonics [A. Garon, R. Zeier, and S. J. Glaser, Phys. Rev. A **91**, 042122 (2015)]. We develop a general methodology to experimentally recover these shapes by measuring expectation values of rotated axial spherical tensor operators and provide an interpretation in terms of fictitious multipole potentials. Our approach is experimentally demonstrated for quantum systems consisting of up to three spins using nuclear magnetic resonance spectroscopy.

DOI: 10.1103/PhysRevA.96.063413

I. INTRODUCTION

Optical homodyne tomography can be applied to experimentally measure the quantum state of light [1–5]. One thereby recovers an infinite-dimensional Wigner function [6–8] as a classically motivated phase-space representation, providing a useful tool for the characterization and visualization of quantum-optical systems [9]. This results in an advantageous dualism between measurement scheme and phase-space representation, which we would like to transfer to the case of finite-dimensional, *coupled* spin systems.

One important representation of finite-dimensional quantum systems relies on discrete Wigner functions [10–15]. But we will restrict ourselves to continuous representations in order to naturally reflect the inherent rotational symmetries of spins. Individual spins are faithfully described by their magnetization vector (or Bloch vector), which, however, neglects relevant parts of the full density matrix in the case of multiple, coupled spins. These missing parts include zero- and multiple-quantum or antiphase coherence as well as spin alignment [16], which are partially characterized by visual approaches based on single-transition operators [16–18].

We will follow the general strategy of Stratonovich [19] which specifies criteria for the definition of continuous Wigner functions for finite-dimensional quantum systems. The case of single spins is widely studied in the literature [20–25], and visualizations for multiple spins have been considered in [7,26–29] with various degrees of generality. However, until very recently, it was not clear [28,29] if a general Wigner representation also exists for arbitrary, coupled spin systems, and even the case of three coupled spins $1/2$ was open.

Fortunately, a general Wigner representation for characterizing and visualizing arbitrary coupled spin systems has been developed in [30]. It is based on mapping arbitrary operators to a set of spherical functions which are denoted as droplets, while preserving crucial features of the quantum system. The characteristic shapes of these droplets can be interpreted as the result of an abstract mapping, but we also ask in this paper how they are related to experimentally measurable quantities. The general Wigner representation introduced in [30] is denoted as the DROPS representation (discrete representation of operators for spin systems), and its basics are recalled in Sec. II where important properties are also summarized.

In this paper, we theoretically develop a tomography scheme for spherical functions of arbitrary multispin quantum states. We study experimental schemes to reconstruct the generalized Wigner representation of a given density operator (representing mixed or pure quantum states). Extensions to quantum process tomography [31] as given by the experimental reconstruction of entire propagators (e.g., representing quantum gates) are, however, beyond the scope of this paper. Our scheme is particularly tailored to the Wigner representation of [30], for which an interpretation in terms of fictitious multipole potentials is provided. We will focus on systems consisting of spins $1/2$, even though our approach is applicable to arbitrary spin numbers. We also provide explicit experimental protocols for our Wigner tomography scheme and demonstrate its feasibility using nuclear magnetic resonance (NMR) experiments. Motivated by our experiments, most of the discussed examples consider only the traceless part of the density matrix.

This paper is organized as follows. A brief summary of the DROPS representation is presented in Sec. II. Our general methodology for sampling spherical functions of multispin operators is introduced in Sec. III, which also states the main technical results for the Wigner tomography. Section IV provides a physical interpretation of spherical functions in terms of fictitious multipole potentials. The performed NMR experiments are summarized in Sec. V, and Sec. VI discusses the use of temporal averaging. The precise experimental scheme and its implementation on a spectrometer are detailed in Secs. VII and VIII. We conclude by summarizing and discussing theoretical and experimental aspects, while also contrasting our paper with other tomography approaches. Further details are deferred to the Appendices.

II. VISUALIZATION OF OPERATORS USING SPHERICAL FUNCTIONS

We summarize the approach of [30] to obtain a Wigner representation of arbitrary operators A in coupled spin systems using multiple spherical functions, which is based on a general one-to-one mapping from spherical tensor operators

[*]david.leiner@tum.de
[†]zeier@tum.de
[‡]steffen.glaser@tum.de

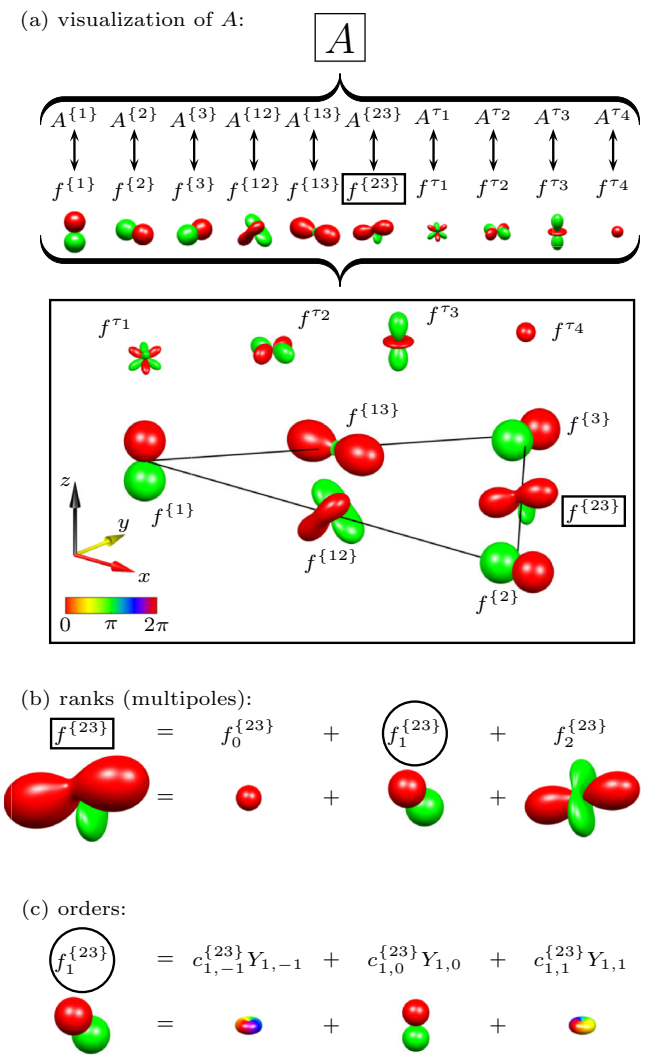

FIG. 1. (a) Three-spin operator $A = I_{1z} + I_{2x} + I_{3y} + 2I_{1x}I_{2z} + I_{2x}I_{3x} + I_{2x}I_{3y} + I_{2x}I_{3z} + 2I_{1x}I_{3x} + 4I_{1x}I_{2x}I_{3x}$ [16,41] visualized using multiple spherical functions $f^{(\ell)} = f^{(\ell)}(\theta,\phi)$, and individual components $A^{(\ell)}$ of A mapped to $f^{(\ell)}$ and graphically visualized; $A^{\emptyset}$ is here zero; trilinear labels "$\{123\},\tau_p$" are shortened to "τ_p". (b) $f^{\{23\}}$ (box) decomposed into its 2^j-multipole contributions $f_j^{\{23\}}$ with $j \in \{0,1,2\}$ (monopole, dipole, and quadrupole). (c) $f_1^{\{23\}}$ (circle) decomposed into spherical harmonics of order $m \in \{-1,0,1\}$; $Y_{1,-1}$ and $Y_{1,1}$ are rainbow colored [42].

to spherical harmonics. An operator

$$A = \sum_{\ell \in L} A^{(\ell)} \tag{1}$$

is decomposed according to a suitable set L of labels ℓ (i.e., quantum numbers) inducing a bijective mapping between the components $A^{(\ell)}$ and spherical functions $f^{(\ell)} = f^{(\ell)}(\theta,\phi)$. These spherical functions can be plotted together as seen in the example of Fig. 1(a) where the corresponding mapping is highlighted. This provides a pictorial representation of the operator A, which conserves important properties and symmetries depending on the chosen label set L.

The components $A^{(\ell)}$ and the spherical functions $f^{(\ell)} = f^{(\ell)}(\theta,\phi)$ can be further split up into their multipole contributions $A_j^{(\ell)}$ and $f_j^{(\ell)} = f_j^{(\ell)}(\theta,\phi)$ depending on the ranks $j \in J(\ell)$ occurring for each label ℓ as shown in Fig. 1(b), i.e.,

$$A^{(\ell)} = \sum_{j \in J(\ell)} A_j^{(\ell)} \quad \text{and} \quad f^{(\ell)} = \sum_{j \in J(\ell)} f_j^{(\ell)}. \tag{2}$$

Finally, the rank-j multipole contributions [see Fig. 1(c)]

$$A_j^{(\ell)} = \sum_{m=-j}^{j} c_{jm}^{(\ell)} T_{jm}^{(\ell)} \quad \text{and} \quad f_j^{(\ell)} = \sum_{m=-j}^{j} c_{jm}^{(\ell)} Y_{jm} \tag{3}$$

can be decomposed into components of irreducible spherical tensor operators $T_{jm}^{(\ell)}$ [32–37] and the corresponding spherical harmonics Y_{jm} [38,39] of order m with $-j \leqslant m \leqslant j$. Note the identical expansion coefficients $c_{jm}^{(\ell)}$ in Eq. (3). The dualism in Eqs. (2) and (3) exploits the well-known correspondence between irreducible tensor operators and spherical harmonics [36,37]. In summary, an operator A is mapped to a set of spherical functions $f^{(\ell)}$, each of which is referred to as a droplet identified by ℓ. The whole representation (and its visualization) was introduced in [30] and is denoted as the DROPS representation (discrete representation of operators for spin systems), and it lends itself to interactively exploring the dynamics of multispin systems, e.g., by use of the free application [40].

The example presented in Fig. 1 uses one particular version of this representation which relies on the LISA tensor operator basis as defined in [30], which is characterized by the linearity of the basis operators, the involved subsystem, and auxiliary criteria, such as permutation symmetry. For coupled spins 1/2, operators are first decomposed in this basis according to the set of involved spins, e.g., one introduces the labels $\{k\}$ and $\{kl\}$ for linear and bilinear operators acting on a subset of one or two spins numbered by k and l, and so forth. Secondly, the LISA basis for operators acting on three or more spins needs to also distinguish symmetry properties under permutations, i.e., combined labels such as "$\{klm\},\tau_p$" are used, where the permutation symmetry type τ_p is given by a Young tableau [43]. Finally, further *ad hoc* labels are necessary for operators involving six or more spins. Arbitrary operators of a coupled spin system can be uniquely represented using this LISA tensor operator basis. Additional details for the visualization technique are given in [30] which also discusses alternative labeling approaches for DROPS representations.

The presented Wigner representation can be applied to general mixed quantum states as represented by the density operator, and it is not limited to pure quantum states as given by a state function. In fact, it can be used to represent arbitrary operators of spin systems: examples include Hermitian operators as Hamiltonians or density operators representing observables as well as non-Hermitian operators such as propagators or general quantum gates [30].

The Wigner representation using the LISA basis is particularly attractive for the visualization and analysis of quantum states in magnetic resonance spectroscopy [16] and quantum

information processing [44] and its properties have been discussed in [30]:

(a) The *location* of the droplets informs about which and how many spin operators are involved in a given quantum state and what symmetries under particle exchange are present [see Fig. 1(a)].

(b) The *shape* and *colors* of the droplets reflect spectroscopically important properties. For example, states with defined coherence order p [16] can be recognized by their axially symmetric shape, and the magnitude as well as sign of the coherence order p are represented by the number and direction of "rainbows" per revolution around the z axis [see Figs. 5 and 6]. This also allows us to recognize characteristic states, such as in-phase and antiphase coherences.

(c) Furthermore, our representation directly depicts information about reduced density matrices and thereby conveys information related to entanglement measures, which would have to be first computed from the density-matrix description via partial traces. In particular, the size of the droplets corresponding to linear terms [positioned in the vertices of the triangle in Fig. 1(a)] provides information on the amount of bipartite entanglement measured by the concurrence (see Sec. IV E in [30]). This is an example of the fact that relevant information is often determined already by a subset of all droplets in the LISA basis. The LISA basis thereby offers a more structured picture than the density matrix, even though the number of droplets grows rapidly with increasing number of spins. However, as pointed out in [30], this number grows less rapidly than the number of density-matrix elements.

(d) The droplets *rotate* under nonselective pulses in a natural way. In combination with the characteristic droplet shapes, this property makes it in many cases possible to design experiments that transfer a given initial state into a desired target state without detailed calculations. Beyond merely interpreting the occurring characteristic shapes as a result of an abstract mapping, it is interesting to ask whether they are connected to experimentally measurable quantities.

III. SAMPLING SPHERICAL FUNCTIONS OF MULTISPIN OPERATORS

We explain now how the shape of spherical functions can be characterized by suitable chosen spherical samples. This will be particularly relevant for spherical functions representing spin operators as discussed in Sec. II for which these spherical samples can be experimentally measured. One obtains a reconstruction method for the quantum state in terms of spherical functions. In the general case, the associated rank-j components $g_j(\theta,\phi)$ of an arbitrary spherical function $g(\theta,\phi)$ are determined by its scalar product with rotated versions $R_{\alpha\beta}Y_{j0}(\theta,\phi)$ of axial spherical harmonics $Y_{j0}(\theta,\phi)$, which have rank j and order zero. Given two spherical functions $h(\theta,\phi)$ and $g(\theta,\phi)$, we recall the definition of their scalar product $\langle h(\theta,\phi)|g(\theta,\phi)\rangle_{L^2} := \int_{\theta=0}^{\pi}\int_{\phi=0}^{2\pi} h^*(\theta,\phi)\,g(\theta,\phi)\sin\theta\,d\theta\,d\phi$. The rotation operator $R_{\alpha\beta}$ acts on a spherical function $h(\theta,\phi)$ by first rotating it around the y axis by a polar angle β and then rotating the result around the z axis by an azimuthal angle α, i.e., $R_{\alpha\beta}h(\theta,\phi) := h[R_{\alpha\beta}^{-1}(\theta,\phi)] = h(\theta-\beta,\phi-\alpha)$. After these preparations, the mathematical result underpinning our reconstruction method states that the value of the rank-j component $g_j(\beta,\alpha)$ is proportional to the scalar product of $R_{\alpha\beta}Y_{j0}(\theta,\phi)$ with $g(\theta,\phi)$.

Result 1. Consider a spherical function $g(\theta,\phi) = \sum_j g_j(\theta,\phi)$. The rank-$j$ components $g_j(\beta,\alpha)$ for angles β and α can be obtained from the scalar products

$$g_j(\beta,\alpha) = s_j\,\langle R_{\alpha\beta}Y_{j0}(\theta,\phi)|g(\theta,\phi)\rangle_{L^2} \tag{4}$$

with $s_j := \sqrt{(2j+1)/(4\pi)}$.

Assuming that an operator A is represented by a set of spherical functions $f^{(\ell)}(\theta,\phi)$, we can apply Result 1 by setting $g(\theta,\phi) := f^{(\ell)}(\theta,\phi)$ for each label ℓ separately. We extend Result 1 such that the spherical rank-j components $f_j^{(\ell)}(\beta,\alpha)$ can also be recovered by comparing the operator A directly with rotated axial tensor operators $\mathcal{R}_{\alpha\beta}T_{j0}^{(\ell)}$. Consequently, the values of the rank-j spherical components $f_j^{(\ell)}(\beta,\alpha)$ can be experimentally measured for any combination of polar angles β and azimuthal angles α. Here, $\mathcal{R}_{\alpha\beta}C := \mathfrak{R}_{\alpha\beta}C\mathfrak{R}_{\alpha\beta}^{-1}$ describes the rotation of an n-spin operator C where the simultaneous rotation $\mathfrak{R}_{\alpha\beta} = e^{-i\alpha F_z}e^{-i\beta F_y}$ of all spins is defined using the total spin operators $F_z = \sum_{k=1}^n I_{kz}$ and $F_y = \sum_{k=1}^n I_{ky}$ [16,41]. We recall the scalar product $\langle C|B\rangle = \mathrm{tr}(C^\dagger B)$ for operators C and B as well as the definition of the expectation value $\langle B\rangle_\rho = \mathrm{tr}(\rho B)$ of an operator B if the state of the spin system is given by the density matrix ρ. Our result for recovering rank-j droplet components of an operator can now be stated as follows.

Result 2. Consider a multispin operator A which is represented by a set of spherical functions $f^{(\ell)}(\theta,\phi) = \sum_{j\in J(\ell)} f_j^{(\ell)}(\theta,\phi)$. For each label ℓ, the rank-j component $f_j^{(\ell)}(\beta,\alpha)$ can be experimentally measured for arbitrary angles β and α via the scalar products

$$f_j^{(\ell)}(\beta,\alpha) = s_j\,\langle \mathcal{R}_{\alpha\beta}T_{j0}^{(\ell)}|A\rangle. \tag{5}$$

If the density matrix ρ of a spin system can be prepared to be identical to the operator A, the rank-j droplet components are given by the expectation values

$$f_j^{(\ell)}(\beta,\alpha) = s_j\,\langle \mathcal{R}_{\alpha\beta}T_{j0}^{(\ell)}\rangle_\rho. \tag{6}$$

The proofs of Results 1 and 2 are deferred to Appendices A and B. Equation (6) implies that the rank-j droplet components $f_j^{(\ell)}(\beta,\alpha)$ for a density matrix ρ can be calculated from the expectation values of rotated axial tensor operators $\mathcal{R}_{\alpha\beta}T_{j0}^{(\ell)}$. Result 2 shows that one can retrace the shapes of the spherical functions $f^{(\ell)}(\beta,\alpha)$ representing any operator that can be mapped onto the density matrix if one experimentally measures $f^{(\ell)}(\beta,\alpha)$ for sufficiently many angles β and α.

IV. DROPLETS AS MULTIPOLE POTENTIALS

The methodology of Wigner tomography as presented in Sec. III can be motivated by relating spherical functions to physical multipole potentials. Section IV A details connections to dipole potentials, which is then generalized to fictitious multipole potentials in Sec. IV B. This allows us to interpret the proposed Wigner tomography as measuring a fictitious potential using axial multipole sensors (see Sec. IV C).

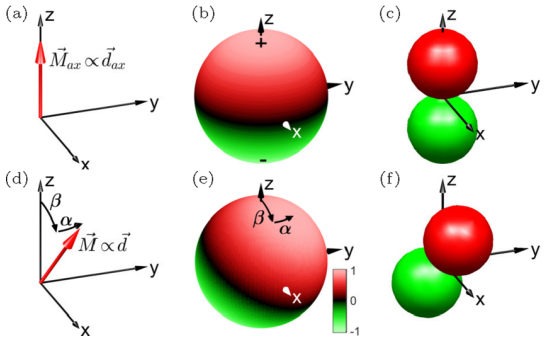

FIG. 2. (a) Axial magnetization vector $\vec{M}_{ax}$ and collinear axial dipole vector $\vec{d}_{ax}$. (b) Corresponding dipole potential visualized on a sphere, with magnitude and sign specified by brightness and color. (c) Similar to panel (b), but with magnitude specified by the distance from the origin. (d–f) Rotated nonaxial dipole $\vec{d}$ [42].

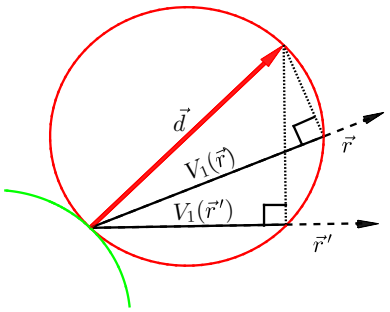

FIG. 3. Slice of Fig. 2(f): dipole potential $V_1(\vec{r})$ proportional to scalar product $\vec{d} \cdot \vec{r}$ (projection of $\vec{d}$ onto $\vec{r}$) due to Thales' theorem, and similar for $\vec{r}\,'$; results are shown in positive red (dark gray) and negative green (light gray) spheres in Fig. 2(f); for $\measuredangle\{\vec{d},\vec{r}\} > 90$ deg, the negative scalar product leads to the negative sphere.

A. Spherical functions and dipole potentials

The most direct physical interpretation of spherical functions is found for Hermitian single-spin terms [16,41]

$$\rho_k = m_x I_{kx} + m_y I_{ky} + m_z I_{kz} \tag{7}$$

of the density matrix with (possibly time-dependent) real coefficients m_x, m_y, and m_z. The corresponding spherical function $f^{\{k\}}(\theta,\phi)$ is now related to a magnetic dipole potential. The operator ρ_k associated with spin k is interpreted as a magnetization vector (or Bloch vector) $\vec{M} = (m_x,m_y,m_z)^T$ the components of which are proportional to the expectation values of the spin operators I_{kx}, I_{ky}, and I_{kz}. An actual (time-dependent) magnetic dipole $\vec{d} \propto \vec{M}$ creates a detectable signal in an NMR experiment by inducing a voltage in a detection coil. It is associated with a scalar dipole potential $V_1(\vec{r})$ at $\vec{r} = |\vec{r}|(\sin\theta\cos\phi,\ \sin\theta\sin\phi,\ \cos\theta)$, where θ and ϕ are polar and azimuthal angles, respectively. At a constant distance $|\vec{r}|$ from the dipole, the potential $V_1(\vec{r})$ is proportional to the scalar product $\vec{d} \cdot \vec{r}$ [38]. In the case of an axial dipole $\vec{d}_{ax} \propto (0,0,1)^T$ oriented along the z axis, the dipole potential is proportional to the axial spherical harmonic $Y_{10}(\theta,\phi) = \sqrt{3/(4\pi)}\cos\theta$ as detailed in Figs. 2(a)–2(c). For a general dipole $\vec{d} = R_{\alpha\beta}\,\vec{d}_{ax} \propto (\sin\beta\cos\alpha,\ \sin\beta\sin\alpha,\ \cos\beta)^T$, the dipole potential $V_1(\vec{r}) \propto R_{\alpha\beta}Y_{10}(\theta,\phi)$ is rotated accordingly as shown in Figs. 2(d)–2(f). Recall that $R_{\alpha\beta}$ denotes a rotation around the y axis by a polar angle β followed by one around the z axis by an azimuthal angle α.

A scalar dipole potential $V_1(\vec{r}) = V_1(\theta,\phi)$ can be indicated by its values on the surface of a sphere by encoding its sign by the color and its magnitude by the brightness [see Figs. 2(b) and 2(e)]. Alternatively, its magnitude can be represented by the distance from the origin as in Figs. 2(c) and 2(f), where dipole potentials are shown as a positive red (dark gray) sphere and a negative green (light gray) one which touch each other at the origin. This characteristic shape arises as $V_1(\theta,\phi)$ is proportional to the projection of the dipole $\vec{d}$ onto $\vec{r}$ as depicted in Fig. 3. Also, the vector from the center of the negative sphere to the positive one is collinear with $\vec{d}$.

In summary, a single-spin axial spherical tensor operator $T_{10}^{\{k\}} = \sqrt{2}I_{kz}$ is mapped to the axial spherical harmonics $Y_{10}(\theta,\phi)$, and ρ_k from Eq. (7) is mapped to

$$f^{\{k\}}(\theta,\phi) = |\vec{M}|\,R_{\alpha\beta}Y_{10}(\theta,\phi)/\sqrt{2}, \tag{8}$$

where $\beta = \operatorname{atan}(m_z/\sqrt{m_x^2+m_y^2})$, $\alpha = \operatorname{atan}(m_y/m_x)$, and $|\vec{M}| = \sqrt{m_x^2+m_y^2+m_z^2}$. Although the direct correspondence between spherical functions and actual physical dipole potentials appears to be limited to the case of single-spin terms, it suggests the following interpretation for other spherical functions presented here.

B. Fictitious multipole potentials

Any spherical function $f^{(\ell)}(\theta,\phi)$ can be regarded as the potential $V^{(\ell)}(\vec{r})$ of a fictitious charge distribution $\sigma^{(\ell)}(\vec{r})$ localized in a small volume close to the origin, i.e., $\sigma^{(\ell)}(\vec{r})$ is nonzero only for $|\vec{r}| \ll 1$. At a radius of $|\vec{r}| = 1$, the potential can be expressed as a sum $V^{(\ell)}(\theta,\phi) = \sum_j V_j^{(\ell)}(\theta,\phi)$ of different 2^j-pole potentials $V_j^{(\ell)}(\theta,\phi)$. Although a large number of multipole potentials might be required in general, only a moderate number of components with different rank j appear for up to three spins in the DROPS representation of Sec. II [30]. Fictitious multipole potentials sufficient to completely describe the potential $V^{(\ell)}(\theta,\phi)$ are detailed in Table I: one has monopoles ($2^0 = 1$), dipoles ($2^1 = 2$), quadrupoles ($2^2 = 4$), and octupoles ($2^3 = 8$). For a two-spin droplet with label "$\{kl\}$," only ranks j of zero, one, and two occur, which correspond to fictitious monopole, dipole, and quadrupole potentials, whereas the fully symmetric three-spin droplet with label "$\{123\},\tau_1$" has only rank-1 and rank-3 components associated with dipole and octupole terms.

C. Axial multipole sensors

Based on the provided interpretation of droplet functions as fictitious multipole potentials, the results of Sec. III on how to experimentally measure spherical functions of spin operators can be mapped to the analogous problem of measuring an unknown electrostatic potential. This analogy is complete for Hermitian spin operators with real-valued spherical functions [30]. Suppose we would like to determine an unknown (real-valued) electrostatic potential $V(\theta,\phi)$ at a radius $|\vec{r}| = 1$ that is created by an object located in the interior of a unit

TABLE I. Number n of involved spins, components $A^{(\ell)}$ and $f^{(\ell)}$, possible ranks j, rank-j contributions $A_j^{(\ell)}$ and $f_j^{(\ell)}$, as well as 2^j-pole potentials $V_j^{(\ell)}$ are listed for up to three spins 1/2 and all labels (ℓ); k and l indicate the involved spins [30].

n	$A^{(\ell)}$	$f^{(\ell)}$	j	$A_j^{(\ell)}$	$f_j^{(\ell)}$	2^j	2^j pole	$V_j^{(\ell)}$
0	$A^{\emptyset}$	$f^{\emptyset}$	0	$A_0^{\emptyset}$	$f_0^{\emptyset}$	1	Monopole	$V_0^{\emptyset}$
1	$A^{\{k\}}$	$f^{\{k\}}$	1	$A_1^{\{k\}}$	$f_1^{\{k\}}$	2	Dipole	$V_1^{\{k\}}$
2	$A^{\{kl\}}$	$f^{\{kl\}}$	0	$A_0^{\{kl\}}$	$f_0^{\{kl\}}$	1	Monopole	$V_0^{\{kl\}}$
			1	$A_1^{\{kl\}}$	$f_1^{\{kl\}}$	2	Dipole	$V_1^{\{kl\}}$
			2	$A_2^{\{kl\}}$	$f_2^{\{kl\}}$	4	Quadrupole	$V_2^{\{kl\}}$
3	A^{τ_1}	f^{τ_1}	1	$A_1^{\tau_1}$	$f_1^{\tau_1}$	2	Dipole	$V_1^{\tau_1}$
			3	$A_3^{\tau_1}$	$f_3^{\tau_1}$	8	Octupole	$V_3^{\tau_1}$
	A^{τ_2}	f^{τ_2}	1	$A_1^{\tau_2}$	$f_1^{\tau_2}$	2	Dipole	$V_1^{\tau_2}$
			2	$A_2^{\tau_2}$	$f_2^{\tau_2}$	4	Quadrupole	$V_2^{\tau_2}$
	A^{τ_3}	f^{τ_3}	1	$A_1^{\tau_3}$	$f_1^{\tau_3}$	2	Dipole	$V_1^{\tau_3}$
			2	$A_2^{\tau_3}$	$f_2^{\tau_3}$	4	Quadrupole	$V_2^{\tau_3}$
	A^{τ_4}	f^{τ_4}	0	$A_0^{\tau_4}$	$f_0^{\tau_4}$	1	Monopole	$V_0^{\tau_4}$

sphere. An electric point charge q at position $\vec{r}$ in an electric potential $V(\vec{r})$ has a potential energy $U_{\text{pot}}(\vec{r}) = qV(\vec{r})$. Given an electrostatic potential $V(\theta,\phi)$, the electrostatic potential energy of a (nonconducting) unit sphere with the surface charge distribution $\sigma(\theta,\phi)$ is given by

$$U_{\text{pot}}(\beta,\alpha) = \int_{\theta=0}^{\pi}\int_{\phi=0}^{2\pi} \sigma(\theta,\phi)\, V(\theta,\phi)\, \sin\theta\, d\theta\, d\phi, \qquad (9)$$

which is equivalent to $U_{\text{pot}}(\beta,\alpha) = \langle\sigma(\theta,\phi)|V(\theta,\phi)\rangle_{L^2}$ for real-valued $\sigma(\theta,\phi)$ as in Eq. (4) of Sec. III.

The 2^j-pole components $V_j(\theta,\phi)$ of an unknown multipole potential $V(\theta,\phi)$ can be sampled by a set of axial 2^j-pole sensors, each consisting of a charge distribution $\sigma_{j0}(\theta,\phi)$ proportional to the axial spherical harmonics $Y_{j0}(\theta,\phi)$. Each individual sample $V_j(\beta,\alpha)$ can be determined using Eq. (9) by measuring the potential energy

$$V_j(\beta,\alpha) \propto U_{\text{pot}}(\beta,\alpha) = \langle R_{\alpha\beta}\, \sigma_{j0}(\theta,\phi)|V(\theta,\phi)\rangle$$

of the axial 2^j-pole sensor rotated by the polar angle β around the y axis followed by a rotation by the azimuthal angle α around the z axis. The full electrostatic 2^j-pole potential $V_j(\theta,\phi)$ can be recovered by systematically incrementing β and α. In summary, the analogy between real-valued spherical functions and multipole potentials helps to better understand our results of Sec. III on the measurement of spherical functions. It can also be extended in a straightforward manner to non-Hermitian spin operators by considering complex, fictitious multipole potentials.

V. SUMMARY OF NMR EXPERIMENTS

Building on the previous sections, we demonstrate the Wigner tomography of various prepared density-matrix components in spin-1/2 systems using nuclear magnetic resonance. Experimental details are deferred to Secs. VII and VIII where the precise experimental scheme and its implementation on a spectrometer are discussed. The experiments were performed on one-, two-, and three-spin systems. The shapes of the spherical functions are recovered for the prepared Cartesian product operators listed in Table II, where also their respective experimental reconstruction errors are given. Experimental and theoretical results for the reconstruction are visually compared for four examples in Fig. 4. For the rightmost example of $4I_{1x}I_{2y}I_{3z}$ in Fig. 4, multiple droplets corresponding to different permutation symmetries are necessary to completely describe the quantum operator, as outlined in Sec. II (see Fig. 1 and [30]).

TABLE II. Root-mean-square error of the experimental reconstruction for the prepared Cartesian product operators on one-, two-, and three-spin systems; $I_{abc} := I_{1a}I_{2b}I_{3c}$.

Spins	Prod. op.	Error	Spins	Prod. op.	Error
1	I_x	0.0519	3	$4I_{xxx}$	0.0797
	I_y	0.1187		$4I_{yyy}$	0.0509
	I_z	0.0356		$4I_{xyz}$	0.0617
2	$2I_{1x}I_{2x}$	0.0173		$4I_{xyy}$	0.0395
	$2I_{1y}I_{2y}$	0.0154		$4I_{yxy}$	0.0476
	$2I_{1z}I_{2z}$	0.0850		$4I_{yyx}$	0.0954
	$2I_{1x}I_{2y}$	0.0487		$4I_{xxy}$	0.0587
	$2I_{1y}I_{2x}$	0.0152		$4I_{xyx}$	0.0638
	$2I_{1z}I_{2x}$	0.0319		$4I_{yxx}$	0.0692

VI. TEMPORAL AVERAGING

Reusing our experimental data as summarized in Sec. V, we can also highlight how temporal averaging [45] is used to emulate the preparation of quantum operators. The direct experimental preparation of Hermitian operators would be also possible, but we have chosen temporal averaging for its simplicity and convenience. The experimental values are shown in Fig. 5, while the corresponding theoretical predictions are given in Fig. 6. The Cartesian operators $2I_{1x}I_{2x}$, $2I_{1y}I_{2y}$, $2I_{1x}I_{2y}$, and $2I_{1y}I_{2x}$ had been sequentially measured

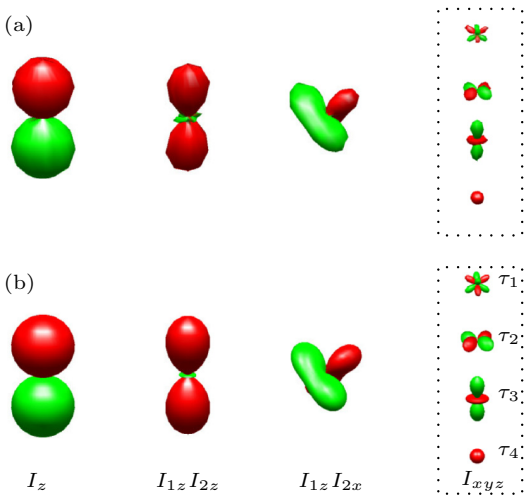

FIG. 4. Spherical functions from (a) experiment and (b) theory; $I_{xyz} := I_{1x}I_{2y}I_{3z}$ splits into f^{τ_1}, f^{τ_2}, f^{τ_3}, and f^{τ_4} (see Fig. 1) [42]. Further examples are shown in Figs. 5 and 6.

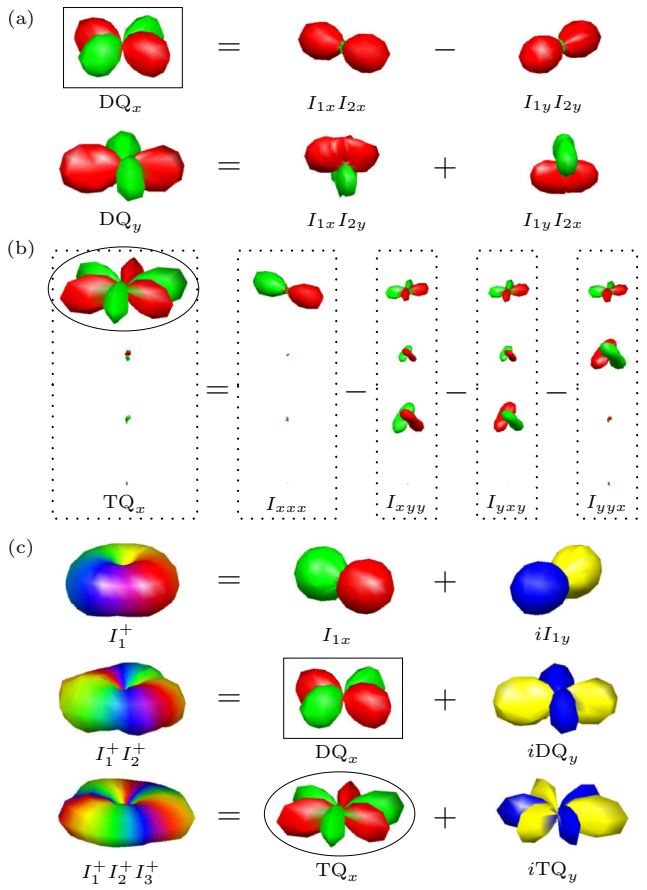

FIG. 5. Temporal averaging: decomposition of (a) DQ_x [box, see also panel (c)], DQ_y, and (b) TQ_x [f^{τ_1} ellipse, see also panel (c)], $I_{abc} := I_{1a}I_{2b}I_{3c}$. (c) Non-Hermitian operators I_1^+, $I_1^+I_2^+$, and $I_1^+I_2^+I_3^+$ as complex linear combinations of Hermitian ones (see Fig. 4).

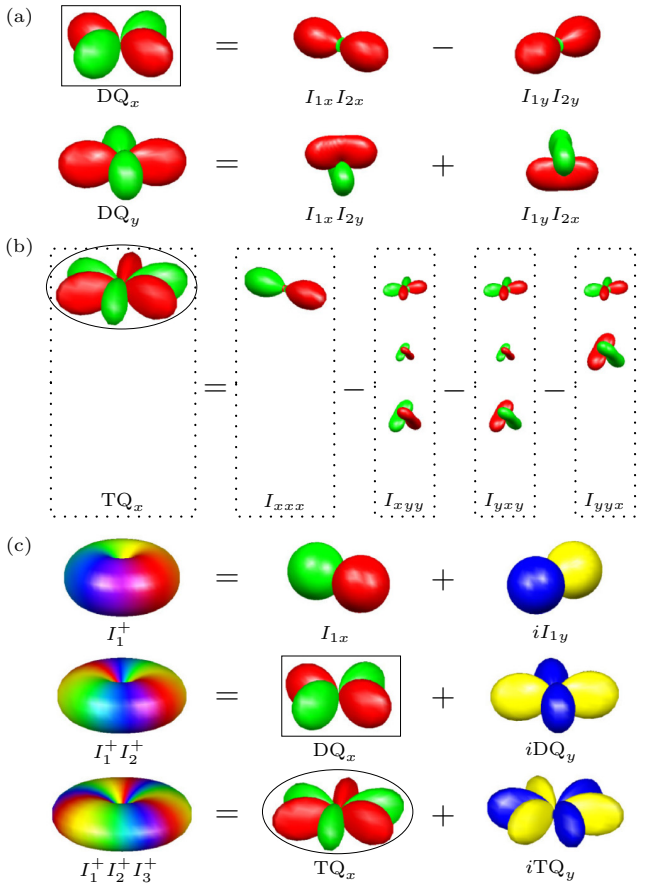

FIG. 6. Theoretical predictions corresponding to Fig. 5; $I_{abc} := I_{1a}I_{2b}I_{3c}$.

and are now combined in Fig. 5(a) to form the double quantum operators

$$\mathrm{DQ}_x := I_{1x}I_{2x} - I_{1y}I_{2y} \text{ and } \mathrm{DQ}_y := I_{1x}I_{2y} + I_{1y}I_{2x}.$$

Their characteristic shapes reflect the fact that they have coherence order $|p| = 2$ and are invariant under nonselective rotations around the z axis by an integer multiple of 180 deg [30]. This is in contrast to single-quantum operators such as the linear operators I_x or I_y [see Fig. 5(c)] or the bilinear operator $2I_{1z}I_{2x}$ (see Fig. 4) which are only invariant under nonselective rotations around the z axis by an integer multiple of 360 deg [16].

In general, $|p|$-quantum operators are invariant under nonselective rotations around the z axis by an integer multiple of $360/|p|$ deg, and their spherical functions illustrate this symmetry. Figure 5(b) exemplifies the invariance under 120-deg rotations around the z axis in the case of $|p| = 3$ for the triple-quantum operator

$$\mathrm{TQ}_x := I_{1x}I_{2x}I_{3x} - I_{1x}I_{2y}I_{3y} - I_{1y}I_{2x}I_{3y} - I_{1y}I_{2y}I_{3x},$$

similar to the case of

$$\mathrm{TQ}_y := I_{1y}I_{2x}I_{3x} + I_{1x}I_{2y}I_{3x} + I_{1x}I_{2x}I_{3y} - I_{1y}I_{2y}I_{3y}.$$

Up to experimental imperfections, only the spherical function f^{τ_1} contributes to the operator TQ_x.

Finally, we also consider temporal averaging for non-Hermitian operators which obviously cannot be directly prepared in experiments (see also Sec. VII). Figure 5(c) presents the non-Hermitian operators $I_1^+ = I_{1x} + iI_{2y}$, $I_1^+I_2^+ = \mathrm{DQ}_x + i\,\mathrm{DQ}_y$, and $I_1^+I_2^+I_3^+ = \mathrm{TQ}_x + i\,\mathrm{TQ}_y$. These operators have the respective coherence orders p of 1, 2, and 3 which results in donut-shaped spherical functions the colors of which cycle through one, two, or three rainbows [30].

VII. WIGNER TOMOGRAPHY USING NMR

We complement our results in Sec. III and describe the experimental scheme for an NMR-based implementation of our Wigner tomography. Recall that Eq. (5) of Result 2 provides an approach for measuring an arbitrary operator. This can be translated into the diagram of Fig. 7(a): The operator A is decomposed into its components $A_j^{(\ell)}$ which are mapped by the Wigner transformation W to spherical samples $f_j^{(\ell)}(\beta,\alpha)$. The spherical samples can be recovered using Eq. (5). Very similarly, Fig. 7(b) depicts the equivalent measurement procedure for density matrices which relies on Eq. (6) of Result 2.

Before proceeding to the NMR-based scheme, it is important to emphasize that only traceless operators can be measured

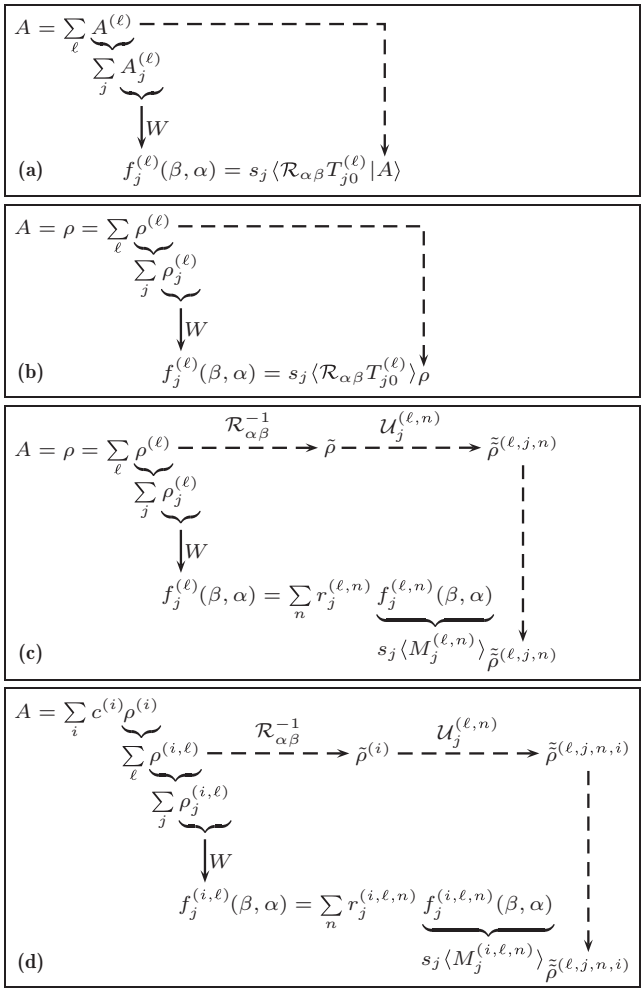

FIG. 7. Sampling schemes for spherical functions using (a) scalar products of rotated axial tensor operators and A [Result 2, Eq. (5)]. (b) Expectation values of rotated axial tensor operators w.r.t. ρ [Result 2, Eq. (6)]. (c) Experimentally measurable expectation values as in panel (b) [Result 3, Eqs. (12)–(14)]. (d) Non-Hermitian operators averaged as complex combinations of Hermitian terms $\rho^{(i)}$ [see Eq. (15)]. The Wigner transformation W maps an operator to its spherical function.

in NMR experiments [16], which rules out the identity component of a density matrix. However, the traceless part of a density matrix covers most of its important features, and it is sufficient to calculate the time evolution and all relevant expectation values. Hence, we will consider in the following only the traceless part which is for simplicity also denoted by ρ.

Further complications arise from the fact that signatures of Cartesian product operators [16] that contain only a single transverse Cartesian operator I_{ka} with $a \in \{x,\ y\}$ can be measured *directly*; examples are I_{ka}, $2I_{ka}I_{lz}$, and $4I_{ka}I_{lz}I_{mz}$. This complication can be resolved in two steps. First, any traceless operator can be decomposed into (Hermitian) Cartesian product operators $C_j^{(\ell,n)}$. This decomposition of relevant axial tensors

$$T_{j0}^{(\ell)} = \sum_n r_j^{(\ell,n)} C_j^{(\ell,n)} \tag{10}$$

TABLE III. Axial tensor operators $T_{j0}^{(\ell)}$ and their decomposition into Cartesian product operators $C_j^{(\ell,n)}$ for three spins [30].

$T_{j0}^{(\ell)}$	$\sum_n r_j^{(\ell,n)} C_j^{(\ell,n)}$
$T_{10}^{\{k\}}$	$\sqrt{2}I_{kz}$
$T_{00}^{\{kl\}}$	$(2I_{kx}I_{lx}+2I_{ky}I_{ly}+2I_{kz}I_{lz})/\sqrt{3}$
$T_{10}^{\{kl\}}$	$(2I_{kx}I_{ly}-2I_{ky}I_{lx})/\sqrt{2}$
$T_{20}^{\{kl\}}$	$[-2I_{kx}I_{lx}-2I_{ky}I_{ly}+2(2I_{kz}I_{lz})]/\sqrt{6}$
$T_{10}^{\tau_1}$	$\sqrt{8}(I_{xxz}+I_{xzx}+I_{zxx}+I_{yyz}+I_{yzy}+I_{zyy}+3I_{zzz})/\sqrt{15}$
$T_{30}^{\tau_1}$	$-2(I_{xxz}+I_{xzx}+I_{zxx}+I_{yyz}+I_{yzy}+I_{zyy}-2I_{zzz})/\sqrt{5}$
$T_{10}^{\tau_2}$	$\sqrt{2}[-2(I_{xxz}+I_{yyz})+I_{zxx}+I_{xzx}+I_{zyy}+I_{yzy}]/\sqrt{3}$
$T_{20}^{\tau_2}$	$\sqrt{2}(I_{yzx}+I_{zyx}-I_{xzy}-I_{zxy})$
$T_{10}^{\tau_3}$	$\sqrt{2}(I_{zxx}-I_{xzx}+I_{zyy}-I_{yzy})$
$T_{20}^{\tau_3}$	$\sqrt{2}[-2(I_{xyz}-I_{yxz})+I_{zxy}-I_{xzy}+I_{yzx}-I_{zyx}]/\sqrt{3}$
$T_{00}^{\tau_4}$	$2(I_{xyz}-I_{xzy}-I_{yxz}+I_{yzx}+I_{zxy}-I_{zyx})/\sqrt{3}$

with respect to real coefficients $r_j^{(\ell,n)}$ is given in Table III. For example, the axial tensor operator $T_{10}^{\{k\}}$ acting on the kth spin decomposes directly into the Cartesian product operator $C_1^{(\{k\},1)} = I_{kz}$ with the coefficient $r_1^{(\{k\},1)} = \sqrt{2}$.

Secondly, the Cartesian product operators have to be transformed into NMR-measurable ones:

$$M_j^{(\ell,n)} = \mathcal{U}_j^{(\ell,n)} C_j^{(\ell,n)} := U_j^{(\ell,n)} C_j^{(\ell,n)} U_j^{(\ell,n)\dagger}. \tag{11}$$

The unitary operators $U_j^{(\ell,n)}$ can be experimentally realized using radio-frequency (rf) pulses and evolution periods under couplings as discussed in Sec. VIII B and their explicit form is detailed in Appendix D. Combining both steps leads to an *indirect* approach for measuring spherical functions of density operators, as schematically outlined in Fig. 7(c). The density matrix is equivalently rotated inversely in contrast to Figs. 7(a) and 7(b) where the axial tensor operator $T_{j0}^{(\ell)}$ is rotated. The complete measurement scheme is formalized along the lines of Result 2.

Result 3. Consider a density operator ρ which is represented by a set of spherical functions $f^{(\ell)}(\theta,\phi) = \sum_{j\in J(\ell)} f_j^{(\ell)}(\theta,\phi)$. For each label ℓ, the rank-j component $f_j^{(\ell)}(\beta,\alpha)$ can be measured for arbitrary angles β and α by determining the expectation values

$$f_j^{(\ell)}(\beta,\alpha) = s_j \sum_n r_j^{(\ell,n)} \left\langle M_j^{(\ell,n)} \right\rangle_{\tilde{\tilde{\rho}}^{(\ell,j,n)}} \tag{12}$$

of suitable operators $M_j^{(\ell,n)}$ as in Eq. (11), where

$$\tilde{\tilde{\rho}}^{(\ell,j,n)} = \mathcal{U}_j^{(\ell,n)}\, \tilde{\rho} = U_j^{(\ell,n)}\, \tilde{\rho}\, U_j^{(\ell,n)\dagger}, \tag{13}$$

$$\tilde{\rho} = \mathcal{R}_{\alpha\beta}^{-1}\, \rho = \mathfrak{R}_{\alpha\beta}^{-1}\, \rho\, \mathfrak{R}_{\alpha\beta}, \tag{14}$$

and $\mathfrak{R}_{\alpha\beta} = \exp(-i\alpha \sum_{k=1}^n I_{kz}) \exp(-i\beta \sum_{k=1}^n I_{ky})$.

A detailed derivation of Eq. (12) is provided in Appendix C. In summary, the rank-j components $f_j^{(\ell)}$ of spherical functions $f^{(\ell)}$ representing the density matrix ρ can be sampled in NMR experiments by transforming the density operator ρ to the states $\tilde{\tilde{\rho}}^{(n)}$ and then measuring a set of expectation

values of suitable operators $\langle M_j^{(\ell,n)}\rangle_{\tilde{\rho}^{(\ell,j,n)}}$. The explicit form of the Cartesian operators $C_j^{(\ell,n)}$, their NMR-measurable forms $M_j^{(\ell,n)}$, and the transformations $U_j^{(\ell,n)}$ for up to three spins is given in Appendix D.

The approach of Result 3 can be extended to non-Hermitian operators, even though these cannot be prepared directly in an experiment. We apply temporal averaging [45] as already discussed in Sec. VI. Any operator A can be expressed as a complex linear combination $A = \sum_i c^{(i)}\rho^{(i)}$ of Hermitian operators $\rho^{(i)}$. As the DROPS representation is linear, we can sample the traceless part of any operator A using the spherical functions

$$\begin{aligned} f_j^{(\ell)}(\beta,\alpha) &= \sum_i c^{(i)} f_j^{(i,\ell)}(\beta,\alpha) \\ &= \sum_i c^{(i)} s_j \left\langle \mathcal{R}_{\alpha\beta} T_{j0}^{(\ell)} \right\rangle_{\rho^{(i)}} \\ &= \sum_i c^{(i)} s_j \sum_n r_j^{(\ell,n)} \left\langle M_j^{(\ell,n)} \right\rangle_{\tilde{\tilde{\rho}}^{(\ell,j,n,i)}}. \end{aligned} \quad (15)$$

In an experiment, temporal averaging of Hermitian operators $\rho^{(i)}$ can be implemented by sequentially measuring spherical functions for each operator $\rho^{(i)}$ and linearly combining the results $f_j^{(i,\ell)}(\beta,\alpha) = s_j \langle \mathcal{R}_{\alpha\beta} T_{j0}^{(\ell)} \rangle_{\rho^{(i)}} = s_j \sum_n r_j^{(\ell,n)} \langle M_j^{(\ell,n)} \rangle_{\tilde{\tilde{\rho}}^{(\ell,j,n,i)}}$ as illustrated in Fig. 7(d).

VIII. EXPERIMENTAL IMPLEMENTATION

After outlining the experimental scheme for Wigner tomography in Sec. VII, we present now the details for the experimental implementation which results in the spherical functions in Figs. 4 and 5. We start by describing the molecules and experimental setting in Sec. VIII A. We continue in Sec. VIII B with the experimental protocol, and we finally discuss experimental errors in Sec. VIII C.

A. Molecules and experimental setting

In order to simplify the experiments, the linear and bilinear Cartesian product operators have been prepared and measured using respective single-spin and two-spin samples: The single-spin sample was prepared by dissolving 5% H_2O in D_2O, which resulted in a sample containing about 10% HDO, i.e., water molecules in which one of the ^{1}H spins is replaced by deuterium (^{2}D) [see Fig. 8(a)]. In case of two spins, we have used a 10% sample of chloroform dissolved in fully deuterated DMSO-d6, where the ^{1}H spin and the ^{13}C spin of each chloroform molecule form a system consisting of two coupled heteronuclear spins 1/2 [see Fig. 8(b)]. A three-spin sample consisting of 2-^{13}C-2-fluoromalonic-acid-diethyl-ester dissolved in CD_3CN [see Fig. 8(c)] was utilized for the preparation and reconstruction of trilinear operators. All liquid samples were measured in 5-mm Shigemi NMR tubes at room temperature (298 K) in a 14.1-T magnet using a Bruker Avance III 600 spectrometer.

B. Experimental protocol

Our experimental protocol is composed of five main building blocks (see Fig. 9). In the first block $\mathcal{P}$, the desired density operator ρ is prepared starting from the initial thermal equilibrium density operator which in the high-temperature limit is proportional to [16] $\rho_{\text{th}} = \sum_{k=1}^{N} \gamma_k I_{kz}$, where γ_k denotes the gyromagnetic ratio of the kth nuclear spin. This requires unitary transformations which are created by pulses and evolution periods under the effect of couplings and frequency offsets as well as nonunitary transformations which are implemented by pulsed magnetic-field gradients. The explicit pulse sequences are discussed in Appendix D.

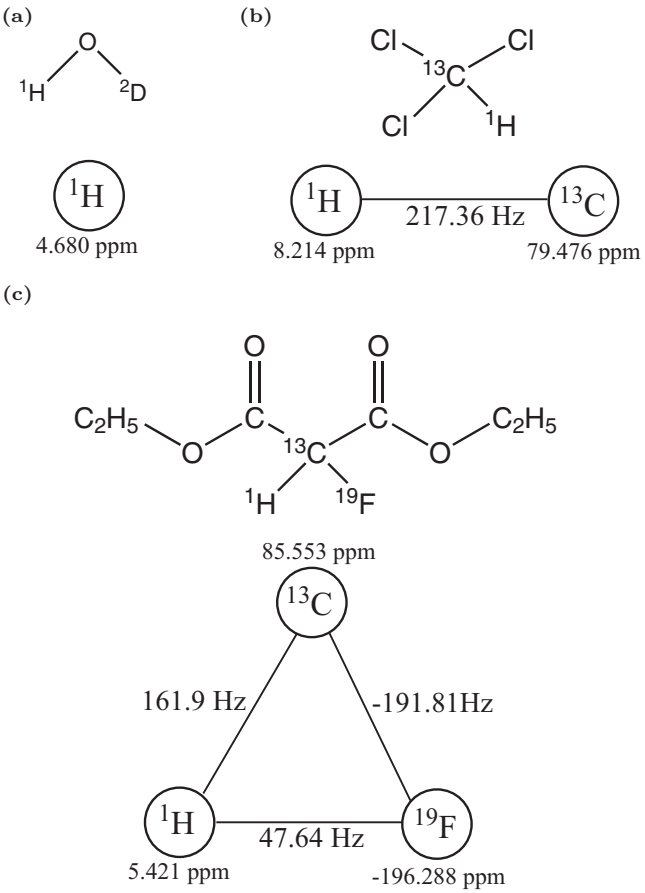

FIG. 8. Molecules (a) HDO, (b) chloroform, and (c) 2-^{13}C-2-fluoromalonic-acid-diethyl-ester used in experiments with their schematic spin systems and coupling topologies; individual spins are labeled by chemical shifts (in parts per million); heteronuclear J couplings (lines) are labeled by coupling constants J_{kl} (in hertz).

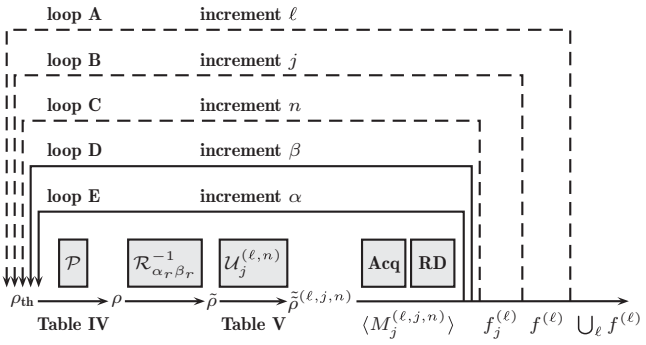

FIG. 9. Tomography scheme proposed by Result 3; note that $\langle M_j^{(\ell,j,n)}\rangle := \langle M_j^{(\ell,j,n)}\rangle_{\tilde{\rho}^{(\ell,j,n)}}$.

Table II in Sec. V summarizes all the different Cartesian product operators which have been experimentally prepared.

The second block consists of the rotation $\mathcal{R}^{-1}_{\alpha_r\beta_r}$ which rotates the prepared density operator ρ into $\tilde{\rho}$ in order to probe the corresponding spherical functions $f^{(\ell)}_j(\beta_r,\alpha_r)$ for different polar angles β_r and azimuthal angles α_r using axial tensor operators, i.e., axial multipole sensors, (see Result 3). The rotation $\mathcal{R}^{-1}_{\alpha_r\beta_r}$ is implemented by rf pulses $[\beta_r]_{\alpha_r-\pi/2}$ with flip angle β_r and phase $(\alpha_r-\pi/2)$ which are simultaneously applied to all spins.

The unitary transformations $\mathcal{U}^{(\ell,n)}_j$ [see Eq. (13) of Result 3] are applied in the third block in order to transform the density matrix $\tilde{\rho}$ into directly detectable Cartesian product operators for the various linear, bilinear, and trilinear operators (see Table III in Sec. VII). The specific experimental implementation of the unitary transformations $\mathcal{U}^{(\ell,n)}_j$ consists of rf pulses with flip angle $\pi/2$ as detailed in Appendix D.

In the fourth block, the NMR signal is measured in an acquisition period Acq which has a duration of 5.7 ms (one spin), 11.4 ms (two spins), and 14.9 ms (three spins). In the last block, a relaxation delay RD with a duration of 7 s (one spin), 10 s (two spins), and 15 s (three spins) recovers the initial equilibrium state $\rho_{\rm th}$,

In the tomography experiment, all blocks are repeated multiple times (see Fig. 9). The outer loop A runs over all possible droplets $\ell \in L$. Loop B runs over all ranks j contributing to the droplet ℓ. Loop C cycles through all Cartesian product operators $C^{(\ell,n)}_j$ [see Eq. (10)] appearing in the decomposition of the axial tensor operator $T^{(\ell)}_{j0}$ (see Table III in Sec. VII). Finally, the discretized angles $\beta_r \in \{0,15,30,\ldots,180\}$ and $\alpha_r \in \{0,15,30,\ldots,360\}$ (both in degrees) are incremented in the innermost loops D and E. Although not explicitly indicated in Fig. 9, one further loop is necessary for a temporal averaging scheme [see Eq. (15)].

The whole protocol allows us to determine expectation values $\langle M^{(\ell,n)}_j\rangle_{\tilde{\rho}^{(\ell,j,n)}}$, which are normalized and range between 1 and -1. As illustrated in Fig. 10, the spherical functions $f^{(\ell)}(\theta,\phi)$ can be reconstructed by plotting the spherical samples $f^{(\ell)}(\beta_r,\alpha_r)$ for all angles $\beta_r \in \{0,\ldots,180\}$ and $\alpha_r \in \{0,\ldots,360\}$ (both in degrees) at a distance $|f^{(\ell)}(\beta_r,\alpha_r)|$ from the origin. The phase $\varphi^{(\ell)}(\beta_r,\alpha_r) = \mathrm{atan}(\mathrm{Im}\{f^{(\ell)}(\beta_r,\alpha_r)\}/\mathrm{Re}\{f^{(\ell)}(\beta_r,\alpha_r)\})$ is color coded. For example, the spherical function of the Hermitian operator I_{1x} is given by a real function, and the positive and negative values of $f^{(\ell)}(\theta,\phi)$ are indicated by the colors red (dark gray) and green (light gray), respectively.

C. Experimental errors

A reasonable match between the experimentally reconstructed and theoretical predicted spherical functions is found in Figs. 4–6. Deviations are attributed to experimental imperfections, such as the finite experimental signal-to-noise ratio, finite accuracy of pulse calibration, B_0 and B_1 inhomogeneity [16,46], pulse shape distortions due to the amplifiers and the finite bandwidth of the resonator [47], relaxation losses during the preparation and detection blocks, partial saturation of the signal due to a finite relaxation period between scans, radiation damping effects [48], and truncation effects in the

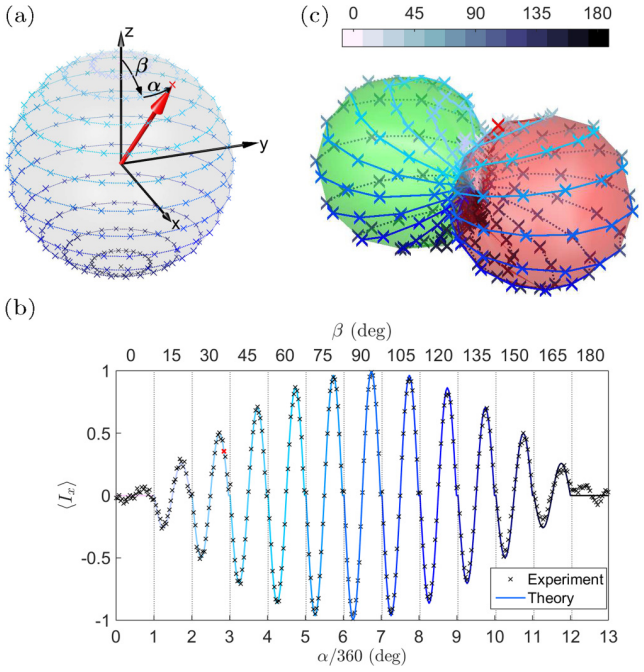

FIG. 10. Reconstruction of a spherical function from experimental samples $f^{(\ell)}(\beta_r,\alpha_r)$. (a) Samples (crosses) with different polar angles $\beta_r \in \{0,180\}$ in degrees (circles colored by latitude) and phases $\alpha_r \in \{0,360\}$ in degrees acquired using rf pulses $[\beta_r]_{\alpha_r-\pi/2}$. (b) Predicted expectation values $\langle M^{(1,1)}_1\rangle_{\tilde{\rho}^{(\ell,j,n)}} = \langle I_{1x}\rangle$ depending on a discrete set of polar angles $\beta \in \{0,15,\ldots,180\}$ in degrees and a continuous set of azimuthal angles α. (c) Smooth surface interpolated from individual samples with distance from the origin given by $f^{(\ell)}(\beta_r,\alpha_r)$, the phase of which determines the color of the surface (see Fig. 1).

automated integration and comparison of the spectra. We quantify these deviations by the root-mean-square difference between experiment and theory averaged over all measured angles β_r and α_r. The resulting errors for the prepared and measured Cartesian product operators are summarized in Table II of Sec. VII. In order to minimize the effects of field inhomogeneities, Shigemi tubes were used in the experiments in order to reduce the sample volume. We have tested replacing the simple rectangular pulses $[\beta_r]_{\alpha_r-\pi/2}$ in the implementation of the rotations $\mathcal{R}^{-1}_{\alpha_r\beta_r}$ with composite pulses [49], which, however, did not result in an improved performance.

IX. CONCLUSION

We have theoretically developed and experimentally demonstrated a Wigner tomography scheme the mapping of which between multispin operators and spherical functions is based on [30]. Our approach reconstructs the relevant spherical functions by measuring expectation values of rotated axial tensor operators, i.e., axial multipole sensors. It is universally applicable and not restricted to NMR methodologies or particles with spin 1/2. A reasonable match between theoretical predictions and NMR experiments was found.

Our theoretical analysis provides a simple physical interpretation of the individual spherical functions in terms of fictitious multipole potentials which can be sampled

locally. The objective was to experimentally recover the three-dimensional shapes of the spherical functions for each of the prepared operators. In particular, we have not used any *a priori* information on what shapes to expect. A large number of sampling points is necessary to recover the shapes in sufficient detail. As the simple rectangular grid of sampling points in the space of polar and azimuthal angles used here is highly anisotropic (i.e., more densely concentrated at the poles), a straightforward improvement is to choose more isotropic sampling strategies such as Lebedev grids [50–52]. Moreover, one could use interpolation methods or even adaptive sampling schemes which increase the sampling density in areas where the spherical function varies more strongly. A more quantitative analysis of the complexity of our proposed tomography approach in terms of the number of individual measurements could rely first on a detailed empirical account on how the precision measured by the fidelity depends on the sampling strategy and its density. From the theoretical side, it is clear that the number of measurements for any complete tomography of a quantum state will scale exponentially in the number of qubits (or spins). However, relevant information can be reconstructed in our approach even from a subset of the droplets as discussed under (c) in Sec. II. A more accurate understanding of concrete sampling schemes and their optimization building on our reconstruction method will have to be addressed in future work.

Beyond the optical tomographic methods mentioned at the start of the introduction, tomographic approaches play obviously an important part in almost any experiment in quantum information or quantum physics in general. We will now shortly discuss some selected results from the literature. The proposed reconstruction procedure for spherical functions can be directly extended to other types of spherical representations such as multipole operators [30] or the so-called PROPS representation which is based on products of single-spin representations [53]. Our scheme can also be compared to [54], which introduces Wigner functions built from products of single-spin representations, and a corresponding raster scan method in [55] utilizes the probability to find the rotated system in each of the basis states of a Stern-Gerlach-type experiment. In [56], a similar tomographic method based on filtered back projections (in analogy to planar inverse Radon transforms used, e.g., in medical imaging) is used in Stern-Gerlach-type experiments. However, complementary to these tomographic reconstruction schemes for density matrices relying on Stern-Gerlach-type experiments, our scheme is based on projections of operators onto rotated axial tensor operators or experimentally accessible expectation values of transformed axial tensor operators. The measurement of spherical harmonics components of electromagnetic near-field radiation using specifically designed loop antennas as sensors [57–59] is closely related to our interpretation of droplets as multipole potentials (see Sec. IV).

Further tomographic approaches have been established in [60,61] with applications to molecular systems. In those works, the quantum state given as the wave functions of an excited state is obtained by decomposing the wave function in a series of basis functions and the expansion coefficients are acquired by calculating a set of Fourier integrals from the detected signal. Also, the wave packet is reconstructed in [62] by computing the overlap of the state with well-defined reference states for different time intervals.

We want to also contrast our Wigner tomography approach to the so-called spherical tensor analysis (STA) method developed by Suter and Pearson [63] and van Beek *et al.* [49]. Both Wigner tomography and STA experiments have a similar structure. First, a preparation block (called an excitation sequence in STA) is used to prepare a density operator. In a second step, rotations around several axes are applied in a rotation block. Finally, the density matrix is transformed (by a reconversion sequence in STA) into a detectable basis and the signal is detected during an acquisition period. Despite these similarities and the fact that both methods are based on characteristic properties of spherical tensor operators under rotations, the desired data and therefore also the details of the experiments differ considerably. The goal of STA is not to measure a density operator represented by spherical functions, but to decompose the detectable signal at a later time into individual signal components depending on occurring ranks j and orders m in the current density matrix. In the standard form of STA [49,63], the detected signal of a density matrix is not characterized or decomposed in terms of additional quantum numbers or labels ℓ. While a single reconversion sequence is used in STA, different pulse sequences are applied in the Wigner tomography in order to transform operators to directly detectable ones [see Figs. 7(c) and 7(d) and Table V]. As a final difference, a rotation block in STA uses rotations for three Euler angles α, β, and γ, whereas in the Wigner tomography only two Euler angles α and β are necessary.

Lastly, our Wigner tomography can be seen as a stepping stone along the path to identifying and characterizing operators in terms of expansion coefficients for a suitable chosen basis. One can consider various different bases such as simple matrix coefficients, a spherical tensor basis [30,63] (as the one used here), or a Cartesian product basis [16,45,64–66]. In this context of quantum state tomography, the shapes of spherical functions recovered in the Wigner tomography clearly contain highly redundant information, but they also provide information about random or systematic errors of the tomography process itself. One can also envision Wigner tomography as a component of a more general approach where one would like to optimize the number and location of samples for achieving a desired fidelity and robustness against experimental errors [67,68], or recover a physical density matrix and estimate experimental errors (see, e.g., [69–75] and references therein).

ACKNOWLEDGMENTS

This work was supported in part by the Excellence Network of Bavaria (ENB) through ExQM. R.Z. and S.J.G. acknowledge support from the Deutsche Forschungsgemeinschaft (DFG) through Grant No. Gl 203/7-2. We thank Raimund Marx for providing the samples. The experiments were performed at the Bavarian NMR Center at the Technical University of Munich.

APPENDIX A: PROOF OF RESULT 1

We detail now the arguments leading to our reconstruction formula for a spherical function $g(\theta,\phi)$ as stated in Result 1. This result relies on projections of rotated spherical harmonics.

We use the notation introduced in Sec. III. The angles θ and ϕ indicate generic argument values of a spherical function $g(\theta,\phi)$, but the angles β and α refer to specific argument values. First, the right-hand side $s_j\,\langle R_{\alpha\beta}Y_{j0}(\theta,\phi)|g(\theta,\phi)\rangle_{L^2}$ of Eq. (4) in Result 1 is rewritten as $s_j\,\langle R_{\alpha\beta}Y_{j0}(\theta,\phi)|g_j(\theta,\phi)\rangle_{L^2}$, where the familiar orthogonality relation $\langle Y_{jm}(\theta,\phi)|Y_{j'm'}(\theta,\phi)\rangle_{L^2} = \delta_{jj'}\delta_{mm'}$ of spherical harmonics (see p. 68 of [35]) implies the relation $\langle g_j(\theta,\phi)|g_{j'}(\theta,\phi)\rangle_{L^2} = \delta_{jj'}$ for the rank-j parts $g_j(\theta,\phi)$ in the decomposition $g(\theta,\phi) = \sum_j g_j(\theta,\phi)$. Second, one obtains that $s_j\,\langle R_{\alpha\beta}Y_{j0}(\theta,\phi)|g_j(\theta,\phi)\rangle_{L^2} = s_j\,\langle Y_{j0}(\theta,\phi)|R^{-1}_{\alpha\beta}g_j(\theta,\phi)\rangle_{L^2}$ holds, which can be deduced from the invariance $\langle R_{\alpha\beta}Y_{jm}(\theta,\phi)|R_{\alpha\beta}Y_{j'm'}(\theta,\phi)\rangle_{L^2} = \langle Y_{jm}(\theta,\phi)|Y_{j'm'}(\theta,\phi)\rangle_{L^2}$ under rotations. The last relation is easily verified using the formula $R_{\alpha\beta}Y_{jm}(\theta,\phi) = Y_{jm}(\theta-\beta,\phi-\alpha)$ and a change of variables in the integral defining the scalar product (see Sec. III). Finally, $R^{-1}_{\alpha\beta}g_j(\theta,\phi)$ is expanded into a linear combination $\sum_{m'=-j}^{j} c_{jm'}(\alpha,\beta)Y_{jm'}(\theta,\phi)$ of spherical harmonics [76]. It follows that the right-hand side of Eq. (4) is given by $s_j\,\langle Y_{j0}(\theta,\phi)|\sum_{m'=-j}^{j} c_{jm'}(\alpha,\beta)Y_{jm'}(\theta,\phi)\rangle_{L^2} = s_j\,c_{j0}(\alpha,\beta)$.

Similarly, the left-hand side of Eq. (4) is transformed into $g_j(\beta,\alpha) = R^{-1}_{\alpha\beta}g_j(0,0) = \sum_{m'=-j}^{j} c_{jm'}(\alpha,\beta)Y_{jm'}(0,0) = s_j\,c_{j0}(\alpha,\beta)$, where the formula $Y_{jm'}(0,\phi) = s_j\delta_{m'0}$ (see p. 16 of [77]) has been applied. In summary, we have verified that both sides of Eq. (4) agree, which completes the proof of Result 1.

APPENDIX B: PROOF OF RESULT 2

In this Appendix, we demonstrate the tomography formula as given in Result 2 for an operator A by applying the reconstruction formula of Result 1. The proof relies on mapping A to (a set of) spherical functions $f^{(\ell)}(\theta,\phi)$ as detailed in Sec. II.

TABLE IV. Sequences to prepare the density matrix ρ from the thermal equilibrium state $\rho_{\rm th}$; note $I_{abc} := I_{1a}I_{2b}I_{3c}$.

No. of spins	Sequence	ρ
1	$[\frac{\pi}{2}]_y(I_1)$	I_x
	$[\frac{\pi}{2}]_{-x}(I_1)$	I_y
	identity operation (do nothing)	I_z
2	$\mathcal{P}^{\rm bil}_x$-$[\frac{\pi}{2}]_y(I_2)$	$2I_{1x}I_{2x}$
	$\mathcal{P}^{\rm bil}_y$-$[\frac{\pi}{2}]_{-x}(I_2)$	$2I_{1y}I_{2y}$
	$\mathcal{P}^{\rm bil}_x$-$[\frac{\pi}{2}]_{-y}(I_1)$	$2I_{1z}I_{2z}$
	$\mathcal{P}^{\rm bil}_x$-$[\frac{\pi}{2}]_{-x}(I_2)$	$2I_{1x}I_{2y}$
	$\mathcal{P}^{\rm bil}_y$-$[\frac{\pi}{2}]_y(I_2)$	$2I_{1y}I_{2x}$
	$\mathcal{P}^{\rm bil}_x$-$[\frac{\pi}{2}]_y(I_1)$-$[\frac{\pi}{2}]_{-y}(I_2)$	$2I_{1z}I_{2x}$
3	$\mathcal{P}^{\rm tril}_x$-$[\frac{\pi}{2}]_y(I_2)$-$[\frac{\pi}{2}]_y(I_3)$	$4I_{xxx}$
	$\mathcal{P}^{\rm tril}_x$-$[\frac{\pi}{2}]_{-y}(I_1)$-$[\frac{\pi}{2}]_{-x}(I_1)$-$[\frac{\pi}{2}]_{-x}(I_2)$-$[\frac{\pi}{2}]_{-x}(I_3)$	$4I_{yyy}$
	$\mathcal{P}^{\rm tril}_x$-$[\frac{\pi}{2}]_{-x}(I_2)$-$[\frac{\pi}{2}]_{-x}(I_3)$	$4I_{xyy}$
	$\mathcal{P}^{\rm tril}_x$-$[\frac{\pi}{2}]_{-y}(I_1)$-$[\frac{\pi}{2}]_{-x}(I_1)$-$[\frac{\pi}{2}]_y(I_2)$-$[\frac{\pi}{2}]_{-x}(I_3)$	$4I_{yxy}$
	$\mathcal{P}^{\rm tril}_x$-$[\frac{\pi}{2}]_{-y}(I_1)$-$[\frac{\pi}{2}]_{-x}(I_1)$-$[\frac{\pi}{2}]_{-x}(I_2)$-$[\frac{\pi}{2}]_y(I_3)$	$4I_{yyx}$
	$\mathcal{P}^{\rm tril}_x$-$[\frac{\pi}{2}]_y(I_2)$-$[\frac{\pi}{2}]_{-x}(I_3)$	$4I_{xxy}$
	$\mathcal{P}^{\rm tril}_x$-$[\frac{\pi}{2}]_{-x}(I_2)$-$[\frac{\pi}{2}]_y(I_3)$	$4I_{xyx}$
	$\mathcal{P}^{\rm tril}_x$-$[\frac{\pi}{2}]_{-y}(I_1)$-$[\frac{\pi}{2}]_{-x}(I_1)$-$[\frac{\pi}{2}]_y(I_2)$-$[\frac{\pi}{2}]_y(I_3)$	$4I_{yxx}$
	$\mathcal{P}^{\rm tril}_x$-$[\frac{\pi}{2}]_{-x}(I_2)$	$4I_{xyz}$

TABLE V. Cartesian product operators $C_j^{(\ell,n)}$ with NMR-measurable operators $M_j^{(\ell,n)}$ used in the experiments; note $I_{abc} := I_{1a}I_{2b}I_{3c}$.

ℓ	j	n	$C_j^{(\ell,n)}$	$M_j^{(\ell,n)}$
$\{k\}$	1	1	I_{kz}	I_{kx}
$\{kl\}$	0,2	1	$2I_{kx}I_{lx}$	$2I_{kx}I_{lz}$
		2	$2I_{ky}I_{ly}$	$2I_{ky}I_{lz}$
		3	$2I_{kz}I_{lz}$	$2I_{ky}I_{lz}$
	1	1	$2I_{kx}I_{ly}$	$2I_{kx}I_{lz}$
		2	$2I_{ky}I_{lx}$	$2I_{ky}I_{lz}$
τ_1	1,3	1	$4I_{xxz}$	$4I_{xzz}$
		2	$4I_{xzx}$	$4I_{xzz}$
		3	$4I_{yyz}$	$4I_{yzz}$
		4	$4I_{yzy}$	$4I_{yzz}$
		5	$4I_{zxx}$	$4I_{xzz}$
		6	$4I_{zyy}$	$4I_{xzz}$
		7	I_{zzz}	$4I_{xzz}$
τ_2	1	1	$4I_{xxz}$	$4I_{xzz}$
		2	$4I_{xzx}$	$4I_{xzz}$
		3	$4I_{yyz}$	$4I_{yzz}$
		4	$4I_{yzy}$	$4I_{yzz}$
		5	$4I_{zxx}$	$4I_{xzz}$
		6	$4I_{zyy}$	$4I_{xzz}$
ℓ	j	n	$C_j^{(\ell,n)}$	$M_j^{(\ell,n)}$
τ_2	2	1	$4I_{xzy}$	$4I_{xzz}$
		2	$4I_{yzx}$	$4I_{yzz}$
		3	$4I_{zxy}$	$4I_{xzz}$
		4	$4I_{zyx}$	$4I_{xzz}$
τ_3	1	1	$4I_{xzx}$	$4I_{xzz}$
		2	$4I_{yzy}$	$4I_{yzz}$
		3	$4I_{zxx}$	$4I_{xzz}$
		4	$4I_{zyy}$	$4I_{xzz}$
	2	1	$4I_{xyz}$	$4I_{xzz}$
		2	$4I_{xzy}$	$4I_{xzz}$
		3	$4I_{yxz}$	$4I_{yzz}$
		4	$4I_{yzx}$	$4I_{yzz}$
		5	$4I_{zxy}$	$4I_{xzz}$
		6	$4I_{zyx}$	$4I_{xzz}$
τ_4	0	1	$4I_{xyz}$	$4I_{xzz}$
		2	$4I_{xzy}$	$4I_{xzz}$
		3	$4I_{yxz}$	$4I_{yzz}$
		4	$4I_{yzx}$	$4I_{yzz}$
		5	$4I_{zxy}$	$4I_{xzz}$
		6	$4I_{zyx}$	$4I_{xzz}$

By substituting $g(\theta,\phi)$ with $f^{(\ell)}(\theta,\phi)$ in Result 1 for each label ℓ separately, one obtains that $f_j^{(\ell)}(\beta,\alpha) = s_j \langle R_{\alpha\beta} Y_{j0}(\theta,\phi) | f^{(\ell)}(\theta,\phi)\rangle_{L^2}$. Note that $\langle A^{(\ell)}|B^{(\ell)}\rangle = \langle f_A^{(\ell)}|f_B^{(\ell)}\rangle_{L^2}$ for the spherical functions $f_A^{(\ell)}$ and $f_B^{(\ell)}$ corresponding to the operators A and B, which can easily be verified by expanding the arguments into tensor operators and spherical harmonics and applying their orthonormality relations. Moreover, the correspondence between operators and spherical functions is covariant under rotations (see Proposition 1(d) in [30]), i.e., the operator $\mathcal{R}_{\alpha\beta} T_{j0}^{(\ell)}$ is mapped to $R_{\alpha\beta} Y_{j0}(\theta,\phi)$ [78]. The last two statements imply that $f_j^{(\ell)}(\beta,\alpha) = s_j \langle \mathcal{R}_{\alpha\beta} T_{j0}^{(\ell)} | A^{(\ell)}\rangle = s_j \langle \mathcal{R}_{\alpha\beta} T_{j0}^{(\ell)} | A\rangle$, where the last step follows as $\langle A^{(\ell)}|A^{(\ell')}\rangle = 0$ if $\ell \neq \ell'$ (which is a consequence of the orthonormality of the tensor operators $T_{jm}^{(\ell)}$). This completes the proof of Eq. (5) in Result 2, and Eq. (6) is then a direct consequence due to the fact that $\mathcal{R}_{\alpha\beta} T_{j0}^{(\ell)} = [\mathcal{R}_{\alpha\beta} T_{j0}^{(\ell)}]^\dagger$ is Hermitian.

APPENDIX C: DERIVATION OF EQ. (12)

Here, we derive the formula of Eq. (12) given in Result 3 starting from Result 2. In standard NMR experiments, only the signatures of Cartesian product operators [16] that contain a single transverse Cartesian operator I_{ka} with $a \in \{x, y\}$ (such as I_{ka}, $2I_{ka}I_{lz}$, and $4I_{ka}I_{lz}I_{mz}$) can be measured *directly*, and hence the expectation values of axial operators $T_{j0}^{(\ell)}$ are not *directly* accessible. Nevertheless, these expectation values can be measured *indirectly* since the operators $T_{j0}^{(\ell)} = \sum_n r_j^{(\ell,n)} C_j^{(\ell,n)}$ can always be expressed as real linear combinations of (Hermitian) standard Cartesian product operators $C_j^{(\ell,n)}$ [16]. Thus, the tomography formula of Eq. (12) can be rewritten as $f_j^{(\ell)}(\beta,\alpha) = s_j \sum_n r_j^{(\ell,n)} \langle \mathcal{R}_{\alpha\beta} C_j^{(\ell,n)}\rangle_\rho$. One obtains that $f_j^{(\ell)}(\beta,\alpha) = s_j \sum_n r_j^{(\ell,n)} \mathrm{Tr}\{C_j^{(\ell,n)} \tilde{\rho}\}$ where $\tilde{\rho} := \mathfrak{R}_{\alpha\beta}^\dagger \rho \mathfrak{R}_{\alpha\beta}$ by exploiting the action $\mathcal{R}_{\alpha\beta} C_j^{(\ell,n)} = \mathfrak{R}_{\alpha\beta} C_j^{(\ell,n)} \mathfrak{R}_{\alpha\beta}^\dagger$ via the operator $\mathfrak{R}_{\alpha\beta} := \exp(-i\alpha \sum_{k=1}^n I_{kz}) \exp(-i\beta \sum_{k=1}^n I_{ky})$ and the fact that the trace is invariant under cyclic permutations. The operators $C_j^{(\ell,n)}$ can be transformed into measurable operators $M_j^{(\ell,n)} = U_j^{(\ell,n)} C_j^{(\ell,n)} U_j^{(\ell,n)\dagger}$ with unitary transformations $U_j^{(\ell,n)}$, which can be realized experimentally using radio-frequency pulses and coupling evolutions. Hence, the formula of Eq. (12) is given by $f_j^{(\ell)}(\beta,\alpha) = s_j \sum_n r_j^{(\ell,n)} \mathrm{Tr}\{M_j^{(\ell,n)} \tilde{\tilde{\rho}}^{(\ell,j,n)}\}$, where immaterial cyclic permutations of the trace have again been applied and where $\tilde{\tilde{\rho}}^{(\ell,j,n)} := U_j^{(\ell,n)} \tilde{\rho} U_j^{(\ell,n)\dagger}$. Finally, the definition of the expectation value yields $f_j^{(\ell)}(\beta,\alpha) = s_j \sum_n r_j^{(\ell,n)} \langle M_j^{(\ell,n)}\rangle_{\tilde{\tilde{\rho}}^{(\ell,j,n)}}$.

APPENDIX D: PREPARATION AND DETECTION SEQUENCES

We detail the explicit form of the preparation and detection sequences used in the experiments in order to demonstrate our Wigner tomography. We denote a pulse with flip angle β and phase α that is applied to spin k by $[\beta]_\alpha(I_k)$. Similarly, $[\beta]_\alpha(I_k, I_l)$ specifies two pulses both of flip angle β and phase α that are simultaneously applied to spins k and l. We also use the notation $\mathcal{P}_{x,y}^{\mathrm{bil}} = [\frac{\pi}{2}]_y(I_2)\text{-}G\text{-}[\frac{\pi}{2}]_{x,y}(I_1)\text{-}t_a\text{-}[\pi]_{y,x}(I_1,I_2)\text{-}t_a$ which represents a pulse sequence which is read from left to right. Here, G represents a pulsed magnetic field gradient that dephases all present transverse spin operators and t_a refers to a time delay of length $1/(4J_{12})$, where J_{12} is the coupling constant between the first and second spin. The pulse sequences $\mathcal{P}_x^{\mathrm{bil}}$ and $\mathcal{P}_y^{\mathrm{bil}}$ create from I_z the bilinear product operators $2I_{1x}I_{2z}$ and $2I_{1y}I_{2z}$, respectively. Moreover, the trilinear product operator $4I_{xzz} := 4I_{1x}I_{2z}I_{3z}$ is obtained from I_z by applying the pulse sequence $\mathcal{P}_x^{\mathrm{tril}} = [\frac{\pi}{2}]_y(I_2,I_3)\text{-}G\text{-}[\frac{\pi}{2}]_y(I_1)\text{-}t_b\text{-}[\pi]_y(I_1,I_3)\text{-}t_c\text{-}[\pi]_y(I_2)\text{-}t_d$ where the time delays are $t_b = 1/(4J_{13})$, $t_c = 1/(4J_{13}) - 1/(4J_{12})$, and $t_d = 1/(4J_{12})$. Using these notations, the preparation sequences are given in Table IV.

For the detection, the Cartesian product operators $C_j^{(\ell,n)}$ have to be rotated into NMR-measurable operators $M_j^{(\ell,n)}$. The relevant pairs of operators $C_j^{(\ell,n)}$ and $M_j^{(\ell,n)}$ are provided in Table V. The rotation pulse sequences are easily inferred, e.g., one uses the pulse $[\pi/2]_y(I_k)$ in order to rotate I_{kz} into I_{kx}. Similarly, $[\pi/2]_{-y}(I_k)$, $[\pi/2]_x(I_k)$, and $[\pi/2]_{-x}(I_k)$ rotate, respectively, I_{kx}, I_{ky}, and I_{kz} into I_{kz}, I_{kz}, and I_{ky}. For example, $4I_{zxy}$ is rotated into $4I_{xzz}$ using the pulse sequence $[\frac{\pi}{2}]_x(I_3)\text{-}[\frac{\pi}{2}]_{-y}(I_2)\text{-}[\frac{\pi}{2}]_y(I_1)$.

[1] D. T. Smithey, M. Beck, M. G. Raymer, and A. Faridani, Phys. Rev. Lett. **70**, 1244 (1993).

[2] D. T. Smithey, M. Beck, J. Cooper, M. G. Raymer, and A. Faridani, Phys. Scr. **1993**, 35 (1993).

[3] D. T. Smithey, M. Beck, J. Cooper, and M. G. Raymer, Phys. Rev. A **48**, 3159 (1993).

[4] U. Leonhardt, *Measuring the Quantum State of Light* (Cambridge University, Cambridge, England, 1997).

[5] *Quantum State Estimation*, edited by M. Paris and J. Rehacek (Springer, Berlin, 2004).

[6] E. Wigner, Phys. Rev. **40**, 749 (1932).

[7] W. P. Schleich, *Quantum Optics in Phase Space* (Wiley-VCH, Weinheim, 2001).

[8] T. L. Curtright, D. B. Fairlie, and C. K. Zachos, *A Concise Treatise on Quantum Mechanics in Phase Space* (World Scientific, Singapore, 2014).

[9] H. M. Nussenzveig, *Introduction to Quantum Optics* (Gordon and Breach, New York, 1973).

[10] W. K. Wooters, Ann. Phys. **176**, 1 (1987).

[11] U. Leonhardt, Phys. Rev. A **53**, 2998 (1996).

[12] C. Miquel, J. P. Paz, and M. Saraceno, Phys. Rev. A **65**, 062309 (2002).

[13] C. Miquel, J. P. Paz, M. Saraceno, E. Knill, R. Laflamme, and C. Negrevergne, Nature (London) **418**, 59 (2002).

[14] K. S. Gibbons, M. J. Hoffman, and W. K. Wootters, Phys. Rev. A **70**, 062101 (2004).

[15] C. Ferrie and J. Emerson, New J. Phys. **11**, 063040 (2009).

[16] R. R. Ernst, G. Bodenhausen, and A. Wokaun, *Principles of Nuclear Magnetic Resonance in One and Two Dimensions* (Clarendon Press, Oxford, 1987).

[17] D. G. Donne and D. G. Gorenstein, Concepts Magn. Reson. **9**, 95 (1997).

[18] R. Freeman, *A Handbook of Nuclear Magnetic Resonance*, 2nd ed. (Addison-Wesley, Harlow, 1997).

[19] R. L. Stratonovich, J. Exp. Theor. Phys. (USSR) **31**, 1012 (1956).

[20] J. C. Várrily and J. M. Garcia-Bondía, Ann. Phys. **190**, 107 (1989).

[21] C. Brif and A. Mann, Phys. Rev. A **59**, 971 (1999).

[22] A. B. Klimov and P. Espinoza, J. Phys. A **35**, 8435 (2002).

[23] A. B. Klimov and P. Espinoza, J. Opt. B **7**, 183 (2005).

[24] C. Brif and A. Mann, J. Phys. A **31**, L9 (1997).

[25] A. Klimov, J. Math. Phys. **43**, 2202 (2002).

[26] J. P. Dowling, G. S. Agarwal, and W. P. Schleich, Phys. Rev. A **49**, 4101 (1994).

[27] P. S. Jessen, D. L. Haycock, G. Klose, G. A. Smith, I. H. Deutsch, and G. K. Brennen, Quantum Inf. Comput. **1** (Special Issue), 20 (2001).

[28] D. J. Philp and P. W. Kuchel, Concepts Magn. Reson. A **25A**, 40 (2005).

[29] D. Harland, M. J. Everitt, K. Nemoto, T. Tilma, and T. P. Spiller, Phys. Rev. A **86**, 062117 (2012).

[30] A. Garon, R. Zeier, and S. J. Glaser, Phys. Rev. A **91**, 042122 (2015).

[31] A. M. Childs, I. L. Chuang, and D. W. Leung, Phys. Rev. A **64**, 012314 (2001).

[32] E. Wigner, *Gruppentheorie und ihre Anwendung auf die Quantenmechanik der Atomspektren* (Friedrich Vieweg & Sohn, Braunschweig, 1931) (English translation in [33]).

[33] E. P. Wigner, *Group Theory and its Application to the Quantum Mechanics of Atomic Spectra* (Academic Press, London, 1959).

[34] G. Racah, Phys. Rev. **62**, 438 (1942).

[35] L. C. Biedenharn and J. D. Louck, *Angular Momentum in Quantum Physics* (Addison-Wesley, Reading, MA, 1981).

[36] B. L. Silver, *Irreducible Tensor Methods* (Academic Press, New York, 1976).

[37] M. Chaichian and R. Hagedorn, *Symmetries in Quantum Mechanics: From Angular Momentum to Supersymmetry* (Institute of Physics, Bristol, 1998).

[38] J. D. Jackson, *Classical Electrodynamics*, 3rd ed. (Wiley, New York, 1999).

[39] Spherical harmonics $Y_{jm}(\theta,\phi) = r(\theta,\phi)\exp[i\eta(\theta,\phi)]$ (and spherical functions) are plotted throughout this paper by mapping their spherical coordinates θ and ϕ to the radial part $r(\theta,\phi)$ and phase $\eta(\theta,\phi)$.

[40] N. J. Glaser and S. J. Glaser, "SpinDrops [Mobile application]" (2014), itunes.apple.com.

[41] Cartesian operators for single spins are $I_x := \sigma_x/2$, $I_y := \sigma_y/2$, and $I_z := \sigma_z/2$, where the Pauli matrices are $\sigma_x = \left(\begin{smallmatrix}0 & 1\\ 1 & 0\end{smallmatrix}\right)$, $\sigma_y = \left(\begin{smallmatrix}0 & -i\\ i & 0\end{smallmatrix}\right)$, and $\sigma_z = \left(\begin{smallmatrix}1 & 0\\ 0 & -1\end{smallmatrix}\right)$. For n spins, one has the operators $I_{k\eta} := \bigotimes_{s=1}^{n} I_{a_s}$ where a_s is equal to η for $s{=}k$ and is zero otherwise; note $I_0 := \left(\begin{smallmatrix}1 & 0\\ 0 & 1\end{smallmatrix}\right)$.

[42] Hermitian operators lead to positive and negative values which are shown in red (dark gray) and green (light gray).

[43] B. E. Sagan, *The Symmetric Group*, 2nd ed. (Springer, New York, 2001).

[44] M. A. Nielsen and I. L. Chuang, *Quantum Computation and Quantum Information* (Cambridge University Press, Cambridge, England, 2000).

[45] I. L. Chuang, N. Gershenfeld, and M. Kubinec, Phys. Rev. Lett. **80**, 3408 (1998).

[46] M. H. Levitt, *Spin Dynamics: Basics of Nuclear Magnetic Resonance* (Wiley, New York, 2008).

[47] A. Tabuchi, M. Negoroa, K. Takedab, and M. Kitagawa, J. Magn. Reson. **204**, 327 (2010).

[48] M. P. Augustine and E. L. Hahn, Concepts Magn. Reson. **13**, 1 (2001).

[49] J. D. van Beek, M. Carravetta, G. C. Antonioli, and M. H. Levitt, J. Chem. Phys. **122**, 244510 (2005).

[50] V. I. Lebedev, USSR Comput. Math. Math. Phys. **15**, 44 (1975).

[51] V. I. Lebedev, USSR Comput. Math. Math. Phys. **16**, 10 (1976).

[52] V. I. Lebedev and D. N. Laikov, Russian Acad. Sci. Dokl. Math. **59**, 477 (1999).

[53] B. Koczor, R. Zeier, and S. J. Glaser, arXiv:1612.06777.

[54] T. Tilma, M. J. Everitt, J. H. Samson, W. J. Munro, and K. Nemoto, Phys. Rev. Lett. **117**, 180401 (2016).

[55] R. P. Rundle, P. W. Mills, T. Tilma, J. H. Samson, and M. J. Everitt, Phys. Rev. A **96**, 022117 (2017).

[56] R. Schmied and P. Treutlein, New J. Phys. **13**, 065019 (2011).

[57] B. Vincent, O. Chadebec, J.-L. Schanen, C. A. F. Sartori, L. Krähenbühl, R. Perrussel, and K. Berger, J. Microw. Optoelectron. Electromagn. Appl. **8**, 64S (2009).

[58] B. Vincent, O. Chadebec, J. L. Schanen, and K. Berger, IEEE Trans. Instrum. Meas. **59**, 3086 (2010).

[59] A. Bréard, F. Tavernier, Z. Li, and L. Krähenbühl, IEEE Trans. Magn. **52**, 1 (2016).

[60] D. Avisar and D. J. Tannor, Phys. Rev. Lett. **106**, 170405 (2011).

[61] C. Menzel-Jones and M. Shapiro, J. Phys. Chem. Lett. **3**, 3353 (2012).

[62] T. S. Humble and J. A. Cina, Phys. Rev. Lett. **93**, 060402 (2004).

[63] D. Suter and J. Pearson, Chem. Phys. Lett. **144**, 328 (1988).

[64] I. L. Chuang, N. Gershenfeld, M. G. Kubinec, and D. W. Leung, Proc. R. Soc. A **454**, 447 (1998).

[65] R. Das, T. S. Mahesh, and A. Kumar, Phys. Rev. A **67**, 062304 (2003).

[66] G. M. Leskowitz and L. J. Mueller, Phys. Rev. A **69**, 052302 (2004).

[67] A. Miranowicz, K. Bartkiewicz, J. Peřina, M. Koashi, N. Imoto, and F. Nori, Phys. Rev. A **90**, 062123 (2014).

[68] L. L. Rouve, L. Schmerber, O. Chadebec, and A. Foggia, IEEE Trans. Magn. **42**, 1167 (2006).

[69] C. Schwemmer, L. Knips, D. Richart, H. Weinfurter, T. Moroder, M. Kleinmann, and O. Gühne, Phys. Rev. Lett. **114**, 080403 (2015).

[70] L. Knips, C. Schwemmer, N. Klein, J. Reuter, G. Tóth, and H. Weinfurter, arXiv:1512.06866.

[71] P. Faist and R. Renner, Phys. Rev. Lett. **117**, 010404 (2016).

[72] G. B. Silva, S. Glancy, and H. M. Vasconcelos, Phys. Rev. A **95**, 022107 (2017).

[73] A. Steffens, C. A. Riofrí, W. McCutcheon, I. Roth, B. A. Bell, A. McMillan, M. S. Tame, J. G. Rarity, and J. Eisert, Quantum Sci. Technol. **2**, 025005 (2017).

[74] C. A. Riofrí, D. Gross, S. T. Flammia, T. Monz, D. Nigg, R. Blatt, and J. Eisert, Nat. Commun. **8**, 15305 (2017).

[75] D. Suess, Ł. Rudnicki, T. O. Maciel, and D. Gross, New J. Phys. **19**, 093013 (2017).

[76] Even though our arguments do not rely on explicitly knowing the expansion coefficients $c_{jm'}(\alpha,\beta)$, it might be instructive to specify the expansion coefficients in terms of the widely used Wigner-D matrices $D^j_{m'm}(\alpha,\beta,\gamma)$ [35,77]. Let us also assume that the rank-j parts $g_j(\theta,\phi)$ are expanded into $g_j(\theta,\phi)=\sum_{m=-j}^{j}\tilde{c}_{jm}Y_{jm}(\theta,\phi)$ using certain coefficients $\tilde{c}_{jm}$. The theory of Wigner-D matrices [35,77] implies that $R^{-1}_{\alpha\beta}\,Y_{jm}(\theta,\phi)=\sum_{m'=-j}^{j}D^j_{m'm}(0,-\beta,-\alpha)\,Y_{jm'}(\theta,\phi)$. Hence, we obtain the formula $R^{-1}_{\alpha\beta}\,g_j(\theta,\phi)=\sum_{m=-j}^{j}\tilde{c}_{jm}\times\sum_{m'=-j}^{j}D^j_{m'm}(0,-\beta,-\alpha)\,Y_{jm'}(\theta,\phi)$ which shows that $c_{jm'}(\alpha,\beta)=\sum_{m=-j}^{j}\tilde{c}_{jm}\,D^j_{m'm}(0,-\beta,-\alpha)$.

[77] E. O. Steinborn and K. Rueddenberg, Adv. Quantum Chem. **7**, 1 (1973).

[78] This relation can also be established using the theory of Wigner-D matrices [35,77] where $D^j_{m'm}(\alpha,\beta,\gamma)=\langle Y_{jm'}(\theta,\phi)|R_{\alpha\beta\gamma}Y_{jm}(\theta,\phi)\rangle_{L^2}$ (see pp. 41 and 276 of [35]) and $D^j_{m'm}(\alpha,\beta,\gamma)=\langle T^{(\ell)}_{jm'}|\mathcal{R}_{\alpha\beta\gamma}T^{(\ell)}_{jm}\rangle$ (see p. 45 of [35]). Here, $\mathcal{R}_{\alpha\beta\gamma}C:=\mathfrak{R}_{\alpha\beta\gamma}C\mathfrak{R}^{-1}_{\alpha\beta\gamma}$ with $\mathfrak{R}_{\alpha\beta\gamma}:=e^{-i\alpha F_z}e^{-i\beta F_y}e^{-i\gamma F_z}$ (see Sec. III where $\mathcal{R}_{\alpha\beta}=\mathcal{R}_{\alpha\beta0}$).

B Wigner process tomography: Visualization of spin propagators and their spinor properties

Bibliography:

Title: Wigner process tomography: Visualization of spin propagators and their spinor properties

Authors: D. Leiner and S. J. Glaser

Journal: Physical Review A

Volume: 98

Issue: 1

Page: 012112

Published: 10.07.2018

DOI: 10.1103/PhysRevA.98.012112

URL: `https://link.aps.org/doi/10.1103/PhysRevA.98.012112`

Summary and contribution to this manuscript:

In this work, the tomography of time evolution operators, the so-called propagators, is studied for spin systems in the DROPS representation, which completely characterize and visualize operators using shapes assembled from linear combinations of spherical harmonics. It builds on and extends the methodology of the previous work "Wigner tomography of multispin quantum states". Propagators of a N spin 1/2 system are imprinted to the density matrix of an augmented system with an additional ancilla qubit. This can be achieved by applying a sequence of pulses generating a controlled version of the propagator which then transfers the original propagator to the off-diagonal elements of the density operator of the augmented system. A modified version of the Wigner tomography method introduced in "Wigner tomography of multispin quantum states" can then be applied to obtain the spherical functions for the propagator. This idea was proposed by Steffen Glaser. An experimental and generally applicable protocol was derived by David Leiner which was then tailored to NMR techniques. That is, a general procedure to reconstruct spherical functions representing propagators is to prepare a controlled propagator which is used to imprint the original propagator to the state of the augmented system, and then measure sets of expectation values of product operators for different azimuthal and polar angles. This approach is in particular useful to conveniently visualize the spinor properties for spins 1/2. The methodology was experimentally tested using NMR methods by reconstructing various propagators which represent prominent one-qubit gates such as a NOT gate, a $\sqrt{\text{NOT}}$ gate, a Hadamard gate, different phase-gates, and rotations around

the x-axis. The experimental reconstruction procedure is demonstrated using a simple scheme with equidistant steps of azimuthal and polar angles. These experiments were done by David Leiner. We used chloroform as a two-spin model system for the experiments. The paper is concluded by a comprehensive discussion comparing our approach in particular to existing reconstruction schemes in literature. An extensive appendix complements the paper including an illustrative example for this methodology for the case of a single spin 1/2 and an analysis of propagator errors in the DROPS representation which provides information about specific error types corresponding to the type of deviations of droplets from their ideal shapes. Simulations were carried out by David Leiner to compare the experimental results with the theory. A reasonable match between the theoretical predicted and experimentally reconstructed spherical functions is obtained. Deviations are attributed to experimental imperfections such as B_0 and B_1 inhomogeneities, finite accuracy of pulse calibration, and relaxation losses. The manuscript in its original form was also written by David Leiner and revised by Steffen Glaser.

Wigner process tomography: Visualization of spin propagators and their spinor properties

David Leiner* and Steffen J. Glaser†
Technische Universität München, Department Chemie, Lichtenbergstrasse 4, 85747 Garching, Germany

(Received 29 March 2018; revised manuscript received 23 May 2018; published 10 July 2018)

We study the tomography of propagators for spin systems in the context of finite-dimensional Wigner representations, which completely characterize and visualize operators using shapes assembled from linear combinations of spherical harmonics. The Wigner representation of a propagator can be experimentally recovered by measuring expectation values of rotated axial spherical tensor operators in an augmented system with an additional ancilla qubit. The methodology is experimentally demonstrated for standard one-qubit quantum gates using nuclear magnetic resonance spectroscopy. In particular, this approach provides a direct and compelling visualization of the spinor property of the propagators corresponding to the rotation of a spin-1/2 particle.

DOI: 10.1103/PhysRevA.98.012112

I. INTRODUCTION

Phase-space representations provide useful tools for the characterization and visualization of quantum systems [1–3]. Here we consider continuous Wigner representations of individual [4,5] and coupled [6–8] spin systems. In particular, we focus on the so-called DROPS (discrete representation of operators for spin systems) representation [6,9], which provides an intuitive visualization of the states and operators of coupled spin systems, reflecting physically relevant properties, such as symmetries with respect to rotations and permutations of spins. The DROPS representation has also been implemented in a free, interactive application software [10,11]. Following the general strategy of Stratonovich [4], which specifies criteria for the definition of continuous Wigner functions for finite-dimensional quantum systems, the DROPS representation is based on a mapping of arbitrary operators to a set of spherical functions which are denoted as *droplets*. In particular, as illustrated in [6,12], the DROPS representation is also applicable to propagators and not limited to density operators.

We recently studied an experimental quantum state tomography scheme to scan generalized Wigner representations of the *density operator* for arbitrary multispin quantum states [9]. We also provided explicit experimental protocols for our Wigner tomography scheme and demonstrated its feasibility using nuclear magnetic resonance (NMR) experiments.

In contrast to *state tomography*, where the purpose is to characterize the state of a system, the aim of *process tomography* [13–18] is to fully characterize a quantum process that can be applied to arbitrary states. In the standard process tomography scheme, a set of defined input states is prepared and the output of the unknown quantum process is measured. In general, a quantum process can be described by a completely positive map [19]. In the special case of closed quantum systems with negligible relaxation, quantum processes are characterized by a unitary time evolution operator, the so-called *propagator*.

In this work we ask whether our earlier approach [9] for the tomography of the Wigner representation of quantum states can be extended to experimentally scan the Wigner representation of *propagators*. This would lead to an alternative form of (Wigner) process tomography for the characterization of pulse sequence elements or entire pulse sequences in spectroscopy and in quantum information processing (quantum gates, quantum algorithms). The idea is to imprint a given propagator onto the density operator ρ and to use a variant of the scanning scheme introduced in [9] to reconstruct the Wigner representation of these propagators. We will focus on systems consisting of spins 1/2, even though our approach is applicable to arbitrary spin systems. Additionally, explicit experimental protocols for our Wigner tomography scheme are provided and experimentally demonstrated using methods of NMR.

The proposed Wigner tomography of propagators also provides a direct way to visualize the spinor properties of spin-1/2 rotation operators. Following [20], a spinor is defined as a mathematical entity that changes its sign under a 2π rotation. As discussed in [20], the *propagators* for the rotations of half-integer spins are spinors and a direct consequence of this property is that also the *state vectors* of half-integer spins are spinors. Previous works regarding the measurement of the spinor property of state vectors were based on neutron interferometry [21–24] and also NMR spectroscopy [25–27]. However, to our knowledge the underlying spinor property of entire *propagators* has so far not explicitly been demonstrated. As shown in the following, this property can be directly visualized by observing the sign change of the Wigner representation of rotation propagators.

The paper is organized as follows. An overview of the representation and visualization method for coupled spin systems is given in Sec. II. A brief summary of the scanning approach [9] for the Wigner function of the *density operator* is presented in Sec. III. The generalized methodology for sampling spherical functions representing the Wigner function of *propagators* is introduced in Sec. IV, which also states the main technical

*david.leiner@tum.de
†steffen.glaser@tum.de

results. The experimental protocol and its implementation on an NMR spectrometer are detailed in Secs. V and VI. The results of the NMR experiments are summarized in Sec. VII. We conclude in Secs. VIII and IX by summarizing and discussing theoretical and experimental aspects and with an outlook on possible extensions of the presented approach. Further technical details and illustrative examples are deferred to the Appendix.

II. VISUALIZATION OF OPERATORS USING SPHERICAL FUNCTIONS

For a system consisting of a single spin, any spin operator can be mapped bijectively to a *single* (in general complex) spherical function using the Wigner representation [4,6]. This is achieved by expressing the operator as a linear combination of spherical tensor operators and mapping the spherical tensor operators to the corresponding spherical harmonics [4]. For a system of coupled spins, this approach to map an arbitrary operator to a *single* spherical function is in general not bijective. However, in this case a bijective Wigner representation can still be found if a spin operator A is not mapped to a single spherical function but to a discrete *set* of spherical functions, called the DROPS representation [6]. The individual spherical functions are called droplet functions or simply *droplets* and are denoted $f^{(\ell)} = f^{(\ell)}(\theta,\phi)$ with $\ell \in L$, where L is a set of labels ℓ. The angles θ and ϕ are polar and azimuthal angles, respectively. This mapping requires decomposing the operator A into a sum of a corresponding discrete *set* of droplet operators $A^{(\ell)}$:

$$A = \sum_{\ell \in L} A^{(\ell)}. \tag{1}$$

As discussed in more detail in [6], many different partitions are possible but here we focus on the so-called LISA basis, which characterizes each droplet operator $A^{(\ell)}$ uniquely by its linearity (i.e., the number of involved spins) and the subsystem (i.e., the identity of the involved spins). For three or more spins, additional auxiliary criteria, such as permutation symmetry, etc., are needed to uniquely label the droplets [6]. This is illustrated in Fig. 1(a) for the simple case of two coupled spins 1/2 denoted I_1 and I_2. In this case, the set of droplet operators $A^{(\ell)}$ consists of four elements with labels {1}, {2}, {12}, and {∅}. The linear droplet operators $A^{\{1\}}$ and $A^{\{2\}}$ act only on spins I_1 and I_2, respectively. The bilinear droplet operator $A^{\{12\}}$ acts on both spins I_1 and I_2, whereas the droplet operator $A^{\{\emptyset\}}$ is proportional to the identity operator $\mathbf{1}$ and acts neither on spin I_1 nor on spin I_2.

As shown in the center of Fig. 1(a), the operators $A^{\{1\}}$, $A^{\{2\}}$, $A^{\{12\}}$, and $A^{\{\emptyset\}}$ can be mapped to the droplet functions $f^{\{1\}}$, $f^{\{2\}}$, $f^{\{12\}}$, and $f^{\{\emptyset\}}$, which can be graphically displayed as colored three-dimensional shapes. In these three-dimensional polar plots of the droplets $f^{(\ell)}(\theta,\phi)$, the distance from the origin to a point on the surface represents the absolute value $|f^{(\ell)}(\theta,\phi)|$ and the color represents the phase $\varphi = \arg[f^{(\ell)}(\theta,\phi)]$ as defined by the color bar. At the bottom of Fig. 1(a), the four droplets are arranged such that the positions of the two linear droplets $f^{\{1\}}$ and $f^{\{2\}}$ correspond to the positions of the two spins I_1 and I_2. The bilinear droplet $f^{\{12\}}$ is positioned in the center of the line connecting $f^{\{1\}}$ and $f^{\{2\}}$ and the droplet $f^{\{\emptyset\}}$ is plotted separately below the other droplets. This graphical representation of the droplets closely corresponds to physical intuition and makes it easy, e.g., to follow the dynamics of spin operators and the involved spins.

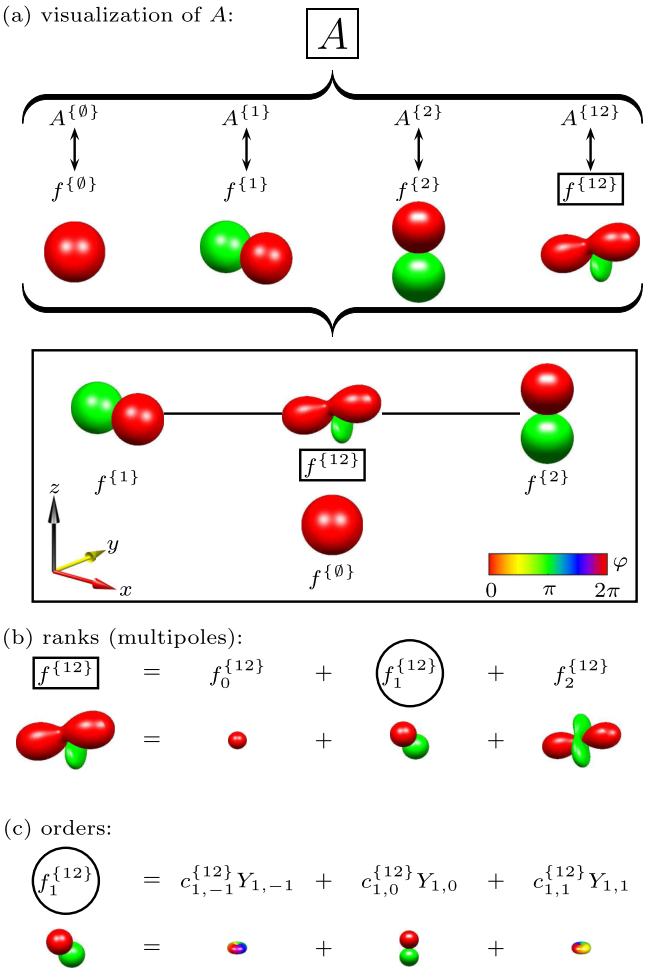

FIG. 1. (a) The two-spin operator $A = \frac{1}{2}\mathbf{1} + I_{1x} + I_{2z} + I_{1x}I_{2x} + I_{1x}I_{2y} + I_{1x}I_{2z}$ [28,29] is represented using multiple spherical functions $f^{(\ell)} = f^{(\ell)}(\theta,\phi)$, and individual components $A^{(\ell)}$ of A mapped to $f^{(\ell)}$ and graphically visualized. (b) $f^{\{12\}}$ (box) decomposed into its 2^j-multipole contributions $f_j^{\{12\}}$ with $j \in \{0,1,2\}$. (c) $f_1^{\{12\}}$ (circle) decomposed into spherical harmonics of order $m \in \{-1,0,1\}$; $Y_{1,-1}$ and $Y_{1,1}$ are rainbow colored [30].

The droplet operators $A^{(\ell)}$ can be further decomposed into multipole components $A_j^{(\ell)}$ with different ranks j, where each $A^{(\ell)}$ only contains a finite number of possible ranks:

$$A^{(\ell)} = \sum_{j \in J(\ell)} A_j^{(\ell)}. \tag{2}$$

The set $J(\ell)$ includes all occurring ranks j of a given droplet ℓ [6]. For example, for the bilinear droplet operator $A^{\{12\}}$ possible values of the rank j are 0, 1, and 2, for the linear droplet operators $A^{\{1\}}$ and $A^{\{2\}}$ the only possible rank is $j = 1$, and for $A^{(\emptyset)}$ the only possible rank is $j = 0$ [6].

The decomposition of each droplet operator $A^{(\ell)}$ is reflected by a decomposition of the corresponding droplet function $f^{(\ell)}$:

$$f^{(\ell)} = \sum_{j\in J(\ell)} f_j^{(\ell)}. \tag{3}$$

This is illustrated in Fig. 1(b) for the decomposition of $f^{\{12\}}$ into the three rank-j droplet functions $f_0^{\{12\}}$, $f_1^{\{12\}}$, and $f_2^{\{12\}}$.

Finally, the rank-j droplet operators $A_j^{(\ell)}$ can be decomposed into a linear combination of components of irreducible spherical tensor operators $T_{jm}^{(\ell)}$ [31–36] of order m with $-j \leqslant m \leqslant j$ and (in general complex) coefficients $c_{jm}^{(\ell)}$. It is at this level that the DROPS representation exploits the well-known mathematical correspondence between irreducible tensor operators and spherical harmonics $Y_{jm} = Y_{jm}(\theta,\phi)$ [35,36]. Mapping the operators $T_{jm}^{(\ell)}$ to the corresponding functions Y_{jm} results in the following mapping between the rank-j component $A_j^{(\ell)}$ of the operator $A^{(\ell)}$ to the rank-j component of $f_j^{(\ell)}$ of the droplet function $f^{(\ell)}$:

$$A_j^{(\ell)} = \sum_{m=-j}^{j} c_{jm}^{(\ell)} T_{jm}^{(\ell)} \quad\longleftrightarrow\quad f_j^{(\ell)} = \sum_{m=-j}^{j} c_{jm}^{(\ell)} Y_{jm}, \tag{4}$$

where the coefficients $c_{jm}^{(\ell)}$ in the left and the right sums are identical. Figure 1(c) illustrates the synthesis of the bilinear rank 1 droplet function $f_1^{\{12\}}$ based on the linear combination of the spherical harmonics $Y_{1,-1}$, $Y_{1,0}$, and $Y_{1,1}$ with coefficients $c_{1,-1}^{\{12\}}$, $c_{1,0}^{\{12\}}$, and $c_{1,1}^{\{12\}}$.

Overall, this results in a bijective mapping between each droplet operator $A^{(\ell)}$ and the corresponding spherical droplet functions $f^{(\ell)}$,

$$A^{(\ell)} = \sum_{j\in J(\ell)} A_j^{(\ell)} \quad\longleftrightarrow\quad f^{(\ell)} = \sum_{j\in J(\ell)} f_j^{(\ell)}, \tag{5}$$

and in the mapping of any arbitrary operator A to a corresponding set of droplet functions $f^{(\ell)}$,

$$A = \sum_{\ell\in L} A^{(\ell)} \quad\longleftrightarrow\quad \bigcup_{\ell\in L} f^{(\ell)}. \tag{6}$$

III. SUMMARY OF THE SCANNING APPROACH FOR DENSITY OPERATORS

We summarize the experimental reconstruction approach of [9] to obtain a Wigner representation of a density operator. Consider an arbitrary multispin operator A, whose Wigner representation corresponds to a set of spherical droplet functions $f^{(\ell)}(\theta,\phi) = \sum_{j\in J(\ell)} f_j^{(\ell)}(\theta,\phi)$ as introduced in Sec. II. The angles θ and ϕ indicate generic argument values of a spherical function $g(\theta,\phi)$, whereas in the following the angles α and β will be used to refer to specific argument values. In order to distinguish matrices of different size, in the following we use the notation $A^{[N]}$, where the superscript $[N]$ indicates the number of spins in the spin system. The label ℓ discriminates between the different spherical droplet functions. For each label ℓ, the rank-j component $f_j^{(\ell)}(\beta,\alpha)$ of $f^{(\ell)} = \sum_{j\in J(\ell)} f_j^{(\ell)}$ can be determined for polar angles $0 \leqslant \beta \leqslant \pi$ and azimuthal angles $0 \leqslant \alpha < 2\pi$ by

$$f_j^{(\ell)}(\beta,\alpha) = s_j \left\langle T_{j,\alpha\beta}^{(\ell)[N]} \middle| A^{[N]} \right\rangle \tag{7}$$

with the scalar product

$$\left\langle T_{j,\alpha\beta}^{(\ell)[N]} \middle| A^{[N]} \right\rangle = \mathrm{tr}\left\{ \left(T_{j,\alpha\beta}^{(\ell)[N]}\right)^{\dagger} A^{[N]} \right\}, \tag{8}$$

and where

$$T_{j,\alpha\beta}^{(\ell)[N]} = R_{\alpha\beta}^{[N]} \left(T_{j0}^{(\ell)}\right)^{[N]} \left(R_{\alpha\beta}^{[N]}\right)^{\dagger} \tag{9}$$

is the rotated version of an axial tensor operator $(T_{j0}^{(\ell)})^{[N]}$ of rank j and order 0 as introduced in Sec. II (see also Result 2 in [9]). The rotation operator $R_{\alpha\beta}^{[N]} = \exp\{-i\alpha F_z^{[N]}\}\exp\{-i\beta F_y^{[N]}\}$ with the total spin operators $F_z^{[N]} = \sum_{k=1}^{N} I_{kz}^{[N]}$ and $F_y^{[N]} = \sum_{k=1}^{N} I_{ky}^{[N]}$ corresponds to rotation around the y axis by β followed by rotation around the z axis by α. The operators $I_{kb}^{[N]}$ with $b \in \{x,y,z\}$ are spin operators acting only on the kth spin I_k [28]. The prefactors s_j are given by $s_j = \sqrt{(2j+1)/(4\pi)}$.

If the density matrix $\rho^{[N]}$ of a spin system can be prepared to be identical to the operator $A^{[N]}$, for all droplets ℓ the rank-j droplet components $f_j^{(\ell)}$ for $j \in J(\ell)$ become experimentally accessible by measuring expectation values [9]

$$f_j^{(\ell)}(\beta,\alpha) = s_j \left\langle T_{j,\alpha\beta}^{(\ell)[N]} \right\rangle_{\rho^{[N]}}, \tag{10}$$

with the expectation value given by

$$\left\langle T_{j,\alpha\beta}^{(\ell)[N]} \right\rangle_{\rho^{[N]}} = \mathrm{tr}\left\{ T_{j,\alpha\beta}^{(\ell)[N]} \rho^{[N]} \right\}. \tag{11}$$

This is due to the fact that the expectation value in Eq. (11) is identical to the scalar products $\langle T_{j,\alpha\beta}^{(\ell)[N]} | A^{[N]} \rangle$ of Eq. (8), since the rotated axial tensor operators are Hermitian and hence $(T_{j,\alpha\beta}^{(\ell)[N]})^{\dagger} = T_{j,\alpha\beta}^{(\ell)[N]}$.

Equation (10) states that the value of the rank-j droplet components $f_j^{(\ell)}(\beta,\alpha)$ for a density matrix $\rho^{[N]}$ can be calculated from expectation values of rotated axial tensor operators $\langle T_{j,\alpha\beta}^{(\ell)[N]} \rangle_{\rho^{[N]}}$ and further implies that one can then retrace the shapes of the spherical function $f^{(\ell)} = \sum_{j\in J(\ell)} f_j^{(\ell)}$ representing $\rho^{[N]}$ if one experimentally measures $f^{(\ell)}(\beta,\alpha)$ as a function of α and β.

IV. THEORY OF THE WIGNER PROCESS TOMOGRAPHY

We are interested in experimentally scanning the shape of the Wigner representation of a propagator $U^{[N]}$, i.e., of the unitary time-evolution operator created by a given pulse sequence. This is of interest to characterize an unknown propagator or to test how well a propagator $U^{[N]}$ created by an experimentally implemented pulse sequence approaches a desired propagator $U_{\mathrm{target}}^{[N]}$. The targeted evolution operator $U_{\mathrm{target}}^{[N]}$ could be a spectroscopically relevant propagator, which is, e.g., designed to create multiple-quantum coherence from thermal equilibrium spin polarization [37], or a target propagator corresponding to a quantum gate, or an entire quantum algorithm [38].

We consider a system consisting of N spins I_k for $1 \leqslant k \leqslant N$. For simplicity, but without loss of generality, here we assume that all spins are spin-1/2 particles (qubits). In this case, the size of the Hilbert space is 2^N and operators $A^{[N]}$ in this

Hilbert space (such as the density operator $\rho^{[N]}$ or propagators $U^{[N]}$) are represented by $2^N \times 2^N$ matrices. If the operator of interest is the *density operator*, $\rho^{[N]}$, of the spin system, according to Eq. (10) the spherical functions $f_j^{(\ell)}(\beta,\alpha)$ representing droplet components can be determined experimentally by measuring the expectation values of the operators $T_{j,\alpha\beta}^{(\ell)[N]}$. Hence, it is possible to scan the DROPS representation of an arbitrary operator $A^{[N]}$ if it can be experimentally mapped onto the density operator. However, as the density operator $\rho^{[N]}$ is a *Hermitian* matrix, whereas the propagator $U^{[N]}$ is represented by a *unitary* matrix, it is in general not possible to map the $2^N \times 2^N$ matrix representations of an arbitrary propagator $U^{[N]}$ on a $2^N \times 2^N$ matrix representing a density operator $\rho^{[N]}$ and Eqs. (11) and (10) are not directly applicable for the tomography of the Wigner functions of unitary operators. However, as shown in the following, this roadblock to experimentally scanning the DROPS representation of a propagator $U^{[N]}$ can be lifted if the spin system is augmented by adding an *ancilla spin* I_0.

A. Inscribing $U^{[N]}$ on the density operator $\rho^{[N+1]}$ of a system augmented by an ancilla spin

In the augmented system consisting of $N+1$ spins, all operators $A^{[N+1]}$ are represented by $2^{N+1} \times 2^{N+1}$ matrices. To simplify the notation and without loss of generality, in the following we characterize the state of the augmented system consisting of $N+1$ spins 1/2 by the traceless part of the full density operator [9,28,39], denoted the *deviation density matrix* [38]. The deviation density matrix $\rho^{[N+1]}$ (with trace zero) is obtained from the full density operator (with trace one) by subtracting the matrix $(1/2^{N+1})\,\mathbf{1}^{[N+1]}$, which is proportional to the $2^{N+1} \times 2^{N+1}$ identity matrix and each diagonal element is given by $(1/2^{N+1})$. The term proportional to the identity operator does not evolve under unitary transformations. Furthermore, in magnetic resonance experiments all detectable operators are traceless. Hence the term proportional to the identity operator does not give rise to detectable signal and can be ignored [38].

It is possible to inscribe a propagator $U^{[N]}$ and its adjoint $(U^{[N]})^\dagger$ of the original system consisting of N spins into the off-diagonal subblocks of the density operator $\rho^{[N+1]}$ of the augmented system in the following way [39–41].

First, it is possible to design a pulse sequence which creates the *controlled* propagator $cU^{[N+1]}$ [39,41,42], which for spins $I_1,\ldots,I_N$ has no effect if the ancilla spin I_0 is in the *up* state $|\uparrow\rangle$ but creates the propagator $U^{[N]}$ if the ancilla spin I_0 is in the *down* state $|\downarrow\rangle$. Hence, the $2^{N+1} \times 2^{N+1}$ matrix representing the propagator $cU^{[N+1]}$ is block-diagonal. The first block corresponds to the $2^N \times 2^N$-dimensional identity matrix $\mathbf{1}^{[N]}$ and the second block is the $2^N \times 2^N$-dimensional propagator $U^{[N]}$:

$$cU^{[N+1]} = \begin{pmatrix} \mathbf{1}^{[N]} & \mathbf{0}^{[N]} \\ \mathbf{0}^{[N]} & U^{[N]} \end{pmatrix}, \tag{12}$$

where $\mathbf{0}^{[N]}$ is the $2^N \times 2^N$-dimensional zero matrix. In the field of quantum information processing, the spin I_0 is called the *control qubit* and the spins $I_1,\ldots,I_N$ on which the unitary operator $U^{[N]}$ act are called the *target qubits* [38].

Second, by putting the ancilla spin I_0 into a superposition state $(|\uparrow\rangle + |\downarrow\rangle)/\sqrt{2}$ and putting the remaining spins into a fully mixed state, the system can be prepared such that the deviation density operator is proportional to

$$\rho_0^{[N+1]} = 2I_{0x}^{[N+1]} = 2I_x \otimes \mathbf{1}^{[N]}. \tag{13}$$

Here the spin operators I_b are defined as $I_b := 1/2\ \sigma_b$ [28,29] for $b \in \{x,y,z\}$, where σ_b is a Pauli spin operator. In NMR implementations, this is achieved by exciting the ancilla spin I_0, i.e., rotating its thermal equilibrium Bloch vector to the x direction and saturating the remaining spins, e.g., by a combination of pulses and pulsed B_0 gradients (see Sec. VI B).

With these ingredients, we can imprint the propagator $U^{[N]}$ on the density operator by applying the controlled propagator $cU^{[N+1]}$ to $\rho_0^{[N+1]}$. This prepares the deviation density matrix [39–41]

$$\rho_U^{[N+1]} = cU^{[N+1]}\,\rho_0^{[N+1]}\,(cU^{[N+1]})^\dagger = \begin{pmatrix} \mathbf{0}^{[N]} & (U^{[N]})^\dagger \\ U^{[N]} & \mathbf{0}^{[N]} \end{pmatrix}, \tag{14}$$

which can be expressed in the form

$$\rho_U^{[N+1]} = I^- \otimes U^{[N]} + I^+ \otimes (U^{[N]})^\dagger \tag{15}$$

using the raising and lowering operators $I^+ = I_x + i\,I_y$ and $I^- = I_x - i\,I_y$ [28]. In Appendix A 1, explicit matrices of the operators $U^{[N]}$, $cU^{[N+1]}$, $\rho_0^{[N]}$, and $\rho_U^{[N+1]}$ are provided for a simple example, where the system of interest consists only of a single spin I_1, augmented by an ancilla spin I_0. Note that the two nonzero off-diagonal subblocks of $\rho_U^{[N+1]}$ are unitary (and in general non-Hermitian), but the overall deviation density operator is Hermitian, i.e., $\rho_U^{[N+1]} = (\rho_U^{[N+1]})^\dagger$.

B. Scanning the DROPS Wigner representation of U based on the density operator of the augmented spin system

As shown in Sec. III, and in more detail in [9], the key to the scanning approach of the DROPS Wigner representation of operators is the experimental determination of scalar products between rotated axial tensor operators $T_{j,\alpha\beta}^{(\ell)[N]}$ and the operator of interest $A^{[N]}$:

$$\langle T_{j,\alpha\beta}^{(\ell)[N]} | A^{[N]} \rangle = \langle T_{j,\alpha\beta}^{(\ell)[N]} \rangle_{\rho^{[N]}}, \tag{16}$$

if $\rho^{[N]} = A^{[N]}$. As shown in Appendix A 2, for $A^{[N]} = U^{[N]}$ and $\rho_U^{[N+1]}$, the corresponding scalar products can be obtained by the following complex linear combination of expectation values of the Hermitian operators $I_x \otimes T_{j,\alpha\beta}^{(\ell)[N]}$ and $I_y \otimes T_{j,\alpha\beta}^{(\ell)[N]}$:

$$\langle T_{j,\alpha\beta}^{(\ell)[N]} | U^{[N]} \rangle = \langle I_x \otimes T_{j,\alpha\beta}^{(\ell)[N]} \rangle_{\rho_U^{[N+1]}} + i\,\langle I_y \otimes T_{j,\alpha\beta}^{(\ell)[N]} \rangle_{\rho_U^{[N+1]}}. \tag{17}$$

In Appendixes A 1 and A 3, this is also illustrated for a simple example. Thus, an analog formula to Eq. (10) for the reconstruction of Wigner functions representing propagators is given by the following result.

Result 1. Consider a propagator $U^{[N]}$ which is represented by a set of spherical functions $f^{(\ell)}(\theta,\phi) = \sum_{j \in J(\ell)} f_j^{(\ell)}(\theta,\phi)$.

The rank-j components $f_j^{(\ell)}(\beta,\alpha)$ can be experimentally measured in the augmented system for arbitrary angles β in the range $[0,\pi]$ and α in the range $[0,2\pi]$ via the complex linear combination of expectation values

$$f_j^{(\ell)}(\beta,\alpha) = s_j\left(\left\langle I_x\otimes T_{j,\alpha\beta}^{(\ell)[N]}\right\rangle_{\rho_U^{[N+1]}} + i\left\langle I_y\otimes T_{j,\alpha\beta}^{(\ell)[N]}\right\rangle_{\rho_U^{[N+1]}}\right) \quad (18)$$

with $s_j := \sqrt{(2j+1)/(4\pi)}$ and, to simplify notation, where $T_{j,\alpha\beta}^{(\ell)[N]} = R_{\alpha\beta}^{[N]}(T_{j0}^{(\ell)})^{[N]}(R_{\alpha\beta}^{[N]})^\dagger$ is a rotated axial tensor operator $(T_{j0}^{(\ell)})^{[N]}$. The rotation operator $R_{\alpha\beta}^{[N]} = \exp\{-i\alpha\sum_{k=1}^N I_{kz}^{[N]}\}\exp\{-i\beta\sum_{k=1}^N I_{ky}^{[N]}\}$ corresponds to a rotation around the y axis by β followed by a rotation around the z axis by α as shown in Fig. 2.

A general procedure to reconstruct the spherical functions $f^{(\ell)}(\beta,\alpha)$ representing a propagator $U^{[N]}$ for the system of interest $I_1,\ldots,I_N$ is first to prepare the augmented system $I_0,\ldots,I_N$ in the state $\rho_0^{[N+1]}$ and apply the controlled unitary $cU^{[N+1]}$ to $\rho_0^{[N+1]}$ to generate $\rho_U^{[N+1]}$ [see Eqs. (12)–(14)]. Then, for all droplets ℓ according to Result 1, the shape of $f^{(\ell)}(\beta,\alpha)$ can be scanned by measuring the expectation values $\langle I_x\otimes T_{j,\alpha\beta}^{(\ell)[N]}\rangle_{\rho_U^{[N+1]}}$ and $\langle I_y\otimes T_{j,\alpha\beta}^{(\ell)[N]}\rangle_{\rho_U^{[N+1]}}$ for all $j\in J(\ell)$ as a function of the angles α and β as exemplified in Fig. 2. Different sampling schemes for α and β are discussed in Sec. VI B (see also Figs. 2 and 3) and in Sec. VIII.

V. NMR IMPLEMENTATION

For simplicity, but without loss of generality, let us assume that the ancilla spin I_0 is coupled to all spins of the system of interest $(I_1,\ldots,I_N)$. We will now outline the experimental implementation of Result 1 using methods of nuclear magnetic resonance. We start in Sec. V A by presenting an NMR-adapted version of Result 1. An example for the case $N=1$ will be given in Sec. V B. The realization of controlled propagators $cU^{[N+1]}$ and the implementation of rotation operations are outlined in Secs. V C and V D.

A. NMR-based reconstruction

The expectation values $\langle I_x\otimes T_{j,\alpha\beta}^{(\ell)[N]}\rangle_{\rho_U^{[N+1]}}$ and $\langle I_y\otimes T_{j,\alpha\beta}^{(\ell)[N]}\rangle_{\rho_U^{[N+1]}}$ of Result 1 are not directly obtainable with methods of nuclear magnetic resonance. An NMR-adapted version of Result 1 will be presented in the following. This NMR-based experimental reconstruction scheme of propagators is analogous to the scheme described in [9] for the reconstruction of density operators. First, instead of rotating the axial tensors $(T_{j0}^{(\ell)})^{[N]}$, the density matrix $\rho_U^{[N+1]}$ is rotated inversely, resulting in

$$\left\langle I_x\otimes T_{j,\alpha\beta}^{(\ell)[N]}\right\rangle_{\rho_U^{[N+1]}} = \left\langle I_x\otimes\left(T_{j0}^{(\ell)}\right)^{[N]}\right\rangle_{\tilde\rho_U^{[N+1]}}, \quad (19)$$

$$\left\langle I_y\otimes T_{j,\alpha\beta}^{(\ell)[N]}\right\rangle_{\rho_U^{[N+1]}} = \left\langle I_y\otimes\left(T_{j0}^{(\ell)}\right)^{[N]}\right\rangle_{\tilde\rho_U^{[N+1]}}, \quad (20)$$

with

$$\tilde\rho_U^{[N+1]} = \left(\tilde R_{\alpha\beta}^{[N+1]}\right)^{-1}\rho_U^{[N+1]}\tilde R_{\alpha\beta}^{[N+1]} \quad (21)$$

and with $\tilde R_{\alpha\beta}^{[N+1]} = \mathbf{1}^{[1]}\otimes R_{\alpha\beta}^{[N]}$, as discussed in more detail in Appendix A 4.

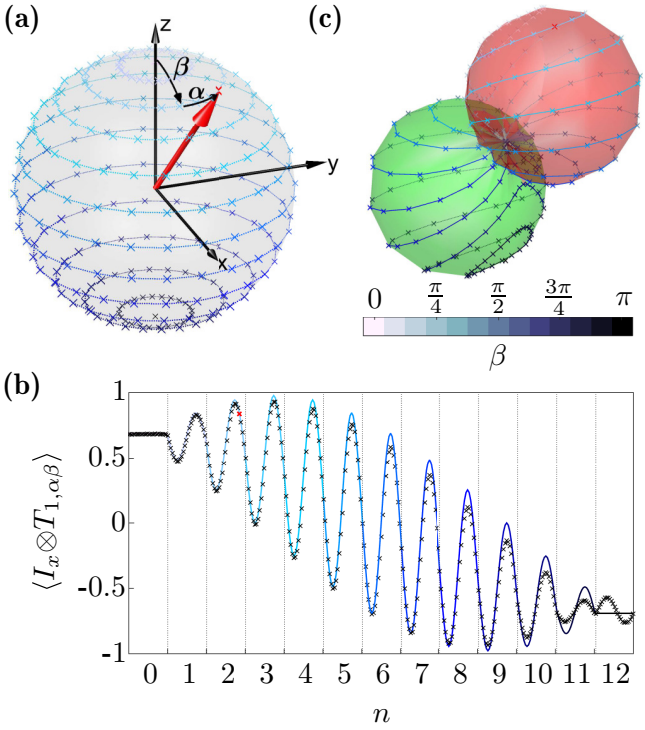

FIG. 2. For a system of interest consisting of a single ($N=1$) spin 1/2, the figure illustrates the tomographic reconstruction of a spherical function $f^{(\ell)}(\beta,\alpha)$ representing the Hadamard gate based on Result 1. (a) Samples (crosses) with different polar angles β in the range $[0,\pi]$ and phases α in the range $[0,2\pi]$ acquired by expectation values $\langle I_a\otimes T_{j,\alpha\beta}^{(\ell)[N]}\rangle_{\rho_U^{[N+1]}}$ with $a\in\{x,y\}$ and $j\in\{0,1\}$. The colors (shades of gray) of the circles of latitude are defined as a function of the polar angle β by the given color bar (gray scale). (b) Predicted expectation values (line) and experimentally measured expectation values $\langle I_x\otimes T_{1,\alpha\beta}\rangle := \langle I_x\otimes T_{1,\alpha\beta}^{(\ell)[N]}\rangle_{\rho_U^{[N+1]}}$ (crosses) for a simple sampling scheme with an equidistant discrete set of polar angles $\beta\in\{0,\frac{\pi}{12},\frac{2\pi}{12},\ldots,\pi\}$ and azimuthal angles $\alpha\in\{0,\frac{\pi}{12},\frac{2\pi}{12},\ldots,2\pi\}$. For each discrete value $\beta_n = n\pi/12$ with $n\in\{0,1,2,\ldots,12\}$, the azimuthal angle α is incremented in steps of $\pi/12$ from 0 to 2π. This scheme results in $13\times25 = 325$ measurement points acquired in 13 cycles to fully scan the sphere. Note that the remaining expectation values $\langle I_x\otimes T_{0,\alpha\beta}^{(\ell)[N]}\rangle_{\rho_U^{[N+1]}}$, $\langle I_y\otimes T_{0,\alpha\beta}^{(\ell)[N]}\rangle_{\rho_U^{[N+1]}}$, and $\langle I_y\otimes T_{1,\alpha\beta}^{(\ell)[N]}\rangle_{\rho_U^{[N+1]}}$ are zero and not shown here. (c) Smooth surface interpolated from individual samples with distance from the origin given by $f^{(\ell)}(\beta,\alpha)$, the phase of which determines the color (gray scale) of the surface (see Fig. 4).

Second, the (Hermitian) rank-j tensor components $(T_{j0}^{(\ell)})^{[N]}$ can be decomposed into (Hermitian) Cartesian product operators [28] $(C_{j,n}^{(\ell)})^{[N]}$ via

$$\left(T_{j0}^{(\ell)}\right)^{[N]} = \sum_n r_{j,n}^{(\ell)[N]}\left(C_{j,n}^{(\ell)}\right)^{[N]} \quad (22)$$

with real expansion coefficients $r_{j,n}^{(\ell)[N]}\in\mathbb{R}$. The decompositions of relevant axial tensor components for up to three qubits were given explicitly in [9]. Hence, the expectation values of Eqs. (19) and (20) can be obtained if we can measure the expectation values of the Cartesian product operators $I_a\otimes(C_{j,n}^{(\ell)})^{[N]}$ with $a\in\{x,y\}$. As in NMR experiments the

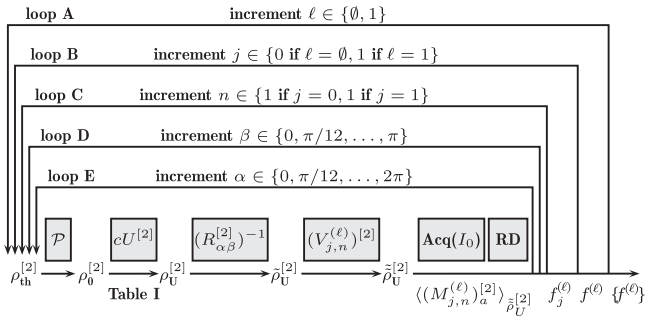

FIG. 3. Schematic representation of the tomography scheme proposed by Result 2 to scan the spherical functions $f^{(\ell)}(\beta,\alpha)$ for the case $N = 1$ with $\ell \in \{\emptyset,1\}$ by measuring the expectation values $\langle (M^{(\ell)}_{j,n})^{[2]}_a \rangle_{\tilde{\tilde{\rho}}^{[2]}_U}$ for $j \in \{0,1\}$, $n = 1$, and $a \in \{x,y\}$ as described in Sec. V B. See also Fig. 2.

signatures of Cartesian product operators can be measured directly only if they contain exactly *onetransverse* Cartesian spin operator I_{ka}; the expectation values $\langle I_a \otimes (C^{(\ell)}_{j,n})^{[N]} \rangle_{\tilde{\rho}^{[N+1]}_U}$ are only measurable directly if the terms $(C^{(\ell)}_{j,n})^{[N]}$ do not contain any transverse Cartesian spin operator. If this is not the case, the Cartesian product operators $I_a \otimes (C^{(\ell)}_{j,n})^{[N]}$ are transformed into NMR-measurable operators [28] $(M^{(\ell)}_{j,n})^{[N+1]}_a \in \{I_{0a}, 2I_{0a}I_{1z}, 4I_{0a}I_{1z}I_{2z}, \ldots\}$ by applying unitary operations

$$\left(M^{(\ell)}_{j,n}\right)^{[N+1]}_a = \left(\tilde{V}^{(\ell)}_{j,n}\right)^{[N+1]} \left(I_a \otimes (C^{(\ell)}_{j,n})^{[N]}\right) \left[\left(\tilde{V}^{(\ell)}_{j,n}\right)^{[N+1]}\right]^\dagger \quad (23)$$

with $(\tilde{V}^{(\ell)}_{j,n})^{[N+1]} = \mathbf{1}^{[1]} \otimes (V^{(\ell)}_{j,n})^{[N]}$ and with the actions of this operation on an operator $A^{[N+1]}$ given by $(\tilde{V}^{(\ell)}_{j,n})^{[N+1]} A^{[N+1]} [(\tilde{V}^{(\ell)}_{j,n})^{[N+1]}]^\dagger$ [see Table IV in [9] for some realizations of $(V^{(\ell)}_{j,n})^{[N]}$]. The unitary operators $(V^{(\ell)}_{j,n})^{[N]}$ can be experimentally implemented using radio-frequency pulses and evolution periods under couplings. The experimental signatures of the Cartesian product operators $(M^{(\ell)}_{j,n})^{[N+1]}_a$ are obtained by detecting the ancilla spin I_0.

This approach to measure spherical functions corresponding to the DROPS representation of propagators recasts Result 1 into the following NMR-adapted version:

Result 2. Consider a propagator $U^{[N]}$ which is represented by a set of spherical functions $f^{(\ell)}(\theta,\phi) = \sum_{j \in J(\ell)} f^{(\ell)}_j(\theta,\phi)$. The rank-$j$ components $f^{(\ell)}_j(\beta,\alpha)$ can be experimentally measured with NMR methods in the augmented system for arbitrary angles β in the range $[0,\pi]$ and α in the range $[0,2\pi]$ via the complex linear combination of expectation values

$$f^{(\ell)}_j(\beta,\alpha) = s_j \sum_n r^{(\ell)[N]}_{j,n} \Big(\Big\langle \left(M^{(\ell)}_{j,n}\right)^{[N+1]}_x \Big\rangle_{\tilde{\tilde{\rho}}^{[N+1]}_U} + i \Big\langle \left(M^{(\ell)}_{j,n}\right)^{[N+1]}_y \Big\rangle_{\tilde{\tilde{\rho}}^{[N+1]}_U} \Big) \quad (24)$$

with $s_j := \sqrt{(2j+1)/(4\pi)}$ and Cartesian product operators $(M^{(\ell)}_{j,n})^{[N+1]}_a$ with $a \in \{x,y\}$ given in Eq. (23) in which only the ancilla qubit has a transversal component, where

$$\tilde{\tilde{\rho}}^{[N+1]}_U = \left(V^{(\ell)}_{j,n}\right)^{[N+1]} \tilde{\rho}^{[N+1]}_U \left[\left(V^{(\ell)}_{j,n}\right)^{[N+1]}\right]^\dagger, \quad (25)$$

$$\tilde{\rho}^{[N+1]}_U = \left(R^{[N+1]}_{\alpha\beta}\right)^{-1} \rho^{[N+1]}_U R^{[N+1]}_{\alpha\beta}, \quad (26)$$

and

$$R^{[N+1]}_{\alpha\beta} = \mathbf{1}^{[1]} \otimes R^{[N]}_{\alpha\beta}, \quad (27)$$

$$R^{[N]}_{\alpha\beta} = \exp\left\{-i\alpha \sum_{k=1}^N I^{[N]}_{kz}\right\} \exp\left\{-i\beta \sum_{k=1}^N I^{[N]}_{ky}\right\}. \quad (28)$$

The rank-j components $f^{(\ell)}_j(\beta,\alpha)$ of the spherical functions $f^{(\ell)}(\beta,\alpha)$ representing the propagator $U^{[N]}$ can be sampled in NMR experiments by preparing the state $\tilde{\tilde{\rho}}^{[N+1]}_U$ in the augmented system and measuring a set of expectation values of suitable operators $(M^{(\ell)}_{j,n})^{[N+1]}_x$ and $(M^{(\ell)}_{j,n})^{[N+1]}_y$ as a function of the angles α and β.

B. The case $N = 1$

If the system of interest is just a single spin I_1, i.e., $N = 1$ and $\ell \in \{\emptyset,1\}$, we have rank $j = 0$ for $\ell = \{\emptyset\}$ and rank $j = 1$ for $\ell = \{1\}$. In both cases, only a single ($n = 1$) Cartesian product operator is necessary to express the axial tensor operator components $(T^{(\emptyset)}_{00})^{[1]} = \frac{1}{\sqrt{2}}\mathbf{1}^{[1]}$ and $(T^{(1)}_{10})^{[1]} = \sqrt{2} I^{[1]}_{1z}$; see Eq. (22). Here, the right-hand sides of Eqs. (19) and (20) reduce to

$$\left\langle I_x \otimes \left(T^{(\emptyset)}_{00}\right)^{[1]} \right\rangle_{\tilde{\rho}^{[N+1]}_U} = \left\langle \frac{1}{\sqrt{2}} I^{[2]}_{0x} \right\rangle_{\tilde{\rho}^{[N+1]}_U}, \quad (29)$$

$$\left\langle I_y \otimes \left(T^{(\emptyset)}_{00}\right)^{[1]} \right\rangle_{\tilde{\rho}^{[N+1]}_U} = \left\langle \frac{1}{\sqrt{2}} I^{[2]}_{0y} \right\rangle_{\tilde{\rho}^{[N+1]}_U}, \quad (30)$$

for $\ell = \{\emptyset\}$, and

$$\left\langle I_x \otimes \left(T^{(1)}_{10}\right)^{[1]} \right\rangle_{\tilde{\rho}^{[N+1]}_U} = \left\langle \frac{1}{\sqrt{2}} (2I_{0x}I_{1z})^{[2]} \right\rangle_{\tilde{\rho}^{[N+1]}_U}, \quad (31)$$

$$\left\langle I_y \otimes \left(T^{(1)}_{10}\right)^{[1]} \right\rangle_{\tilde{\rho}^{[N+1]}_U} = \left\langle \frac{1}{\sqrt{2}} (2I_{0y}I_{1z})^{[2]} \right\rangle_{\tilde{\rho}^{[N+1]}_U}, \quad (32)$$

for $\ell = \{1\}$. Note that $I^{[2]}_{0a} := I_a \otimes \mathbf{1}^{[1]}$ and $(2I_{0a}I_{1z})^{[2]} := 2I_a \otimes I_z$ for $a \in \{x,y\}$. Since the signatures of the four Cartesian product operators $I^{[2]}_{0x}$, $I^{[2]}_{0y}$, $(2I_{0x}I_{1z})^{[2]}$, and $(2I_{0y}I_{1z})^{[2]}$ are already directly observable in NMR experiments, further transformations $(V^{(\ell)}_{j,1})^{[2]}$ [see Eq. (23)] are not necessary, i.e., $(V^{(\ell)}_{j,1})^{[2]} = \mathbf{1}^{[2]}$ for all ℓ and j and thus $\tilde{\tilde{\rho}}^{[2]}_U = \tilde{\rho}^{[2]}_U$. Hence, based on Result 2, we only need to measure the two expectation values for $\ell = \{\emptyset\}$,

$$\left\langle \left(M^{(\emptyset)}_{0,1}\right)^{[2]}_x \right\rangle_{\tilde{\tilde{\rho}}^{[2]}_U} = \frac{1}{\sqrt{2}} \left\langle I^{[2]}_{0x} \right\rangle_{\tilde{\rho}^{[2]}_U}, \quad (33)$$

$$\left\langle \left(M^{(\emptyset)}_{0,1}\right)^{[2]}_y \right\rangle_{\tilde{\tilde{\rho}}^{[2]}_U} = \frac{1}{\sqrt{2}} \left\langle I^{[2]}_{0y} \right\rangle_{\tilde{\rho}^{[2]}_U}, \quad (34)$$

and the two expectation values for $\ell = \{1\}$,

$$\left\langle \left(M^{(1)}_{1,1}\right)^{[2]}_x \right\rangle_{\tilde{\tilde{\rho}}^{[2]}_U} = \frac{1}{\sqrt{2}} \left\langle (2I_{0x}I_{1z})^{[2]} \right\rangle_{\tilde{\rho}^{[2]}_U}, \quad (35)$$

$$\left\langle \left(M^{(1)}_{1,1}\right)^{[2]}_y \right\rangle_{\tilde{\tilde{\rho}}^{[2]}_U} = \frac{1}{\sqrt{2}} \left\langle (2I_{0y}I_{1z})^{[2]} \right\rangle_{\tilde{\rho}^{[2]}_U}, \quad (36)$$

as a function of the angles α and β to reconstruct the spherical functions $f^{(\ell)}(\beta,\alpha)$ for each $\ell \in \{\emptyset,1\}$. This is achieved by

TABLE I. Matrix representations for the propagator $U^{[1]}$ and the pulse sequences realizing the corresponding controlled propagator $cU^{[2]}$ [up to a global phase factor (see Appendix A 5)] to prepare the density matrix $\rho_U^{[2]}$ from $\rho_0^{[2]}$. J_{01} is the coupling constant between spins I_0 and I_1. We denote a pulse with flip angle β and phase α that is applied to spin k by $[\beta]_\alpha(I_k)$. Similarly, $[\beta_1,\beta_2]_{\alpha_1,\alpha_2}(I_k,I_l)$ specifies two pulses of flip angles β_1 and β_2 with phases α_1 and α_2 that are simultaneously applied to spins k and l. Here, we use the common shorthand notations x, y, $-x$, and $-y$ for the phases 0, $\pi/2$, π, and $3\pi/2$, respectively.

Gate	$U^{[1]}$	Sequence to prepare $cU^{[2]}$
Id	$\begin{pmatrix}1&0\\0&1\end{pmatrix}$	
NOT	$\begin{pmatrix}0&1\\1&0\end{pmatrix}$	$[\frac{\pi}{2}]_y(I_1)-\frac{1}{2J_{01}}-[\frac{\pi}{2}]_{-y}(I_0,I_1)-[\frac{\pi}{2}]_{-x,x}(I_0,I_1)-[\frac{\pi}{2}]_y(I_0)$
$\sqrt{\text{NOT}}$	$\frac{1}{2}\begin{pmatrix}1+i&1-i\\1-i&1+i\end{pmatrix}$	$[\frac{\pi}{2}]_y(I_1)-\frac{1}{4J_{01}}-[\frac{\pi}{2}]_{-y}(I_0,I_1)-[\frac{\pi}{4}]_{-x,x}(I_0,I_1)-[\frac{\pi}{2}]_y(I_0)$
Hadamard	$\frac{1}{\sqrt{2}}\begin{pmatrix}1&1\\1&-1\end{pmatrix}$	$[\pi,\frac{\pi}{4}]_{-x,-y}(I_0,I_1)-\frac{1}{2J_{01}}-[\frac{\pi}{2}]_{x,y}(I_0,I_1)-[\frac{\pi}{2}]_{y,x}(I_0,I_1)-[\frac{\pi}{2},\frac{\pi}{4}]_{x,-y}(I_0,I_1)$
$\frac{\pi}{2}$ phase shift	$\frac{1}{\sqrt{2}}\begin{pmatrix}1&0\\0&i\end{pmatrix}$	$[\pi]_x(I_0)-\frac{1}{4J_{01}}-[\pi]_{-x}(I_0)-[\frac{\pi}{2}]_y(I_0,I_1)-[\frac{\pi}{4}]_x(I_0,I_1)-[\frac{\pi}{2}]_{-y}(I_0,I_1)$
π phase shift	$\frac{1}{\sqrt{2}}\begin{pmatrix}1&0\\0&-1\end{pmatrix}$	$[\pi]_x(I_0)-\frac{1}{2J_{01}}-[\pi]_{-x}(I_0)-[\frac{\pi}{2}]_y(I_0,I_1)-[\frac{\pi}{2}]_x(I_0,I_1)-[\frac{\pi}{2}]_{-y}(I_0,I_1)$
$\frac{3\pi}{2}$ phase shift	$\frac{1}{\sqrt{2}}\begin{pmatrix}1&0\\0&-i\end{pmatrix}$	$[\pi]_x(I_0)-\frac{3}{4J_{01}}-[\pi]_{-x}(I_0)-[\frac{\pi}{2}]_y(I_0,I_1)-[\frac{3\pi}{4}]_x(I_0,I_1)-[\frac{\pi}{2}]_{-y}(I_0,I_1)$
2π phase shift	$\frac{1}{\sqrt{2}}\begin{pmatrix}1&0\\0&1\end{pmatrix}$	$[\pi]_x(I_0)-\frac{1}{J_{01}}-[\pi]_{-x}(I_0)-[\frac{\pi}{2}]_y(I_0,I_1)-[\pi]_x(I_0,I_1)-[\frac{\pi}{2}]_{-y}(I_0,I_1)$
$[\frac{\pi}{2}]_x$ rotation	$\frac{1}{\sqrt{2}}\begin{pmatrix}1&-i\\-i&1\end{pmatrix}$	$c[[\frac{\pi}{2}]_x\text{ rotation}]:=[\frac{\pi}{2}]_y(I_1)-\frac{1}{4J_{01}}-[\frac{\pi}{2}]_{-y}(I_1)-[\frac{\pi}{4}]_x(I_1)$
$[\pi]_x$ rotation	$\begin{pmatrix}0&-i\\-i&0\end{pmatrix}$	$c[[\pi]_x\text{ rotation}]:=[\frac{\pi}{2}]_y(I_1)-\frac{1}{2J_{01}}-[\frac{\pi}{2}]_{-y}(I_1)-[\frac{\pi}{2}]_x(I_1)$
$[\frac{3\pi}{2}]_x$ rotation	$\frac{1}{\sqrt{2}}\begin{pmatrix}-1&-i\\-i&-1\end{pmatrix}$	$c[[\pi]_x\text{ rotation}]-c[[\frac{\pi}{2}]_x\text{ rotation}]$
$[2\pi]_x$ rotation	$\begin{pmatrix}-1&0\\0&-1\end{pmatrix}$	$c[[\pi]_x\text{ rotation}]-c[[\pi]_x\text{ rotation}]$
$[\frac{5\pi}{2}]_x$ rotation	$\frac{1}{\sqrt{2}}\begin{pmatrix}-1&i\\i&-1\end{pmatrix}$	$c[[\pi]_x\text{ rotation}]-c[[\pi]_x\text{ rotation}]-c[[\frac{\pi}{2}]_x\text{ rotation}]$
$[3\pi]_x$ rotation	$\begin{pmatrix}0&i\\i&0\end{pmatrix}$	$c[[\pi]_x\text{ rotation}]-c[[\pi]_x\text{ rotation}]-c[[\pi]_x\text{ rotation}]$
$[\frac{7\pi}{2}]_x$ rotation	$\frac{1}{\sqrt{2}}\begin{pmatrix}1&i\\i&1\end{pmatrix}$	$c[[\pi]_x\text{ rotation}]-c[[\pi]_x\text{ rotation}]-c[[\pi]_x\text{ rotation}]-c[[\frac{\pi}{2}]_x\text{ rotation}]$
$[4\pi]_x$ rotation	$\begin{pmatrix}1&0\\0&1\end{pmatrix}$	$c[[\pi]_x\text{ rotation}]-c[[\pi]_x\text{ rotation}]-c[[\pi]_x\text{ rotation}]-c[[\pi]_x\text{ rotation}]$

measuring the spectrum of the ancilla qubit I_0 and fitting reference spectra of the operators $I_{0x}^{[2]}$, $I_{0y}^{[2]}$, $(2I_{0x}I_{1z})^{[2]}$, and $(2I_{0y}I_{1z})^{[2]}$ [9].

C. Implementation of controlled unitary transformation

It is always possible to implement a controlled unitary propagator using unitary transformations in NMR [42]. These are realized by radio-frequency pulses and evolutions under couplings. The explicit matrix representations of $U^{[N]}$ and the corresponding pulse sequences for all considered propagators $cU^{[N+1]}$ are summarized in Table I.

D. Implementation of rotations

The (inverse) rotation $(R_{\alpha\beta}^{[N+1]})^{-1}$ transforms the density operator after the controlled gate $\rho_U^{[N+1]}$ into $\tilde{\rho}_U^{[N+1]}$ in order to probe the corresponding spherical functions representing the propagator $U^{[N]}$ for the polar angles β and azimuthal angles α. This operation is implemented by radio-frequency pulses $[\beta]_{\alpha-\pi/2}$ with flip angle β and phase $(\alpha-\pi/2)$, which are simultaneously applied to all spins in the system of interest $(I_1,\ldots,I_N)$ but not to the ancilla spin I_0.

VI. NMR EXPERIMENTS FOR $N=1$

After summarizing the theory and the basis of NMR implementations for the Wigner process tomography of propagators in the previous sections IV and V, we will now outline the experimental procedure which is directly based on Result 2 using methods of nuclear magnetic resonance for a system with one system qubit and one ancilla qubit, i.e., $N=1$ (see Sec. V B). The experimental setting is given in Sec. VI A followed by the protocol in Sec. VI B.

A. Experimental setting

For all Wigner process tomography demonstration experiments, we used a liquid sample of the two-qubit molecule chloroform dissolved in CD_3CN. The ^{1}H spin (with a chemical shift of 7.61 ppm) is defined as the ancilla qubit and the ^{13}C spin (with a chemical shift of 78.18 ppm) as the system qubit. Thus, the ^{1}H and ^{13}C nuclear spins of each chloroform molecule form a system consisting of two coupled spins 1/2. The coupling constant J_{HC} is 214.15 Hz. All experiments were performed at room temperature (298 K) in a 14.1 T magnet using a Bruker Avance III 600 spectrometer.

B. Experimental protocol

As summarized in Fig. 3, the experiment is composed of six main building blocks. In the first block $\mathcal{P}$, the initial operator $\rho_0^{[2]} = 2I_{0x}^{[2]}$ of the augmented system is prepared from the thermal equilibrium density operator. In the high-temperature limit, the deviation density matrix at thermal equilibrium is proportional to $\rho_{\text{th}}^{[2]} = 2\sum_{k=0}^{1}\gamma_k I_{kz}$, with γ_k being the gyromagnetic ratio of the kth nuclear spin [28,39]. The (traceless) operator $\rho_0^{[2]} = 2I_{0x}^{[2]}$ is obtained from $\rho_{\text{th}}^{[2]}$ by the following pulse sequence:

$$\mathcal{P} = \left[\frac{\pi}{2}\right]_x (I_1) - G - \left[\frac{\pi}{2}\right]_y (I_0). \tag{37}$$

First, a pulse with flip angle $\frac{\pi}{2}$ and phase 0 is applied to spin I_1, followed by a pulsed B_0 gradient G. This dephases the magnetization of spin I_1 and the deviation density operator is proportional to $2I_{0z}^{[2]}$. Finally, a pulse with flip angle $\pi/2$ and phase $\pi/2$ is applied to spin I_0, resulting in $\rho_0^{[2]} \propto 2I_{0x}^{[2]}$.

As described in Sec. IV A, the second block $cU^{[2]}$ realizes the controlled propagator based on $U^{[1]}$, which transforms $\rho_0^{[2]} = 2I_{0x}^{[2]}$ to $\rho_U^{[2]}$. The explicit pulse sequences for all used controlled propagators $cU^{[2]}$ are summarized in Table I.

According to Result 2, the third block consists of the rotation $(R_{\alpha\beta}^{[N+1]})^{-1}$ realized by the pulse $[\beta]_{\alpha-\pi/2}(I_1)$ which transforms the operator $\rho_U^{[2]}$ into $\tilde{\rho}_U^{[2]}$ in order to probe the rank-j components of the spherical functions $f_j^{(\ell)}(\beta,\alpha)$ for different polar angles β and azimuthal angles α. This rotation is only applied to the system qubit I_1.

In a general ($N > 1$) Wigner process tomography, an additional (fourth) transformation block $(V_{j,n}^{(\ell)})^{[N+1]}$ is required directly after the rotation step (block three) to generate $\tilde{\tilde{\rho}}_U^{[N+1]}$. However, as described in Sec. V B, for the case $N = 1$, we find $(V_{j,1}^{(\ell)})^{[2]} = \mathbf{1}^{[2]}$ for all ℓ and j, which directly results in $\tilde{\tilde{\rho}}_U^{[2]} = \tilde{\rho}_U^{[2]}$.

In the fifth block, the NMR signal of the ancilla spin I_0 is measured in the acquisition period Acq and the expectation values of the four Cartesian operators $I_{0x}^{[2]}$, $I_{0y}^{[2]}$, $(2I_{0x}I_{1z})^{[2]}$, and $(2I_{0y}I_{1z})^{[2]}$ are obtained as discussed in Sec. V B. In a final step, a relaxation delay RD of about 50 s recovers the initial thermal equilibrium state $\rho_{\text{th}}^{[2]}$.

In a complete tomography experiment, all blocks are repeated multiple times. The outer loop A cycles through all droplets $\ell \in \{\emptyset,1\}$. Loop B runs over all rank-j components of each droplet ℓ. Loop C cycles through all Cartesian product operators $(C_{j,n}^{(\ell)})^{[N]}$ appearing in the decomposition of the axial tensor operator $(T_{j0}^{(\ell)})^{[N]}$ in Eq. (22). This loop is shown for completeness, although for the considered case of $N = 1$, it is obsolete because $n = 1$ for all combinations of ℓ and j. Finally, the angles $\beta \in \{0,\pi/12,2\pi/12,\ldots,\pi\}$ and $\alpha \in \{0,\pi/12,2\pi/12,\ldots,2\pi\}$ are incremented in an equidistant scheme in the two innermost loops D and E (see Fig. 3).

VII. RESULTS OF NMR EXPERIMENTS

Here we present the experimental results of the Wigner process tomography scheme detailed in the previous section for $N = 1$. In Sec. VII A, we reconstructed the DROPS representations for the Identity, NOT, $\sqrt{\text{NOT}}$, and Hadamard gates. In Sec. VII B, the reconstructed Wigner functions of propagators realizing phase-shift gates for different phase shifts are presented. In Sec. VII C, tomographic results of the Wigner representation for rotations around the x axis are shown for rotation angles between 0 and 4π.

Note that in the standard DROPS representation introduced in [6], separate spherical droplet functions $f^{(\ell)}(\theta,\phi)$ are displayed for operator components corresponding to the identity operator (i.e., operator components that do not contain any spin operator and hence $\ell = \{\emptyset\}$), for linear terms involving only a single spin operator (e.g., $\ell = \{1\}$), and for bilinear terms, etc. In the present case of a single qubit ($N = 1$), only the two functions $f^{\{\emptyset\}}(\theta,\phi)$ and $f^{\{1\}}(\theta,\phi)$ exist and it is convenient to combine them into a single spherical function $f(\theta,\phi) = f^{\{\emptyset\}}(\theta,\phi) + f^{\{1\}}(\theta,\phi)$. This is possible without compromising the bijectivity of the mapping between operators and droplets [6] because the ranks j of $f^{\{\emptyset\}}(\theta,\phi)$ (with $j = 0$) and $f^{\{1\}}(\theta,\phi)$ (with $j = 1$) are different. However, as discussed in more detail in Appendix A 6, for some applications it can be of advantage to separately plot the droplet functions $f^{\{\emptyset\}}(\theta,\phi)$ and $f^{\{1\}}(\theta,\phi)$. An explicit functional form of the theoretically expected droplet functions for arbitrary rotations is provided in Appendix A 7.

A. Identity, NOT, $\sqrt{\text{NOT}}$, and Hadamard gates

In an initial series of demonstration experiments, we reconstructed the Wigner functions $f(\theta,\phi) = f^{\{\emptyset\}}(\theta,\phi) + f^{\{1\}}(\theta,\phi)$ for propagators $U^{[1]}$ implementing the identity operation Id, a NOT gate, a square root of a NOT gate ($\sqrt{\text{NOT}}$), and a Hadamard gate. The matrix representation for $U^{[1]}$ and the corresponding pulse sequences for the controlled propagators $cU^{[2]}$ are summarized in Table I. The experimental results and the theoretically expected spherical functions are illustrated in Fig. 4.

B. Phase-shift gates

We also demonstrate our reconstruction approach to tomograph the Wigner representation $f(\theta,\phi) = f^{\{\emptyset\}}(\theta,\phi) + f^{\{1\}}(\theta,\phi)$ of propagators realizing phase shifts of $0,\pi/2,\pi$, $3\pi/2$, and 2π. The matrix representations for these gates are shown in Table I and the results of the tomographic reconstruction for the spherical functions are presented in Fig. 5. In this figure, we also show the results for the phase-shift gate corresponding to a phase shift of 0, for which the pulse

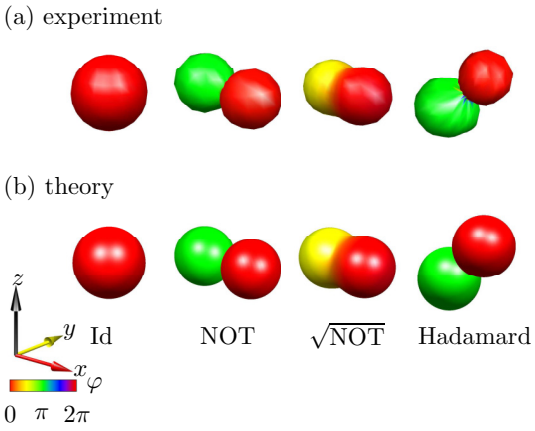

FIG. 4. Experimentally reconstructed (a) and theoretical (b) spherical functions $f(\theta,\phi)$ representing propagators for the Id, NOT, $\sqrt{\text{NOT}}$, and the Hadamard gate. The colors red (dark gray), yellow (light gray), green (gray), and blue (black) correspond to phase factors $\exp(i\varphi)$ of 1, i, -1, and $-i$ [9]. See the color bar (gray scale) for $0 \leqslant \varphi \leqslant 2\pi$.

sequence is identical to cId (see Table I). This figure reflects the 2π periodicity of the phase-shift gates. The propagator representing a phase shift of 0 is identical to the identity operator $U^{[N]}(0) = \mathbf{1}^{[N]}$ which is a positive red (dark gray) sphere in the DROPS representation. After a phase shift of 2π, the propagator becomes the identity operator again, i.e., $U^{[N]}(2\pi) = U^{[N]}(0) = \mathbf{1}^{[N]}$, which is represented by the same red (dark gray) sphere. This highlights the contrast to the spinor property of propagators for rotations of a spin-1/2 particle as shown in Sec. VII C which results in a periodicity of 4π (see Appendix A 8).

C. Rotations

We also reconstructed the Wigner functions $f(\theta,\phi) = f^{\{\emptyset\}}(\theta,\phi) + f^{(1)}\{\theta,\phi\}$ of propagators corresponding to rotations around the x axis for rotation angles $0,\pi/2,\pi,3\pi/2,2\pi,5\pi/2,3\pi,7\pi/2$, and 4π. Again, the matrix representations for the given propagators are summarized in Table I and the tomography results are shown in Fig. 6.

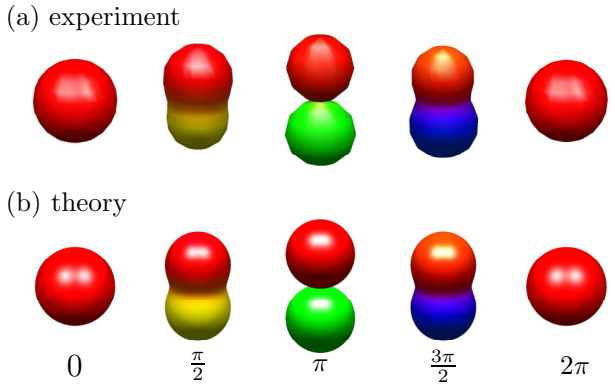

FIG. 5. Experimentally reconstructed (a) and theoretical (b) spherical functions $f(\theta,\phi)$ representing propagators of phase-shift gates for 0, $\pi/2$, π, $3\pi/2$, and 2π.

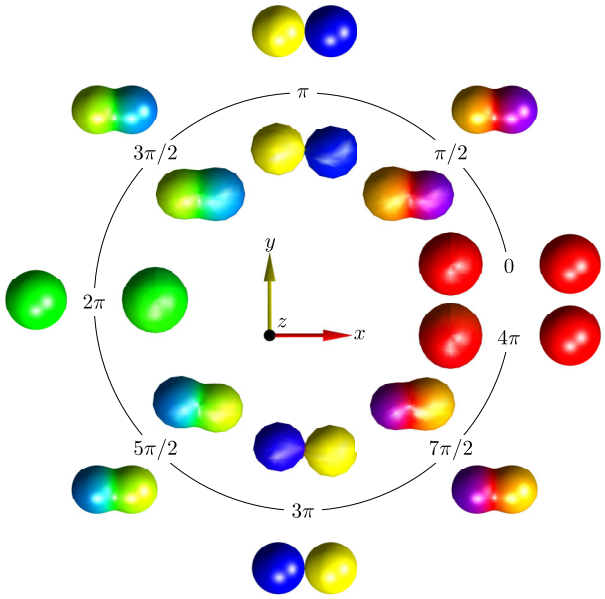

FIG. 6. Reconstructed spherical functions $f(\theta,\phi)$ representing propagators for rotations around the x axis for rotation angles $0,\pi/2,\pi,3\pi/2,2\pi,5\pi/2,3\pi,7\pi/2$, and 4π. The experimentally sampled shapes are positioned along the inner circle, whereas the theoretical functions are positioned along the outer circle. The colors red (dark gray), yellow (light gray), green (gray), and blue (black) correspond to phase factors $\exp(i\varphi)$ of 1, i, -1, and $-i$; see the color bar (gray scale) in Fig. 4. Note the sign change of the experimentally measured and theoretical DROPS representation when a given rotation angle is increased by 2π, nicely illustrating the spinor property of propagators corresponding to rotations of spin-1/2 particles.

This figure probably represents one of the most direct and compelling visualizations of the experimentally measured spinor property of the propagators corresponding to the rotation of a spin-1/2 particle. For a rotation angle of 0, the propagator $U^{[N]}(0)$ corresponds to the identity operator $\mathbf{1}^{[N]}$, which is represented by a positive red (dark gray) sphere in the DROPS representation. However, for a rotation angle of 2π, the propagator $U^{[N]}(2\pi)$ does not correspond to the identity operator $\mathbf{1}^{[N]}$ but to $-\mathbf{1}^{[N]}$, represented by a negative green (gray) sphere in the DROPS representation, i.e., $U^{[N]}(2\pi) = -U^{[N]}(0)$. Only after a rotation of 4π, the propagator becomes the identity operator again, i.e., $U^{[N]}(4\pi) = U^{[N]}(0) = \mathbf{1}^{[N]}$ [20] (see Appendix A 8).

VIII. DISCUSSION

Here, we introduced a general approach to experimentally measure the Wigner representation of quantum-mechanical propagators. The approach based on Result 1 can be applied to individual quantum systems consisting of qubits studied in the context of quantum information processing. Result 2 extends this approach to ensembles of spin systems studied in nuclear magnetic resonance (NMR) or electron spin resonance (ESR). Demonstration experiments have been implemented in an NMR setting.

A useful property of the DROPS Wigner representation of rotations is the fact that the orientation of the droplet

shape directly reflects the orientation of the rotation axis. For example, for the case of rotations around the x axis (see Fig. 6) the droplet shapes are aligned along the x axis, whereas in the case of the Hadamard gate, the rotation axis is aligned along the bisector of the angle between the x and the z axis (see Fig. 4). Furthermore, the DROPS Wigner representation makes it possible to directly see the spinor property of rotation propagators, which results in a sign change that is reflected by a corresponding color change. For example, for rotation angles of 0 and 2π, the propagators are represented by a red and and a green sphere (dark gray and gray), respectively. For a rotation angle of π, the droplet consists of a blue and yellow sphere (black and light gray) and for a rotation angle of 3π the colors are interchanged.

A reasonable match between the experimentally reconstructed and theoretical predicted spherical functions is found in Figs. 4–9. Deviations are due to experimental imperfections, such as finite experimental signal-to-noise ratio, finite accuracy of pulse calibration, B_0 and B_1 inhomogeneities [28,43], pulse shape distortions due to the amplifiers and the finite bandwidth of the resonator [44], relaxation losses during the preparation block, the implementation of the cU operation and the detection block, partial saturation of the signal due to a finite relaxation period between scans, radiation damping effects [45], and truncation effects in the automated integration and comparison of the spectra.

As discussed previously in [9], the Wigner tomography can only measure the deviation density matrix, i.e., the *traceless* part of a given *density* operator $\rho^{[N]}$ when performed using standard NMR or ESR experiments. This is because experimentally available observables in magnetic resonance experiments are traceless operators. This restriction is irrelevant in most cases of practical interest, because the part of the density operator that is proportional to the identity operator neither evolves during an experiment nor gives rise to any detectable signals in the experiments. However for *propagators*, the part that is proportional to the identity operator plays an important role and it would be a serious restriction if only the traceless part of a propagator $U^{[N]}$ could be determined using NMR or ESR experiments. Fortunately, this is not the case for the presented approach based on the mapping of the propagator $U^{[N]}$ to *off-diagonal* blocks of the density operator $\rho^{[N+1]}$ of the spin system augmented by an additional ancilla spin; i.e., also in standard NMR and ESR experiments the *full* propagator $U^{[N]}$ can be reconstructed and not only its traceless part. For example, for a system consisting only of a single spin 1/2, this allows us to distinguish the propagators corresponding to rotations about the same axis but with different rotation angles $\pi - \alpha$ and $\pi + \alpha$, which for arbitrary angles α only differ by the sign of the identity operator contribution to $U^{[N]}$. This is illustrated in Figs. 6, 8, and 9, where due to the sign of the contribution of the identity operator, e.g., the propagators of $\pi/2$ and $3\pi/2$ can be clearly distinguished.

The presented proof-of-principle experiments exploited the fact that a controlled propagator $cU^{[N+1]}$ can be constructed in a straightforward way for any given (i.e., previously known) unitary operator $U^{[N]}$. However, it is important to note that this tomography approach based on a single ancilla qubit can be generalized to the experimental reconstruction of the Wigner function representing an *unknown* propagator $U^{[N]}$ based on additional ancilla qubits and controlled-SWAP operations [46]. As discussed in more detail in Appendix A 9, in this case, the Wigner process tomography can provide valuable information to identify sources of systematic and random errors of a given implementation of a desired unitary transformation.

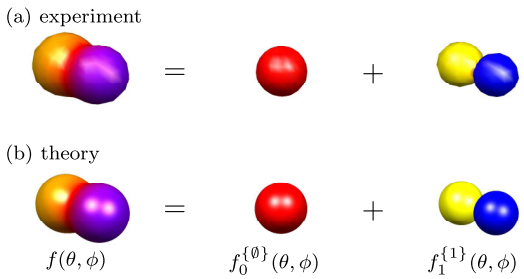

FIG. 7. The Wigner representation $f(\theta,\phi)$ of a $[\frac{\pi}{2}]_x$ rotation propagator is decomposed into its contributions $f_0^{\{\emptyset\}}(\theta,\phi)$ and $f_1^{\{1\}}(\theta,\phi)$.

The objective of this work was to show how the spherical functions of the DROPS representation of a set of propagators of interest can be experimentally scanned. If no *a priori* information of the expected droplet shapes is available, a large number of sampling points is necessary to ensure that all features of the shapes are captured in sufficient detail. Here, the experimental scanning procedure was demonstrated using a simple sampling scheme with equidistant steps of the polar and

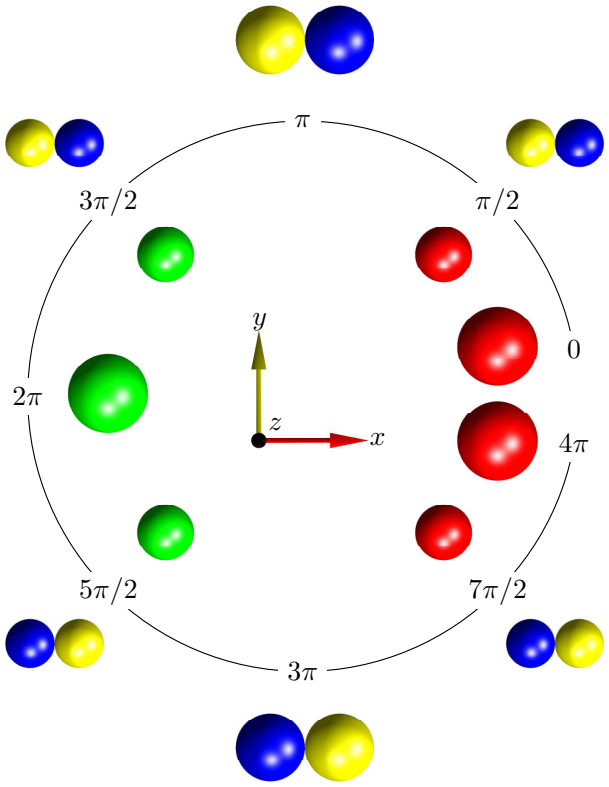

FIG. 8. Theoretical Wigner function $f(\theta,\phi)$ representing various propagators realizing x rotations decomposed into its contributions $f_0^{\{\emptyset\}}(\theta,\phi)$ (positioned along the inner circle) and $f_1^{\{1\}}(\theta,\phi)$ (positioned along the outer circle).

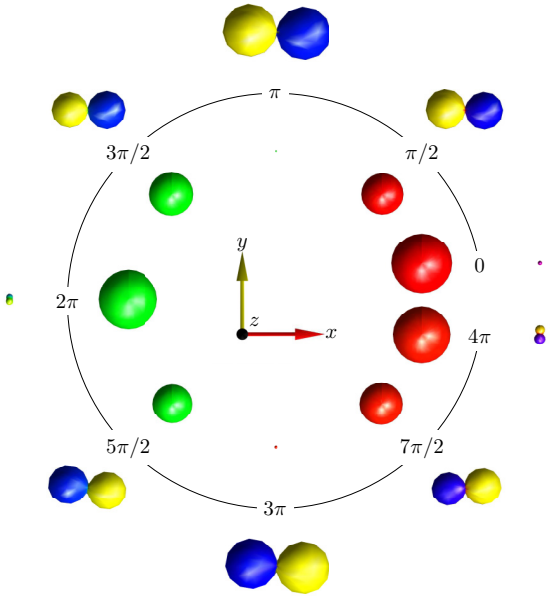

FIG. 9. Experimentally reconstructed Wigner function $f(\theta,\phi)$ representing various propagators realizing x rotations decomposed into its contributions $f_0^{\{\emptyset\}}(\theta,\phi)$ (positioned along the inner circle) and $f_1^{\{1\}}(\theta,\phi)$ (positioned along the outer circle).

azimuthal angles β and α as shown in Fig. 2. Based on previous simulations, increments of $\pi/12$ were chosen for β and α in the presented demonstration experiments, which formed a reasonable compromise between the overall duration of the experiments and a sufficiently good resolution to visually show all characteristic features of the droplet functions. However, as previously discussed in the context of Wigner tomography of density operators [9], more efficient sampling schemes are available.

In the ideal case of noiseless data, only a relatively small number of sampling points would be necessary to determine the correct expansion coefficients of spherical harmonics. This is a result of the fact that each droplet function is band-limited; i.e., for each function $f^{(\ell)}$ the maximum value $j_{\max}^{(\ell)}$ of the rank $j \in J(\ell)$ is known [see Eq. (3)] [6]. For example, in the case $N = 2$ shown in Fig. 1, the maximal ranks of the different droplet functions are $j_{\max}^{\{\emptyset\}} = 0$, $j_{\max}^{\{1\}} = j_{\max}^{\{2\}} = 1$, and $j_{\max}^{\{12\}} = 2$. The minimal number of sampling points for band-limited spherical functions is given by the *optimal dimensionality* $(j_{\max}^{(\ell)} + 1)^2$ [47] and a number of different sampling strategies have been proposed in the literature which approach this limit. The equiangular schemes based the sampling theorems by Driscoll & Healy [48,49] and McEwen & Wiaux [50] exceed the minimal number of sampling points by factors of four and two, respectively. The Gauss-Legendre quadrature on the sphere [51] requires $(2j_{\max}^{(\ell)} + 1)(j_{\max}^{(\ell)} + 1)$ samples. Recently, an optimal isolatitude sampling scheme with a fast and stable spherical harmonics transform was proposed by Khalid *et al.* [47]. In the limit of large $j_{\max}^{(\ell)}$, the optimal dimensionality is also approached by Lebedev *two-angle sets* [52–54]. Related Lebedev *three-angle* sets have been previously used for the experimental decomposition of detected NMR signals in terms of the rank j and order m of the *density operator* at a chosen time point during an experiment [55]. In the presence of noise and instrumental variations it was found that Lebedev sets with large differences in the weights provide larger errors compared to sets with nearly uniform weights [55].

It is interesting to note that for some droplet functions $f^{(\ell)}$ the number of sampling points may be even further reduced compared to the optimal dimensionality $(j_{\max}^{(\ell)} + 1)^2$ of band-limited spherical functions because the set $J(\ell)$ of ranks j in general does not include all values of j between 0 and $j_{\max}^{(\ell)}$ [6]. For example, the set $J(\ell)$ of possible j values only consists of $j = j_{\max}^{\{1\}} = 1$ (and does not include the case of $j = 0$) for the droplet function $f^{\{1\}}$; see Sec. V B and Figs. 7–9. Furthermore, for the analysis of some error terms, only a subset of all droplet functions may be of interest, which makes it possible to further decrease the number of measurements.

IX. CONCLUSION

In this work, we have theoretically developed and experimentally demonstrated a Wigner process tomography scheme by extending the reconstruction approach of the Wigner representation for multiqubit states of [9]. Our scheme reconstructs the relevant spherical functions representing propagators by imprinting these operators on the density matrix of an augmented system with an additional ancilla spin and subsequently measuring expectation values of rotated axial tensor operators. The approach is universally applicable and not restricted to NMR methodologies or to particles with spin 1/2. In the presented proof-of-concept experiments, a reasonable match was found between the theoretical and the experimentally reconstructed Wigner functions of a range of important single-qubit propagators. In particular, the method provided a direct demonstration of the spinor property of propagators corresponding to the rotation of a spin-1/2 particle.

ACKNOWLEDGMENTS

D.L. acknowledges support from the Ph.D. program *Exploring Quantum Matter* (ExQM) within the *Excellence Network of Bavaria* (ENB). S.J.G. acknowledges support from the Deutsche Forschungsgemeinschaft (DFG) through Grant No. Gl 203/7-2. We thank Raimund Marx for providing the NMR samples. The experiments were performed at the Bavarian NMR Center (BNMRZ) at the Technical University of Munich.

APPENDIX

1. Example of the imprinting of a propagator $U^{[N]}$ on the density operator $\rho_U^{[N+1]}$ of an augmented spin system

Here the operators $U^{[N]}$, $cU^{[N+1]}$, $\rho_0^{[N+1]}$, and $\rho_U^{[N+1]}$ defined in Sec. IV A of the main text are explicitly given for a simple example, where the *system of interest* consists only of one $(N = 1)$ spin 1/2 denoted I_1, which is augmented by an *ancilla* spin 1/2 denoted I_0. In this case, the matrix representation of the propagator $U^{[N]} = U^{[1]}$ to be scanned is of dimension 2×2 and has the general form

$$U^{[1]} = \begin{pmatrix} u_{11} & u_{12} \\ u_{21} & u_{22} \end{pmatrix}. \tag{A1}$$

The matrix representation of the controlled propagator $cU^{[N+1]} = cU^{[2]}$ in the augmented system is of dimension 4×4

and is given by

$$cU^{[2]} = \begin{pmatrix} 1 & 0 & 0 & 0 \\ 0 & 1 & 0 & 0 \\ 0 & 0 & u_{11} & u_{12} \\ 0 & 0 & u_{21} & u_{22} \end{pmatrix}. \tag{A2}$$

For the prepared initial state of the augmented spin system, the deviation density operator [see Eq. (13)] is proportional to

$$\rho_0^{[2]} = 2I_{0x}^{[N+1]} = \begin{pmatrix} 0 & 1 \\ 1 & 0 \end{pmatrix} \otimes \begin{pmatrix} 1 & 0 \\ 0 & 1 \end{pmatrix} = \begin{pmatrix} 0 & 0 & 1 & 0 \\ 0 & 0 & 0 & 1 \\ 1 & 0 & 0 & 0 \\ 0 & 1 & 0 & 0 \end{pmatrix} \tag{A3}$$

and applying Eq. (14) results in

$$\rho_U^{[2]} = cU^{[2]}\,\rho_0^{[2]}\,(cU^{[2]})^\dagger = \begin{pmatrix} 0 & 0 & u_{11}^* & u_{21}^* \\ 0 & 0 & u_{12}^* & u_{22}^* \\ u_{11} & u_{12} & 0 & 0 \\ u_{21} & u_{22} & 0 & 0 \end{pmatrix}. \tag{A4}$$

Note that this operator is still Hermitian but according to Eq. (15) can be decomposed into the two non-Hermitian operators $I^- \otimes U^{[1]}$ and $I^+ \otimes U^{[1]}$:

$$\begin{aligned} \rho_U^{[2]} &= \begin{pmatrix} 0 & 0 \\ 1 & 0 \end{pmatrix} \otimes \begin{pmatrix} u_{11} & u_{12} \\ u_{21} & u_{22} \end{pmatrix} + \begin{pmatrix} 0 & 1 \\ 0 & 0 \end{pmatrix} \otimes \begin{pmatrix} u_{11}^* & u_{21}^* \\ u_{12}^* & u_{22}^* \end{pmatrix} \\ &= \begin{pmatrix} 0 & 0 & 0 & 0 \\ 0 & 0 & 0 & 0 \\ u_{11} & u_{12} & 0 & 0 \\ u_{21} & u_{22} & 0 & 0 \end{pmatrix} + \begin{pmatrix} 0 & 0 & u_{11}^* & u_{21}^* \\ 0 & 0 & u_{12}^* & u_{22}^* \\ 0 & 0 & 0 & 0 \\ 0 & 0 & 0 & 0 \end{pmatrix}. \end{aligned} \tag{A5}$$

2. Proof of Result 1

We start with Eq. (7) (see also Result 2 in [9]). If the density operator of an augmented spin system, consisting of an ancilla spin I_0 in addition to the spins $I_1, \ldots, I_N$, can be prepared in the state

$$\rho_A^{[N+1]} = \begin{pmatrix} \mathbf{0}^{[\mathbf{N}]} & (A^{[N]})^\dagger \\ A^{[N]} & \mathbf{0}^{[N]} \end{pmatrix}, \tag{A6}$$

the (in general complex) value of the scalar product $\langle T_{j,\alpha\beta}^{(\ell)[N]} | A^{[N]} \rangle$ can be experimentally obtained by measuring the expectation value of the operator $I^+ \otimes T_{j,\alpha\beta}^{(\ell)[N]}$:

$$\begin{aligned} \left\langle I^+ \otimes T_{j,\alpha\beta}^{(\ell)[N]} \right\rangle_{\rho_A^{[N+1]}} &= \mathrm{tr}\left\{ \left[I^+ \otimes T_{j,\alpha\beta}^{(\ell)[N]} \right] \rho_A^{[N+1]} \right\} \\ &= \mathrm{tr}\left\{ \begin{pmatrix} 0 & T_{j,\alpha\beta}^{(\ell)[N]} \\ 0 & 0 \end{pmatrix} \begin{pmatrix} \mathbf{0}^{[\mathbf{N}]} & (A^{[N]})^\dagger \\ A^{[N]} & \mathbf{0}^{[N]} \end{pmatrix} \right\} \\ &= \mathrm{tr}\left\{ \begin{pmatrix} T_{j,\alpha\beta}^{(\ell)[N]} A^{[N]} & \mathbf{0}^{[N]} \\ \mathbf{0}^{[N]} & \mathbf{0}^{[N]} \end{pmatrix} \right\} \\ &= \mathrm{tr}\left\{ T_{j,\alpha\beta}^{(\ell)[N]} A^{[N]} \right\} \\ &= \mathrm{tr}\left\{ (T_{j,\alpha\beta}^{(\ell)[N]})^\dagger A^{[N]} \right\} \\ &= \left\langle T_{j,\alpha\beta}^{(\ell)[N]} | A^{[N]} \right\rangle. \end{aligned} \tag{A7}$$

Note that the operator $I^+ \otimes T_{j,\alpha\beta}^{(\ell)[N]}$ is not Hermitian and hence is not an observable that can be directly measured. However, based on the definition of I^+ [28], we can decompose the expectation value of Eq. (A7) into a complex linear combination of the expectation values of the Hermitian operators $I_x \otimes T_{j,\alpha\beta}^{(\ell)[N]}$ and $I_y \otimes T_{j,\alpha\beta}^{(\ell)[N]}$:

$$\begin{aligned} \left\langle I^+ \otimes T_{j,\alpha\beta}^{(\ell)[N]} \right\rangle_{\rho_A^{[N+1]}} &= \left\langle (I_x + i I_y) \otimes T_{j,\alpha\beta}^{(\ell)[N]} \right\rangle_{\rho_A^{[N+1]}} \\ &= \left\langle I_x \otimes T_{j,\alpha\beta}^{(\ell)[N]} \right\rangle_{\rho_A^{[N+1]}} + i \left\langle I_y \otimes T_{\alpha\beta}^{[N]} \right\rangle_{\rho_A^{[N+1]}}. \end{aligned} \tag{A8}$$

3. Example of the measurement of the scalar product between a rotated axial tensor operator and a propagator

Considering the same spin system as in Appendix A 1, we show how the procedure outlined in the main text allows us to obtain scalar products of the form [see Eq. (17)]

$$\left\langle T_{j,\alpha\beta}^{(\ell)[N]} | U^{[N]} \right\rangle = \left\langle I_x \otimes T_{j,\alpha\beta}^{(\ell)[N]} \right\rangle_{\rho_U^{[N+1]}} + i \left\langle I_y \otimes T_{j,\alpha\beta}^{(\ell)[N]} \right\rangle_{\rho_U^{[N+1]}}. \tag{A9}$$

Here, the operator

$$T_{j,\alpha\beta}^{(\ell)[N]} = R_{\alpha\beta}^{[N]} \left(T_{j0}^{(\ell)} \right)^{[N]} \left(R_{\alpha\beta}^{[N]} \right)^\dagger \tag{A10}$$

is a rotated axial tensor operator $(T_{j0}^{(\ell)})^{[N]}$.

For example, the rank $j = 1$ axial tensor operator for the droplet corresponding to spin I_1 is given by

$$\left(T_{10}^{(1)} \right)^{[1]} = \sqrt{2} I_{1z}^{[1]} = \begin{pmatrix} 1/\sqrt{2} & 0 \\ 0 & -1/\sqrt{2} \end{pmatrix}, \tag{A11}$$

and for $\alpha = 0$ and $\beta = \pi/2$, the rotated axial tensor operator is

$$\begin{aligned} T_{1,0,\pi/2}^{(1)[1]} &= R_{0,\pi/2}^{[1]} \left(T_{10}^{(1)} \right)^{[N]} \left(R_{0,\pi/2}^{[1]} \right)^\dagger \\ &= \sqrt{2} I_{1x}^{[1]} = \begin{pmatrix} 0 & 1/\sqrt{2} \\ 1/\sqrt{2} & 0 \end{pmatrix}. \end{aligned} \tag{A12}$$

With

$$\begin{aligned} I_x \otimes T_{1,0,\pi/2}^{(1)[1]} &= \begin{pmatrix} 0 & 1/2 \\ 1/2 & 0 \end{pmatrix} \otimes \begin{pmatrix} 0 & 1/\sqrt{2} \\ 1/\sqrt{2} & 0 \end{pmatrix} \\ &= \frac{1}{2\sqrt{2}} \begin{pmatrix} 0 & 0 & 0 & 1 \\ 0 & 0 & 1 & 0 \\ 0 & 1 & 0 & 0 \\ 1 & 0 & 0 & 0 \end{pmatrix} \end{aligned} \tag{A13}$$

and

$$\begin{aligned} I_y \otimes T_{1,0,\pi/2}^{(1)[1]} &= \begin{pmatrix} 0 & -i/2 \\ i/2 & 0 \end{pmatrix} \otimes \begin{pmatrix} 0 & 1/\sqrt{2} \\ 1/\sqrt{2} & 0 \end{pmatrix} \\ &= -\frac{i}{2\sqrt{2}} \begin{pmatrix} 0 & 0 & 0 & 1 \\ 0 & 0 & 1 & 0 \\ 0 & -1 & 0 & 0 \\ -1 & 0 & 0 & 0 \end{pmatrix} \end{aligned} \tag{A14}$$

we find the expectation values

$$\begin{aligned}\left\langle I_x \otimes T^{(1)[1]}_{1,0,\pi/2}\right\rangle_{\rho_U^{[2]}} &= \frac{1}{2\sqrt{2}}\,\mathrm{tr}\left\{\begin{pmatrix}0&0&0&1\\0&0&1&0\\0&1&0&0\\1&0&0&0\end{pmatrix}\right.\\ &\quad\left.\times\begin{pmatrix}0&0&u_{11}^*&u_{21}^*\\0&0&u_{12}^*&u_{22}^*\\u_{11}&u_{12}&0&0\\u_{21}&u_{22}&0&0\end{pmatrix}\right\}\\ &= \frac{1}{2\sqrt{2}}\,\mathrm{tr}\left\{\begin{pmatrix}u_{21}&0&0&0\\0&u_{12}&0&0\\0&0&u_{12}^*&0\\0&0&0&u_{21}^*\end{pmatrix}\right\}\\ &= \frac{1}{2\sqrt{2}}\,(u_{21}+u_{12}+u_{12}^*+u_{21}^*)\\ &= \frac{1}{\sqrt{2}}\,(\mathrm{Re}\{u_{12}\}+\mathrm{Re}\{u_{21}\}) \qquad \text{(A15)}\end{aligned}$$

and

$$\begin{aligned}\left\langle I_y \otimes T^{(1)[1]}_{1,0,\pi/2}\right\rangle_{\rho_U^{[2]}} &= -\frac{i}{2\sqrt{2}}\,\mathrm{tr}\left\{\begin{pmatrix}0&0&0&1\\0&0&1&0\\0&-1&0&0\\-1&0&0&0\end{pmatrix}\right.\\ &\quad\left.\times\begin{pmatrix}0&0&u_{11}^*&u_{21}^*\\0&0&u_{12}^*&u_{22}^*\\u_{11}&u_{12}&0&0\\u_{21}&u_{22}&0&0\end{pmatrix}\right\}\\ &= -\frac{i}{2\sqrt{2}}\,\mathrm{tr}\left\{\begin{pmatrix}u_{21}&0&0&0\\0&u_{12}&0&0\\0&0&-u_{12}^*&0\\0&0&0&-u_{21}^*\end{pmatrix}\right\}\\ &= -\frac{i}{2\sqrt{2}}(u_{21}+u_{12}-u_{12}^*-u_{21}^*)\\ &= \frac{1}{\sqrt{2}}\,(\mathrm{Im}\{u_{12}\}+\mathrm{Im}\{u_{21}\}). \qquad \text{(A16)}\end{aligned}$$

Hence, we find

$$\begin{aligned}&\left\langle I_x \otimes T^{(1)[1]}_{1,0,\pi/2}\right\rangle_{\rho_U^{[N+1]}} + i\left\langle I_y \otimes T^{(1)[1]}_{1,0,\pi/2}\right\rangle_{\rho_U^{[N+1]}}\\ &\quad= \frac{1}{\sqrt{2}}\,(\mathrm{Re}\{u_{12}\}+i\,\mathrm{Im}\{u_{12}\}+\mathrm{Re}\{u_{21}\}+i\,\mathrm{Im}\{u_{21}\})\\ &\quad= \frac{1}{\sqrt{2}}\,(u_{12}+u_{21}). \qquad \text{(A17)}\end{aligned}$$

This is identical to the scalar product

$$\begin{aligned}\left\langle T^{(1)[1]}_{1,0,\pi/2}\middle|U^{[1]}\right\rangle &= \mathrm{tr}\left\{\left(T^{(1)[1]}_{1,0,\pi/2}\right)^\dagger U^{[1]}\right\}\\ &= \mathrm{tr}\left\{\begin{pmatrix}0&1/\sqrt{2}\\1/\sqrt{2}&0\end{pmatrix}^\dagger\begin{pmatrix}u_{11}&u_{12}\\u_{21}&u_{22}\end{pmatrix}\right\}\\ &= \mathrm{tr}\left\{\begin{pmatrix}0&1/\sqrt{2}\\1/\sqrt{2}&0\end{pmatrix}\begin{pmatrix}u_{11}&u_{12}\\u_{21}&u_{22}\end{pmatrix}\right\}\\ &= 1/\sqrt{2}\,\mathrm{tr}\left\{\begin{pmatrix}u_{21}&u_{22}\\u_{11}&u_{12}\end{pmatrix}\right\}\\ &= 1/\sqrt{2}\,(u_{12}+u_{21}); \qquad \text{(A18)}\end{aligned}$$

see Eq. (A9).

4. Proof of Equations (19) and (20)

Here we show that

$$\left\langle I_a\otimes T^{(\ell)[N]}_{j,\alpha\beta}\right\rangle_{\rho_U^{[N+1]}} = \left\langle I_a\otimes\left(T^{(\ell)}_{j0}\right)^{[N]}\right\rangle_{\tilde{\rho}_U^{[N+1]}} \qquad \text{(A19)}$$

for $a\in\{x,y\}$. This can be seen by a sequence of reformulations and by exploiting properties of the trace operation and of the tensor product:

$$\begin{aligned}&\left\langle I_a\otimes T^{(\ell)[N]}_{j,\alpha\beta}\right\rangle_{\rho_U^{[N+1]}}\\ &\quad= \mathrm{tr}\left\{\left[I_a\otimes T^{(\ell)[N]}_{j,\alpha\beta}\right]\rho_U^{[N+1]}\right\}\\ &\quad= \mathrm{tr}\left\{\left[I_a\otimes R^{[N]}_{\alpha\beta}\left(T^{(\ell)}_{j0}\right)^{[N]}\left(R^{[N]}_{\alpha\beta}\right)^\dagger\right]\rho_U^{[N+1]}\right\}\\ &\quad= \mathrm{tr}\left\{\left[\mathbf{1}^{[1]}\otimes R^{[N]}_{\alpha\beta}\right]\left[I_a\otimes\left(T^{(\ell)}_{j0}\right)^{[N]}\right]\left[\mathbf{1}^{[1]}\otimes R^{[N]}_{\alpha\beta}\right]^\dagger\rho_U^{[N+1]}\right\}\\ &\quad= \mathrm{tr}\left\{R^{[N+1]}_{\alpha\beta}\left[I_a\otimes\left(T^{(\ell)}_{j0}\right)^{[N]}\right]\left(R^{[N+1]}_{\alpha\beta}\right)^\dagger\rho_U^{[N+1]}\right\}\\ &\quad= \mathrm{tr}\left\{\left[I_a\otimes\left(T^{(\ell)}_{j0}\right)^{[N]}\right]\left(R^{[N+1]}_{\alpha\beta}\right)^\dagger\rho_U^{[N+1]}R^{[N+1]}_{\alpha\beta}\right\}\\ &\quad= \mathrm{tr}\left\{\left[I_a\otimes\left(T^{(\ell)}_{j0}\right)^{[N]}\right]\tilde{\rho}_U^{[N+1]}\right\}\\ &\quad= \left\langle I_a\otimes\left(T^{(\ell)}_{j0}\right)^{[N]}\right\rangle_{\tilde{\rho}_U^{[N+1]}} \qquad \text{(A20)}\end{aligned}$$

with

$$\begin{aligned}\tilde{\rho}_U^{[N+1]} &= \left(R^{[N+1]}_{\alpha\beta}\right)^\dagger\rho_U^{[N+1]}R^{[N+1]}_{\alpha\beta}\\ &= \left(R^{[N+1]}_{\alpha\beta}\right)^{-1}\rho_U^{[N+1]}R^{[N+1]}_{\alpha\beta}, \qquad \text{(A21)}\end{aligned}$$

$R^{[N+1]}_{\alpha\beta} = \mathbf{1}^{[1]}\otimes R^{[N]}_{\alpha\beta}$, and $a\in\{x,y\}$. Here, we used the properties of the tensor product $AB\otimes CD = (A\otimes C)(B\otimes D)$ and the invariance of the trace operation under cyclic permutations. Note that the rotation $R^{[N+1]}_{\alpha\beta}$ affects only the system qubits $I_1,\ldots,I_N$ and not the ancilla qubit I_0.

5. Role of global phase factors in $U^{[N]}$ and $cU^{[N+1]}$

Consider two propagators $U^{[N]}$ and $\hat{U}^{[N]}$ that differ only by a global phase factor $e^{i\eta}$, i.e., $\hat{U}^{[N]} = e^{i\eta}U^{[N]}$. In the construction of $cU^{[N+1]}$ and $c\hat{U}^{[N+1]}$, the phase factor manifests itself as an additional phase factor that is *only* applied to the second block on the diagonal:

$$cU^{[N+1]} = \begin{pmatrix}\mathbf{1}^{[N]}&0\\0&U^{[N]}\end{pmatrix} \qquad \text{(A22)}$$

but

$$c\hat{U}^{[N+1]} = \begin{pmatrix}\mathbf{1}^{[N]}&0\\0&e^{i\eta}U^{[N]}\end{pmatrix}; \qquad \text{(A23)}$$

i.e., the *global* phase factor $e^{i\eta}$ of a propagator $\hat{U}^{[N]}$ is transformed into a *relative* phase factor in the propagator $c\hat{U}^{[N+1]}$

of the augmented system and hence becomes experimentally measurable.

However, any *global* phase factor of $cU^{[N+1]}$ is irrelevant in the considered experiments because it cancels when $cU^{[N+1]}$ is applied to the density operator [see Eq. (A4)]. Hence, such a global phase factor can be ignored when designing experimental pulse sequences to realize $cU^{[N+1]}$; see Table I.

6. Decomposition into individual droplet ℓ contributions

The proposed (experimental) Wigner process tomography scheme (see Results 1 and 2) also allows one to decompose the function $f(\theta,\phi)$ into a part $f_0^{\{\emptyset\}}(\theta,\phi)$ corresponding to the identity operator (with rank $j=0$) and a part $f_1^{\{1\}}(\theta,\phi)$ corresponding to terms involving spin I_1 (with rank $j=1$). Although this creates some redundancy, the separation may help to analyze and to delineate different sources of errors in an experiment. For example, the expected shape of $f_0^{\{\emptyset\}}(\theta,\phi)$ is a perfect sphere, and deviations of the experimentally reconstructed shape of this droplet can give clues about the size of systematic and stochastic errors and dominant experimental imperfections, such as pulse miscalibration, radio-frequency inhomogeneity, or relaxation effects. Figure 7 illustrates the decomposition of $f(\theta,\phi)$ into $f_0^{\{\emptyset\}}(\theta,\phi)$ and $f_1^{\{1\}}(\theta,\phi)$ for the case of a propagator corresponding to a $[\pi/2]_x$ rotation. Figures 8 and 9 show decomposed theoretical and experimental droplet functions $f_0^{\{\emptyset\}}(\theta,\phi)$ and $f_1^{\{1\}}(\theta,\phi)$ corresponding to the combined droplet functions $f(\theta,\phi)$ that are shown in Fig. 6 for the set of rotation angles $0,\pi/2,\ldots,4\pi$.

7. Explicit functional form of the droplets $f^{\{\emptyset\}}$ and $f^{\{1\}}$ for arbitrary rotations

For an arbitrary rotation with rotation angle Ψ and a rotation axis defined by the normalized vector

$$\vec{n} = \begin{pmatrix} n_x \\ n_y \\ n_z \end{pmatrix}, \tag{A24}$$

the propagator $U^{[1]}$ has the general form [56,57]

$$U^{[1]} = \cos\frac{\Psi}{2}\mathbf{1} - 2\,i\,\sin\frac{\Psi}{2}(n_x I_x + n_y I_y + n_z I_z). \tag{A25}$$

Using the general relations $T_{00} = 1/\sqrt{2}\,\mathbf{1}$, $T_{1,-1} = I^- = I_x + i I_y$, $T_{10} = \sqrt{2}\;I_z$, and $T_{11} = -I^+ = -(I_x - i I_y)$ between Cartesian spin operators and spherical tensor operators [6,28] and the DROPS mapping between spherical tensor operators T_{jm} and spherical harmonics Y_{jm} (see Sec. II), a straightforward calculation yields the following explicit functional forms for the $\ell = \{\emptyset\}$ and $\ell = \{1\}$ components of the droplet function

$$f(\theta,\phi) = f_0^{\{\emptyset\}}(\theta,\phi) + f_1^{\{1\}}(\theta,\phi)\,: \tag{A26}$$

$$f_0^{\{\emptyset\}}(\theta,\phi) = \sqrt{\frac{1}{2\pi}}\,\cos\frac{\Psi}{2} \tag{A27}$$

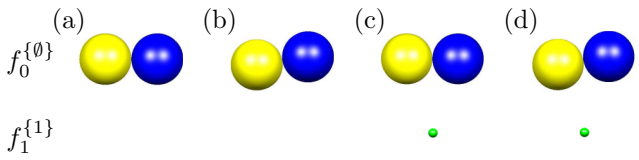

FIG. 10. For the case of a system consisting only of a single ($N=1$) spin 1/2, the simulations show how different sources of propagator errors can be identified in the DROPS representation: (a) Ideal case of a rotation with rotation angle $\Psi=\pi$ and rotation axis $\vec{n}$ with $n_x=1$ and $n_y=n_z=0$, (b) rotation angle increased by 10%, (c) rotation axis deviating by an angle of $\pi/10$ from the x axis resulting in $n_x=\cos(\pi/10)$ and $n_y=\sin(\pi/10)$ and $n_z=0$, and (d) simultaneous error of the flip angle as in case (b) and of the rotation axis as in case (c).

and

$$f_1^{\{1\}}(\theta,\phi) = -i\,\sqrt{\frac{3}{2\pi}}\,\sin\frac{\Psi}{2}\,(n_x\sin\theta\cos\phi + n_y\sin\theta\sin\phi + n_z\cos\theta). \tag{A28}$$

Note that the droplet function $f_0^{\{\emptyset\}}(\theta,\phi)$ is real-valued and independent of the polar and azimuthal angles θ and ϕ. Hence it is represented either by a red (positive real) or green (negative real) sphere (dark gray and gray) that is centered at the origin in three-dimensional polar plots; see Figs. 8–10 and the color bar in Fig. 1. The droplet function $f_1^{\{1\}}(\theta,\phi)$ is purely imaginary and is represented in three-dimensional polar plots by a yellow (positive imaginary) and blue (negative imaginary) sphere (light gray and black), which touch at the origin; see Figs. 8–10. The vector connecting the centers of the yellow and blue spheres (light gray and black) is collinear with the rotation axis $\vec{n}$. Due to the factor $\cos\frac{\Psi}{2}$, the function $f_0^{\{\emptyset\}}(\theta,\phi)$ is zero if the rotation angle Ψ is an odd multiple of π. Conversely, the function $f_1^{\{1\}}(\theta,\phi)$ is zero if Ψ is an even multiple of π due to the factor $\sin\frac{\Psi}{2}$; see Figs. 7, 8, and 10. Note that some of the standard quantum gates are only identical to the propagator of a rotation up to a global phase factor. For example, the propagator of the Hadamard gate (see Table I) is only up to $e^{-i\pi/2} = -i$ identical to a rotation with rotation angle $\Psi=\pi$ and rotation axis $\vec{n}$ with $n_x = n_z = 1/\sqrt{2}$ and $n_y = 0$. This additional global phase factor changes the colors of the spheres of $f_1^{\{1\}}(\theta,\phi)$ in Figs. 2 and 4 from yellow and blue to green (negative real) and red (positive real) (light gray and black to gray and dark gray), respectively.

8. Periodicities of phase-shift gate and rotation propagator for spin 1/2

In Secs. VII B and VII C, it was stated that for a spin 1/2 the propagator $U^{[1]}$ corresponding to a phase gate $U_{ph}^{[1]}(\gamma)$ and to a rotation $U_{\text{rot}}^{[1]}(\delta)$ has a periodicity of 2π for γ but of 4π for δ. This is a result of the fact that the matrix elements of

$$U_{\text{rot}}^{[1]}(\delta) = \begin{pmatrix} e^{-i\delta/2} & 0 \\ 0 & e^{i\delta/2} \end{pmatrix} \tag{A29}$$

are exponential functions of the half angle $\delta/2$ whereas the matrix elements of

$$U_{ph}^{[1]}(\gamma) = \begin{pmatrix} 1 & 0 \\ 0 & e^{i\gamma} \end{pmatrix} \tag{A30}$$

are exponential functions of the full angle γ, resulting in $U_{ph}^{[1]}(\gamma + 2\pi) = U_{ph}^{[1]}(\gamma)$ but $U_{\text{rot}}^{[1]}(\delta + 2\pi) = -U_{\text{rot}}^{[1]}(\delta)$ and $U_{\text{rot}}^{[1]}(\delta + 4\pi) = U_{\text{rot}}^{[1]}(\delta)$.

9. Analysis of propagator errors in the DROPS representation of propagators

Here, we consider possible advantages of the DROPS representation of propagators $U^{[N]}$ in the identification and quantification of propagator errors. As demonstrated in this paper, the DROPS representation of a propagator can be measured directly by experimentally scanning expectation values of given observables as a function of polar and azimuthal angles for a set of droplet functions $f^{(\ell)}$. (Alternatively, conventional process tomography schemes [13–18] could be used to estimate the matrix elements of the propagator and to numerically calculate the corresponding DROPS representation of this matrix.)

As discussed in Sec. VIII, possible contributions to errors of the experimentally sampled points of the droplet functions include errors in the preparation of the initial density operator, in the implementation of the controlled version $cU^{[N+1]}$ of the propagator $U^{[N]}$, noise in the detection process (see Fig. 3), and truncation effects in the automated integration and comparison of the spectra. For simplicity, here we focus on an idealized scenario, where the errors of the tomography scheme are negligibly small and the scheme has been extended in analogy to [46] to the tomography of unknown propagators $U^{[N]}$ as discussed in Sec. VIII. Suppose we are trying to implement a desired target operator $U_{\text{targ}}^{[N]}$ by a new pulse sequence and we want to identify and quantify the errors in the experimentally realized propagator $U_{\text{exp}}^{[N]}$. The DROPS tomography of $U_{\text{exp}}^{[N]}$ provides a set of experimentally measured droplet functions, which (according to our assumption of negligible tomography errors) closely approach the ideal droplet functions corresponding to $U_{\text{exp}}^{[N]}$.

If the system of interest consists of several spins, deviations of droplets from their ideal shapes corresponding to $U_{\text{targ}}^{[N]}$ provide information about specific error types. For example, if in a system with $N = 2$ (see Fig. 1), errors of the propagator that only affect spin I_1 but not spin I_2 would be reflected by distortions of the droplet functions $f^{\{1\}}$ and $f^{\{12\}}$ but not of the droplets $f^{\{2\}}$. For the simple case with $N = 1$ and an ideal rotation with rotation angle $\Psi = \pi$ and rotation axis $\vec{n}$ with $n_x = 1$ and $n_y = n_z = 0$, the effects of errors in Ψ and/or $\vec{n}$ on the droplet functions are simulated in Fig. 10. Figure 10(a) shows the ideal case, where the two spheres representing droplet $f^{\{1\}}$ are aligned with the x axis and the droplet function $f^{\{\emptyset\}}$ is zero. Figure 10(b) shows the case where the actual rotation axis deviates by an angle $\pi/10$ in the x-y axis [resulting in $n_x = \cos(\pi/10)$, $n_y = \sin(\pi/10)$, and $n_z = 0$], which is reflected by a corresponding deviation of the $f^{\{1\}}$ orientation [the vector connecting the yellow and blue spheres (light gray and black)] from the x axis. In contrast, an error in the rotation angle is signaled by a nonvanishing droplet function $f^{\{\emptyset\}}$ (as well as a slightly reduced size of the $f^{\{1\}}$ droplet). This is shown in Fig. 10(c) for the case of $\Psi = 1.1\pi$ and ideal rotation axis $n_x = 1$ and $n_y = n_z = 0$, where a small negative green (gray) sphere of $f^{\{\emptyset\}}$ indicates that the actual rotation angle Ψ is larger than the desired rotation angle of π; see Eq. (A27). Finally, Fig. 10(d) shows the effect of simultaneous errors of the rotation angle and the rotation axis with $\Psi = 1.1\pi, n_x = \cos(\pi/10), n_y = \sin(\pi/10)$, and $n_z = 0$, where the DROPS representation clearly shows both types of errors. These examples show how the DROPS reconstruction can help to identify the source of systematic errors of a unitary propagator and to quantify the size of the respective errors. Random errors of the propagator can, e.g., be identified by repeated measurements of droplet functions for the same polar and azimuthal angles.

[1] W. P. Schleich, *Quantum Optics in Phase Space* (Wiley-VCH, Weinheim, 2001).

[2] T. L. Curtright, D. B. Fairlie, and C. K. Zachos, *A Concise Treatise on Quantum Mechanics in Phase Space* (World Scientific, Singapore, 2014).

[3] M. A. De Gosson, *The Wigner Transform* (World Scientific, Singapore, 2017).

[4] R. L. Stratonovich, J. Exp. Theor. Phys. (USSR) **31**, 1012 (1956).

[5] J. P. Dowling, G. S. Agarwal, and W. P. Schleich, Phys. Rev. A **49**, 4101 (1994).

[6] A. Garon, R. Zeier, and S. J. Glaser, Phys. Rev. A **91**, 042122 (2015).

[7] P. S. Jessen, D. L. Haycock, G. Klose, G. A. Smith, I. H. Deutsch, and G. K. Brennen, Quantum Inf. Comput. **1** (Special Issue), 20 (2001).

[8] T. Tilma, M. J. Everitt, J. H. Samson, W. J. Munro, and K. Nemoto, Phys. Rev. Lett. **117**, 180401 (2016).

[9] D. Leiner, R. Zeier, and S. J. Glaser, Phys. Rev. A **96**, 063413 (2017).

[10] N. J. Glaser, M. Tesch, and S. J. Glaser, SpinDrops (Version 1.2.2) [mobile application], 2015, http://itunes.apple.com.

[11] M. Tesch, N. J. Glaser, B. Koczor, and S. J. Glaser, SpinDrops 2.0, 2018, https://spindrops.org.

[12] L. V. Damme, D. Leiner, P. Mardešić, S. J. Glaser, and D. Sugny, Sci. Rep. **7**, 3998 (2017).

[13] I. L. Chuang and M. A. Nielsen, J. Mod. Opt. **44**, 2455 (1997).

[14] J. F. Poyatos, J. I. Cirac, and P. Zoller, Phys. Rev. Lett. **78**, 390 (1997).

[15] A. M. Childs, I. L. Chuang, and D. W. Leung, Phys. Rev. A **64**, 012314 (2001).

[16] J. B. Altepeter, D. Branning, E. Jeffrey, T. C. Wei, P. G. Kwiat, R. T. Thew, J. L. O'Brien, M. A. Nielsen, and A. G. White, Phys. Rev. Lett. **90**, 193601 (2003).

[17] C. T. Schmiegelow, A. Bendersky, M. A. Larotonda, and J. P. Paz, Phys. Rev. Lett. **107**, 100502 (2011).

[18] A. Gaikwad, D. Rehal, A. Singh, Arvind, and K. Dorai, Phys. Rev. A **97**, 022311 (2018).

[19] T. Heinosaari and M. Ziman, *The Mathematical Language of Quantum Theory: From Uncertainty to Entanglement* (Cambridge University Press, Cambridge, 2011).

[20] W. J. Thompson, *Angular Momentum* (Wiley-VCH, Weinheim, 1994).

[21] S. Massimiliano, Found. Sci. **22**, 627 (2017).

[22] F. Mezei, A. Ioffe, P. Fischer, M. Arif, and D. L. Jacobson, Physica B **276–278**, 979 (2000).

[23] S. A. Werner, R. Colella, A. W. Overhauser, and C. F. Eagen, Phys. Rev. Lett. **35**, 1053 (1975).

[24] G. Badurek, H. Rauch, A. Zeilinger, W. Bauspiess, and U. Bonse, Phys. Lett. A **56**, 244 (1976).

[25] M. Mehring, P. Höfer, A. Grupp, and H. Seidel, Phys. Lett. A **106**, 146 (1984).

[26] D. Suter, A. Pines, and M. Mehring, Phys. Rev. Lett. **57**, 242 (1986).

[27] M. E. Stoll, A. J. Vega, and R. W. Vaughan, Phys. Rev. A **16**, 1521 (1977).

[28] R. R. Ernst, G. Bodenhausen, and A. Wokaun, *Principles of Nuclear Magnetic Resonance in One and Two Dimensions* (Clarendon Press, Oxford, 1987).

[29] Cartesian operators for single spins are $I_x := \sigma_x/2$, $I_y := \sigma_y/2$, and $I_z := \sigma_z/2$, where the Pauli matrices are $\sigma_x = \begin{pmatrix} 0 & 1 \\ 1 & 0 \end{pmatrix}$, $\sigma_y = \begin{pmatrix} 0 & -i \\ i & 0 \end{pmatrix}$, and $\sigma_z = \begin{pmatrix} 1 & 0 \\ 0 & -1 \end{pmatrix}$. For N spins, one has the operators $I_{k\eta} := \bigotimes_{s=1}^{N} I_{a_s}$ where a_s is equal to η for $s = k$ and is zero otherwise; note $I_0 := \begin{pmatrix} 1 & 0 \\ 0 & 1 \end{pmatrix}$.

[30] Hermitian operators lead to positive and negative values which are shown in red (dark gray) and green (gray). .

[31] E. Wigner, *Gruppentheorie und ihre Anwendung auf die Quantenmechanik der Atomspektren* (Friedrich Vieweg & Sohn, Braunschweig, 1931) (English translation in [32]).

[32] E. P. Wigner, *Group Theory and its Application to the Quantum Mechanics of Atomic Spectra* (Academic Press, London, 1959).

[33] G. Racah, Phys. Rev. **62**, 438 (1942).

[34] L. C. Biedenharn and J. D. Louck, *Angular Momentum in Quantum Physics* (Addison-Wesley, Reading, MA, 1981).

[35] B. L. Silver, *Irreducible Tensor Methods* (Academic Press, New York, 1976).

[36] M. Chaichian and R. Hagedorn, *Symmetries in Quantum Mechanics: From Angular Momentum to Supersymmetry* (Institute of Physics, Bristol, 1998).

[37] S. S. Köcher, T. Heydenreich, Y. Zhang, G. N. M. Reddy, S. Caldarelli, H. Yuan, and S. J. Glaser, J. Chem. Phys. **144**, 164103 (2016).

[38] M. A. Nielsen and I. L. Chuang, *Quantum Computation and Quantum Information* (Cambridge University Press, Cambridge, 2000).

[39] A. F. Fahmy, R. Marx, W. Bermel, and S. J. Glaser, Phys. Rev. A **78**, 022317 (2008).

[40] J. M. Myers, A. F. Fahmy, S. J. Glaser, and R. Marx, Phys. Rev. A **63**, 032302 (2001).

[41] R. Marx, A. F. Fahmy, L. Kauffman, S. Lomonaco, A. Spörl, N. Pomplun, T. Schulte-Herbrüggen, J. M. Myers, and S. J. Glaser, Phys. Rev. A **81**, 032319 (2010).

[42] A. Barenco, C. H. Bennett, R. Cleve, D. P. DiVincenzo, N. Margolus, P. Shor, T. Sleator, J. A. Smolin, and H. Weinfurter, Phys. Rev. A **52**, 3457 (1995).

[43] M. H. Levitt, *Spin Dynamics: Basics of Nuclear Magnetic Resonance* (Wiley, New York, 2008).

[44] A. Tabuchi, M. Negoroa, K. Takedab, and M. Kitagawa, J. Magn. Reson. **204**, 327 (2010).

[45] M. P. Augustine and E. L. Hahn, Concepts Magn. Reson. **13**, 1 (2001).

[46] X.-Q. Zhou, T. C. Ralph, P. Kalasuwan, M. Zhang, A. Peruzzo, B. P. Lanyon, and J. L. O'Brien, Nat. Commun. **2**, 413 (2011).

[47] Z. Khalid, R. A. Kennedy, and J. D. McEwen, IEEE Trans. Signal Process. **62**, 4597 (2014).

[48] J. R. Driscoll and D. M. Healy, Adv. Appl. Math. **15**, 202 (1994).

[49] R. A. Kennedy and P. Sadeghi, *Hilbert Space Methods in Signal Processing* (Cambridge University Press, Cambridge, 2013).

[50] J. D. McEwen and Y. Wiaux, IEEE Trans. Signal Process. **59**, 5876 (2011).

[51] Bull. géodésique **60**, 1 (1986).

[52] V. I. Lebedev, USSR Comput. Math. Math. Phys. **15**, 44 (1975).

[53] V. I. Lebedev, USSR Comput. Math. Math. Phys. **16**, 10 (1976).

[54] V. I. Lebedev and D. N. Laikov, Russian Acad. Sci. Dokl. Math. **59**, 477 (1999).

[55] J. D. van Beek, M. Carravetta, G. C. Antonioli, and M. H. Levitt, J. Chem. Phys. **122**, 244510 (2005).

[56] M. Goldman and G. A. Webb, *Quantum Description of High Resolution NMR in Liquids* (Oxford University Press, Oxford, 1988).

[57] K. Kobzar, S. Ehni, T. E. Skinner, S. J. Glaser, and B. Luy, J. Magn. Reson. **225**, 142 (2012).

C Symmetry-adapted decomposition of tensor operators and the visualization of coupled spin systems

Bibliography:

Title: Symmetry-adapted decomposition of tensor operators and the visualization of coupled spin systems

Authors: D. Leiner, R. Zeier, and S. J. Glaser

Journal: arXiv.org preprint server

Identifier: 1809.09006

Pages: 28

Published: 24.09.2018

URL: http://arxiv.org/abs/1809.09006

This manuscript is a preprint

Summary and contribution to this manuscript:
Using the DROPS representation by Garon. et al [1], multi-spin operators can be decomposed into a symmetry-adapted tensor basis and they are mapped to discrete sets of spherical functions that are each assembled from linear combinations of spherical harmonics. In order to obtain this basis, projection operators are applied, which are however corrupted for system with five and more spins 1/2 (qubits) due to certain computational challenges. The visualization approach is thus restricted to maximally four coupled spins 1/2. In this paper, the DROPS representation is generalized to systems consisting of arbitrary number of spins 1/2 and to two-coupled spins with arbitrary spin numbers. In order to circumvent the problem of corrupted projection operators, a purely linear algebraic approach is introduced exploiting transformation matrices, which are assembled from coefficients of fractional parentage (CFP). The symmetry-adapted tensor basis can then be iteratively built up by first coupling a single spin to the full symmetrized tensor basis for $g-1$ spins to obtain partially symmetrized tensors of the g spin system and second using these CFP-matrices to transform them to complete symmetrized tensors for the g spin system. The theory and the algorithmic methodology was worked out by David Leiner. In addition, the projector approach is extended to the regime of spins with arbitrary spin numbers in particular for coupled two-spin systems by introducing an additional criteria to classify tensors based on parent sublabels, which provide a more natural way to identify tensors in systems consisting of spins with large spin numbers. An indication on how to generalize the DROPS representation to many-spin systems with spin numbers larger than 1/2 completes the paper. These technical details were also worked out by David Leiner. Robert Zeier provided huge amount of assistance in deriving both methods. To highlight the richness of this visualization approach, random matrices for a four, five, and six spin system, entangled states such as the Dicke state and a state

consisting of two EPR pairs of a four spin system, and prominent operators in NMR including fully symmetrical, antiphase, and non-Hermitian operators in systems up to six coupled spins 1/2 were illustrated. Also a system with a spin 1 coupled to a spin 1/2 is depicted. Furthermore, the dynamics of a set of experiments are visualized including the creation of maximum-quantum coherence, polarization transfers under isotropic mixing conditions, and coherent state transfers in system consisting of four, five, and six qubits, respectively. A comprehensive section on the corrupted projection operators occurring in systems larger than four spins complements this paper, which also discusses open problems and was worked out by Robert Zeier. The computations and the figures were done by David Leiner. The full manuscript was written in its first version by David Leiner and revised by Robert Zeier and Steffen Glaser.

Symmetry-adapted decomposition of tensor operators and the visualization of coupled spin systems

David Leiner,[a] Robert Zeier,[b] and Steffen J. Glaser[c]
Technical University of Munich, Department of Chemistry, Lichtenbergstrasse 4, 85747 Garching, Germany

(Dated: 24 September 2018)

We study the representation and visualization of finite-dimensional quantum systems. In a generalized Wigner representation, multi-spin operators can be decomposed into a symmetry-adapted tensor basis and they are mapped to multiple spherical plots that are each assembled from linear combinations of spherical harmonics. We apply two different approaches based on explicit projection operators and coefficients of fractional parentage in order to obtain this basis for up to six spins 1/2 (qubits), for which various examples are presented. An extension to two coupled spins with arbitrary spin numbers (qudits) is provided, also highlighting a quantum system of a spin 1/2 coupled to a spin 1 (qutrit).

I. Introduction

Quantum systems exhibit an intricate structure and numerous methods have been established for the visualization of their quantum state. A two-level quantum system, such as a single spin 1/2 (qubit), can always be faithfully represented by a three-dimensional vector (Bloch vector), as shown in the seminal work of Feynman et al.[1] Applications of the Bloch vector are frequently found in the field of quantum physics, in particular in magnetic resonance imaging,[2,3] spectroscopy,[3] and quantum optics.[4] However, for systems consisting of coupled spins, standard Bloch vectors can only partially represent the density matrix, whereas important terms, such as multiple-quantum coherence[3] or spin alignment,[3] are not captured. In this case, the complete density operator can be visualized by bar charts, in which the real and imaginary parts of each element of the density matrix is represented a vertical bar, an approach which is commonly used to graphically display the experimental results of quantum state tomography.[5] Alternatively, energy-level diagrams can can be illustrate populations by circles on energy levels and coherences by lines between energy levels.[6] Density operators can also be visualized by non-classical vector representations based on single-transition operators.[3,7,8] However, these techniques are inconvenient for larger spin systems and often do not provide an intuitive view of the spin dynamics.

Phase space representations,[4,9–11] in particular Wigner functions,[4,9,12] which originally arise in the description of the infinite-dimensional quantum state of light,[13–17] provide a powerful alternative approach for the characterization and visualization of finite-dimensional quantum systems. One valuable class for the representation of finite-dimensional systems are discrete Wigner functions[18–23] but we will focus on continuous representations, which naturally reflect the inherent rotational symmetries of spins. General criteria for defining continuous Wigner functions for finite-dimensional quantum systems had been established in the work by Stratonovich[24] and the case of single-spin systems has been studied in the literature.[25–32] Extensions to multiple spins have been considered in Ref. 4, 33–36, but a general strategy for multiple coupled spins was still missing.[35,36] Recently, Garon et al.[37] identified such a general strategy. Subsequently, further approaches to phase-space representations have been developed,[38–43] while rotated parity operators[29,38,40–43] and tomographic techniques[40,42,44,45] became further focal points.

We build in this work on the general Wigner representation for multiple coupled spins introduced in Ref. 37. This Wigner representation is denoted as DROPS representation (discrete representation of operators for spin systems). It is based on mapping operators to a finite set of spherical plots, which are each assembled from linear combinations of spherical harmonics[46] and which are denoted as *droplets* or *droplet functions*.[37] These characteristic droplets preserve crucial symmetries of the quantum system. One particular version of this representation relies on a specific choice of a tensor-operator basis, the so-called LISA basis,[37] which characterizes tensors according to their linearity, their set of involved spins, their permutation symmetries with respect to spin permutations, and their rotation symmetries under rotations that operate uniformly on each spin. These symmetry-adapted tensors can be constructed using explicit projection operators given as elements of the group ring of the symmetric group.[37,47–53] We apply this approach to a larger number of coupled spins 1/2 (qubits) and also to two-spin systems with arbitrary spin numbers (qudits).

[a] david.leiner@tum.de
[b] zeier@tum.de
[c] glaser@tum.de

In addition, we implement a second, alternative computational methodology that relies on so-called coefficients of fractional parentage (CFP)[54–60] in order to obtain the symmetry-adapted LISA basis.

Our contribution can also be put into a general context of symmetry-adapted decompositions of tensor operators. Symmetry-adapted (tensor) bases have a very long tradition in physics. Important mathematical contributions were made by Weyl[61–64] and Wigner,[65,66] even though the corresponding group theory was (at least in the beginning) not universally embraced in the physics community (see p. 10-11 in Ref. 67). Building on Ref. 67, Racah[54,68–72] developed tensor-operator methods for the analysis of electron spectra. These tensor methods have been widely studied[57,73–75] and initiated an active exchange between group theory and physics.[50,51,53,63,66,76,77] Moreover, tensor operators (as well as coefficients of fractional parentage) play an important role in applications to atomic and nuclear structure for which an expansive literature exsists.[55,56,58,78–86] In this context, we also mention the work of Listerud et al.[87,88] which partly motivated the approach taken in Ref. 37 and this work.

This paper is structured as follows. In Sec. II, we introduce the symmetry-adapted tensor basis and its mapping to Wigner functions. An overview of the construction process of this tensor basis using either explicit projection operators or fractional parentage coefficients is presented in Sec. III. In Sec. IV, the tensor-operator basis is illustrated for up to six coupled spins 1/2 by examples and applications from quantum information and nuclear magnetic resonance spectroscopy. Coupled two-spin systems with arbitrary spin numbers are treated in Sec. V. The explicit construction of the tensor-operator basis is detailed in Sec. VI. Before we conclude, challenges related to the construction method that relies on explicit projection operators are discussed in Sec. VII. Additional illustrative examples for spins 1/2 are presented in Appendix A and Appendix B lists the employed values of the fractional parentage coefficients.

II. Symmetry-adapted decomposition and visualization of operators of coupled spin systems

We summarize the approach of Ref. 37 (see also Refs. 44 and 45) to visualize operators of coupled spin systems using multiple droplet functions which are chosen according to a suitable symmetry-adapted decomposition of the tensor-operator space. This allows us to also fix the setting and notation for this work. The general idea relies on mapping[57,85] components $T^{(\ell)}_{jm}$ of irreducible tensor operators[65,66,69,89] $T^{(\ell)}_{j}$ to spherical harmonics[46,90] $Y_{jm} = Y_{jm}(\theta,\phi)$. An arbitrary operator A in a coupled spin system can be expanded into linear combinations

$$A = \sum_{\ell} A^{(\ell)} = \sum_{\ell} \sum_{j\in\mathcal{J}(\ell)} \sum_{m=-j}^{j} c^{(\ell)}_{jm} T^{(\ell)}_{jm} \tag{1}$$

of tensor components $T^{(\ell)}_{jm}$ according to rank j and order m with $-j \leq m \leq j$ and suitably chosen labels (or quantum numbers) ℓ, such that the set $\mathcal{J}(\ell)$ of ranks j occurring for each label ℓ does not contain any rank twice. Depending on the chosen labels, certain properties and symmetries of the spin system are emphasized. Each component $A^{(\ell)}$ is now bijectively mapped to a droplet function $f^{(\ell)} = f^{(\ell)}(\theta,\phi)$, which can be decomposed into

$$f^{(\ell)} = \sum_{j\in\mathcal{J}(\ell)} \sum_{m=-j}^{j} c^{(\ell)}_{jm} Y_{jm}, \tag{2}$$

where the coefficients $c^{(\ell)}_{jm}$ in Eqs. (1) and (2) are identical. This approach enables us to represent each operator component $A^{(\ell)}$ by a droplet function $f^{(\ell)}$, which is given by its expansion into spherical harmonics, refer to the example on the r.h.s of Table I. The droplet functions $f^{(\ell)}$ are denoted as *droplets* and the set of all droplets form the full DROPS representation of an arbitrary operator A.

The task to find suitable labels ℓ that allow for a complete decomposition of the tensor-operator space according to Eq. (1) has been widely studied[86,91–93] and is related to the search for a complete set of mutually commuting operators or good quantum numbers.[94] Different possibilities have been discussed in Ref. 37, but here we will focus on the LISA basis,[37] whose labeling scheme is outlined in Tab. I. First, tensor basis operators are subdivided with respect to the cardinality $g \in \{0,1,\ldots,N\}$ of the set of involved spins (i.e. their g-linearity), where N denotes the total number of spins. Second, tensor operators with identical g-linearity are further partitioned according to the explicit set $G \in \binom{\{1,2,\ldots,N\}}{g}$ of involved spins, where $\binom{\{1,2,\ldots,N\}}{g}$ denotes the set of all subsets of $\{1,2,\ldots,N\}$ with cardinality $|G| = g$. For example for $g = 2$ and $N = 4$, we obtain $G \in \{\{1,2\},\{1,3\},\{1,4\},\{2,3\},\{2,4\},\{3,4\}\}$. Third, we further partition with respect to the symmetry type given by a standard Young tableau[50–52,95] $\tau^{[g]}_i$ of size g (and with at most $(2J+1)^2-1 = 4J(J+1)$ rows, depending on the spin number J), which results in a decomposition according to symmetries under permutations of the set G. For reference, all potentially occurring symmetry types

TABLE I. Overview of how irreducible tensor operators $T_j^{(\ell)}$ with components $T_{jm}^{(\ell)}$ are partitioned in the LISA basis according to their label ℓ and rank j for the prototypical case of six spins 1/2 (left). For a generic operator with randomly chosen complex matrix elements, the droplet functions $f^{(\ell)}$ are illustrated separately for each label ℓ (right). For all droplet functions, the maximum radii are normalized to one for better visibility. Each label ℓ consists of a number of sublabels: the cardinality g of the set of involved spins (i.e. the g-linearity) and the explicit set G, the symmetry type given by a standard Young tableau $\tau_i^{[g]}$ of size g and, possibly, an *ad hoc* label given by a roman numeral. *Ad hoc* sublabels are necessary for $g = 6$ as otherwise one could not distinguish, for instance, between the doubly occurring rank 2 (in bold) for the symmetry type $\tau_7^{[6]}$. The structure of the partitioning is illustrated on the right for the zero-linear term (Id) and selected linear, bilinear, trilinear, and 6-linear components. Plots for all possible droplet functions are shown in Table II for a system consisting of four spins and in Figs. 10 and 11 for six spins.

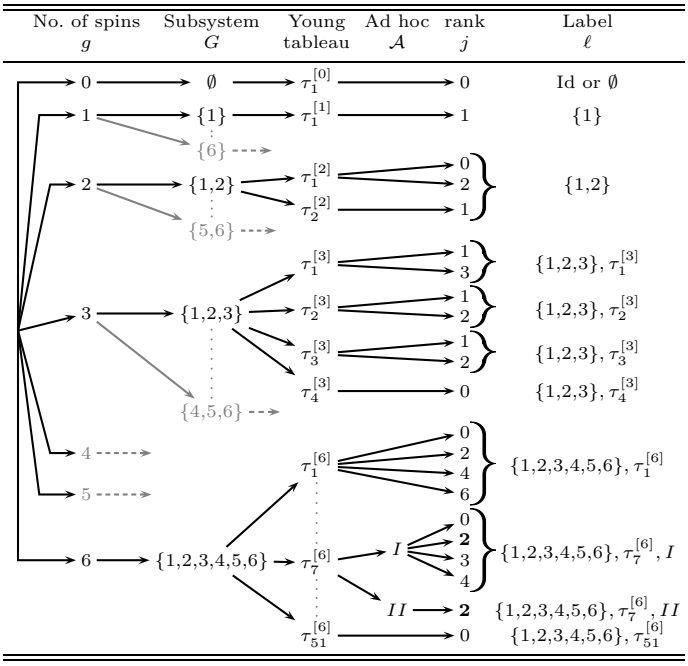

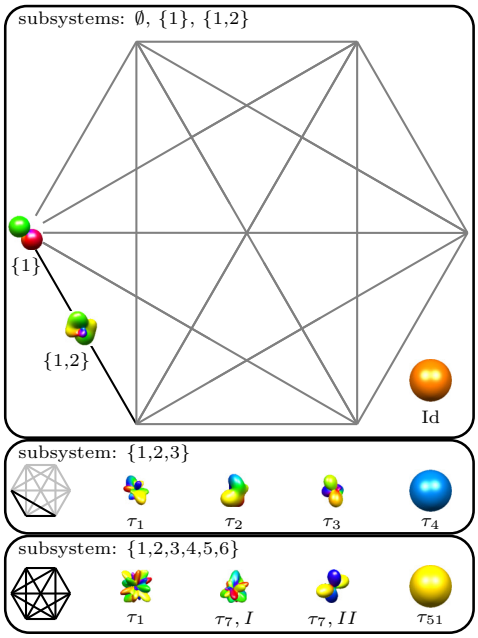

$\tau_i^{[g]}$ for $g \in \{1, 2, 3, 4, 5, 6\}$ are uniquely enumerated and specified according to their index i in Tables II and VI. For $g = 3$ and $G = \{1,2,3\}$ we have the symmetry types

$$\tau_1^{[3]} = \begin{array}{|c|c|c|}\hline 1&2&3\\\hline\end{array},\ \tau_2^{[3]} = \begin{array}{|c|c|}\hline 1&2\\\hline 3\\\cline{1-1}\end{array},\ \tau_3^{[3]} = \begin{array}{|c|c|}\hline 1&3\\\hline 2\\\cline{1-1}\end{array},\ \tau_4^{[3]} = \begin{array}{|c|}\hline 1\\\hline 2\\\hline 3\\\hline\end{array}, \tag{3}$$

and equivalent symmetry types arise for all the other sets $G \in \binom{\{1,2,\ldots,N\}}{3}$ of involved spins with $|G| = g = 3$. Fourth, an *ad hoc* sublabel $\mathcal{A}$ given by a roman numeral is used to distinguish between cases if the same rank occurs more than one.[60,96] For $g = 6$ and the symmetry type $\tau_7^{[6]}$, the rank of $j = 2$ (as shown in bold on the l.h.s. of Table I) would occur twice if these cases would have not been distinguished by the *ad hoc* sublabels I and II. In summary, our labeling scheme for the LISA basis is given by $\ell := (G, \tau^{[g]}, \mathcal{A})$. We often suppress redundant sublabels. As discussed in more detail in Sec. V, for systems containing spins with spin numbers larger than 1/2, the decomposition structure is considerably simplified by additional parent sublabels $\mathcal{P}$.

III. Summary of the computational techniques used to construct the LISA basis

In this section, we provide an overview how to explicitly construct the LISA basis, which has been introduced in Sec. II. We focus on spin systems where each spin has the same spin number $J \in \{1/2, 1, 3/2, \ldots\}$. The LISA basis is a symmetry-adapted basis according to symmetries under simultaneous SU(2) rotations of spins as well as under spin permutations. As discussed in Sec. II, these symmetries of a tensor operator $T_{jm}^{(G,\tau^{[g]},\mathcal{A})}$ are specified by the rank j and order m as well as the symmetry type $\tau^{[g]}$. We start by discussing the simple cases of zero and one spins and explain how to use the Clebsch-Gordan decomposition[66,89,97,98] to symmetrize tensors according to SU(2) symmetries

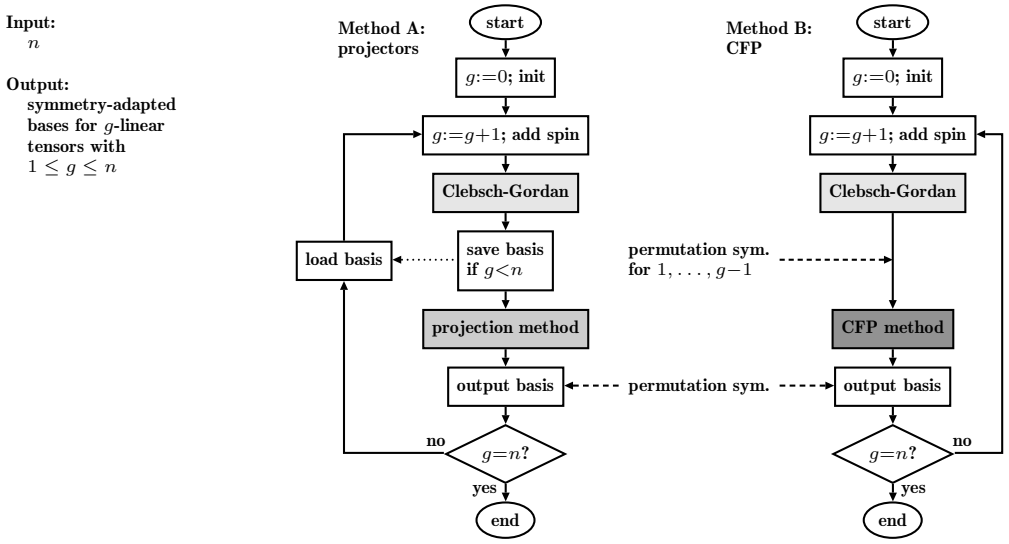

FIG. 1. Flow charts for methods A and B used to iteratively construct g-linear tensors for $g \in \{1,\ldots,n\}$. Both methods rely first on a Clebsch-Gordan decomposition to symmetrize tensors according to SU(2) symmetries after adding an additional spin. In a second step, Method A applies projection operators to symmetrize the tensors with respect to permutations. Method B uses a basis change according to fractional parentage coefficients (CFP), in order to completely permutation symmetrize the tensors, which already have been partially symmetrized with respect to the first $g-1$ spins in the previous iteration.

when a new spin is added to a spin system. This is the first step of the iterative construction, which is schematically illustrated in Fig. 1. Depending on the spin system, in the second step two alternative methods (denoted A and B) are used for the symmetrizing with respect to spin permutations. Method A relies on explicit projection operators[50–53,99] and symmetrizes all g-linear tensors in one step. Method B uses a basis change according to fractional parentage coefficients[54–60] (CFP) and iteratively symmetrizes g-linear tensors with respect to spin permutations, which in the previous iteration have already been partially symmetrized with respect to the first $g-1$ spins. We close this section by discussing sign conventions and how to embed g-linear tensors into larger spin systems. Further details are deferred to Sec. VI.

For zero-linear tensors (i.e. $g = 0$), we have the tensor operator $T_0^{[0]}$ with the single component $T_{00}^{[0]}$. We use the notation $T_j^{[g]}$ for general g-linear tensors of rank j, but we will often drop the index $[g]$. For the spin number $J = 1/2$, we in particular obtain[3]

$$T_{00}^{[0]} = T_{00} = \frac{1}{\sqrt{2}} \begin{pmatrix} 1 & 0 \\ 0 & 1 \end{pmatrix}. \tag{4}$$

For linear tensors and spin number $J = 1/2$ (i.e. qubits), we have the three components[3]

$$T_{1,-1}^{[1]} = T_{1,-1} = \begin{pmatrix} 0 & 0 \\ 1 & 0 \end{pmatrix},\ T_{10}^{[1]} = T_{10} = \frac{1}{\sqrt{2}} \begin{pmatrix} 1 & 0 \\ 0 & -1 \end{pmatrix},\ T_{11}^{[1]} = T_{11} = \begin{pmatrix} 0 & -1 \\ 0 & 0 \end{pmatrix} \tag{5}$$

of the tensor operator $T_1^{[1]}$. For a general spin number J (i.e. qudits), all tensor operators ${}^J T_j^{[1]} = {}^J T_j$ with $j \in \{1,\ldots,2J\}$ are present. Their tensor operator components ${}^J T_{jm}$ with $m \in \{-j,\ldots,j\}$ are given as (see, e.g., Refs. 27, 89, and 100)

$$\left[{}^J T_{jm}\right]_{m_1 m_2} = \sqrt{\tfrac{2j+1}{2J+1}} C^{Jm_1}_{Jm_2 jm} = (-1)^{J-m_2} C^{jm}_{Jm_1 J,-m_2} \tag{6}$$

in terms of Clebsch-Gordan coefficients[66,89,97,98] where $m_1, m_2 \in \{J,\ldots,-J\}$. Clebsch-Gordan coefficients are the expansion coefficients of a (coupled) total angular momentum eigenbasis in an (uncoupled) tensor product basis. We note that the Clebsch-Gordan coefficients in Eq. (6) describe the (tensor-product) combination of pure states into a density matrix $|\psi_1\rangle\langle\psi_2| = |\psi_1\rangle \otimes \langle\psi_2|$ of a single spin. Tables for the Clebsch-Gordan coefficients can be found in literature[98] and there also exist several methods for their computation including recursion relations and explicit formulas.[66,89,101,102]

After adding an additional spin, a basis change according to Clebsch-Gordan coefficients[66,89,97,98] is applied in both methods A and B (see Fig. 1). The Clebsch-Gordon decomposition[66,89,97,98] describes how a tensor product of two irreducible representations is expanded into a direct sum of irreducible representations: the tensor product of two tensor operators T_{j_1} and T_{j_2} with ranks j_1 and j_2 are split up according to

$$T_{j_1} \otimes T_{j_2} = \bigoplus_{j=|j_1-j_2|}^{j_1+j_2} T_j. \tag{7}$$

The $2j+1$ tensor components T_{jm} with $m \in \{-j, \ldots, j\}$ of each tensor T_j on the r.h.s. of Eq. (7) are given by

$$T_{jm} = \sum_{j=|j_1-j_2|}^{j_1+j_2} \sum_{m=m_1+m_2} C^{jm}_{j_1 m_1 j_2 m_2} \, T_{j_1 m_1} \otimes T_{j_2 m_2} \tag{8}$$

via the Clebsch-Gordon coefficients[66,89,97,98] $C^{jm}_{j_1 m_1 j_2 m_2}$. Here, the Clebsch-Gordan coefficients in Eq. (8) describe how tensor operators for $g-1$ spins are combined with the ones for a single spin into tensor operators for g spins. In the case of spins 1/2, tensor operators T_{j_1} obtained from the last iteration are combined with the tensor operator $T_{j_2} = T_1$ (see Eqs. (7) and (8)). For higher spin numbers J, the tensor operator T_{j_2} is substituted by the direct sum $\oplus_{q=1}^{2J} T_q$. More concretely, a $(g-1)$-spin system is joined with a single spin J, which results in a g-spin system such that a $(g-1)$-linear tensor T_{j_1} generates a set of g-linear tensors T_j:

$$T_{j_1} \otimes \left(\bigoplus_{q=1}^{2J} T_q \right) = \bigoplus_{q=1}^{2J} \bigoplus_{j=|j_1-q|}^{j_1+q} T_j. \tag{9}$$

The corresponding g-linear tensor components T_{jm} with $m = m_1 + k$ and $k \in \{-q, \ldots, q\}$ are determined from the tensor components $T_{j_1 m_1}$ and T_{qk} via Clebsch-Gordan coefficients as detailed in Eq. (8). After the Clebsch-Gordan basis change, either method A or B is used for the symmetrization with respect to spin permutations. Details are treated in Sec. VI.

The discussed g-linear tensor operator components T_{jm} of a rank j and degree m are only defined up to a phase. We employ the Condon-Shortley phase convention[66,67,89] $T_{jm} = (-1)^m T^\dagger_{jm}$ that restricts the phase freedom to a freedom of choosing an arbitrary sign for each rank j. In order to uniquely specify the tensor operators, we fix these sign factors as detailed in Sec. VI C. Finally, the g-linear tensor operators are embedded into various N-spin systems via $N-g$ tensor products with suitably positioned tensor operators ${}^J T^\emptyset_{00}$, which are proportional to identity matrices. For each N-spin system, the g-linear tensor operators are embedded according to the $\binom{N}{g}$ available subsets $G \in \binom{\{1,\ldots,N\}}{g}$. For example, we denote by $T^\emptyset_{00}$ the embedded variant of the zero-linear tensor operator component $T^{[0]}_{00}$ and the linear tensor operators $T^{[1]}_j$ result in the embedded tensor operator T^G_j for each single-element set $G \in \{\{1\}, \{2\}, \ldots, \{N\}\}$ of involved spins.

IV. Examples and applications for multiple spins 1/2

In this section, we present examples and applications for multiple spins 1/2 and thereby illustrate and motivate our visualization approach. We focus on four and more spins 1/2, as examples for the case of up to three spins 1/2 have already been discussed in Ref. 37. Building on the general outline given in Sec. II, we start by discussing the labels and their structure for four spins 1/2.

The left part of Table II describes the decomposition of the tensor space. For each subsystem size g, we list the potentially occurring partitions[50–52,95] λ and the associated tableaux $\tau^{[g]}_i$, which are given together with their quantity and index. Also, for each λ we state the appearing tensor ranks j. The bilinear tensors for a fixed subsystem $G \in \binom{\{1,\ldots,4\}}{2}$ are combined into a single droplet function, which is possible as the relevant ranks 0, 2, and 1 do not contain any repetition. Note that for $g = 4$, the partition [1,1,1,1] and its tableau $\tau^{[6]}_{10}$ do not correspond to any rank j (indicated by "-" at the bottom of the last column of the table at the left side of Tab. II). For each of the possible subsystems $G \in \binom{\{1,\ldots,4\}}{g}$, we have in total one label for the zero-linear tensor, one label for linear tensors, one label for bilinear tensors, four labels for trilinear tensors, and nine labels for four-linear tensors. This labeling structure for a system of four spins 1/2 is reflected on the right of Table II, where a 16×16 complex random matrix is visualized using multiple droplet functions. The upper left panel on the right of Table II highlights the topology of

TABLE II. Decomposition structure of four coupled spins 1/2 into linearity g, tableau $\tau_i^{[g]}$ (or simply τ_i for fixed g), and ranks j (left). For each subsystem $G \in \binom{\{1,..,4\}}{2}$, the *bilinear* tensors corresponding to different tableaux are assembled in a single droplet function and hence the label ℓ of bilinear droplets does not contain a sublabel corresponding to a specific tableau $\tau_i^{[4]}$. The permutation symmetry corresponding to tableau $\tau_{10}^{[4]}$ does not appear in the four-spin-1/2 system, i.e. no rank j exists, which is indicated by "-" at the bottom of the last column. On the right side, all droplet functions visualize together a complex random matrix. For each linearity g multiple subsystems $G \in \binom{\{1,..,4\}}{g}$ occur.

g	Partition λ	No. of $\tau_i^{[g]}$	Indices i	Tableaux $\tau_i^{[g]}$	Ranks j
1	[1]	1	1	1	1
2	[2]	1	1	1 2	{0,2
	[1,1]	1	2	1 / 2	1}
3	[3]	1	1	1 2 3	1,3
	[2,1]	2	2,3	1 2 / 3 , 1 3 / 2	1,2
	[1,1,1]	1	4	1 / 2 / 3	0
4	[4]	1	1	1 2 3 4	0,2,4
	[3,1]	3	2,3,4	1 2 3 / 4 , 1 2 4 / 3 , 1 3 4 / 2	1,2,3
	[2,2]	2	5,6	1 2 / 3 4 , 1 3 / 2 4	0,2
	[2,1,1]	3	7,8,9	1 2 / 3 / 4 , 1 3 / 2 / 4 , 1 4 / 2 / 3	1
	[1,1,1,1]	1	10	1 / 2 / 3 / 4	–

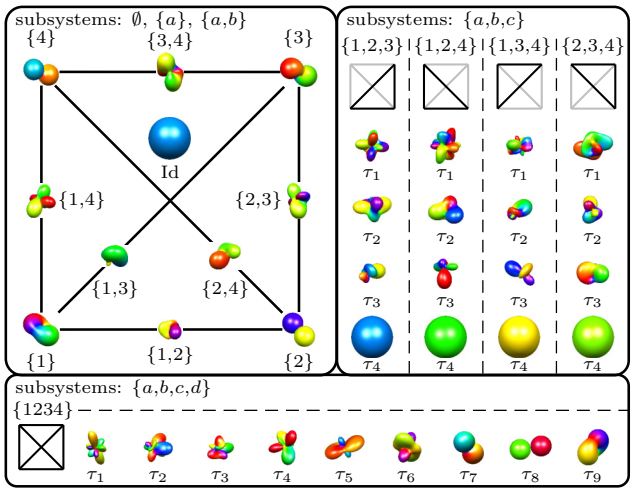

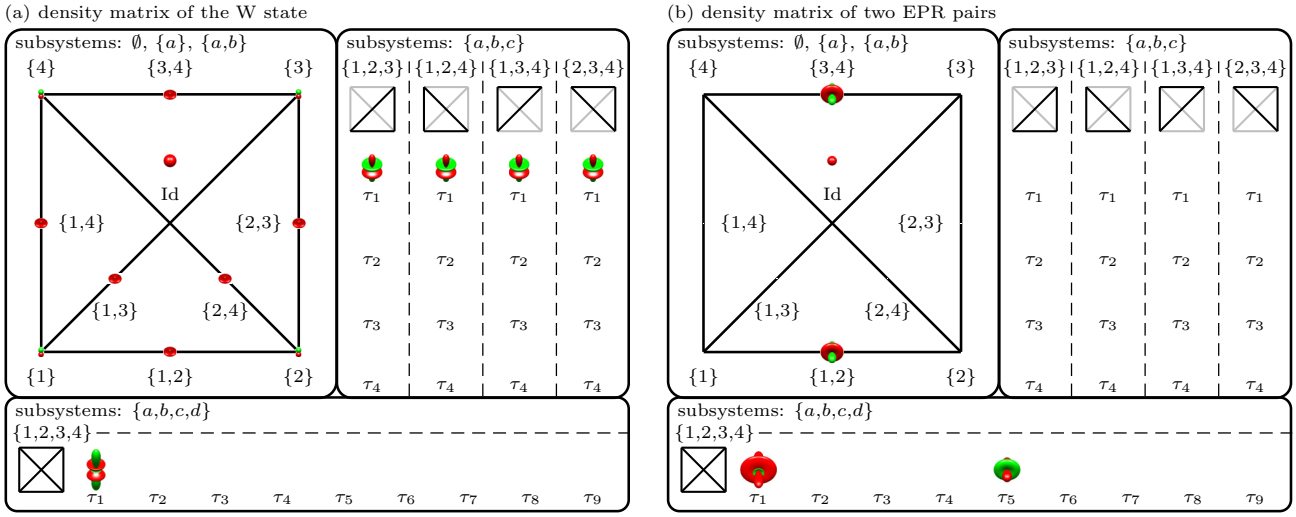

FIG. 2. (a) Visualizations of the density matrix $|W\rangle\langle W|$ of the four-qubit W state $|W\rangle$, the droplet function for the subsystem {1,2,3,4} is scaled to 2/3 of its original size. (b) Visualizations of the density matrix $|\psi\rangle\langle\psi|$ of two EPR pairs $|\psi\rangle = (|0000\rangle + |1111\rangle + |0011\rangle + |1100\rangle)/2$ (between spins 1 and 2 as well as 3 and 4).

the spin system, where nodes represent single spins 1/2 and edges correspond to bilinear tensors. Each droplet $f^{(\ell)}$ is arranged according to its label ℓ. The visualization of the zero-linear tensor is labeled by $\ell = \mathrm{Id}$, linear tensors by their subsystem $\ell = \{a\}$ for $a \in \{1,..,4\}$, and bilinear tensors also by their subsystem $\ell = \{a,b\}$ for $a, b \in \{1,..,4\}$ with $a < b$, i.e., $\ell \in \{\{1,2\},\{1,3\},\{1,4\},\{2,3\},\{2,4\},\{3,4\}\}$. We use $\ell = (G, \tau_i^{[g]})$ for $3 \leq g \leq 4$, which explicitly specifies the tableau $\tau_i^{[g]}$. On the right of Table II, we also see the labels given by the four tableaux $\tau_i^{[3]}$ for each of the trilinear subsystems $G \in \{\{1,2,3\},\{1,2,4\},\{1,3,4\},\{2,3,4\}\}$, where the edges between involved spins are indicated by bold black lines whereas edges to non-involved spins are grayed out. In the four-linear subsystem {1,2,3,4}, non-zero droplet functions can only occur for the nine tableaux $\tau_1^{[4]}$-$\tau_9^{[4]}$. Hence in a system consisting of four spins 1/2, the information contained in an arbitrary operator (consisting of $(2^4)^2 = 256$ complex matrix elements) is represented by

36 droplet functions, which have the correct transformation properties under non-selective rotations and which are organized according to the subset G of involved spins and the type of permutation symmetry specified by a Young tableau $\tau_i^{[g]}$.

The cases of $g = 5$ and $g = 6$ are detailed in Table VI and visualizations of a complex random matrix for systems consisting of five and six spins 1/2 are shown in Figs. 9 and 10 of Appendix A 3, respectively. For subsystem sizes $g \geq 6$, in addition to the set G of involved spins and the Young tabeleau $\tau_i^{[g]}$, the label ℓ for a given droplet function may also include an additional *ad hoc* sublabel $\mathcal{A}$, resulting in $\ell = (G, \tau_i^{[g]}, \mathcal{A})$.

Next, two examples illustrate how inherent symmetries of density matrices are made apparent in our visualization approach. We consider two entangled pure states[103–105] in a four-qubit system (i.e. a system consisting of four spins 1/2), where the corresponding density matrices are highlighted in Fig. 2 following exactly the prototype in Table II. The first example is shown in Fig. 2(a), which represents the density matrix $|W\rangle\langle W|$ of the four-qubit W state[103,104] $|W\rangle = (|0001\rangle + |0010\rangle + |0100\rangle + |1000\rangle)/2$, which is also known as a Dicke state.[106,107] The highly symmetric structure of $|W\rangle\langle W|$ is clearly visible in Fig. 2(a). All droplet functions for different subsystems G of a given linearity g have an identical shape. Also, only the fully permutation symmetric tensors corresponding to the tableaux $\tau_1^{[2]}$, $\tau_1^{[3]}$, and $\tau_1^{[4]}$ appear. In total, only 16 droplet functions are nonzero. This is reflected by the tensor decomposition

$$
\begin{aligned}
|W\rangle\langle W| = T_{00}^{\mathrm{Id}} - \tfrac{1}{2}\sum_{k=1}^{4} T_{10}^{\{k\}} + \left(\sum_{\{k,l\}\in G_2} \tfrac{1}{\sqrt{3}} T_{00}^{\{k,l\}} - \tfrac{1}{\sqrt{6}} T_{20}^{\{k,l\}} \right) \\
+ \left(\sum_{\{k,l,m\}\in G_3} -\tfrac{3}{\sqrt{60}} T_{10}^{(\{k,l,m\},\tau_1^{[3]})} + \tfrac{4}{\sqrt{10}} T_{30}^{(\{k,l,m\},\tau_1^{[3]})} \right) + \left(\tfrac{2}{\sqrt{20}} T_{00}^{\tau_1^{[4]}} - \tfrac{1}{\sqrt{7}} T_{20}^{\tau_1^{[4]}} - \tfrac{16}{\sqrt{70}} T_{40}^{\tau_1^{[4]}} \right)
\end{aligned}
$$

with $G_2 = \{\{1,2\},\{1,3\},\{1,4\},\{2,3\},\{2,4\},\{3,4\}\}$ and $G_3 = \{\{1,2,3\},\{1,2,4\},\{1,3,4\},\{2,3,4\}\}$.

The second example is given by the density matrix $|\psi\rangle\langle\psi|$ of two EPR pairs[105] $|\psi\rangle = (|0000\rangle + |1111\rangle + |0011\rangle + |1100\rangle)/2$ and is illustrated in Fig. 2(b). Again, the symmetry structure of $|\psi\rangle\langle\psi|$ is readily visible. In this case, linear and trilinear droplet functions are completely absent. For the bilinear droplet functions, only the ones corresponding to the subsystems $\{1,2\}$ and $\{3,4\}$ are nonzero as the qubits 1 and 2 as well as 3 and 4 form the EPR pairs. In the second example, we obtain the tensor decomposition

$$
\begin{aligned}
|\psi\rangle\langle\psi| = T_{00}^{\mathrm{Id}} + \left(\tfrac{1}{\sqrt{3}} T_{00}^{\{1,2\}} + T_{2,-2}^{\{1,2\}} + \tfrac{2}{\sqrt{6}} T_{20}^{\{1,2\}} + T_{2,2}^{\{1,2\}} \right) + \left(\tfrac{1}{\sqrt{3}} T_{00}^{\{3,4\}} + T_{2,-2}^{\{3,4\}} + \tfrac{2}{\sqrt{6}} T_{20}^{\{3,4\}} + T_{2,2}^{\{3,4\}} \right) \\
+ \left[\tfrac{7}{\sqrt{45}} T_{00}^{\tau_1^{[4]}} + \tfrac{2}{\sqrt{63}} T_{20}^{\tau_1^{[4]}} + \tfrac{6}{\sqrt{70}} T_{40}^{\tau_1^{[4]}} + \tfrac{2}{\sqrt{42}} \left(\sqrt{6} T_{4,-2}^{\tau_1^{[4]}} + T_{2,-2}^{\tau_1^{[4]}} + T_{22}^{\tau_1^{[4]}} + \sqrt{6} T_{4,2}^{\tau_1^{[4]}} \right) + T_{4,-4}^{\tau_1^{[4]}} + T_{44}^{\tau_1^{[4]}} \right] \\
- \left[\tfrac{2}{3} T_{00}^{\tau_5^{[4]}} + \tfrac{4}{\sqrt{18}} T_{20}^{\tau_5^{[4]}} + \tfrac{2}{\sqrt{3}} \left(T_{2,-2}^{\tau_5^{[4]}} + T_{22}^{\tau_5^{[4]}} \right) \right],
\end{aligned}
$$

which explains the occurrence of four-linear components in Fig. 2(b) even though the state $|\psi\rangle$ is a product state and has no four-particle contributions as a *pure* state. This emphasizes the fact that the DROPS visualization does not (directly) depict the symmetries of a pure state $|\psi\rangle$ but of the corresponding density-matrix $|\psi\rangle\langle\psi|$.

The last example in this section illustrates the value of the DROPS visualization for analyzing the dynamics of controlled quantum systems.[110] This enables us to analyze the effect of control schemes by illustrating the droplets and their symmetries appearing during the time evolution. A free simulation package[111,112] is available, which can be used to simulate systems consisting of up to three spins 1/2. In the context of nuclear magnetic resonance spectroscopy, we consider the creation of maximum-quantum coherence in an Ising chain of four spins 1/2 (see Fig. 3), which is based on a $\pi/2$ excitation pulse followed by a series of delays and $\pi/2$ pulses.[108] An operator A_p has a defined coherence order[3] p if a rotation around the z axis by any angle α generates the same operator A_p up to a phase factor $\exp(-ip\alpha)$, i.e., $\exp(-i\alpha\sum_{k=1}^{N} I_{kz}) A_p \exp(i\alpha\sum_{k=1}^{N} I_{kz}) = A_p \exp(-ip\alpha)$. Recall that Cartesian operators for single spins are $I_x := \sigma_x/2$, $I_y := \sigma_y/2$, and $I_z := \sigma_z/2$, where the Pauli matrices are $\sigma_x = \left(\begin{smallmatrix} 0 & 1 \\ 1 & 0 \end{smallmatrix}\right)$, $\sigma_y = \left(\begin{smallmatrix} 0 & -i \\ i & 0 \end{smallmatrix}\right)$, and $\sigma_z = \left(\begin{smallmatrix} 1 & 0 \\ 0 & -1 \end{smallmatrix}\right)$. For n spins, one has the operators $I_{k\eta} := \bigotimes_{s=1}^{n} I_{a_s}$ where a_s is equal to η for $s{=}k$ and is zero otherwise; note $I_0 := \left(\begin{smallmatrix} 1 & 0 \\ 0 & 1 \end{smallmatrix}\right)$. All tensor-operator components T_{jm} have the unique coherence order $p = m$. The Cartesian product operator I_{kx}, which corresponds to observable transverse magnetization, contains coherence order $p = \pm 1$ and a triple-quantum coherence state is a linear combination of tensor operators with rank $j \geq 3$ and order $m = \pm 3$. The maximal coherence order is limited by the number of spins and thus by the maximal rank j of tensors. Note that a droplet $f^{(\ell)}$ representing an operator A_p with coherence order p exhibits the same rotation properties as A_p. That is $f^{(\ell)}$ is reproduced up to a phase factor $\exp(-ip\alpha)$ if $f^{(\ell)}$ is rotated around the z axis by α, refer also to Fig. 7. The experiment considered in Ref. 108 generates maximal quantum coherence states starting from the

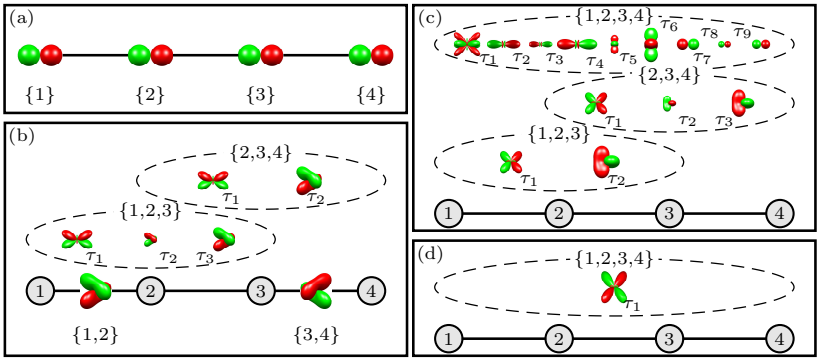

FIG. 3. Generation of a completely symmetric four-linear state in a chain of four spins 1/2 following Table S2 in Ref. 108. Starting from $\rho_0 = \sum_{k=1}^{4} I_{kz}$ a $[\pi/2]_y$ pulse on each spin results in (a), the evolution under coupling with time $t = 1/(2\mathrm{J})$ followed by a $[\pi/2]_y$ pulse on each spin is repeating three times and visualized at various stages (b)-(d). The droplet function in (d) is scaled to 1/3 of its original size. Linear and bilinear droplet functions are plotted on the nodes (i.e. spins) and edges (i.e. couplings), respectively. General g-linear components are indicated by dashed ellipses.[109]

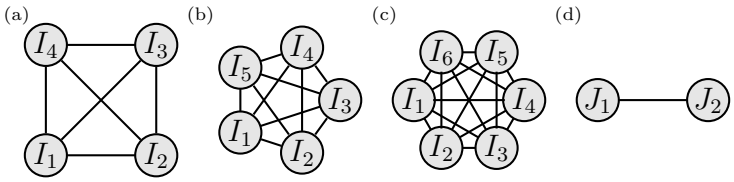

FIG. 4. Interaction structure of visualized spin systems (nodes represent spins): (a)-(c) systems with $N \in \{4, 5, 6\}$ spins 1/2 (see Sec. IV), (d) two spins with arbitrary spin numbers J_1 and J_2 as discussed in Sec. V.

initial state $\rho_0 = \sum_{k=1}^{4} I_{kz}$, which is specified using the Cartesian product operators I_{kz}. All coupling constants in the drift (or system) Hamiltonian are assumed to be equal, i.e., $\mathrm{J} = \mathrm{J}_{12} = \mathrm{J}_{23} = \mathrm{J}_{34}$. In a first step, a $[\pi/2]_y$ pulse is applied on each spin. Then, a transfer block consisting of an evolution under the coupling with coupling period $t = 1/(2\mathrm{J})$ followed by a $[\pi/2]_y$ pulse on each spin is repeated three times. The panels in Fig. 3 show the state of the spin system for different points in time: Panel (a) represents the initial state $\rho_0 = \sum_{k=1}^{4} I_{kz}$ after a $\pi/2$ pulse with phase y is applied to each spin. Panels (b), (c), and (d) depict the state after one, two, and three repetitions of the transfer block, respectively. In panel (d), the initial state has been fully transferred to a single 4-linear droplet function corresponding to fully permutation-symmetric tensors (as denoted by $\tau_1^{[4]}$), which also contains the desired maximum-coherence orders[108] $p = \pm 4$. A similar example for an Ising chain consisting of five spins 1/2 is shown in Appendix A 2 [refer to Fig. 8(a1)-(a5)].

Additional examples and applications of the DROPS visualization are illustrated in Appendix A. In Fig. 4(a)-(c), general systems consisting of four to six spins 1/2 are schematically represented as complete graphs. In the following, we discuss the generalization of the DROPS representation to systems consisting of two, see Fig. 4(d), or more spins with arbitrary spin numbers.

V. Representation of systems consisting of spins with arbitrary spin numbers

Building on our description in Sec. II, we now consider the case of two coupled spins with arbitrary spin numbers. Even though spins 1/2 (which are also known as qubits) constitute the most important case, spins with higher spin number $J > 1/2$ are highly relevant and widely studied as exemplified by bosonic systems, such as photons and gluons, composite particles as deuterium or helium-4, and quasiparticles such as Cooper pairs or phonons. We start in Sec. V A with the case of two coupled spins with arbitrary but identical spin number J. We extend this case to two coupled spins with different spin numbers $J_1 \neq J_2$ in Sec. V B, which also discusses examples and illustrations for the concrete spin numbers $J_1 = 1/2$ and $J_2 = 1$. Generalizations of our approach to an arbitrary number of coupled spins with arbitrary spin numbers are discussed in Sec. V C.

TABLE III. Multiplicities of ranks j occurring for bilinear tensors in two-spin systems with equal spin numbers $J_1 = J_2 = J$ (left) and different spin numbers $J_1 \neq J_2$ (right).

J	λ	$j=0$	1	2	3	4	5	6	7	8	9	10	11	12	13	14
1/2	[2]	1		1												
	[1,1]		1													
1	[2]	2	1	3	1	1										
	[1,1]		3	1	2											
3/2	[2]	3	2	6	3	4	1	1								
	[1,1]		5	3	5	2	2									
2	[2]	4	3	9	6	8	4	4	1	1						
	[1,1]		7	5	9	5	6	2	2							
5/2	[2]	5	4	12	9	13	8	9	4	4	1	1				
	[1,1]		9	7	13	9	11	6	6	2	2					
3	[2]	6	5	15	12	18	13	15	9	9	4	4	1	1		
	[1,1]		11	9	17	13	17	11	12	6	6	2	2			
7/2	[2]	7	6	18	15	23	18	22	15	16	9	9	4	4	1	1
	[1,1]		13	11	21	17	23	17	19	12	12	6	6	2	2	

J_1	J_2	$j=0$	1	2	3	4	5	6	7	8	9	10	11
1/2	1	1	2	2	1								
1/2	3/2	1	2	3	2	1							
1/2	2	1	2	3	3	2	1						
1/2	5/2	1	2	3	3	3	2	1					
1/2	3	1	2	3	3	3	3	2	1				
1/2	7/2	1	2	3	3	3	3	3	2	1			
1	3/2	2	5	6	5	3	1						
1	2	2	5	7	7	5	3	1					
1	5/2	2	5	7	8	7	5	3	1				
1	3	2	5	7	8	8	7	5	3	1			
1	7/2	2	5	7	8	8	8	7	5	3	1		
3/2	2	3	8	11	11	9	6	3	1				
3/2	5/2	3	8	12	13	12	9	6	3	1			
3/2	3	3	8	12	14	14	12	9	6	3	1		
2	5/2	4	11	16	18	17	14	10	6	3	1		
2	3	4	11	17	20	20	18	14	10	6	3	1	

TABLE IV. Labeling scheme for bilinear tensors of two coupled spins. For $J_1 = J_2 = J$ (left), parent sublabels $\mathcal{P}$ and Young tableaux sublabels $\tau_i^{[g]}$ are used. For $J_1 \neq J_2$ (right), Young tableaux are replaced by *ad hoc* sublabels. Both cases result in $4J_1J_2$ droplet functions.

$\mathcal{P}$	$\tau_i^{[g]}$	j	ℓ $(J_1 = J_2 = J)$
1,1	τ_1	0,2	$\{1,2\},1,1$
	τ_2	1	
2,2	τ_1	0,2,4	$\{1,2\},2,2$
	τ_2	1,3	
⋮		⋮	⋮
$2J$,$2J$	τ_1	0,2,4,..,$2J$	$\{1,2\},2J,2J$
	τ_2	1,3,..,$2J-1$	
1,2	τ_1	1,2,3	$\{1,2\},1,2,\tau_1$
	τ_2	1,2,3	$\{1,2\},1,2,\tau_2$
⋮		⋮	⋮
k,l $(l \neq k)$	τ_1	$\lvert k-l\rvert$,..,$k+l$	$\{1,2\},k,l,\tau_1$
	τ_2	$\lvert k-l\rvert$,..,$k+l$	$\{1,2\},k,l,\tau_2$
⋮		⋮	⋮
$2J-1$,$2J$	τ_1	1,..,$2J-1$	$\{1,2\},2J-1,2J,\tau_1$
	τ_2	1,..,$2J-1$	$\{1,2\},2J-1,2J,\tau_2$

$\mathcal{P}$	$\mathcal{A}$	j	ℓ $(J_1 \neq J_2)$
1,1		0,1,2	$\{1,2\},1,1$
2,2		0,1,2,3,4	$\{1,2\},2,2$
⋮		⋮	
$2J_1, 2J_1$		0,..,$4J_1$	$\{1,2\},2J_1,2J_1$
2,3	I	1,..,5	$\{1,2\},2,3,I$
	II	1,..,5	$\{1,2\},2,3,II$
⋮		⋮	
k,l $(l>k)$	I	$l-k$,..,$l+k$	$\{1,2\},k,l,I$
	II	$l-k$,..,$l+k$	$\{1,2\},k,l,II$
⋮		⋮	
$2J_1-1, 2J_1$	I	1,..,$2J_1-1$	$\{1,2\},2J_1-1,2J_1,I$
	II	1,..,$2J_1-1$	$\{1,2\},2J_1-1,2J_1,II$
$2J_1, 2J_1+1$		1,..,$2J_1+1$	$\{1,2\},2J_1,2J_1+1$
⋮		⋮	
$2J_1, 2J_2$		$2J_1-2J_2$,..,$2J_1+2J_2$	$\{1,2\},2J_1,2J_2$

A. Two coupled spins with equal spin numbers

Recall from Sec. II that the state of a single spin J can be described by $2J+1$ tensor operators T_j with ranks $j \in \{0,\ldots,2J\}$ where each tensor operator T_j has $2j+1$ tensor-operator components $T_{jm} \in \mathbb{C}^{(2J+1)\times(2J+1)}$ with $m \in \{-j,\ldots,j\}$. The rank $j=0$ corresponds to a zero-linear tensor operator and the ranks $1 \leq j \leq 2J$ correspond to linear tensor operators. Compared to the case of spins 1/2, the number and multiplicity of the occurring ranks j in tensor decompositions for multiple spins grow even more rapidly for general spin numbers. This is already appreciable for bilinear tensors of two spins as detailed for different values of $J_1 = J_2 = J$ on the left of Table III, where multiplicities of the occurring ranks are listed separately for the permutation symmetries corresponding to the partitions [2] and [1,1]. Additional sublabels are required to distinguish between multiply appearing ranks j in order

g	G	$\mathcal{P}$	j	ℓ
0	$\emptyset$	0	0	Id
1	{1}	1	1	{1}
	{2}	1 2	1 2	{2}
2	{1,2}	1,1	0,1,2	{1,2},1,1
		1,2	1,2,3	{1,2},1,2

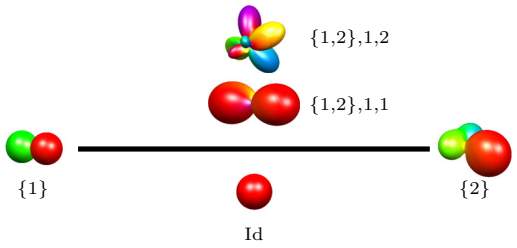

FIG. 5. The labeling scheme for two spins with spin numbers $J_1 = 1/2$ and $J_2 = 1$ results in five groups of tensors (left). The right panel visualizes the corresponding droplet functions for a 6×6-dimensional complex random matrix.

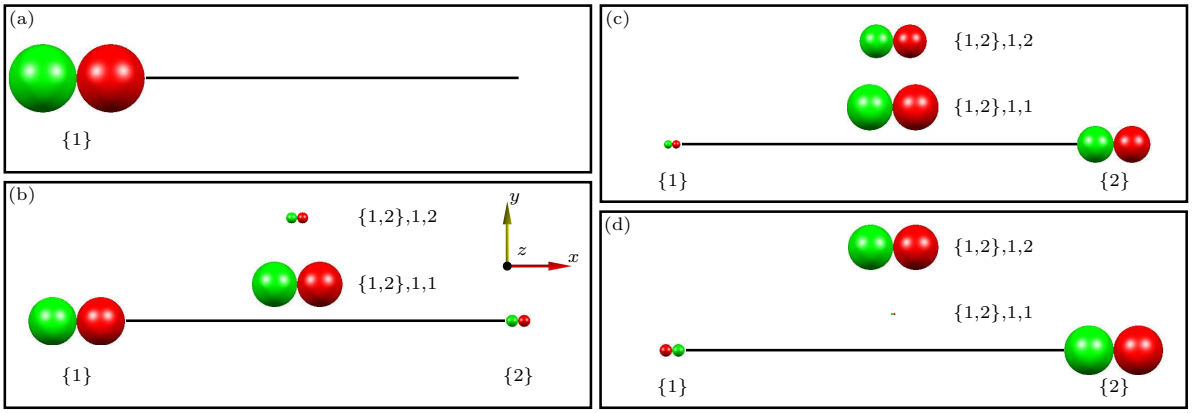

FIG. 6. Visualization of a negative polarization transfer under isotropic mixing conditions in a two-spin system consisting of a spin 1/2 and a spin 1 (see Ref. 113): (a) 0 ms, (b) 10 ms, (c) 20 ms, and (d) 30 ms.

to maintain the bijectivity of the mapping from tensor operators to spherical harmonics following Sec. II.

For two coupled spins, there are zero-linear, linear, and bilinear tensors as given by the different numbers $g \in \{0, 1, 2\}$ of involved spins. The treatment of the cases with $g \in \{0, 1\}$ follows Sec. II. For $g = 0$, the set $G = \emptyset$ of involved spins is empty. The corresponding single zero-linear tensor operator of rank $j = 0$ requires no further partitioning and is given the label $\ell = \mathrm{Id}$. The linear tensors are partitioned according to the set $G \in \{\{1\}, \{2\}\}$ of involved spins, which contains either the first or the second spin. For both cases, $2J$ linear tensor operators with ranks $j \in \{1, 2, \ldots, 2J\}$ are present and no rank appears twice. This ensures that no additional sublabels are necessary and the labels $\ell = \{1\}$ and $\ell = \{2\}$ can be used to uniquely specify the linear tensor operators. So far, the tensor operators corresponding to the labels $\ell \in \{\mathrm{Id}, \{1\}, \{2\}\}$ result jointly in three droplet functions.

For bilinear tensors, the occurring ranks j and their multiplicity are detailed on the left of Table III separately for the partitions [2] and [1,1]. Additional sublabels are necessary for $J > 1/2$ to uniquely distinguish the appearing tensor operators. This is also true after the sublabels for permutation symmetries given by the partitions [2] and [1,1] (or the related Young tableaux τ_i) have been applied. *Ad hoc* sublabels could be used, but they usually do not correlate with any physical properties of the quantum system. Instead, here we employ so-called parent sublabels (or parents), which are motivated by classical methods.[54–56,58,59,67,69–71,86] Recall that a bilinear tensor operator T_j of rank j is obtained in the Clebsch-Gordon decomposition [see Eq. (7)] from the tensor product of the two linear tensor operators T_{j_1} and T_{j_2}. The ranks j_1 and j_2 (with $j_1 \leq j_2$) form the parent sublabel $\mathcal{P} = (j_1,j_2)$ of T_j. For example, the bilinear tensor operator T_1 appears in the decomposition of $T_1 \otimes T_2$. This results in the parent sublabel (or parents) $\mathcal{P} = (1,2)$ for this bilinear tensor operator T_1, representing the ranks $j_1 = 1$ and $j_2 = 2$ of the linear tensor operators T_1 and T_2. One significant advantage of using parent sublabels is that they naturally arise in the construction of tensor operators. All parents that appear for bilinear tensors of two coupled spins with arbitrary but equal spin number are detailed on the left-hand side of Table IV. The bilinear tensors are grouped according to their parents and their Young tableaux τ_i, which specify permutation symmetries as discussed above. This scheme results in $(2J)^2$ droplet functions representing bilinear tensors. In total, $(2J)^2 + 3$ droplet functions are needed to completely specify the quantum state of two coupled spins with identical spin number J. Recall that for two coupled spins 1/2 (i.e. with $J_1 = J_2 = J = 1/2$), bilinear tensors can be uniquely represented by only one ($(2J)^2 = 1$) droplet function, which is fully specified by the label $\ell = G = \{1, 2\}$, which indicates that it contains operators acting on the first and

second spin. However, for two coupled spins with $J_1 = J_2 = J' = 1$, four ($(2J')^2 = 4$) droplet functions are necessary to represent all bilinear tensors, which obviously are not uniquely specified by the set $G = \{1, 2\}$ of involved spins. Of these four bilinear droplet functions, two function have identical parent ranks ($j_1 = j_2$) and are fully characterized by a label of the form $\ell = (G, \mathcal{P})$: the complete label for $j_1 = j_2 = 1$ is ($\{1,2\}, 1, 1$) and ($\{1,2\}, 2, 2$) for $j_1 = j_2 = 2$. The two remaining bilinear droplet functions have parent ranks $j_1 = 1$ and $j_2 = 2$ but different Young tableaux τ_i. They are fully specified by the labels ($\{1,2\}, 1, 2, \tau_1$) and ($\{1,2\}, 1, 2, \tau_2$), respectively (c.f. fourth column in Table IV).

B. Two coupled spins with different spin numbers

Building on the methodology introduced in Sec. V A, we address in this section the case of two coupled spins with different spin numbers $J_1 \neq J_2$. As before, the appearing bilinear tensor ranks j and their multiplicity grows rapidly as shown on the right of Table III. Zero-linear and linear tensors can be—as before—represented using three droplet functions. In contrast to the case of equal spin numbers, we can no longer rely on permutation symmetries to label bilinear droplet functions, because permuting spins with different spin numbers does not preserve the global structure of the quantum system. This forces us to combine parent sublabels with *ad hoc* sublabels in order to completely subdivide all bilinear tensors. The resulting labeling scheme for bilinear tensors is summarized on the right of Table IV. Overall, $4J_1J_2$ different droplet functions exist for bilinear tensors and arbitrary operators are represented by $4J_1J_2 + 3$ droplet functions.

A concrete example is given in Fig. 5 for the case of two coupled spins with the spin numbers $J_1 = 1/2$ and $J_2 = 1$. The labeling scheme is detailed on left of Fig. 5. One observes the tensor rank of zero for the zero-linear tensors, the linear tensor rank of one for the spin 1/2, and the linear tensor ranks of one and two for the spin 1. The bilinear tensor ranks are given by zero, one, and two for the parent sublabel P = (1,1) as well as one, two, and three for the parent sublabel P = (1,2). The right panel of Fig. 5 shows the corresponding droplet functions, which are arranged according to their labels.

For the same case of one spin 1/2 and one spin 1, we visualize in Fig. 6 the dynamics of quantum states during an isotropic mixing polarization transfer experiment. In this experiment, x polarization of the first spin (represented by droplet {1}), which corresponds to the initial density operator S_{1x}, is transferred via bilinear operators [represented by the droplets ($\{1,2\}, 1, 1$) and ($\{1,2\}, 1, 1$)] to x polarization of the second spin (represented by droplet {2}) under the effective isotropic mixing (Heisenberg) coupling Hamiltonian $H_{\text{iso}} = 2\pi \text{J}_{\text{iso}}(S_{1x}S_{2x} + S_{1y}S_{2y} + S_{1z}S_{2z})$.[113] The operators in this case are defined by $S_{1\eta_1} := I_{\eta_1} \otimes \text{id}_3$ and $S_{2\eta_2} := \text{id}_2 \otimes S_{\eta_2}$, where

$$S_x = \tfrac{1}{\sqrt{2}} \begin{pmatrix} 0 & 1 & 0 \\ 1 & 0 & 1 \\ 0 & 1 & 0 \end{pmatrix}, \quad S_y = \tfrac{1}{\sqrt{2}i} \begin{pmatrix} 0 & 1 & 0 \\ -1 & 0 & 1 \\ 0 & -1 & 0 \end{pmatrix}, \quad \text{and} \quad S_z = \begin{pmatrix} 1 & 0 & 0 \\ 0 & 0 & 0 \\ 0 & 0 & -1 \end{pmatrix}$$

are the spin-1 matrices and id_n denotes the $n \times n$ identity matrix. For a coupling constant J_{iso} of 11 Hz, the four panels in Fig. 6 show DROPS representations of the density matrix after (a) 0 ms, (b) 10 ms, (c) 20 ms, and (d) 30 ms, respectively. The time-dependent x polarization of the first spin is given by the function $T_{1x}(t) = \{11 + 16\cos(3\pi \text{J}_{\text{iso}}\, t)\}/18$, which is negative for t=30 ms. This is visible in panel (d), where the sign of the linear droplet corresponding to the first spin (labeled {1}) is inverted compared to panels (a) to (c): Whereas initially, the positive (red) lobe of the droplet {1} points in the positive x direction, after 30 ms the positive (red) lobe of the droplet {1} points in the negative x direction. The occurrence of polarization with inverted sign in such a simple two-spin system (consisting of a spin 1/2 and a spin 1) is of interest[113] because at least five spins are necessary to achieve negative polarization in isotropic mixing experiments in systems consisting exclusively of spins 1/2.

C. Generalization to an arbitrary number of spins with arbitrary spin numbers

We discuss now how parent sublabels can be also applied to more than two spins. The most general spin system is composed of an arbitrary number of coupled spins with arbitrary spin numbers J_k. The zero-linear and linear tensors can be described as before. In particular, one has $2J_k$ linear tensors with rank $j \in \{1, \ldots, 2J_k\}$. Bilinear and general g-linear tensors can be initially divided with respect to the set G of involved spins. A g-linear tensor operator T_j is obtained via repeated Clebsch-Gordan decompositions from g linear tensor operators T_{j_k} of rank j_k with $1 \leq k \leq g$. And the parent sublabel $\mathcal{P} = (j_1, j_2, \ldots, j_g)$ of T_j is given by the sequence of ranks. For example, the trilinear tensor operator T_2 is contained in the Clebsch-Gordon decomposition of the tensor product of the three linear tensor operators T_1, T_1, and T_2 and its parent sublabel is given by $\mathcal{P}$ = (1,1,2). Young tableaux specifying permutation symmetries could be at least applied to subsystems with equal spin numbers. Theoretically, *ad hoc* sublabels can always be used to discern between any remaining tensor operators with equal rank. However, the practicability of

this approach, which is related to the scaling of the number of necessary *ad hoc* sublabels, has to be investigated in future work together with the option of subgroup labels.[54–56,58,59,67,69–71,86]

VI. Explicit construction of the symmetry-adapted bases

Here, we present the details for constructing symmetry-adapted bases as outlined in Sec. III. Each tensor operator has to be uniquely identified by a set of sublabels (or quantum numbers). After the space of all tensors has been divided according to their g-linearity and the subsystem G of involved spins, the tensors can be further subdivided with respect to their parents $\mathcal{P}$ (as introduced in Sec. V), their permutation symmetries as given by a Young tableau $\tau^{[g]}$ of size g, and/or necessary *ad hoc* sublabels $\mathcal{A}$ that together with the rank j and order $m \in \{-j, \ldots, j\}$ finally identify a one-dimensional tensor subspace. Some of this information might be redundant or inapplicable in certain cases (as permutation symmetries in the scenario of Sec. V B), and we also do not utilize parent sublabels in spin-1/2 systems. Our explanations start below with the initial construction of zero-linear and linear tensors. In Sec. VI A and Sec. VI B, we then separately describe the iterative construction of g-linear tensor operators (for $g \geq 2$) based on the projection method (denoted as Method A in Sec. III) and on the CFP method relying on fractional parentage coefficients (denoted as Method B in Sec. III). We conclude by explaining the chosen phase convention for DROPS basis tensor operators (see Sec. VI C) and how tensors are embedded into a full N-spin system (see Sec. VI D).

Let us first recall the tensor-operator notation $T^{(G,\mathcal{P},\tau,\mathcal{A})}_{jm}$, which uses the rank j and order m together with all possible sublabels given by the set G of involved spins, the parent sublabel $\mathcal{P}$, the permutation symmetry τ, and the *ad hoc* sublabel $\mathcal{A}$. Below, a superscript $[g]$ is used for each sublabel to indicate a specific linearity g. Before accounting for the embedding in Sec. VI D, the label $G^{[g]}$, is dropped. By default, we assume that for a g-linear term the set of spins consists of the first g spins of the system, i.e. $G^{[g]} = \{1, \ldots, g\}$ for a linearity $g \geq 1$ and $G^{[0]} = \emptyset$.

In the zero-linear case ($g = 0$), the parent sublabel is an empty list $\mathcal{P}^{[0]} = ()$, the tableau sublabel is empty ($\tau^{[0]} = \varnothing$), and the *ad hoc* label is canonically initialized to $\mathcal{A}^{[0]} = I$; also $j^{[0]} = 0$ and $m^{[0]} = 0$. We use the abbreviations T_0 and T_{00} for the tensor operator and its component in the zero-linear case, while emphasizing that their explicit form depends on the spin number J as detailed in Eqs. (4) and (6).

For the case of linear tensors, $\mathcal{P}^{[1]} = (j^{[1]})$ for the rank $j^{[1]}$, $\tau^{[1]} = \boxed{1}$, and $\mathcal{A}^{[1]} = I$. The linear tensor operators and their components can be uniquely identified using the simplified notations T_j and T_{jm} with $j = j^{[1]} \neq 0$. Their explicit form depends again on the spin number J, see Eqs. (5) and (6). After addressing these notational issues and default initializations, we discuss the iterative construction process.

A. Projection method

In the first phase of the projection method, the tensor decomposition from Eq. (9) is iteratively applied in order to construct g-linear tensors from $(g-1)$-linear ones as outlined in Sec. III and Fig. 1. The explicit form of the corresponding tensor components can be computed with the help of Eq. (8) and the knowledge of Clebsch-Gordan coefficients. During this iteration the Young-tableau sublabels are ignored since permutation symmetries are only accounted for in the second and third phase of the projection method. *Ad hoc* sublabels can be suppressed during this phase. The parent sublabels are updated in each iteration by extending the list of parents with that rank $q \in \{1, \ldots, 2J\}$ from the added spin J in Eq. (9) that resulted in the tensor operator under consideration. When Eq. (9) has been repeated sufficiently many times such that the desired linearity g is attained, the first phase of the projection method is completed.

In the second phase of the projection method, we explicitly determine projection operators, which will allow us to project tensor operators (and their components) onto subspaces of well-determined permutation symmetry. We follow the account of Ref. 37 and start by recalling some basic ideas and notations.[50–52,95] A permutation $\sigma \in S_g$ contained in the symmetric group S_g maps elements $i \in G = \{1, \ldots, g\}$ to elements $\sigma(i) \in G$ such that $\sigma(i_1) \neq \sigma(i_2)$ for $i_1 \neq i_2$. The multiplication of two elements $\sigma_2, \sigma_1 \in S_g$ is defined by the composition $(\sigma_2\sigma_1)(i) := (\sigma_2 \circ \sigma_1)(i) = \sigma_2[\sigma_1(i)]$ for $i \in G$. For example, we have (1,2)(1,3) = (1,3,2) using the cycle notation for elements of S_3. Young tableaux are combinatorial objects built from a set of boxes, arranged in left-orientated rows, with the row lengths in non-increasing order. The boxes are filled with the numbers $\{1, 2, \ldots, g\}$ but without repeating any number. A Young tableau is called *standard* if the entries in each row and each column are increasing. The number of boxes a_j in each row j determines a partition $\lambda = [a_1, a_2, \ldots]$, which characterizes the shape of a Young tableau. We use a superscript $[g]$ in a Young tableau $\tau^{[g]}$ in order to clarify the number g of involved spins. The standard Young tableaux for $g \in \{1, 2, 3, 4\}$ are presented in Fig. 2 and $g = 5$ and $g = 6$ are summarized in Tables VI and VII. The set of row-wise permutations $R(\tau)$ of a Young tableau τ is given by all permutations of entries of τ that leave the set of elements in each row of τ fixed. The set of column-wise permutations $C(\tau)$ can be defined similarly. The Young symmetrizer e_τ is an element

of the group ring $\mathbb{R}[S_g]$ of S_g and can then be written for each Young tableau τ as the product

$$e_\tau := f_{\lambda(\tau)}\, H_\tau V_\tau, \tag{10}$$

where $H_\tau = \sum_{\sigma\in R(\tau)} \sigma$, $V_\tau = \sum_{\sigma\in C(\tau)} (-1)^{|\sigma|}\sigma$ and $|\sigma|$ denotes the minimal number of transpositions necessary to write σ as a product thereof. The rational factor $f_{\lambda(\tau)} \in \mathbb{R}$ is equal to the number of standard Young tableaux with the same shape $\lambda(\tau)$ as τ divided by $g!$ and ensures the correct normalization such that $e_\tau e_\tau = e_\tau$; note that $f_\lambda := f_{\lambda(\tau)}$ is fixed by the shape $\lambda(\tau)$ of τ. Next, we determine the projection operators P_p, which are orthogonalized versions of the Young symmetrizers e_{τ_i}. Let us consider the ordered sequence $\tau_r, \ldots, \tau_s$ of all standard Young tableaux of fixed shape, where r denotes the first index in the list and s the last one. The projection operators P_p are defined as

$$P_p = \begin{cases} e_{\tau_p} & \text{if } p = r, \\ f[d\,(a,b) + \varepsilon]P_t & \text{if } p > r. \end{cases} \tag{11}$$

For $r < p \leq s$, the index t and the two boxes $\boxed{a}$ and $\boxed{b}$ (with $b := a + 1$) can be found as follows: There exists $t \in \{r, \ldots, p{-}1\}$ such that the tableau τ_t differs from τ_p only by the position of two boxes $\boxed{a}$ and $\boxed{b}$. The signed axial distance $d \in Z$ from the box $\boxed{a}$ to $\boxed{b}$ in e_{τ_t} is the number of steps from $\boxed{a}$ to $\boxed{b}$ while counting steps down or to the left positively and steps up or to the right negatively. The transposition (a,b) permutes a and b, while ε denotes the identity permutation. The normalization factor $f \in \mathbb{R}$ is chosen such that $P_pP_p = P_p$. We also refer to the example computations in Ref. 37. Note that challenges related to applicability of this orthogonalization procedure (and under which conditions the projection property $P_pP_p = P_p$ holds) are discussed in Sec. VII. This completes the second phase and the projection operator P_p can be used in the third phase.

In the third phase, each projection operator P_p corresponding to a standard Young tableau τ_p is applied to the space of tensor operators. Tensor operators (and their components) are projected onto the tensor subspace, the permutation symmetry of which is defined by τ_p and P_p. In many cases, the tensor components $T^{(\mathcal{P},\tau_p)}_{jm}$ will be uniquely determined by the image of the projection operator P_p, the rank j, the order m, and, possibly, the parent sublabel $\mathcal{P}$. But additional *ad hoc* sublabels $\mathcal{A} \in \{I, II, \ldots\}$ and an *ad hoc* procedure to partition the space of all possible $T^{(\mathcal{P},\tau_p)}_{jm}$ into one-dimensional subspaces identified by $\mathcal{A}$ are necessary in the most general case. It is critical to coordinate the choice of these one-dimensional subspaces for (at least) all projection operators P_p corresponding to Young tableaux τ_p that have the same shape. Therefore, this procedure corresponding to the *ad hoc* sublabels could be applied even before the projection operators. An example where *ad hoc* sublabels are necessary is given by six coupled spins 1/2 (where we do not use parent sublabels) as detailed in Table VI in Appendix A 3.

B. CFP method

We describe in the following how to construct symmetry-adapted bases using a method based on fractional parentage coefficients (CFP).[54–60] We limit our presentation to multiple coupled spins 1/2 and we do not consider any parent sublabels. As explained in Sec. III and Eq. (9), tensors of linearity g are constructed iteratively from the ones with linearity $g{-}1$ in two steps. These two steps can be repeated until the desired linearity has been achieved. In the first step, the Clebsch-Gordan decomposition in Eq. (9) is used to construct g-linear tensors operators $T^{(\tau^{[g-1]},\mathcal{A}^{[g-1]},j^{[g-1]})}_{j^{[g]}}$ from $(g{-}1)$-linear ones $T^{(\tau^{[g-1]},\mathcal{A}^{[g-1]})}_{j^{[g-1]}}$, where the explicit tensor-operator components are again determined using Clebsch-Gordan coefficients and Eq. (8). While executing the Clebsch-Gordan decomposition of Eq. (9), we temporarily record $\tau^{[g-1]}$ and $\mathcal{A}^{[g-1]}$ from the previous generation together with the old rank $j^{[g-1]}$ in the labels of the provisional tensor operators $T^{(\tau^{[g-1]},\mathcal{A}^{[g-1]},j^{[g-1]})}_{j^{[g]}}$. This information is used in the second step below to recombine the provisional tensor operators into their final form and to specify this final form using updated labels. But first, the fractional parentage coefficients and their structure are explained which will finally lead to a characterization of how this second step can be accomplished.

Fractional parentage coefficients can be interpreted as a block-diagonal transformation matrix CFP^g acting on the space of g-linear tensors. This transformation results in g-linear tensor operators that are fully permutation symmetrized assuming that the input tensor operators are permutation symmetrized with respect to the first $g{-}1$ spins. The transformation matrix

$$CFP^g = \bigoplus_{j^{[g]}} CFP^g_{j^{[g]}} = \bigoplus_{j^{[g]}} \bigoplus_{\tau^{[g-1]}} CFP^g_{j^{[g]},\tau^{[g-1]}} \tag{12}$$

can be block-diagonally decomposed according to the rank $j^{[g]}$ of the target tensor operator and the permutation symmetry $\tau^{[g-1]}$ of the initial $(g-1)$-linear tensor operator. In the example of $g = 4$ and $j^{[g]} = 1$, one obtains

$$CFP^4_1 = CFP^4_{1,\ydiagram{3}} \oplus CFP^4_{1,\ydiagram{2,1}} \oplus CFP^4_{1,\ydiagram{2,1}} \oplus CFP^4_{1,\ydiagram{1,1,1}} \tag{13a}$$

$$= \left[\begin{array}{c|c} \ydiagram{3} & 1 \\ \hline \ydiagram{3,1} & 1 \end{array}\right] \oplus \left[\begin{array}{c|cc} \ydiagram{2,1} & 1 & 2 \\ \hline \ydiagram{3,1} & -\sqrt{\frac{5}{8}} & \sqrt{\frac{3}{8}} \\ \ydiagram{2,2} & \sqrt{\frac{3}{8}} & \sqrt{\frac{5}{8}} \end{array}\right] \oplus \left[\begin{array}{c|cc} \ydiagram{2,1} & 1 & 2 \\ \hline \ydiagram{3,1} & -\sqrt{\frac{5}{8}} & \sqrt{\frac{3}{8}} \\ \ydiagram{2,2} & \sqrt{\frac{3}{8}} & \sqrt{\frac{5}{8}} \end{array}\right] \oplus \left[\begin{array}{c|c} \ydiagram{1,1,1} & 0 \\ \hline \ydiagram{2,1,1} & 1 \end{array}\right] \tag{13b}$$

$$= \left[\begin{array}{cc|c|ccccc} & & \tau^{[3]} & \ydiagram{3} & \ydiagram{2,1} & \ydiagram{2,1} & \ydiagram{2,1} & \ydiagram{2,1} & \ydiagram{1,1,1} \\ j^{[4]} & \tau^{[4]} & j^{[3]} & 1 & 1 & 2 & 1 & 2 & 0 \\ \hline 1 & \ydiagram{3,1} & & 1 & & & & & \\ 1 & \ydiagram{3,1} & & & -\sqrt{5/8} & \sqrt{3/8} & & & \\ 1 & \ydiagram{2,2} & & & \sqrt{3/8} & \sqrt{5/8} & & & \\ 1 & \ydiagram{2,1,1} & & & & & -\sqrt{5/8} & \sqrt{3/8} & \\ 1 & \ydiagram{2,1,1} & & & & & \sqrt{3/8} & \sqrt{5/8} & \\ 1 & \ydiagram{2,1,1} & & & & & & & 1 \end{array}\right] \tag{13c}$$

for the transformation matrix resulting in tensor operators of fixed rank $j^{[g]} = 1$ but with varying permutation symmetry $\tau^{[g]}$. We have supplemented the formal decomposition in Eq. (13a) with an explicit description of the column basis for the provisional tensor operators as well as the row basis for the final tensor operators in Eqs. (13b)-(13c). For each block in Eq. (13b), the upper-left corner contains $\tau^{[g-1]}$, the left column enumerates the row basis specified by $\tau^{[g]}$, and the row on the upper right lists the column basis determined by the ranks $j^{[g-1]}$. The associated transformation matrix is located in the lower-right quadrant. Equation (13c) provides essentially the same information. Consequently, one block $CFP^g_{j^{[g]},\tau^{[g-1]}}$ of the transformation matrix CFP^g can be interpreted as the matrix $[CFP^g_{j^{[g]},\tau^{[g-1]}}]_{\tau^{[g]},j^{[g-1]}}$ with row and column indices given by $\tau^{[g]}$ and $j^{[g-1]}$, respectively. A tensor operator

$$T^{(\tau^{[g]})}_{j^{[g]}} = \sum_{j^{[g-1]}} [CFP^g_{j^{[g]},\tau^{[g-1]}}]_{\tau^{[g]},j^{[g-1]}}\ T^{(\tau^{[g-1]},j^{[g-1]})}_{j^{[g]}} \tag{14}$$

of fixed rank $j^{[g]}$ and permutation symmetry $\tau^{[g]}$ is now linearly combined from certain provisional tensor operators $T^{(\tau^{[g-1]},j^{[g-1]})}_{j^{[g]}}$. Note that the value of $\tau^{[g-1]}$ is implicitly determined by $\tau^{[g]}$ (refer also to the next paragraph). In general, Eq. (14) has to be extended to account for potential *ad hoc* sublabels $\mathcal{A}$ by substituting permutation symmetries τ with combinations $(\tau, \mathcal{A})$ of permutation symmetries and *ad hoc* sublabels (and possibly summing over multiple values of $\mathcal{A}^{[g-1]}$). Note that the tensor-operator components $T^{(\tau^{[g]})}_{j^{[g]},m^{[g]}}$ have compared to the tensor operators $T^{(\tau^{[g]})}_{j^{[g]}}$ an additional dimension given by the order $m^{[g]} \in \{-j^{[g]}, \ldots, j^{[g]}\}$. The tensor operator components can be directly computed by extending the transformation matrix $CFP^g_{j^{[g]}}$ to $CFP^g_{j^{[g]}} \otimes \mathrm{id}_{2j^{[g]}+1}$ (where $\mathrm{id}_{2j^{[g]}+1}$ is the identity matrix of dimension $2j^{[g]}+1$) since the fractional parentage coefficients do not depend on the value of the order $m^{[g]}$. In summary, our description of the fractional parentage coefficients provides with Eq. (14) an explicit formula to perform the second step to linearly recombine the provisional tensor operators into their final form.

We close this subsection by further exploring the structure of fractional parentage coefficients. For example, note that one block is repeated in Eq. (13), even though the corresponding row and column bases differ with respect to the appearing permutation symmetries $\tau^{[g]}$ and $\tau^{[g-1]}$ for $CFP^4_{1,\ydiagram{2,1}}$ and $CFP^4_{1,\ydiagram{2,1}}$. The structure of the transformations $CFP^4_{j^{[g]},\tau^{[g-1]}}$ is still completely determined when we substitute the occurring standard Young tableaux τ with partitions $\lambda(\tau)$ given by the shape of τ. The fractional parentage coefficients do *not* explicitly depend on the standard

TABLE V. Sign adjustments, which are multiplied to the g-linear tensors of spins 1/2 that have been obtained using Sec. VI B for up to $g \leq 3$.

g	j =	0		1			2			3
	$\tau_i^{[g]}$ =	τ_1	τ_4	τ_1	τ_2	τ_3	τ_1	τ_2	τ_3	τ_1
0		1								
1				1						
2		-1			-i		1			
3			i	-1	1	1		i	i	1

Young tableaux, but only on their shape. For example, the information in Eq. (13) is equivalent to

$$CFP^4_{1,[3]} \oplus CFP^4_{1,[2,1]} \oplus CFP^4_{1,[1,1,1]} = \left[\begin{array}{c|c} [3] & 1 \\ \hline [3,1] & 1 \end{array}\right] \oplus \left[\begin{array}{c|cc} [2,1] & 1 & 2 \\ \hline [3,1] & -\sqrt{\frac{5}{8}} & \sqrt{\frac{3}{8}} \\ [2,1,1] & \sqrt{\frac{3}{8}} & \sqrt{\frac{5}{8}} \end{array}\right] \oplus \left[\begin{array}{c|c} [1,1,1] & 0 \\ \hline [2,1,1] & 1 \end{array}\right]. \tag{15}$$

One can recover $CFP^4_{1,\boxed{\begin{smallmatrix}1&2\\3\end{smallmatrix}}}$ together with the standard Young tableaux in its row basis from $CFP^4_{1,[2,1]}$. Note that $\tau^{[g]}$ is completely determined by $\tau^{[g-1]}$ and the shape $\lambda(\tau^{[g]})$ of $\tau^{[g]}$. For example, $\tau^{[g]} = \boxed{\begin{smallmatrix}1&2&4\\3\end{smallmatrix}}$ for $\tau^{[g-1]} = \boxed{\begin{smallmatrix}1&2\\3\end{smallmatrix}}$ and $\lambda(\tau^{[g]}) = [3,1]$ as there is only one possibility to add the box $\boxed{4}$ while observing $\lambda(\tau^{[g]}) = [3,1]$. This argument holds in general. The repeated block in Eq. (13) is a consequence of the two possible standard Young tableaux for the partition [2,1]. One might wonder why no standard Young tableaux of shape [2,2] or [1,1,1,1] appear for the rank $j^{[4]} = 1$ in Eq. (13). But these cases are ruled out by a priori arguments[37] leading to left part of Fig. 2, and similar restrictions significantly reduce the appearing cases in general. In this regard, note that $0 \leq j^{[g]} \leq g$. The full dimension of the transformation matrix CFP^g is given by the number of occurring tensor operators. For the examples of systems consisting of three, four, five, and six spins 1/2, the matrices CFP^g have the dimension 7×7, 19×19, 51×51, and 141×141, respectively. The explicit form of the fractional parentage coefficients for up to six spins 1/2 has been extracted from tables in Ref. 60 and is given in Appendix B.

C. Phase and sign convention

The phase and sign of tensor operator components are not uniquely determined by the methods for constructing symmetry-adapted bases and they can be chosen arbitrarily. We follow the convention of Condon and Shortley[67], which fixes the phase up to a sign. We have developed in Ref. 37 criteria to select this sign factor such that droplet functions reflect the properties of the depicted operators: First, droplet functions of Hermitian operators should only feature the colors red and green (for the phases zero and π). Second, droplet functions of identity operators have a positive value that is shown in red. Third, droplet functions of a linear Cartesian operator $I_{n\eta}$ with $\eta \in \{x, y, z\}$ acting on the nth spin are oriented according to its Bloch vector representation. Fourth, the droplet function of a fully permutation-symmetric Cartesian operator $\bigotimes_n I_{n\eta}$ with $\eta \in \{x, y, z\}$, has an elongated shape, and its positive lobe points in the direction of η. Fifth, raising and lowering operators are visualized by donut-shaped and rainbow-colored droplet functions. The number of rainbows directly reflects the coherence order and the color transition of the raising operator is inverted when compared to the one of the lowering operator. Finally, droplet functions of coupling Hamiltonians $2I_{1x}I_{2y} + 2I_{1y}I_{2x}$ exhibit a planar shape. This motivates the sign adjustments in Table V for $g \leq 3$, which are multiplied to g-linear tensors of spins 1/2 that have been obtained using the fractional-parentage approach in Sec. VI B. This convention is consistent with the one used for three spins 1/2 in Ref. 37. The phase factors for tensors with $g > 3$ and rank j can be obtained via the formula $\exp[i\pi(g-j)/2]$. In the following, we assume that the phase factors of tensors have been adjusted according to these rules.

D. Embedding tensors into the full N-spin system

Let us finally explain how to embed g-linear tensors into a full N-spin system. We consider g-linear tensor-operator components $T^{[g]}_{jm}$ where additional sublabels such as parent sublabels $\mathcal{P}$, permutation symmetries τ, and sublabels $\mathcal{A}$

have been suppressed for simplicity. We also assume that the nth spin has spin number J_n. For $g = 0$, the zero-linear tensor component $T^{[0]}_{00}$ is mapped to the embedded tensor operator component $T^{\emptyset}_{00} := \otimes_{n=1}^{N} {}^{J_n}T_{00}$. For $g > 0$, we assume that the set of involved spins is given by $G = \{b_1, \ldots, b_g\}$ where $b_p < b_q$ for $p < q$. This enables us to define the permutation $\zeta := (1,b_1) \cdots (g,b_g)$ while adopting the convention that $(p,p) := \varepsilon$ denotes the identity permutation. The g-linear tensor-operator components $T^{[g]}_{jm}$ are transformed into their embedded counterparts T^{G}_{jm} relative to the set G of involved spins using the definition

$$T^{G}_{jm} := \zeta \cdot \left[T^{[g]}_{jm} \otimes \left(\bigotimes_{n=g+1}^{N} {}^{J_{\zeta(n)}}T_{00} \right) \right], \tag{16}$$

where ζ acts by permuting the tensor factors. We assume that $T^{[g]}_{jm}$ fits to the spins and their spin number into which it is embedded. For $N = 3$ and $G = \{2, 3\}$, one obtains the example of $\zeta = (1,2)(2,3) = (1,2,3)$ and

$$T^{\{2,3\}}_{jm} = \zeta \cdot \left(T^{[2]}_{jm} \otimes {}^{J_1}T_{00} \right). \tag{17}$$

VII. Discussion and open problems related to the projection method for more than four spins 1/2

In this section, we discuss challenges related to the projection method which appear for more than five spins 1/2. For up to six spins 1/2, we have verified that the projectors $P_{\tau_i} = P_i$ that have been computed using the method explained in Sec. VI A are in *almost* all cases compatible with the tensor-operator basis that has been obtained using the method based on the fractional parentage coefficients as detailed in Sec. VI B. Everything is fine for up to four spins 1/2. But for five and six spins, a few projectors which are given as elements of the group ring of the symmetric group are corrupted as they do not even observe the projection property $P_{\tau_i} P_{\tau_i} = P_{\tau_i}$ (or more precisely, they cannot be normalized such that they are projections): For five spins, the single projector corresponding to the Young tableau

$$\tau_{16} = \begin{array}{|c|c|c|} \hline 1 & 4 & 5 \\ \hline 2 \\ \cline{1-1} 3 \\ \cline{1-1} \end{array}$$

is corrupted. For six spins, the four projectors corresponding to the Young tableaux

$$\tau_{15} = \begin{array}{|c|c|c|c|} \hline 1 & 3 & 5 & 6 \\ \hline 2 & 4 \\ \cline{1-2} \end{array}, \quad \tau_{21} = \begin{array}{|c|c|c|c|} \hline 1 & 2 & 5 & 6 \\ \hline 3 \\ \cline{1-1} 4 \\ \cline{1-1} \end{array}, \quad \tau_{24} = \begin{array}{|c|c|c|c|} \hline 1 & 3 & 5 & 6 \\ \hline 2 \\ \cline{1-1} 4 \\ \cline{1-1} \end{array}, \quad \text{and} \quad \tau_{25} = \begin{array}{|c|c|c|c|} \hline 1 & 4 & 5 & 6 \\ \hline 2 \\ \cline{1-1} 3 \\ \cline{1-1} \end{array}$$

are corrupted. This very limited failure of the projection method as explained in Sec. VI A is puzzling. In the following, we explain the corresponding mathematical structure in further detail and discuss potential reasons for this limited failure. But from an applications point of view, the second method based on the fractional parentage coefficients (see Sec. VI B) works without any problems and we have used it as a substitute in order to determine the symmetry-adapted decomposition of tensor operators for up to six spins 1/2.

In order to clarify the subsequent discussion, we shortly recall how an element of the symmetric group S_g acts on the tensor space, but we limit ourselves to the case of spins 1/2 (i.e. qubits). Given $\sigma \in S_g$, one has $\sigma(A_1 \otimes \cdots \otimes A_g) := A_{\sigma^{-1}(1)} \otimes \cdots \otimes A_{\sigma^{-1}(g)}$ for $A_i \in \mathbb{C}^{2\times 2}$. The action on the full tensor space is then obtained by linearity. The symmetric group S_g is generated by the transpositions $(i,i+1)$ with $i \in \{1, \ldots, g-1\}$ and the action of S_g on the tensor space can consequently be made even more explicit if we identify the action of the transpositions $(i,i+1)$. In particular, the action of $(1,2) \in S_2$ can be described using the commutation (or swap) matrix[114,115] K as follows

$$(1,2)(A_1 \otimes A_2) = K\,(A_1 \otimes A_2)\,K = A_2 \otimes A_1 \quad \text{with} \quad K = \begin{pmatrix} 1 & 0 & 0 & 0 \\ 0 & 0 & 1 & 0 \\ 0 & 1 & 0 & 0 \\ 0 & 0 & 0 & 1 \end{pmatrix}. \tag{18}$$

Equation (18) can be vectorized using the formula[114,115] $\mathrm{vec}(ABC) = (C^T \otimes A)\,\mathrm{vec}(B)$, where $\mathrm{vec}(B)$ denotes the vector of stacked columns of a matrix B. One obtains $(K^T \otimes K)\,\mathrm{vec}(A_1 \otimes A_2) = \mathrm{vec}(A_2 \otimes A_1)$ and (e.g.) $[(K \otimes I_0 \otimes I_0)^T \otimes (K \otimes I_0 \otimes I_0)]\,\mathrm{vec}(A_1 \otimes A_2 \otimes A_3 \otimes A_4) = \mathrm{vec}(A_2 \otimes A_1 \otimes A_3 \otimes A_4)$, where I_0 is the 2×2 identity matrix. This approach allows us to explicitly specify the action of elements σ of the symmetric group or its group ring on the tensor space using (albeit large) matrices $\Upsilon(\sigma)$ that operate linearly (by multiplication) on vectorized tensor-operator components. Note that $\Upsilon(\sigma)$ acts implicitly on all tensor-operator components and not only the g-linear ones (assuming that g is equal to the number of spins). Also, the transformation based on fractional parentage coefficients (i.e. the second step in Sec. VI B) operates directly on tensor-operator components and can be therefore interpreted as a matrix transformation on the same space as $\Upsilon(\sigma)$ but restricted to g-linear tensor operators. The

explicit form of the action of the symmetric group ring on tensors given by Υ will facilitate our further analysis. As Υ is a linear representation of the group ring of S_g, projection operators $P \in \mathbb{R}[S_g]$ with $P^2 = P$ are mapped by Υ to projection operators $\Upsilon(P)$ with $\Upsilon(P)^2 = \Upsilon(P)\Upsilon(P) = \Upsilon(P^2) = \Upsilon(P)$. The representation Υ of the group ring is faithful (i.e. the map $\sigma \in \mathbb{R}[S_g] \mapsto \Upsilon(\sigma)$ is injective) for $g \leq 4$, but it has a one-dimensional kernel for $g = 5$ and a 26-dimensional kernel for $g = 6$. The existence of a kernel unfortunately complicates the analysis of the corrupt projectors P_{τ_i}. We, however, do not believe that this is the cause for the corruption.

We continue by summarizing important, general properties of projection operators. If a projector $\mathcal{P}$ is given as a matrix [as is, e.g., $\Upsilon(P_{\tau_i})$], then it has only the eigenvalues zero and one, which will usually appear with multiplicity. The eigenvalue-zero eigenspace is equal to the kernel of $\mathcal{P}$, and the image of $\mathcal{P}$ (i.e. the invariant subspace under the projection $\mathcal{P}$) is equal to the eigenvalue-one eigenspace, the dimension of which is given by the trace $\mathrm{Tr}(\mathcal{P})$. In the following, it will be important to distinguish two notions of orthogonality: First, we have introduced in Sec. VI A the projectors P_{τ_i} as *orthogonalized* versions of the Young symmetrizers e_{τ_i} with the intention that the eigenvalue-one eigenspaces of $\Upsilon(P_{\tau_i})$ are *orthogonal* for different Young tableaux τ_i. Second, two projectors P_1 and P_2 [as, e.g., e_{τ_i} or P_{τ_i}, or even $\Upsilon(e_{\tau_i})$ or $\Upsilon(P_{\tau_i})$] are denoted as *orthogonal* if $P_1 P_2 = P_2 P_1 = 0$, i.e., if their sequential application maps everything to zero. These two notions of orthogonality are not necessarily related. For example, one has for $g = 3$ the Young symmetrizers

$$e_{\tau_2} = e_{\begin{array}{|c|c|}\hline 1 & 2 \\ \hline 3 \\ \cline{1-1}\end{array}} = [\varepsilon + (1,2) - (1,3) - (1,3,2)]/3 \quad \text{and} \quad e_{\tau_3} = e_{\begin{array}{|c|c|}\hline 1 & 3 \\ \hline 2 \\ \cline{1-1}\end{array}} = [\varepsilon - (1,2) + (1,3) - (1,2,3)]/3 \tag{19}$$

and the projection operators

$$P_{\tau_2} = e_{\tau_2} \quad \text{and} \quad P_{\tau_3} = [\varepsilon - (1,2) + 2\,(2,3) - (1,3) - 2\,(1,2,3) + (1,3,2)]/3. \tag{20}$$

One obtains that e_{τ_2} and e_{τ_3} are orthogonal (i.e. $e_{\tau_2} e_{\tau_3} = e_{\tau_3} e_{\tau_2} = 0$) while P_{τ_2} and P_{τ_3} are not. But the eigenvalue-one eigenspaces of $\Upsilon(e_{\tau_2})$ and $\Upsilon(e_{\tau_3})$ are not orthogonal, while the ones of $\Upsilon(P_{\tau_2})$ and $\Upsilon(P_{\tau_3})$ are. Orthogonal projections are particularly convenient and, in general, for a given direct-sum decomposition $V = V_1 \oplus \cdots \oplus V_v$ of a vector space V, one can always *choose* v projections $\mathcal{P}_i$ such that (i) all projections $\mathcal{P}_i$ are mutually orthogonal, (ii) $\mathcal{P}_1 + \cdots + \mathcal{P}_v = \mathcal{I}$ (where $\mathcal{I}$ is the identity projection onto V), and (iii) the image of $\mathcal{P}_i$ is equal to V_i (see, e.g., Theorem 4.50 on p. 92 of Ref. 116). Also, the properties (i) and (ii) are closely related as a sum of several projections is again a projection if and only if all projections are mutually orthogonal (see, e.g., Ref. 117).

After these preparations, we can study certain peculiarities of the Young symmetrizers e_τ as defined in Eq. (10) for $g \geq 5$. We will not necessarily assume that the Young tableau τ is a standard Young tableaux, i.e., the boxes of τ are allowed to be arbitrarily filled with the numbers $\{1, \ldots, g\}$ but without repeating any number. It is well known[50,118] that Young symmetrizers are not necessarily orthogonal, even if one only considers standard Young tableaux. In particular, one has $e_{\tau'} e_\tau = 0$ for the Young symmetrizers e_τ and $e_{\tau'}$ if there exist two integers $i, j \in \{1, \ldots, g\}$ such that i and j are in the same row of τ and the same column of τ' (see, e.g., Proposition VI.3.2 in Ref. 118). For example, we have for $g = 5$ only two pairs (τ', τ) of (non-equal) standard Young tableaux such that $e_{\tau'} e_\tau \neq 0$, i.e. $(\tau', \tau) \in \{(\tau_6, \tau_{10}), (\tau_{17}, \tau_{21})\}$. The corresponding shapes are [3,2] and [2,2,1]. Similarly, one has 13 such pairs for $g = 6$ and in particular the pairs (τ_8, τ_{15}) and (τ_9, τ_{15}). The shapes of all the occurring standard Young tableaux (for $g = 6$) are [4,2], [3,3], [3,2,1], and [2,2,2]. This non-orthogonality has also been studied in Ref. 119–121 together with the question of how to find orthogonal sets of projectors. Also, Stembridge[122] notes that all Young symmetrizers for standard Young tableaux of fixed shape λ are mutually orthogonal if and only if $\lambda = [2,2]$, $\lambda = [m]$, or $\lambda = [m,1,\ldots,1]$ for some positive integer m. This observed non-orthogonality may, however, not have any implications for the corruption of the projection operators P_{τ_i}: Both symptoms appear for $g = 6$ and τ_{15}, but this is the only case were both symptoms occur simultaneously for standard Young tableaux of the same shape and $g \in \{5, 6\}$. In addition, the projection operators P_{τ_i} are not even orthogonal for $g = 3$ [as discussed below Eq. (20)]. The non-orthogonality of Young symmetrizers of standard Young tableaux is therefore most likely not the cause (or at least not the only one) for the corruption of the projection operators P_{τ_i}.

In a final step, we restrict our focus to Young tableaux τ of fixed shape as the construction in Sec. VI A essentially operates only on Young tableaux of fixed shape and the corresponding Young symmetrizers e_τ. For a given partition λ, let us define the projector $e_\lambda := f_\lambda \sum_\tau e_\tau = f_\lambda^2 \sum_\tau H_\tau V_\tau$ where the sums go over all (not necessarily standard) Young tableaux τ of shape λ [cf. Eq. (10)]. The projector e_λ is contained in the center of the group ring $\mathbb{R}[S_g]$, i.e., it commutes with $\mathbb{R}[S_g]$ (see Cor. VI.3.7 in Ref. 118). All projectors e_λ are mutually orthogonal and one obtains the identity by summing the e_λ for arbitrary partitions λ. In addition, e_λ projects onto the left ideal of $\mathbb{R}[S_g]$ spanned by the Young symmetrizers e_τ for standard Young tableaux τ of shape λ and this left ideal describes an irreducible representation of S_g.[50,118] Our orthogonalization construction for the projection operators P_{τ_i} (see Sec. VI A) aims at splitting the eigenvalue-one eigenspace of $\Upsilon(e_\lambda)$ into the orthogonal eigenvalue-one eigenspaces of $\Upsilon(P_{\tau_i})$. This, however, fails for (e.g.) τ_{16} and $g = 5$, even though an extension of the relevant eigenspaces of the projections $\Upsilon(P_{\tau_{11}}), \ldots, \Upsilon(P_{\tau_{15}})$ to the one of $\Upsilon(e_{[3,1,1]})$ is possible. An analysis along these lines might give further insight

into how the projection method of Sec. VI A is connected to the method based on fractional parentage coefficients (see Sec. VI B) and why the corruption of the projection operators P_{τ_i} arises. But the high-dimensionality of the corresponding matrices significantly complicates the analysis. In summary, we are currently not able to explain the corruption in the projection method and leave this as an open question. However, the method based on fractional parentage coefficients provides a suitable substitute for practical purposes.

VIII. Conclusion

We have extended the DROPS representation of Ref. 37 to visualize finite-dimensional quantum systems for up to six spins 1/2 and two spins of arbitrary spin number. A general multi-spin operator can be completely characterized and visualized using multiple spherical plots that are each assembled from linear combinations of spherical harmonics $Y(\theta, \phi)$. The DROPS representation relies on decomposing spin operators into a symmetry-adapted tensor basis and subsequently mapping it to linear combinations of spherical harmonics. The construction algorithm in its original form for up to three spins relies on explicit projection operators.[37] Due to the challenges discussed in Sec. VII, the projection method is only directly applicable for up to four coupled spins 1/2. By applying a methodology based on fractional parentage coefficients, we have circumvented these challenges. This methodology relies on consecutive transformations from partially to fully permutation-symmetrized tensors. With this technique, tensors of systems consisting of arbitrary numbers of spins 1/2 can be identified by the sublabels g, G, $\tau^{[g]}$, and, for larger systems with six particles and more, additionally by $\mathcal{A}$, as well as the rank j and order m. These tensors and their mapping to generalized Wigner functions were calculated explicitly for various examples for up to six spins 1/2. Note that the necessity of *ad hoc* sublabels for six and more spins had been already anticipated in Ref. 37.

We further extended the projection method to spins with arbitrary spin numbers. In particular, we discuss the cases of two coupled spins with $J_1 = J_2$ and $J_1 \neq J_2$. Since the number of appearing tensors is rapidly increasing with the spin number, the partitioning of the tensors according to physical features of the system and inherent properties of tensors characterized by g, G, and $\tau^{[g]}$ do not suffice to obtain groups in which every tensor rank j appears only once. Although *ad hoc* sublabels, analogously introduced as in the case of spins 1/2, could resolve this problem, they suffer from a lack of systematics and connections related to tensor properties. For larger spin numbers, the number of occurring tensors is substantially larger compared to systems consisting of spins 1/2 and a large set of $\mathcal{A}$ would be required even for two spins. This inconvenience can be circumvented by relying on parent sublabels which are in particular suitable for larger spin numbers. Parent sublabels can be more methodically and consistently applied and are better connected to tensor properties. Tensors of a system consisting of two spins with $J_1 = J_2$ can be conveniently grouped according to the sublabels g, G, $\mathcal{P}$, and $\tau^{[g]}$. In systems with $J_1 \neq J_2$, where permutation symmetries are not meaningful, tensors are organized with respect to the sublabels g, G, $\mathcal{P}$, and $\mathcal{A}$. We also discuss the extension to a larger number of spins (with arbitrary spin numbers), but an explicit treatment is beyond the scope of the current work.

Illustrative examples for up to six spins 1/2 and a spin 1/2 coupled to a spin 1 are provided. This also includes entangled quantum states. Quantum systems are frequently described by abstract operators or matrices and our methodology is in this regard particularly useful in visualizing quantum concepts and systems by conveniently partitioning the inherent information. The DROPS representation has the favorable property to naturally reflect transformations under non-selective spin rotations as well as spin permutations. This approach is also convenient for highlighting the time evolution of experiments as animations. A free software package[111,112] for the interactive exploration of coupled spin dynamics based on the DROPS visualization in real time is already available for up to three coupled spins 1/2. Potential applications of the DROPS visualization for larger spin systems and for particles with spin number larger than 1/2 range from electron and nuclear magnetic resonance applications in physics, chemistry, biology, and medicine to theoretical and experimental quantum information theory[123] in which quantum information is stored for example by electron or nuclear spins, trapped ions, quantum dots, and superconducting circuits or (quasi-)particles of arbitrary spin numbers.

IX. Acknowledgment

We acknowledge preliminary work towards this project by Ariane Garon. This work was supported in part by the Excellence Network of Bavaria (ENB) through ExQM. R.Z. and S.J.G. acknowledge support from the Deutsche Forschungsgemeinschaft (DFG) through Grant No. Gl 203/7-2. We have relied on the computer algebra systems Magma,[124] Matlab,[125] and Sage[126] for explicit computations.

A. Further visualizations for systems consisting of four, five or six spins 1/2

In this appendix, we provide additional examples to further illustrate experimental spin operators using the DROPS representation. In Appendix A 1, we analyze the Wigner representation of fully symmetric operators [see Eq. (A1)], raising operators, and anti-phase operators typically arising in NMR spectroscopy for up to six coupled spins 1/2. In Appendix A 2, we visualize multiple experiments: First, we show the evolution of droplet functions in the generation of multiple-quantum coherence in a five-spin system, followed by an efficient state-transfer experiment in a spin chain consisting of six spins 1/2. Finally, we present snapshots of droplet functions during an isotropic mixing experiment in a system consisting of four spins 1/2. In Appendix A 3, we present the DROPS representations for (complex) random matrices for systems consisting of five and six spins 1/2.

(a) $A = \prod_{k=1}^{N} I_{k\eta}$

N	ℓ	j	$f^{(\ell)}$	Detail
1	{1}	1		
2	{1,2}	0,2		
3	$\{1,2,3\}, \tau_1^{[3]}$	1,3		
4	$\{1,2,3,4\}, \tau_1^{[4]}$	0,2,4		
5	$\{1,2,3,4,5\}, \tau_1^{[5]}$	1,3,5		
6	$\{1,2,3,4,5,6\}, \tau_1^{[6]}$	0,2,4,6		

(b) $B = \prod_{k=1}^{N} I_k^+$

N	ℓ	j	$f^{(\ell)}$
1	{1}	1	
2	{1,2}	2	
3	$\{1,2,3\}, \tau_1^{[3]}$	3	
4	$\{1,2,3,4\}, \tau_1^{[4]}$	4	
5	$\{1,2,3,4,5\}, \tau_1^{[5]}$	5	
6	$\{1,2,3,4,5,6\}, \tau_1^{[6]}$	6	

(c) $C = I_{1x}(\prod_{k=2}^{N} I_{kz})$: Partition $[N]$

N	ℓ	j	$f^{(\ell)}$	Detail
2	{1,2}	2		
3	$\{1,2,3\}, \tau_1^{[3]}$	1,3		
4	$\{1,2,3,4\}, \tau_1^{[4]}$	2,4		
5	$\{1,2,3,4,5\}, \tau_1^{[5]}$	1,3,5		
6	$\{1,2,3,4,5,6\}, \tau_1^{[6]}$	2,4,6		

(d) $C = I_{1x}(\prod_{k=2}^{N} I_{kz})$: Partition $[N-1, 1]$

N	ℓ	j	$f^{(\ell)}$
2	{1,2}	1	
3	$\{1,2,3\}, \tau_i^{[3]}$	1,2	
4	$\{1,2,3,4\}, \tau_i^{[4]}$	1,2,3	
5	$\{1,2,3,4,5\}, \tau_i^{[5]}$	1,2,3,4	
6	$\{1,2,3,4,5,6\}, \tau_i^{[6]}$	1,2,3,4,5	

FIG. 7. The droplet functions $f^{(\ell)}$ visualizing various operators for up to six coupled spins 1/2 ($N = 6$). The full labels are given in the second column and the occurring tensors ranks j are shown in the third column of each table. The detail column shows the corresponding magnified centers of $f^{(\ell)}$. In Table (a), the spherical functions $f^{(\ell)}$ of the fully symmetrical operator $A = \prod_{k=1}^{N} I_{kx}$ are shown. Table (b) depicts the representations of the non-Hermitian operators $B = \prod_{k=1}^{p} I_k^+$. In Table (c) and (d), the visualizations of the antiphase operators $C = I_{1x}(\prod_{k=2}^{N} I_{kz})$ are depicted. There is only one symmetry type $\tau_1^{[N]}$ for the partition $[N]$ and the related droplet is shown in Table (c) . For the partition $[N-1, 1]$, we find $N-1$ different standard Young tableaux $\tau_i^{[N]}$ with $i \in \{2, \ldots, N\}$ and thus, have $N-1$ droplets $f^{(\ell)}$. They all have identical shapes but different sizes and one representative spherical function for this case is illustrated in Table (d). In total N droplets visualize the antiphase operator from Eq. (A3). In contrast to our usual strategy, droplets for two spins (i.e. $N = 2$) are plotted here separately for the fully permutation-symmetric part (i.e. for the partition $[N]$) in (c) and the remaining part in (d).

1. Wigner representations of prominent spin operators

We show the visualization for some prominent operators in NMR spectroscopy. In Table 7(a), the droplet functions representing the fully symmetric operator

$$A = \prod_{k=1}^{N} I_{k\eta} \tag{A1}$$

with $\eta = x$ for different systems consisting of up to $N = 6$ spin 1/2. The only non-vanishing tensor components have permutation symmetries $\tau_1^{[N]}$ and hence, we find only one droplet function labeled by G or $(G, \tau_1^{[N]})$. The elongated shape with $N-1$ rings, having alternating phases in the center of droplet, is characteristic for the DROPS representation of these operators. The operators for $\eta \in \{y, z\}$ (not shown) exhibit the same shape but are orientated along the y and z axis, respectively.

Table 7(b) shows the droplet functions representing the p-quantum operators

$$B = \prod_{k=1}^{p} I_k^+ \tag{A2}$$

with the single-spin raising operators defined as $I_k^+ = I_{kx} + iI_{ky}$. In the DROPS representation, p-quantum operators are represented by rainbow-colored donut shapes with p rainbows coding for p phase transitions from 0 to 2π when the operator is rotated by 360° around the z axis. The color transition for an operator $I_k^- = I_{kx} - iI_{ky}$ is inverted (not shown). Again, only the coefficients of tensors with symmetry $\tau_1^{[N]}$ are non-zero for both I_k^+ and I_k^- and thus, only one droplet is found.

In Tables 7(c) and (d), the droplet functions representing the antiphase operators

$$C = I_{1x} \left(\prod_{k=2}^{N} I_{kz} \right) \tag{A3}$$

for different sizes of spin-1/2 systems with number of particles $N \in \{2, 3, 4, 5, 6\}$ are shown. Only coefficients of tensors with symmetries given by the partitions $\lambda(\tau_i^{[g]}) = [N]$ and $\lambda(\tau_i^{[g]}) = [N-1, 1]$ are non-vanishing. There is only one symmetry type $\tau_1^{[N]}$ for the partition $[N]$ and the related droplet is shown in Table 7(c). The typical features of the droplet functions $f^{(G,\tau_1^{[N]})}$ are four arms with $N-2$ plates with alternating phases separating the two pairs of arms. For the partition $[N-1, 1]$, we find $N-1$ different occurring symmetries $\tau_i^{[N]}$ with $i \in \{2, \ldots, N\}$ and thus, have $N-1$ droplets $f^{(\ell)}$. They all have identical shapes but different sizes and one representative droplet function for this case is illustrated in Table 7(d). In total N droplets visualize the antiphase operator from Eq. (A3). In addition, for each tensor only orders with $|m| = \pm 1$ occur.

2. Visualization of experiments

We use our approach to represent and visualize experiments with up to six spins 1/2. First we show maximum quantum coherence generation[108] in a chain of five spins 1/2 using $\pi/2$ hard pulses and delays [see Table S2 in Ref. 108]. This is the five-spin analog to the experiment visualized given in Fig. 3 of Sec. IV for four spins. The initial state is $\rho_0 = \sum_{k=1}^{5} I_{kz}$ and the coupling is given by an Ising Hamiltonian. All coupling constants in the drift Hamiltonian are assumed to be equal, i.e., $\mathrm{J} = \mathrm{J}_{12} = \mathrm{J}_{23} = \mathrm{J}_{34} = \mathrm{J}_{45} = \mathrm{J}$. Fig. 8(a1)-(a5) shows the droplet functions for different points in time. Panel (a1) shows the droplet functions after $\pi/2$ pulses with phases y on each spin. A coupling evolution of duration $t = 1/(2\mathrm{J})$ followed again by $\pi/2$ pulses with phases y on all spins is repeated four times. Panels (a2)-(a5) depict the droplets representing the state after each of this sequence block. In the course of the experiment, higher orders of coherence are created, which is reflected by the occurrence of droplets of larger g. Although many different tensors in various subsystems and symmetries appears, the information can still be partitioned in a clear scheme. Eventually, after the experiment in panel (e), the state is fully described by a single 5-linear droplet (representing $G = \{1,2,3,4,5\}$ with the Young tableau sublabel $\tau_1^{[5]}$), which also contains the desired maximum-quantum coherence.

As an additional illustrative example, we present an efficient transfer of an initial state $\rho_0 = I_{1x} + iI_{1y}$ to the target state $\rho_t = I_{6x} + iI_{6y}$ by unitary transformations. We consider a linear chain of six coupled spins 1/2 and only assume

Ising couplings (with identical coupling constant J) between next neighbors and the free evolution Hamiltonian is given by $H = 2\pi \sum_{k=2}^{6} \mathrm{J}\ I_{(k-1)z} I_{kz}$. The approach in Ref. 127 first encodes the initial linear operators into bilinear operators, which can then be efficiently propagated through the spin chain. Fig. 8(b) shows the state visualized by droplet functions for different points in time. The nodes represent the particles and the edges the couplings between the spins. The first row shows the visualization of ρ_0. This initial state is then encoded by applying a $\pi/2$ pulse with phase $-x$ followed by $\pi/2$ pulse with phase y on the first spin, which then evolves under the the coupling Hamiltonian H for a duration $1/(2\mathrm{J})$ resulting in the state shown in the second row of Fig. 8(b). Subsequently, a sequence of a $\pi/2$ pulse with phase x on the first spin, a $\pi/2$ pulse with phase y on the second spin and a free evolution period under

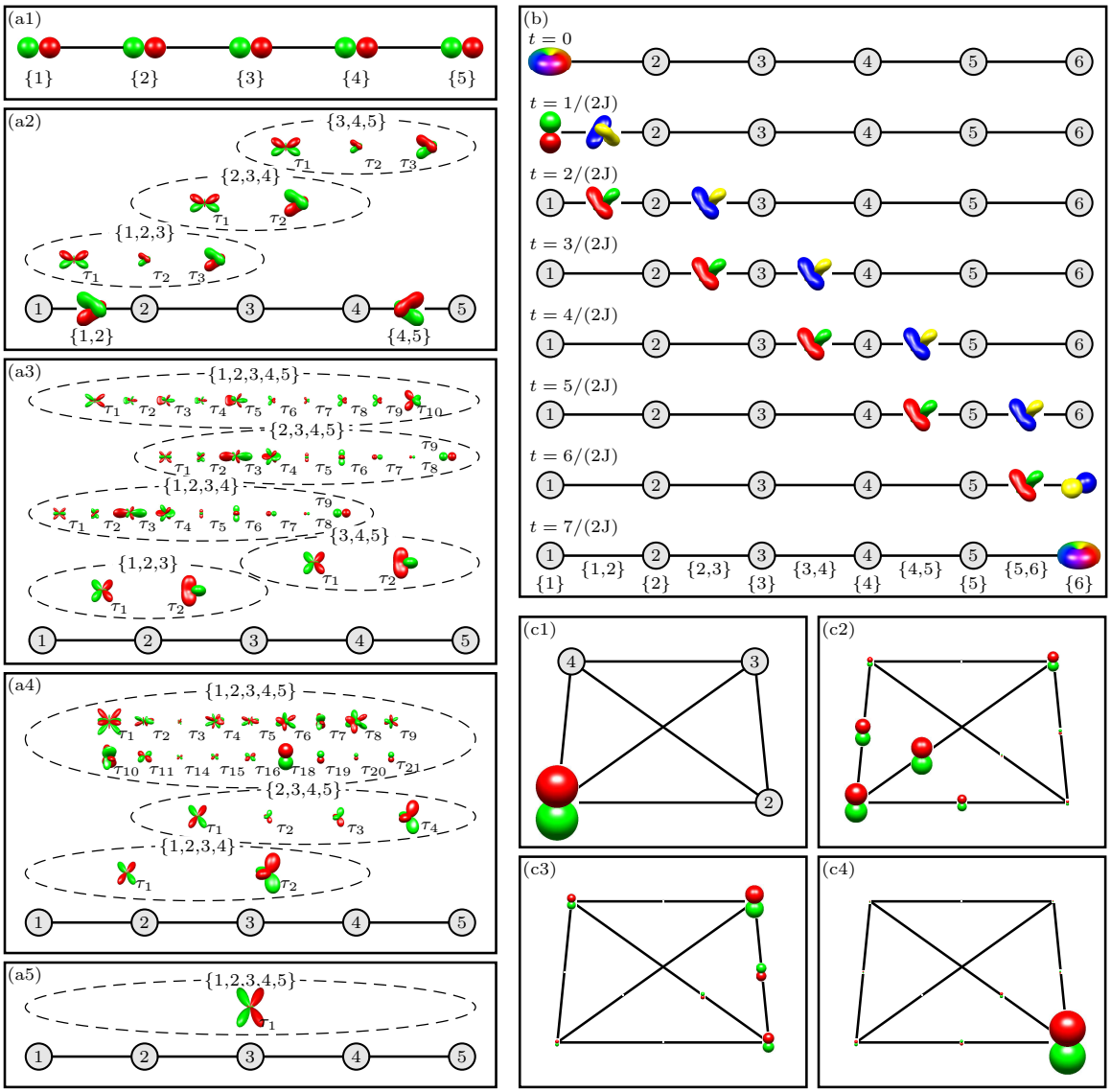

FIG. 8. Visualization of experiments: In panel (a1)-(a5), the generation of five-quantum coherence in a chain consisting of five spins 1/2 is shown for a sequence of $\pi/2$ pulses and optimized delays. The initial state is $\rho_0 = \sum_{k=1}^{5} I_{kz}$. Panel (a1) depicts the visualization of the density matrix after an $[\pi/2]_y$ pulse on each spin. Panels (a2)-(a5) illustrate the state after repeated evolutions under coupling with time $t = 1/(2\mathrm{J})$ followed by $[\pi/2]_y$ pulses on each spin, see also Fig. 3. The droplet in panel (a5) is scaled to 1/3 of its original size. Panel (b) shows the coherent transfer of the initial state $\rho_0 = I_{1x} + iI_{1y}$ to the target state $\rho_N = I_{6x} + iI_{6y}$ by unitary transformations in a six-spin-1/2 chain: bilinear encoded states are created, which can be efficiently transferred, and they are eventually decoded at the end of the spin chain (see Ref. 127). In panels (c1)-(c4), the polarization transfer of a four-spins-1/2 system under isotropic mixing conditions is shown for the times (c1) 0 ms, (c2) 20 ms, (c3) 40 ms, and (c4) 133 ms, while only the linear and bilinear terms are explicitly displayed.

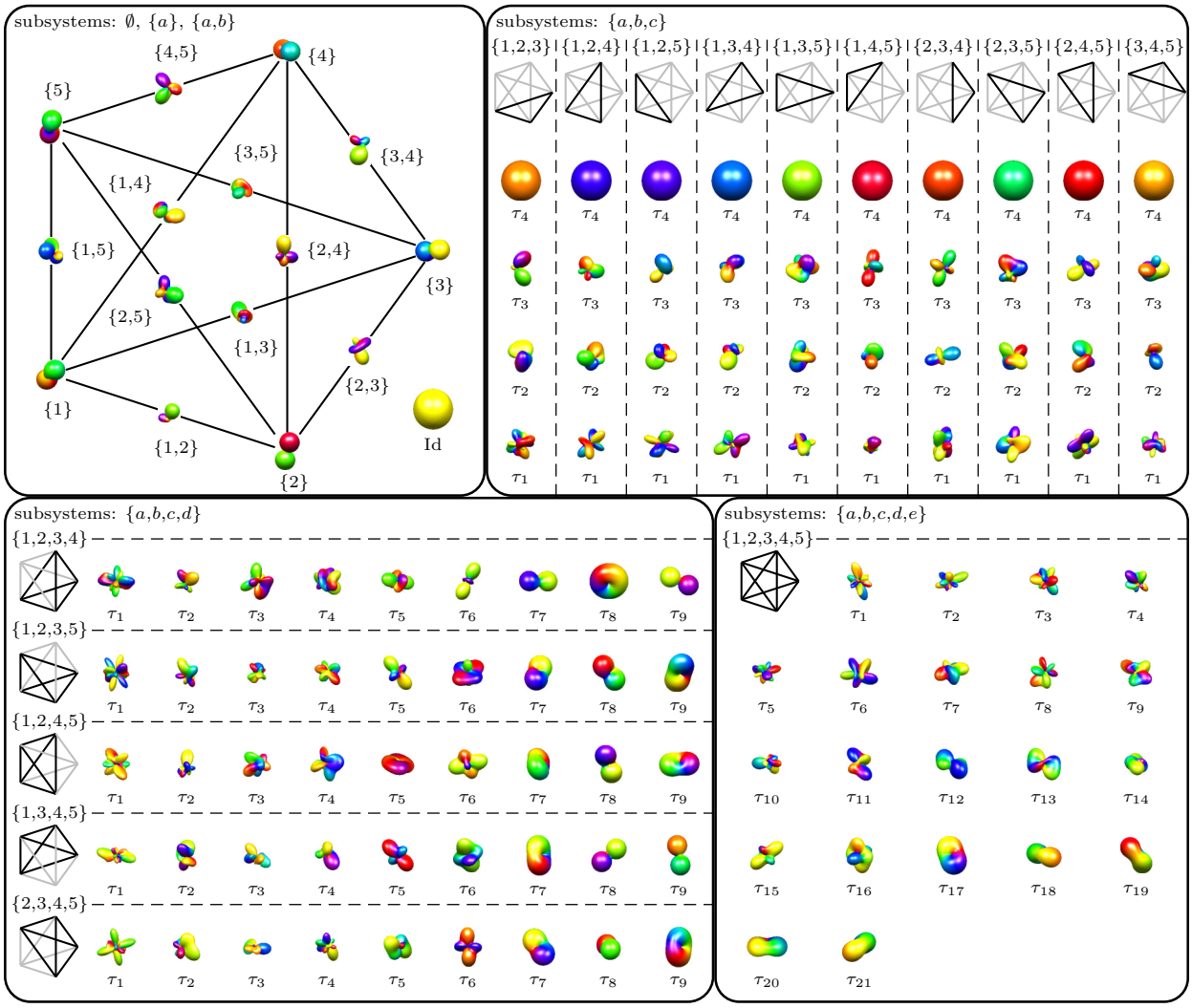

FIG. 9. Visualization of a complex random matrix for five spins 1/2. The droplet functions are arranged according to their g-linearity. The top left panel shows the topology of the system with nodes representing the spins and edges their couplings. Here, f^{Id} is placed beneath the diagram, the droplets corresponding to $g = 1$ are plotted on the nodes and the bilinear droplets for $g = 2$ are placed on the edges. The top right panel illustrates $f^{(G,\tau_i^{[3]})}$ for all possible subsystems with $g = 3$. The bottom left and right panels depict the droplet functions for all occurring subsystems with $g = 4$ and $g = 5$, respectively. The topologies of each G are visualized by diagrams located at each subpanel. Droplet functions are normalized for better visibility.

the coupling Hamiltonian H with duration $1/(2\mathrm{J})$ generates the encoded state, which is shown in the third row of Fig. 8(b). This encoded state, which consists only of bilinear operators can then be efficiently propagated along the spin chain by applying an effective soliton sequence composed of a $\pi/2$ pulse with phase y on all spins followed by a free evolution under coupling with duration $1/(2\mathrm{J})$, which results in the propagation of the encoded state by one spin position. This is repeated three times and the resulting states are depicted in row four to six. The state is then decoded first by repeating the soliton sequence one more time (row seven) and then by a sequence consisting of a $\pi/2$ with phase $-y$ on the fifth spin, a $\pi/2$ with phase x on the sixth spin, a free evolution with duration $1/(2\mathrm{J})$, and a $\pi/2$ with phase x on the sixth spin is applied. This finally generates the desired state $\rho_t = I_{6x} + iI_{6y}$ depicted in row eight. Neglecting the durations of the hard pulses, the total transfer time is $7/(2\mathrm{J})$. For comparison,[127] the same transfer could be achieved by a sequence of five next-neighbor SWAP operations (each with a duration of $3/(2\mathrm{J})$) which would require a total transfer time of $15/(2\mathrm{J})$.

Last, we show the visualization of the dynamics of a polarization transfer from spin one to spin two in a system consisting of four coupled spins 1/2 under isotropic mixing conditions.[128] Isotropic mixing is one of the most important methods to transfer polarization in high-resolution NMR spectroscopy and is frequently used in homonuclear and

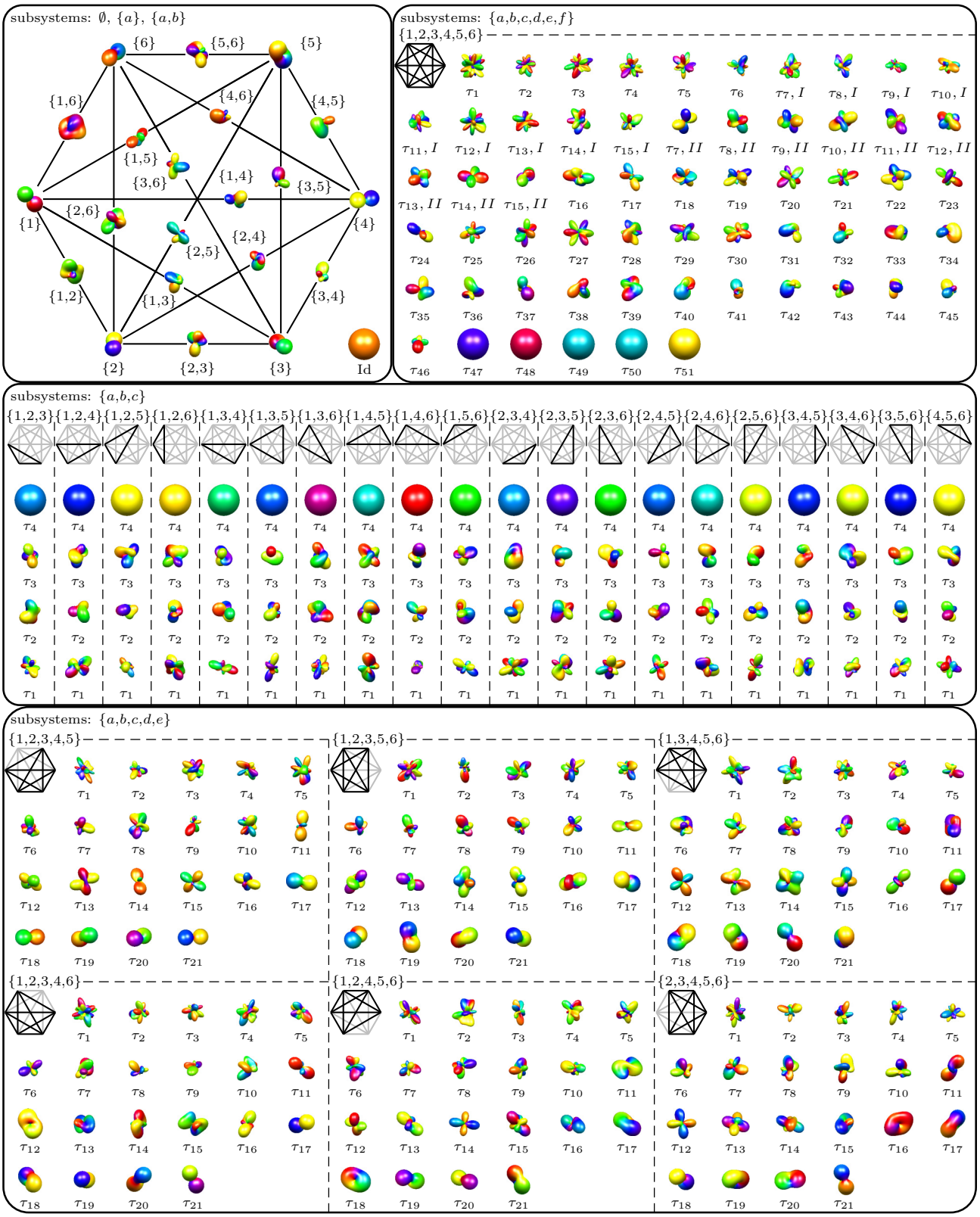

FIG. 10. Visualization of a complex random matrix for six spins 1/2 analog to Fig. 9. Droplet functions for $g \in \{0, 1, 2\}$ are placed on top left panel. The top right, the middle, and the bottom panel illustrate all appearing droplet functions for all subsystems for $g = 6$, $g = 3$, and $g = 5$. Droplet functions are normalized. The four-linear contributions are given in Fig. 11.

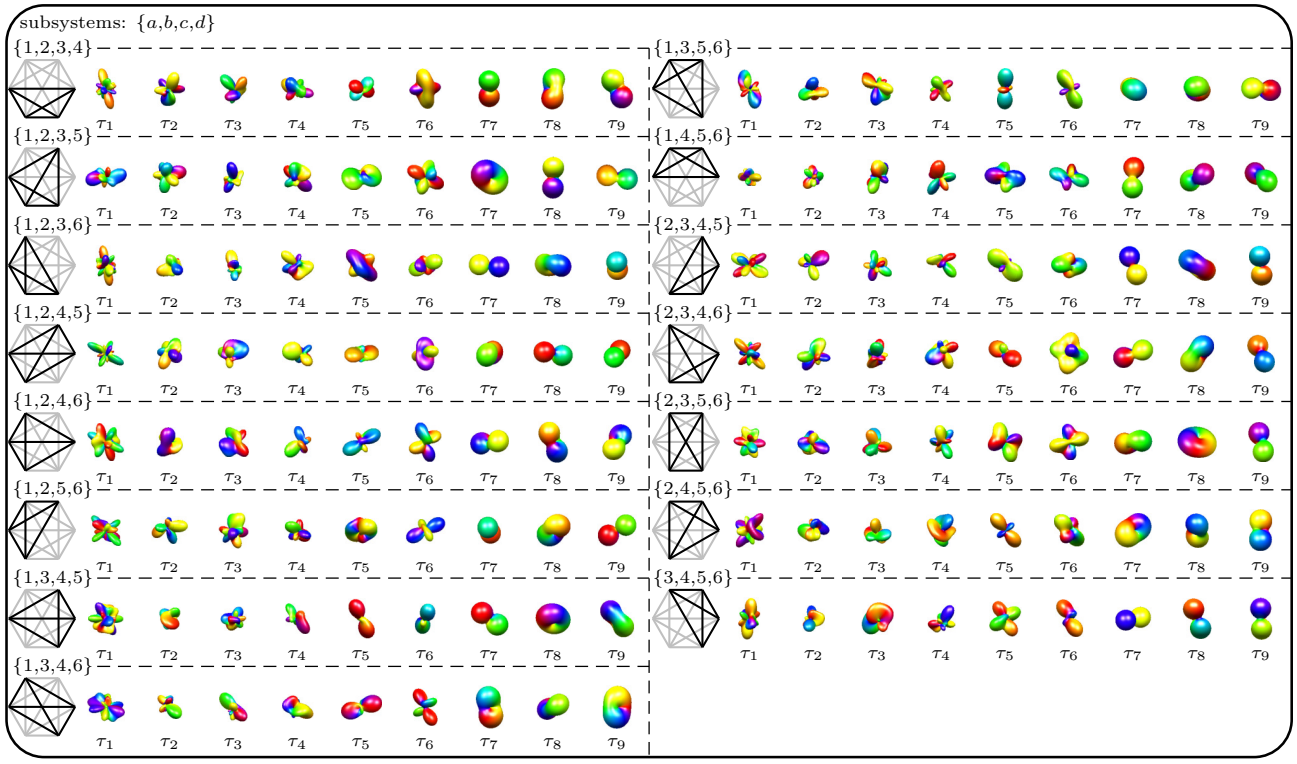

FIG. 11. Four-linear contributions missing in Fig. 10. Spherical functions are normalized.

TABLE VI. Standard Young tableaux $\tau^{[g]}$ for $g \in \{5,6\}$ with the corresponding partitions λ ordered with index i. Also the appearing ranks j for each $\tau^{[g]}$ are shown, see also Ref. 37. *Ad hoc* sublabels are required in the case $g = 6$ for $j = 2$ and $\lambda = [4,2]$.

g	Partition λ	No. of $\tau_i^{[g]}$	Indices i for $\tau_i^{[g]}$	*Ad hoc* $\mathcal{A}$	Ranks j
5	[5]	1	1		1,3,5
	[4,1]	4	2,..,5		1,2,3,4
	[3,2]	5	6,..,10		1,2,3
	[3,1,1]	6	11,..,16		0,2
	[2,2,1]	5	17,..21		1
	[2,1,1,1]	4	22,..,25		–
	[1,1,1,1,1]	1	26		–
6	[6]	1	1		0,2,4,6
	[5,1]	5	2,..,6		1,2,3,4,5
	[4,2]	9	7,..,15	*I*	0,2,3,4
		9	7,..,15	*II*	2
	[4,1,1]	10	16,..,25		1,3
	[3,3]	5	26,..,30		1,3
	[3,2,1]	16	31,..,46		1,2
	[2,2,2]	5	47,..,51		0
	[3,1,1,1]	10	52,..,61		–
	[2,2,1,1]	9	62,..,70		–
	[2,1,1,1,1]	5	71,..,75		–
	[1,1,1,1,1,1]	1	76		–

i: 1 2 3 4 5 6 7 8 9 10

$\tau_i^{[5]}$:
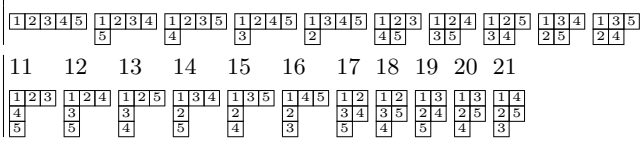

i: 11 12 13 14 15 16 17 18 19 20 21

$\tau_i^{[5]}$:

i: 1 2 3 4 5 6

$\tau_i^{[6]}$:
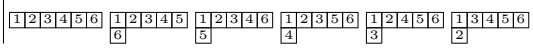

i: 7 8 9 10 11 12 13 14 15

$\tau_i^{[6]}$:
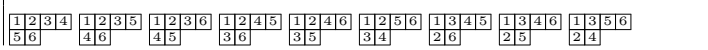

i: 16 17 18 19 20 21 22 23 24 25

$\tau_i^{[6]}$:
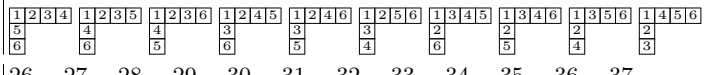

i: 26 27 28 29 30 31 32 33 34 35 36 37

$\tau_i^{[6]}$:
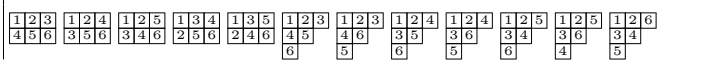

i: 38 39 40 41 42 43 44 45 46 47 48 49 50 51

$\tau_i^{[6]}$:
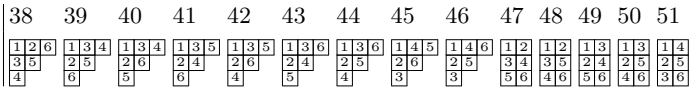

TABLE VII. Explicit values of fractional parentage coefficients, see also Table VIII. Empty boxes in the standard Young tableaux $\tau^{[g-1]}$ have to be filled with all possible values as detailed in Tables II and VI.

g	$j^{[g]}$	$\tau^{[g-1]}$	Transf. matrix	Input $j^{[g-1]}$	Output $\tau^{[g]}$ and $\mathcal{A}$
2	0	$\begin{array}{\|c\|}\hline 1\\\hline\end{array}$	$\begin{bmatrix}1\end{bmatrix}$	1	$\begin{array}{\|c\|c\|}\hline 1&2\\\hline\end{array}$
	1	$\begin{array}{\|c\|}\hline 1\\\hline\end{array}$	$\begin{bmatrix}1\end{bmatrix}$	1	$\begin{array}{\|c\|}\hline 1\\\hline 2\\\hline\end{array}$
	2	$\begin{array}{\|c\|}\hline 1\\\hline\end{array}$	$\begin{bmatrix}1\end{bmatrix}$	1	$\begin{array}{\|c\|c\|}\hline 1&2\\\hline\end{array}$
3	0	$\begin{array}{\|c\|}\hline 1\\\hline 2\\\hline\end{array}$	$\begin{bmatrix}1\end{bmatrix}$	1	$\begin{array}{\|c\|}\hline 1\\\hline 2\\\hline 3\\\hline\end{array}$
	1	$\begin{array}{\|c\|c\|}\hline 1&2\\\hline\end{array}$	$\begin{bmatrix}\frac{\sqrt{5}}{3} & \frac{2}{3}\\ \frac{2}{3} & \frac{-\sqrt{5}}{3}\end{bmatrix}$	0,2	$\begin{array}{\|c\|c\|c\|}\hline 1&2&3\\\hline\end{array}$, $\begin{array}{\|c\|c\|}\hline 1&2\\\hline 3\\\cline{1-1}\end{array}$
		$\begin{array}{\|c\|}\hline 1\\\hline 2\\\hline\end{array}$	$\begin{bmatrix}1\end{bmatrix}$	1	$\begin{array}{\|c\|c\|}\hline 1&3\\\hline 2\\\cline{1-1}\end{array}$
	2	$\begin{array}{\|c\|c\|}\hline 1&2\\\hline\end{array}$	$\begin{bmatrix}1\end{bmatrix}$	2	$\begin{array}{\|c\|c\|}\hline 1&2\\\hline 3\\\cline{1-1}\end{array}$
		$\begin{array}{\|c\|}\hline 1\\\hline 2\\\hline\end{array}$	$\begin{bmatrix}1\end{bmatrix}$	1	$\begin{array}{\|c\|c\|}\hline 1&3\\\hline 2\\\cline{1-1}\end{array}$
	3	$\begin{array}{\|c\|c\|}\hline 1&2\\\hline\end{array}$	$\begin{bmatrix}1\end{bmatrix}$	2	$\begin{array}{\|c\|c\|c\|}\hline 1&2&3\\\hline\end{array}$
4	0	$\begin{array}{\|c\|c\|c\|}\hline 1&2&3\\\hline\end{array}$	$\begin{bmatrix}1\end{bmatrix}$	1	$\begin{array}{\|c\|c\|c\|c\|}\hline 1&2&3&4\\\hline\end{array}$
		$\begin{array}{\|c\|c\|}\hline 1\\\hline\multicolumn{1}{c}{}\\\cline{1-1}\end{array}$	$\begin{bmatrix}1\end{bmatrix}$	1	$\begin{array}{\|c\|c\|}\hline 1\\\hline\multicolumn{1}{c}{}&4\\\cline{2-2}\end{array}$
	1	$\begin{array}{\|c\|c\|c\|}\hline 1&2&3\\\hline\end{array}$	$\begin{bmatrix}1\end{bmatrix}$	1	$\begin{array}{\|c\|c\|c\|}\hline 1&2&3\\\hline 4\\\cline{1-1}\end{array}$
		$\begin{array}{\|c\|c\|}\hline 1\\\hline\multicolumn{1}{c}{}\\\cline{1-1}\end{array}$	$\begin{bmatrix}\frac{-\sqrt{5}}{\sqrt{8}} & \frac{\sqrt{3}}{\sqrt{8}}\\ \frac{\sqrt{3}}{\sqrt{8}} & \frac{\sqrt{5}}{\sqrt{8}}\end{bmatrix}$	1,2	$\begin{array}{\|c\|c\|c\|}\hline 1&\multicolumn{1}{c}{}&4\\\hline\multicolumn{1}{c}{}\\\cline{1-1}\end{array}$, $\begin{array}{\|c\|c\|}\hline 1\\\hline\multicolumn{1}{c}{}\\\cline{1-1}4\\\cline{1-1}\end{array}$
		$\begin{array}{\|c\|}\hline 1\\\hline 2\\\hline 3\\\hline\end{array}$	$\begin{bmatrix}1\end{bmatrix}$	0	$\begin{array}{\|c\|}\hline 1\\\hline 4\\\hline 2\\\hline 3\\\hline\end{array}$
	2	$\begin{array}{\|c\|c\|c\|}\hline 1&2&3\\\hline\end{array}$	$\begin{bmatrix}\frac{\sqrt{7}}{\sqrt{10}} & \frac{\sqrt{3}}{\sqrt{10}}\\ \frac{\sqrt{3}}{\sqrt{10}} & \frac{-\sqrt{7}}{\sqrt{10}}\end{bmatrix}$	1,3	$\begin{array}{\|c\|c\|c\|c\|}\hline 1&2&3&4\\\hline\end{array}$, $\begin{array}{\|c\|c\|c\|}\hline 1&2&3\\\hline 4\\\cline{1-1}\end{array}$
		$\begin{array}{\|c\|c\|}\hline 1\\\hline\multicolumn{1}{c}{}\\\cline{1-1}\end{array}$	$\begin{bmatrix}\frac{\sqrt{3}}{2} & \frac{1}{2}\\ \frac{-1}{2} & \frac{\sqrt{3}}{2}\end{bmatrix}$	1,2	$\begin{array}{\|c\|c\|c\|}\hline 1&\multicolumn{1}{c}{}&4\\\hline\multicolumn{1}{c}{}\\\cline{1-1}\end{array}$, $\begin{array}{\|c\|c\|}\hline 1\\\hline\multicolumn{1}{c}{}\\\cline{1-1}4\\\cline{1-1}\end{array}$
	3	$\begin{array}{\|c\|c\|c\|}\hline 1&2&3\\\hline\end{array}$	$\begin{bmatrix}1\end{bmatrix}$	3	$\begin{array}{\|c\|c\|c\|c\|}\hline 1&2&3&4\\\hline\end{array}$
		$\begin{array}{\|c\|c\|}\hline 1\\\hline\multicolumn{1}{c}{}\\\cline{1-1}\end{array}$	$\begin{bmatrix}1\end{bmatrix}$	2	$\begin{array}{\|c\|c\|c\|}\hline 1&\multicolumn{1}{c}{}&4\\\hline\multicolumn{1}{c}{}\\\cline{1-1}\end{array}$
	3	$\begin{array}{\|c\|c\|c\|}\hline 1&2&3\\\hline\end{array}$	$\begin{bmatrix}1\end{bmatrix}$	3	$\begin{array}{\|c\|c\|c\|c\|}\hline 1&2&3&4\\\hline\end{array}$
5	0	$\begin{array}{\|c\|c\|c\|}\hline 1&\multicolumn{1}{c}{}&\multicolumn{1}{c}{}\\\hline\multicolumn{1}{c}{}\\\cline{1-1}\end{array}$	$\begin{bmatrix}1\end{bmatrix}$	1	$\begin{array}{\|c\|c\|c\|}\hline 1&\multicolumn{1}{c}{}&\multicolumn{1}{c}{}\\\hline\multicolumn{1}{c}{}\\\cline{1-1}5\\\cline{1-1}\end{array}$
		$\begin{array}{\|c\|c\|}\hline 1\\\hline\multicolumn{1}{c}{}\\\cline{1-1}\multicolumn{1}{c}{}\\\cline{1-1}\end{array}$	$\begin{bmatrix}1\end{bmatrix}$	1	$\begin{array}{\|c\|c\|c\|}\hline 1&\multicolumn{1}{c}{}&5\\\hline\multicolumn{1}{c}{}\\\cline{1-1}\multicolumn{1}{c}{}\\\cline{1-1}\end{array}$
	1	$\begin{array}{\|c\|c\|c\|c\|}\hline 1&2&3&4\\\hline\end{array}$	$\begin{bmatrix}\frac{\sqrt{7}}{\sqrt{15}} & \frac{\sqrt{8}}{\sqrt{15}}\\ \frac{\sqrt{8}}{\sqrt{15}} & \frac{-\sqrt{7}}{\sqrt{15}}\end{bmatrix}$	0,2	$\begin{array}{\|c\|c\|c\|c\|c\|}\hline 1&2&3&4&5\\\hline\end{array}$, $\begin{array}{\|c\|c\|c\|c\|}\hline 1&2&3&4\\\hline 5\\\cline{1-1}\end{array}$
		$\begin{array}{\|c\|c\|c\|}\hline 1&\multicolumn{1}{c}{}&\multicolumn{1}{c}{}\\\hline\multicolumn{1}{c}{}\\\cline{1-1}\end{array}$	$\begin{bmatrix}\frac{\sqrt{2}}{\sqrt{3}} & \frac{1}{\sqrt{3}}\\ \frac{1}{\sqrt{3}} & \frac{-\sqrt{2}}{\sqrt{3}}\end{bmatrix}$	1,2	$\begin{array}{\|c\|c\|c\|c\|c\|}\hline 1&\multicolumn{1}{c}{}&\multicolumn{1}{c}{}&\multicolumn{1}{c}{}&5\\\hline\multicolumn{1}{c}{}\\\cline{1-1}\end{array}$, $\begin{array}{\|c\|c\|c\|}\hline 1&\multicolumn{1}{c}{}&\multicolumn{1}{c}{}\\\hline\multicolumn{1}{c}{}&\multicolumn{1}{c}{}&5\\\cline{2-3}\end{array}$
		$\begin{array}{\|c\|c\|}\hline 1&\multicolumn{1}{c}{}\\\hline\multicolumn{1}{c}{}&4\\\cline{2-2}\end{array}$	$\begin{bmatrix}\frac{-\sqrt{5}}{\sqrt{6}} & \frac{1}{\sqrt{6}}\\ \frac{1}{\sqrt{6}} & \frac{\sqrt{5}}{\sqrt{6}}\end{bmatrix}$	0,2	$\begin{array}{\|c\|c\|c\|c\|}\hline 1&\multicolumn{1}{c}{}&5\\\hline\multicolumn{1}{c}{}&4\\\cline{2-2}\end{array}$, $\begin{array}{\|c\|c\|}\hline 1&\multicolumn{1}{c}{}\\\hline\multicolumn{1}{c}{}&4\\\hline 5\\\cline{1-1}\end{array}$
		$\begin{array}{\|c\|c\|}\hline 1\\\hline\multicolumn{1}{c}{}\\\cline{1-1}\multicolumn{1}{c}{}\\\cline{1-1}\end{array}$	$\begin{bmatrix}1\end{bmatrix}$	1	$\begin{array}{\|c\|c\|}\hline 1\\\hline\multicolumn{1}{c}{}&5\\\cline{2-2}\multicolumn{1}{c}{}\\\cline{1-1}\end{array}$
5	2	$\begin{array}{\|c\|c\|c\|c\|}\hline 1&2&3&4\\\hline\end{array}$	$\begin{bmatrix}1\end{bmatrix}$	2	$\begin{array}{\|c\|c\|c\|c\|}\hline 1&2&3&4\\\hline 5\\\cline{1-1}\end{array}$
		$\begin{array}{\|c\|c\|c\|}\hline 1&\multicolumn{1}{c}{}&\multicolumn{1}{c}{}\\\hline\multicolumn{1}{c}{}\\\cline{1-1}\end{array}$	$\begin{bmatrix}\frac{\sqrt{126}}{15} & \frac{-\sqrt{35}}{15} & \frac{\sqrt{64}}{15}\\ \frac{\sqrt{18}}{\sqrt{45}} & \frac{\sqrt{20}}{\sqrt{45}} & \frac{-\sqrt{7}}{\sqrt{45}}\\ \frac{-1}{5} & \frac{\sqrt{10}}{5} & \frac{\sqrt{14}}{5}\end{bmatrix}$	1,2,3	$\begin{array}{\|c\|c\|c\|c\|c\|}\hline 1&\multicolumn{1}{c}{}&\multicolumn{1}{c}{}&\multicolumn{1}{c}{}&5\\\hline\multicolumn{1}{c}{}\\\cline{1-1}\end{array}$, $\begin{array}{\|c\|c\|c\|c\|}\hline 1&\multicolumn{1}{c}{}&\multicolumn{1}{c}{}&\multicolumn{1}{c}{}\\\hline\multicolumn{1}{c}{}&\multicolumn{1}{c}{}&\multicolumn{1}{c}{}&5\\\cline{2-4}\end{array}$, $\begin{array}{\|c\|c\|c\|}\hline 1&\multicolumn{1}{c}{}&\multicolumn{1}{c}{}\\\hline\multicolumn{1}{c}{}\\\cline{1-1}\multicolumn{1}{c}{}\\\cline{1-1}5\\\cline{1-1}\end{array}$
		$\begin{array}{\|c\|c\|}\hline 1&\multicolumn{1}{c}{}\\\hline\multicolumn{1}{c}{}&4\\\cline{2-2}\end{array}$	$\begin{bmatrix}1\end{bmatrix}$	2	$\begin{array}{\|c\|c\|c\|}\hline 1&\multicolumn{1}{c}{}&5\\\hline\multicolumn{1}{c}{}&4\\\cline{2-2}\end{array}$
		$\begin{array}{\|c\|c\|}\hline 1&\multicolumn{1}{c}{}\\\hline\multicolumn{1}{c}{}\\\cline{1-1}\multicolumn{1}{c}{}\\\cline{1-1}\end{array}$	$\begin{bmatrix}1\end{bmatrix}$	1	$\begin{array}{\|c\|c\|c\|}\hline 1&\multicolumn{1}{c}{}&5\\\hline\multicolumn{1}{c}{}\\\cline{1-1}\multicolumn{1}{c}{}\\\cline{1-1}\end{array}$
	3	$\begin{array}{\|c\|c\|c\|c\|}\hline 1&2&3&4\\\hline\end{array}$	$\begin{bmatrix}\frac{\sqrt{27}}{\sqrt{35}} & \frac{\sqrt{8}}{\sqrt{35}}\\ \frac{\sqrt{8}}{\sqrt{35}} & \frac{-\sqrt{27}}{\sqrt{35}}\end{bmatrix}$	2,4	$\begin{array}{\|c\|c\|c\|c\|c\|}\hline 1&2&3&4&5\\\hline\end{array}$, $\begin{array}{\|c\|c\|c\|c\|}\hline 1&2&3&4\\\hline 5\\\cline{1-1}\end{array}$
		$\begin{array}{\|c\|c\|c\|}\hline 1&\multicolumn{1}{c}{}&\multicolumn{1}{c}{}\\\hline\multicolumn{1}{c}{}\\\cline{1-1}\end{array}$	$\begin{bmatrix}\frac{\sqrt{8}}{3} & \frac{1}{3}\\ \frac{1}{3} & \frac{-\sqrt{8}}{3}\end{bmatrix}$	2,3	$\begin{array}{\|c\|c\|c\|c\|c\|}\hline 1&\multicolumn{1}{c}{}&\multicolumn{1}{c}{}&\multicolumn{1}{c}{}&5\\\hline\multicolumn{1}{c}{}\\\cline{1-1}\end{array}$, $\begin{array}{\|c\|c\|c\|}\hline 1&\multicolumn{1}{c}{}&\multicolumn{1}{c}{}\\\hline\multicolumn{1}{c}{}&\multicolumn{1}{c}{}&5\\\cline{2-3}\end{array}$
		$\begin{array}{\|c\|c\|}\hline 1&\multicolumn{1}{c}{}\\\hline\multicolumn{1}{c}{}&4\\\cline{2-2}\end{array}$	$\begin{bmatrix}-1\end{bmatrix}$	2	$\begin{array}{\|c\|c\|c\|}\hline 1&\multicolumn{1}{c}{}&5\\\hline\multicolumn{1}{c}{}&4\\\cline{2-2}\end{array}$
	4	$\begin{array}{\|c\|c\|c\|c\|}\hline 1&2&3&4\\\hline\end{array}$	$\begin{bmatrix}1\end{bmatrix}$	4	$\begin{array}{\|c\|c\|c\|c\|}\hline 1&2&3&4\\\hline 5\\\cline{1-1}\end{array}$
		$\begin{array}{\|c\|c\|c\|}\hline 1&\multicolumn{1}{c}{}&\multicolumn{1}{c}{}\\\hline\multicolumn{1}{c}{}\\\cline{1-1}\end{array}$	$\begin{bmatrix}1\end{bmatrix}$	3	$\begin{array}{\|c\|c\|c\|c\|}\hline 1&\multicolumn{1}{c}{}&\multicolumn{1}{c}{}&5\\\hline\multicolumn{1}{c}{}\\\cline{1-1}\end{array}$
	5	$\begin{array}{\|c\|c\|c\|c\|}\hline 1&2&3&4\\\hline\end{array}$	$\begin{bmatrix}1\end{bmatrix}$	4	$\begin{array}{\|c\|c\|c\|c\|c\|}\hline 1&2&3&4&5\\\hline\end{array}$
6	0	$\begin{array}{\|c\|c\|c\|c\|c\|}\hline 1&2&3&4&5\\\hline\end{array}$	$\begin{bmatrix}1\end{bmatrix}$	1	$\begin{array}{\|c\|c\|c\|c\|c\|c\|}\hline 1&2&3&4&5&6\\\hline\end{array}$
		$\begin{array}{\|c\|c\|c\|c\|}\hline 1&\multicolumn{1}{c}{}&\multicolumn{1}{c}{}&\multicolumn{1}{c}{}\\\hline\multicolumn{1}{c}{}\\\cline{1-1}\end{array}$	$\begin{bmatrix}1\end{bmatrix}$	1	$\begin{array}{\|c\|c\|c\|c\|}\hline 1&\multicolumn{1}{c}{}&\multicolumn{1}{c}{}&\multicolumn{1}{c}{}\\\hline\multicolumn{1}{c}{}&6\\\cline{2-2}\end{array}$
		$\begin{array}{\|c\|c\|c\|}\hline 1&\multicolumn{1}{c}{}&\multicolumn{1}{c}{}\\\hline\multicolumn{1}{c}{}&\multicolumn{1}{c}{}\\\cline{1-2}\end{array}$	$\begin{bmatrix}-1\end{bmatrix}$	1	$\begin{array}{\|c\|c\|c\|c\|}\hline 1&\multicolumn{1}{c}{}&\multicolumn{1}{c}{}&6\\\hline\multicolumn{1}{c}{}&\multicolumn{1}{c}{}&\multicolumn{1}{c}{}\\\cline{2-3}\end{array}$
		$\begin{array}{\|c\|c\|c\|}\hline 1&\multicolumn{1}{c}{}&\multicolumn{1}{c}{}\\\hline\multicolumn{1}{c}{}&\multicolumn{1}{c}{}\\\cline{1-2}\multicolumn{1}{c}{}\\\cline{1-1}\end{array}$	$\begin{bmatrix}1\end{bmatrix}$	1	$\begin{array}{\|c\|c\|c\|}\hline 1&\multicolumn{1}{c}{}&\multicolumn{1}{c}{}\\\hline\multicolumn{1}{c}{}&\multicolumn{1}{c}{}&\multicolumn{1}{c}{}\\\cline{2-3}\multicolumn{1}{c}{}&6\\\cline{2-2}\end{array}$
	1	$\begin{array}{\|c\|c\|c\|c\|c\|}\hline 1&2&3&4&5\\\hline\end{array}$	$\begin{bmatrix}1\end{bmatrix}$	1	$\begin{array}{\|c\|c\|c\|c\|c\|}\hline 1&2&3&4&5\\\hline 6\\\cline{1-1}\end{array}$
		$\begin{array}{\|c\|c\|c\|c\|}\hline 1&\multicolumn{1}{c}{}&\multicolumn{1}{c}{}&\multicolumn{1}{c}{}\\\hline\multicolumn{1}{c}{}\\\cline{1-1}\end{array}$	$\begin{bmatrix}\frac{\sqrt{7}}{\sqrt{12}} & \frac{-\sqrt{5}}{\sqrt{12}}\\ \frac{\sqrt{5}}{\sqrt{12}} & \frac{\sqrt{7}}{\sqrt{12}}\end{bmatrix}$	1,2	$\begin{array}{\|c\|c\|c\|c\|c\|c\|}\hline 1&\multicolumn{1}{c}{}&\multicolumn{1}{c}{}&\multicolumn{1}{c}{}&\multicolumn{1}{c}{}&6\\\hline\multicolumn{1}{c}{}\\\cline{1-1}\end{array}$, $\begin{array}{\|c\|c\|c\|c\|c\|}\hline 1&\multicolumn{1}{c}{}&\multicolumn{1}{c}{}&\multicolumn{1}{c}{}&\multicolumn{1}{c}{}\\\hline\multicolumn{1}{c}{}&\multicolumn{1}{c}{}&\multicolumn{1}{c}{}&\multicolumn{1}{c}{}&6\\\cline{2-5}\end{array}$
		$\begin{array}{\|c\|c\|c\|}\hline 1&\multicolumn{1}{c}{}&\multicolumn{1}{c}{}\\\hline\multicolumn{1}{c}{}&\multicolumn{1}{c}{}\\\cline{1-2}\end{array}$	$\begin{bmatrix}\frac{\sqrt{2}}{\sqrt{3}} & \frac{-1}{\sqrt{3}}\\ \frac{1}{\sqrt{3}} & \frac{\sqrt{2}}{\sqrt{3}}\end{bmatrix}$	1,2	$\begin{array}{\|c\|c\|c\|c\|}\hline 1&\multicolumn{1}{c}{}&\multicolumn{1}{c}{}&\multicolumn{1}{c}{}\\\hline\multicolumn{1}{c}{}&\multicolumn{1}{c}{}&\multicolumn{1}{c}{}&6\\\cline{2-4}\end{array}$, $\begin{array}{\|c\|c\|c\|}\hline 1&\multicolumn{1}{c}{}&\multicolumn{1}{c}{}\\\hline\multicolumn{1}{c}{}&\multicolumn{1}{c}{}&\multicolumn{1}{c}{}\\\cline{2-3}\multicolumn{1}{c}{}&6\\\cline{2-2}\end{array}$
		$\begin{array}{\|c\|c\|c\|}\hline 1&\multicolumn{1}{c}{}&\multicolumn{1}{c}{}\\\hline\multicolumn{1}{c}{}\\\cline{1-1}\multicolumn{1}{c}{}\\\cline{1-1}\end{array}$	$\begin{bmatrix}\frac{\sqrt{5}}{3} & \frac{2}{3}\\ \frac{2}{3} & \frac{-\sqrt{5}}{3}\end{bmatrix}$	0,2	$\begin{array}{\|c\|c\|c\|c\|c\|}\hline 1&\multicolumn{1}{c}{}&\multicolumn{1}{c}{}&\multicolumn{1}{c}{}&6\\\hline\multicolumn{1}{c}{}\\\cline{1-1}\end{array}$, $\begin{array}{\|c\|c\|c\|}\hline 1&\multicolumn{1}{c}{}&\multicolumn{1}{c}{}\\\hline\multicolumn{1}{c}{}&\multicolumn{1}{c}{}&6\\\cline{2-3}\multicolumn{1}{c}{}\\\cline{1-1}\end{array}$
		$\begin{array}{\|c\|c\|}\hline 1&\multicolumn{1}{c}{}\\\hline\multicolumn{1}{c}{}\\\cline{1-1}\multicolumn{1}{c}{}\\\cline{1-1}\end{array}$	$\begin{bmatrix}1\end{bmatrix}$	1	$\begin{array}{\|c\|c\|c\|}\hline 1&\multicolumn{1}{c}{}&6\\\hline\multicolumn{1}{c}{}\\\cline{1-1}\multicolumn{1}{c}{}\\\cline{1-1}\end{array}$
	2	$\begin{array}{\|c\|c\|c\|c\|c\|}\hline 1&2&3&4&5\\\hline\end{array}$	$\begin{bmatrix}\frac{\sqrt{15}}{5} & \frac{\sqrt{10}}{5}\\ \frac{\sqrt{10}}{5} & \frac{-\sqrt{15}}{5}\end{bmatrix}$	1,3	$\begin{array}{\|c\|c\|c\|c\|c\|c\|}\hline 1&2&3&4&5&6\\\hline\end{array}$, $\begin{array}{\|c\|c\|c\|c\|c\|}\hline 1&2&3&4&5\\\hline 6\\\cline{1-1}\end{array}$
		$\begin{array}{\|c\|c\|c\|c\|}\hline 1&\multicolumn{1}{c}{}&\multicolumn{1}{c}{}&\multicolumn{1}{c}{}\\\hline\multicolumn{1}{c}{}\\\cline{1-1}\end{array}$	$\begin{bmatrix}\frac{\sqrt{63}}{\sqrt{120}} & \frac{\sqrt{25}}{\sqrt{120}} & \frac{\sqrt{32}}{\sqrt{120}}\\ \frac{-\sqrt{9}}{\sqrt{240}} & \frac{\sqrt{175}}{\sqrt{240}} & \frac{-\sqrt{56}}{\sqrt{240}}\\ \frac{\sqrt{7}}{4} & \frac{-1}{4} & \frac{-\sqrt{8}}{4}\end{bmatrix}$	1,2,3	$\begin{array}{\|c\|c\|c\|c\|c\|c\|}\hline 1&\multicolumn{1}{c}{}&\multicolumn{1}{c}{}&\multicolumn{1}{c}{}&\multicolumn{1}{c}{}&6\\\hline\multicolumn{1}{c}{}\\\cline{1-1}\end{array}$, $\begin{array}{\|c\|c\|c\|c\|c\|}\hline 1&\multicolumn{1}{c}{}&\multicolumn{1}{c}{}&\multicolumn{1}{c}{}&\multicolumn{1}{c}{}\\\hline\multicolumn{1}{c}{}&6\\\cline{2-2}\end{array}$ I, $\begin{array}{\|c\|c\|c\|c\|c\|}\hline 1&\multicolumn{1}{c}{}&\multicolumn{1}{c}{}&\multicolumn{1}{c}{}&\multicolumn{1}{c}{}\\\hline\multicolumn{1}{c}{}&6\\\cline{2-2}\multicolumn{1}{c}{}\\\cline{1-1}\end{array}$ II
		$\begin{array}{\|c\|c\|c\|}\hline 1&\multicolumn{1}{c}{}&\multicolumn{1}{c}{}\\\hline\multicolumn{1}{c}{}\\\cline{1-1}\end{array}$	$\begin{bmatrix}\frac{\sqrt{18}}{\sqrt{30}} & \frac{-\sqrt{5}}{\sqrt{30}} & \frac{-\sqrt{7}}{\sqrt{30}}\\ \frac{\sqrt{14}}{\sqrt{50}} & \frac{\sqrt{35}}{\sqrt{50}} & \frac{1}{\sqrt{50}}\\ \frac{-\sqrt{9}}{\sqrt{75}} & \frac{\sqrt{10}}{\sqrt{75}} & \frac{-\sqrt{56}}{\sqrt{75}}\end{bmatrix}$	1,2,3	$\begin{array}{\|c\|c\|c\|c\|c\|c\|}\hline 1&\multicolumn{1}{c}{}&\multicolumn{1}{c}{}&\multicolumn{1}{c}{}&\multicolumn{1}{c}{}&6\\\hline\multicolumn{1}{c}{}\\\cline{1-1}\end{array}$ I, $\begin{array}{\|c\|c\|c\|c\|c\|c\|}\hline 1&\multicolumn{1}{c}{}&\multicolumn{1}{c}{}&\multicolumn{1}{c}{}&\multicolumn{1}{c}{}&6\\\hline\multicolumn{1}{c}{}&\multicolumn{1}{c}{}\\\cline{2-2}\end{array}$ II, $\begin{array}{\|c\|c\|c\|}\hline 1&\multicolumn{1}{c}{}&\multicolumn{1}{c}{}\\\hline\multicolumn{1}{c}{}\\\cline{1-1}\multicolumn{1}{c}{}\\\cline{1-1}6\\\cline{1-1}\end{array}$

TABLE VIII. Explicit values of fractional parentage coefficients absent in Table VII. Empty boxes in the standard Young tableaux $\tau^{[g-1]}$ have to be filled with all possible values as detailed in Table VI.

g	$j^{[g]}$	$\tau^{[g-1]}$	Transf. matrix	Input $j^{[g-1]}$	Output $\tau^{[g]}$ and $\mathcal{A}$
6	2	$\begin{array}{|c\|\cr\hline\cr\hline\cr\hline\end{array}$	$\begin{bmatrix}1\end{bmatrix}$	2	$\begin{array}{|c\|\cr\hline 6\cr\hline\cr\hline\end{array}$
		$\begin{array}{|c\|\cr\hline\cr\hline\cr\hline\end{array}$	$\begin{bmatrix}1\end{bmatrix}$	1	$\begin{array}{|c\|c\|\cr\hline\cr\hline\cr\hline\end{array}$
	3	$\begin{array}{\|c\|c\|c\|c\|c\|}\hline 1&2&3&4&5\\\hline\end{array}$	$\begin{bmatrix}1\end{bmatrix}$	3	$\begin{array}{\|c\|c\|c\|c\|c\|\cr\hline 6\cr\hline\end{array}$
		$\begin{array}{|c\|c\|c\|\cr\hline\cr\hline\end{array}$	$\begin{bmatrix}\frac{-\sqrt{80}}{\sqrt{112}} & \frac{\sqrt{7}}{\sqrt{112}} & \frac{-\sqrt{25}}{\sqrt{112}}\\ \frac{\sqrt{80}}{\sqrt{336}} & \frac{\sqrt{175}}{\sqrt{336}} & \frac{-\sqrt{81}}{\sqrt{336}}\\ \frac{-\sqrt{4}}{\sqrt{84}} & \frac{\sqrt{35}}{\sqrt{84}} & \frac{\sqrt{45}}{\sqrt{84}}\end{bmatrix}$	2,3,4	$\begin{array}{\|c\|c\|c\|c\|c\|\cr\hline\cr\hline\end{array}$, $\begin{array}{\|c\|c\|c\|c\|\cr\hline\cr\hline 6\cr\hline\end{array}$, $\begin{array}{\|c\|c\|c\|c\|\cr\hline\cr\hline\cr\hline 6\cr\hline\end{array}$
		$\begin{array}{|c\|c\|\cr\hline\cr\hline\end{array}$	$\begin{bmatrix}\frac{\sqrt{2}}{\sqrt{3}} & \frac{-1}{\sqrt{3}}\\ \frac{1}{\sqrt{3}} & \frac{\sqrt{2}}{\sqrt{3}}\end{bmatrix}$	2,3	$\begin{array}{\|c\|c\|c\|c\|c\|\cr\hline\cr\hline\end{array}$, $\begin{array}{\|c\|c\|c\|c\|\cr\hline\cr\hline 6\cr\hline\end{array}$
		$\begin{array}{|c\|c\|\cr\hline\cr\hline\cr\hline\end{array}$	$\begin{bmatrix}1\end{bmatrix}$	2	$\begin{array}{\|c\|c\|c\|c\|c\|\cr\hline\cr\hline\cr\hline\end{array}$
6	4	$\begin{array}{\|c\|c\|c\|c\|c\|}\hline 1&2&3&4&5\\\hline\end{array}$	$\begin{bmatrix}\frac{\sqrt{22}}{\sqrt{27}} & \frac{\sqrt{5}}{\sqrt{27}}\\ \frac{\sqrt{5}}{\sqrt{27}} & \frac{-\sqrt{22}}{\sqrt{27}}\end{bmatrix}$	3,5	$\begin{array}{\|c\|c\|c\|c\|c\|c\|\cr\hline\cr\hline\end{array}$, $\begin{array}{\|c\|c\|c\|c\|c\|\cr\hline\cr\hline 6\cr\hline\end{array}$
		$\begin{array}{\|c\|c\|c\|\cr\hline\cr\hline\end{array}$	$\begin{bmatrix}\frac{\sqrt{15}}{4} & \frac{1}{4}\\ \frac{1}{4} & \frac{-\sqrt{15}}{4}\end{bmatrix}$	3,4	$\begin{array}{\|c\|c\|c\|c\|c\|\cr\hline\cr\hline\end{array}$, $\begin{array}{\|c\|c\|c\|c\|\cr\hline\cr\hline 6\cr\hline\end{array}$
		$\begin{array}{\|c\|c\|\cr\hline\cr\hline\cr\hline\end{array}$	$\begin{bmatrix}1\end{bmatrix}$	3	$\begin{array}{\|c\|c\|c\|\cr\hline\cr\hline\end{array}$
	5	$\begin{array}{\|c\|c\|c\|c\|c\|}\hline 1&2&3&4&5\\\hline\end{array}$	$\begin{bmatrix}1\end{bmatrix}$	5	$\begin{array}{\|c\|c\|c\|c\|c\|\cr\hline 6\cr\hline\end{array}$
		$\begin{array}{\|c\|c\|c\|c\|\cr\hline\cr\hline\end{array}$	$\begin{bmatrix}1\end{bmatrix}$	4	$\begin{array}{\|c\|c\|c\|c\|c\|\cr\hline\cr\hline\end{array}$
	6	$\begin{array}{\|c\|c\|c\|c\|c\|}\hline 1&2&3&4&5\\\hline\end{array}$	$\begin{bmatrix}1\end{bmatrix}$	5	$\begin{array}{\|c\|c\|c\|c\|c\|c\|\cr\hline\cr\hline\end{array}$

heteronuclear experiments to maximize polarization transfer. Its efficiency depends extremely on the mixing time duration. For four coupled spins 1/2, the ideal isotropic mixing Hamiltonian has the form $H = 2\pi \sum_{i<j}^{4} \mathrm{J}_{ij}(I_{ix}I_{jx} + I_{iy}I_{jy} + I_{iz}I_{jz})$. For the model system consisting of the ^{1}H nuclear spins of trans-phenylcyclopropane carboxylic acid, the coupling constants are given by $\mathrm{J}_{12} = 4.1$ Hz, $\mathrm{J}_{13} = 9.4$ Hz, $\mathrm{J}_{14} = 6.8$ Hz, $\mathrm{J}_{23} = 5.3$ Hz, $\mathrm{J}_{24} = 8.2$ Hz, and $\mathrm{J}_{34} = -4.6$ Hz. Starting with the initial density density operator $\rho(0) = I_{1z}$, Fig. 8(c1)-(c4) shows the DROPS representation of the states for different mixing times: (c1) 0 ms, (c2) 20 ms, (c3) 40 ms, and (c4) 133 ms. Again, nodes represent the particles and edges their couplings. Note that for simplicity, here we only plotted the linear and bilinear tensor components. During the course of the experiment, the free evolution under isotropic mixing conditions results in the generation of coherences, which is reflected by the occurrence of non-vanishing bilinear tensors ($g = 2$) and visualized by droplets located on the edges. Also small amounts of polarization occurs on the other spins depicted by the droplet functions on these nodes. After 133 ms [panel (c4)], almost all polarization has been transferred from spin one to spin two.

3. Representing systems consisting of five and six coupled spins 1/2 systems

We also show the droplet functions for a (complex) random matrix $A \in \mathbb{C}^{32\times 32}$ for a five-spin-1/2 system. Although such systems are quite complex, with our approach, we can conveniently partition the information in different subsystems given by the panels and subpanels in Fig. 9. We find one zero-linear subsystem $G = \emptyset$ with one droplet, five linear subsystems with one droplet in each $G \in \{\{1\},\{2\},\{3\},\{4\},\{5\}\}$, and ten bilinear subsystems with also one droplet in each $G \in \{\{1,2\},\{1,3\},\{1,4\},\{1,5\},\{2,3\},\{2,4\},\{2,5\},\{3,4\},\{3,5\},\{4,5\}\}$. They can be plotted together as shown in the upper left panel of Fig. 9, where the droplets visualizing the linear subsystems are plotted on the corresponding nodes representing the spins and the droplet functions for the bilinear subsystems are placed on the edges between two spins. The identity part (Id) is placed beneath this scheme. In the upper right panel, the ten trilinear subsystems $G \in \{\{1,2,3\},\{1,2,4\},\{1,2,5\},\{1,3,4\},\{1,3,5\},\{1,4,5\},\{2,3,4\},\{2,3,5\},\{2,4,5\},\{3,4,5\}\}$, each represented by four droplets. The topology of the involved spins of each subsystem are symbolized by the sketch at the top of each subpanel. The bottom left panel shows the five four-linear subsystems with nine droplets for each $G \in \{\{1,2,3,4\},\{1,2,3,5\},\{1,2,4,5\},\{1,3,4,5\},\{2,3,4,5\}\}$. Again, the subsystem is graphically given at the beginning of each subpanel. Finally, the 5-linear subsystem with 21 droplets is illustrated in the bottom right panel of Fig. 9. In total we have 122 droplet functions uniquely representing the matrix A. Note that we omit the superscript $[g]$ for $\tau^{[G]}$ in this figure, since $g = |G|$ holds and G is clear from the context.

We conclude this section by visualizing a (complex) random matrix $A \in \mathbb{C}^{64\times 64}$ for a six coupled spins 1/2 as given in Fig. 10. The information can be analogously partitioned and presented as given in Fig. 9. In the upper left panel, the topology of the system is sketched. The zero-linear subsystem containing one droplet can be located beneath the

scheme. The droplet functions representing the six linear subsystems $G \in \{\{1\},\{2\},\{3\},\{4\},\{5\},\{6\}\}$ are plotted on the nodes, the droplet functions of the fifteen bilinear subsystems with also one droplet in each $G \in \binom{\{1,\ldots,6\}}{2}$ are plotted on the edges. The droplet functions of the six-linear system $G = \{1,2,3,4,5,6\}$ are shown in the upper right panel. The panel in the center presents the twenty trilinear subsystems $G \in \binom{\{1,\ldots,6\}}{3}$ with the related droplet functions. The droplets of the 5-linear systems $G \in \binom{\{1,\ldots,6\}}{5}$ are plotted in the bottom panels of Fig. 10. Finally, the 4-linear subsystems $G \in \binom{\{1,\ldots,6\}}{4}$ with the nine corresponding droplets for each G are given in Fig. 11. In total we find 423 droplets, which uniquely represents the information contained in the $64^2 = 4096$ complex matrix elements of such an operator. Again, we omit the superscript $[g]$ for τ in this figure and we use the additional *ad hoc* sublabels only when required, i.e., for $g = 6$ and $\tau_i^{[6]}$ with $i \in \{7,\ldots,15\}$. The standard Young tableaux for $g = 5$ and $g = 6$ are summarized in Table VI.

B. Explicit values of the fractional parentage coefficients

The explicit values of the fractional parentage coefficients for up to $g = 6$ are given in Tables VII and VII. We have used the fractional parentage coefficients as defined in Ref. 60, and we have *not* applied the phase amendments from the footnote on p. 241 of Ref. 129.

[1] R. P. Feynman, F. L. Vernon, Jr., and R. W. Hellwarth, "Geometrical Representation of the Schrödinger Equation for Solving Maser Problems," J. Appl. Phys. **28**, 49–52 (1957).
[2] M. A. Bernstein, K. F. King, and X. J. Zhou, *Handbook of MRI Pulse Sequences* (Elsevier, Burlington-San Diego-London, 2004).
[3] R. R. Ernst, G. Bodenhausen, and A. Wokaun, *Principles of Nuclear Magnetic Resonance in One and Two Dimensions* (Clarendon Press, Oxford, 1987).
[4] W. P. Schleich, *Quantum Optics in Phase Space* (Wiley-VCH, Weinheim, 2001).
[5] M. A. Nielsen and I. L. Chuang, *Quantum Computation and Quantum Information* (Cambridge University Press, Cambridge (UK), 2000).
[6] O. W. Sørensen, G. W. Eich, M. H. Levitt, G. Bodenhausen, and R. R. Ernst, "Product operator formalism for the description of nmr pulse experiments," Progr. NMR Spectrosc. **16**, 163–192 (1983).
[7] D. G. Donne and D. G. Gorenstein, "A Pictorial Representation of Product Operator Formalism: Nonclassical Vector Diagrams for Multidimensional NMR," Concepts Magn. Reson. **9**, 95–111 (1997).
[8] R. Freeman, *A Handbook of Nuclear Magnetic Resonance*, 2nd ed. (Addison Wesley Longman, Harlow, 1997).
[9] T. L. Curtright, D. B. Fairlie, and C. K. Zachos, *A Concise Treatise on Quantum Mechanics in Phase Space* (World Scientific, Singapore, 2014).
[10] C. K. Zachos, D. B. Fairlie, and T. L. Curtright, *Quantum Mechanics in Phase Space: An Overview with Selected Papers* (World Scientific, Singapore, 2005).
[11] F. E. Schroeck Jr., *Quantum Mechanics on Phase Space* (Springer, Dordrecht, 2013).
[12] E. Wigner, "On the Quantum Correction For Thermodynamic Equilibrium," Phys. Rev. **40**, 749–759 (1932).
[13] D. T. Smithey, M. Beck, M. G. Raymer, and A. Faridani, "Measurement of the Wigner distribution and the density matrix of a light mode using optical homodyne tomography: Application to squeezed states and the vacuum," Phys. Rev. Lett. **70**, 1244–1247 (1993).
[14] D. T. Smithey, M. Beck, J. Cooper, M. G. Raymer, and A. Faridani, "Complete experimental characterization of the quantum state of a light mode via the wigner function and the density matrix: application to quantum phase distributions of vacuum and squeezed-vacuum states," Phys. Scripta **1993**, 35 (1993).
[15] D. T. Smithey, M. Beck, J. Cooper, and M. G. Raymer, "Measurement of number-phase uncertainty relations of optical fields," Phys. Rev. A **48**, 3159–3167 (1993).
[16] U. Leonhardt, *Measuring the Quantum State of Light* (Cambridge University Press, Cambridge, 1997).
[17] M. Paris and J. Rehacek, eds., *Quantum State Estimation* (Springer, Berlin, 2004).
[18] W. K. Wooters, "A Wigner-Function Formulation of Finite-State Quantum Mechanics," Ann. Phys. **176**, 1–21 (1987).
[19] U. Leonhardt, "Discrete Wigner function and quantum-state tomography," Phys. Rev. A **53**, 2998 (1996).
[20] C. Miquel, J. P. Paz, and M. Saraceno, "Quantum computers in phase space," Phys. Rev. A **65**, 062309 (2002).
[21] C. Miquel, J. P. Paz, M. Saraceno, E. Knill, R. Laflamme, and C. Negrevergne, "Interpretation of tomography and spectroscopy as dual forms of quantum computation," Nature **418**, 59–62 (2002).
[22] K. S. Gibbons, M. J. Hoffman, and W. K. Wootters, "Discrete phase space based on finite fields," Phys. Rev. A **70**, 062101 (2004).
[23] C. Ferrie and J. Emerson, "Framed Hilbert space: hanging the quasi-probability pictures of quantum theory," New J. Phys. **11**, 063040 (2009).
[24] R. L. Stratonovich, "On distributions in Representation Space," JETP. (U.S.S.R.) **31**, 1012–1020 (1956).
[25] G. S. Agarwal, "Relation between atomic coherent-state representation, state multipoles, and generalized phase-space distributions," Phys. Rev. A **24**, 2889–2896 (1981).
[26] J. C. Várrily and J. M. Garcia-Bondía, "The Moyal representation for spin," Ann. Phys. **190**, 107–148 (1989).
[27] C. Brif and A. Mann, "Phase-space formulation of quantum mechanics and quantum-state reconstruction for physical systems with Lie-group symmetries," Phys. Rev. A **59**, 971 (1999).
[28] C. Brif and A. Mann, "A general theory of phase-space quasiprobability distributions," J. Phys. A: Math. Gen. **31**, L9–L17 (1997).
[29] S. Heiss and S. Weigert, "Discrete Moyal-type representations for a spin," Phys. Rev. A **63**, 012105 (2000).
[30] A. Klimov, "Exact evolution equations for SU(2) quasidistribution functions," J. Math. Phys. **43**, 2202–2213 (2002).
[31] A. Klimov and P. Espinoza, "Classical evolution of quantum fluctuations in spin-like systems: squeezing and entanglement," J. Opt. B **7**, 183 (2005).

[32]A. B. Klimov and P. Espinoza, "Moyal-like form of the star product for generalized SU(2) Stratonovich-Weyl symbols," J. Phys. A **35**, 8435 (2002).
[33]J. P. Dowling, G. S. Agarwal, and W. P. Schleich, "Wigner distribution of a general angular-momentum state: Applications to a collection of two-level atoms," Phys. Rev. A **49**, 4101–4109 (1994).
[34]P. S. Jessen, D. L. Haycock, G. Klose, G. A. Smith, I. H. Deutsch, and G. K. Brennen, "Quantum control and information processing in optical lattices," Quant. Inf. Computation **1**, 20–32 (2001).
[35]D. J. Philp and P. W. Kuchel, "A Way of Visualizing NMR Experiments on Quadrupolar Nuclei," Concepts Magn. Reson. A **25A**, 40–52 (2005).
[36]D. Harland, M. J. Everitt, K. Nemoto, T. Tilma, and T. P. Spiller, "Towards a complete and continious Wigner function for an ensemble of spins or qubits," Phys. Rev. A **86**, 062117 (2012).
[37]A. Garon, R. Zeier, and S. J. Glaser, "Visualizing operators of coupled spin systems," Phys. Rev. A **91**, 042122 (2015).
[38]T. Tilma, M. J. Everitt, J. H. Samson, W. J. Munro, and K. Nemoto, "Wigner functions for arbitrary quantum systems," Phys. Rev. Lett. **117**, 180401 (2016).
[39]B. Koczor, R. Zeier, and S. J. Glaser, "Time evolution of coupled spin systems in a generalized Wigner representation," (2016), (*Preprint* `arXiv:1612.06777v2`), arXiv:1808.02697.
[40]R. P. Rundle, P. W. Mills, T. Tilma, J. H. Samson, and M. J. Everitt, "Simple procedure for phase-space measurement and entanglement validation," Phys. Rev. A **96**, 022117 (2017).
[41]R. P. Rundle, T. Tilma, J. H. Samson, V. M. Dwyer, R. F. Bishop, and M. J. Everitt, "A general approach to quantum mechanics as a statistical theory," (2017), arXiv:1708.03814v3.
[42]B. Koczor, R. Zeier, and S. J. Glaser, "Continuous phase-space representations for finite-dimensional quantum states and their tomography," (2017), arXiv:1711.07994v2.
[43]B. Koczor, R. Zeier, and S. J. Glaser, "Continuous phase spaces and the time evolution of spins: star products and spin-weighted spherical harmonics," (2018), arXiv:1808.02697.
[44]D. Leiner, R. Zeier, and S. J. Glaser, "Wigner tomography of multispin quantum states," Phys. Rev. A **96**, 063413 (2017).
[45]D. Leiner and S. J. Glaser, "Wigner process tomography: Visualization of spin propagators and their spinor properties," Phys. Rev. A **98**, 012112 (2018).
[46]J. D. Jackson, *Classical Electrodynamics*, 3rd ed. (John Wiley & Sons, New York, 1999).
[47]G. D. James, *The Representation Theory of the Symmetric Group* (Springer, Berlin, 1978).
[48]G. James and A. Kerber, *The Representation Theory of the Symmetric Group* (Addison-Wesley, Reading, MA, 1981).
[49]T. Ceccherini-Silberstein, F. Scarabotti, and F. Tolli, *Representation Theory of the Symmetric Groups* (Cambridge University Press, Cambridge, 2010).
[50]H. Boerner, *Darstellungen von Gruppen*, 2nd ed. (Springer, Berlin, 1967).
[51]M. Hamermesh, *Group Theory* (Addison-Wesley, Reading, MA, 1962).
[52]B. E. Sagan, *The Symmetric Group*, 2nd ed. (Springer, New York, 2001).
[53]W. K. Tung, *Group Theory in Physics* (World Scientific Publishing Company, Incorporated, 1985).
[54]G. Racah, "Group Theory and Spectroscopy," in *Ergebnisse der exakten Naturwissenschaften, 37. Band* (Springer, Berlin, 1965) pp. 28–84.
[55]J. P. Elliott and A. M. Lane, "The Nuclear Shell-Model," in *Encyclopedia of Physics, Volume XXXIX, Structure of Atomic Nuclei* (Springer, Berlin, 1957) pp. 241–410.
[56]I. G. Kaplan, *Symmetry of Many-Electron Systems* (Academic Press, New York, 1975).
[57]B. L. Silver, *Irreducible Tensor Methods* (Academic Press, New York, 1976).
[58]C. D. H. Chisholm, *Group Theoretical Techniques in Quantum Chemistry* (Academic Press, London, 1976).
[59]P. Kramer, G. John, and D. Schenzle, *Group Theory and the Interaction of Composite Nucleon Systems* (Vieweg, Braunschweig, 1981).
[60]H. A. Jahn and H. van Wieringen, "Theoretical studies in nuclear structure IV. Wave functions for the nuclear p-shell Part A. $\langle p^n | p^{n-1} p \rangle$ fractional parentage coefficients," Proc. R. Soc. Lond. A **209**, 502–524 (1951).
[61]H. Weyl, "Quantenmechanik und Gruppentheorie," Z. Phys. **46**, 1–33 (1927).
[62]H. Weyl, *Gruppentheorie und Quantenmechanik*, 2nd ed. (Hirzel, Leipzig, 1931) english translation in[63].
[63]H. Weyl, *The Theory of Groups & Quantum Mechanics*, 2nd ed. (Dover Publ., New York, 1950).
[64]H. Weyl, *The Classical Groups: Their Invariants and Representations*, 2nd ed. (Princeton University Press, Princeton, 1953).
[65]E. Wigner, *Gruppentheorie und ihre Anwendung auf die Quantenmechanik der Atomspektren* (Friedrich Vieweg & Sohn, Braunschweig, 1931) (English translation in[66]).
[66]E. P. Wigner, *Group Theory and its Application to the Quantum Mechanics of Atomic Spectra* (Academic Press, London, 1959).
[67]E. U. Condon and G. H. Shortley, *The Theory of Atomic Spectra* (Cambridge University Press, Cambridge, 1935).
[68]G. Racah, "Theory of Complex Spectra I," Phys. Rev. **61**, 186–197 (1941).
[69]G. Racah, "Theory of Complex Spectra II," Phys. Rev. **62**, 438–462 (1942).
[70]G. Racah, "Theory of Complex Spectra III," Phys. Rev. **63**, 367–382 (1943).
[71]G. Racah, "Theory of Complex Spectra IV," Phys. Rev. **76**, 1353–1365 (1949).
[72]U. Fano and G. Racah, *Irreducible Tensorial Sets* (Academic Press, New York, 1959).
[73]A. R. Edmonds, *Angular momentum in quantum mechanics* (Princeton University Press, Princeton, 1960).
[74]J. S. Griffith, *The Irreducible Tensor Method for Molecular Symmetry Groups* (Dover Publications, Mineola, NY, 2006).
[75]B. R. Judd, *Operator Techniques in Atomic Spectroscopy* (Princeton University Press, Princeton, 1998).
[76]W. Miller, *Symmetry Groups and Their Applications*, Pure and Applied Mathematics (Academic Press, London, 1972).
[77]W. Ludwig and C. Falter, *Symmetries in Physics*, 2nd ed. (Springer, Berlin, 1996).
[78]J. C. Slater, *Quantum Theory of Atomic Structure, Vol. II* (McGraw-Hill, New York, 1960).
[79]A. de-Shalit and I. Talmi, *Nuclear Shell Theory* (Academic Press, New York, 1963).
[80]R. Pauncz, *Alternant Molecular Orbital Method* (W. B. Saunders Company, Philadelphia, 1967).
[81]B. G. Wybourne, *Symmetry Principles and Atomic Spectroscopy* (Wiley-Interscience, New York, 1970).
[82]J. P. Elliott and P. G. Dawber, *Symmetry in Physics, 2 Volumes* (Macmillan, Hampshire, 1979).
[83]E. U. Condon and H. Odabaşi, *Atomic Structure* (Cambridge University Press, Cambridge, 1980).
[84]Z. Rudzikas, *Theoretical Atomic Spectroscopy* (Cambrdige University Press, Cambridge, 1997).

[85]M. Chaichian and R. Hagedorn, *Symmetries in Quantum Mechanics: From Angular Momentum to Supersymmetry* (Institute of Physics, Bristol, 1998).
[86]D. J. Rowe and J. L. Wood, *Fundamentals of Nuclear Models: Foundational Models* (World Scientific Publ., Singapore, 2010).
[87]J. Listerud, *Techniques in Solid State NMR*, Ph.D. thesis, University of Washington (1987).
[88]J. Listerud, S. J. Glaser, and G. P. Drobny, "Symmetry and Isotropic Coherence Transfer. II. Three Spin Calculations Using a Young Tableaux Formulation," Mol. Phys. **78**, 629–658 (1993).
[89]L. C. Biedenharn and J. D. Louck, *Angular Momentum in Quantum Physics* (Addison-Wesley, Reading, MA, 1981).
[90]Spherical harmonics $Y_{jm}(\theta,\phi) = r(\theta,\phi)\exp[i\eta(\theta,\phi)]$ (and droplet functions) are plotted throughout this work by mapping their spherical coordinates θ and ϕ to the radial part $r(\theta,\phi)$ and phase $\eta(\theta,\phi)$.
[91]B. R. Judd, W. Miller, Jr., J. Patera, and P. Winternitz, "Complete sets of commuting operators and O(3) scalars in the enveloping algebra of SU(3)," J. Math. Phys. **15**, 1787–1799 (1974).
[92]R. T. Sharp, "Internal-labeling operators," J. Math. Phys. **16**, 2050–2053 (1975).
[93]F. Iachello and R. D. Levine, *Algebraic Theory of Molecules* (Oxford University Press, New York, 1995).
[94]E. Merzbacher, *Quantum Mechanics*, 3rd ed. (John Wiley & Sons, New York, 1998).
[95]R. Pauncz, *The Symmetric Group in Quantum Chemistry* (CRC Press, Boca Raton, 1995).
[96]E. Feenberg and M. Phillips, "On the Structure of Light Nuclei," Phys. Rev. **51**, 597–608 (1937).
[97]R. N. Zare, *Angular Momentum* (John Wiley & Sons, New York, 1988).
[98]Beringer, J. et al. (Particle Data Group), "The Review of Particle Physics," Phys. Rev. D **86**, 010001 (2012).
[99]B. C. Sanctuary and F. P. Temme, "Multipole N.M.R. XIII. multispin interactions and symmetry in Liouville space," Mol. Phys. **55**, 1049–1062 (1985).
[100]U. Fano, "Geometrical characterization of nuclear states and the theory of angular correlations," Phys. Rev. **90**, 577–579 (1953).
[101]A. Messiah, *Quantum mechanics*, Vol. II (North-Holland, Amsterdam, 1962).
[102]L. D. Landau and E. M. Lifshitz, *Quantum mechanics*, Vol. 3 (Pergamon Press, Oxford, 1977).
[103]W. Dür, G. Vidal, and J. I. Cirac, "Three qubits can be entangled in two inequivalent ways," Phys. Rev. A **62**, 062314 (2000).
[104]H. J. Briegel and R. Raussendorf, "Persistent Entanglement in Arrays of Interacting Particles," Phys. Rev. Lett. **86**, 910–913 (2001).
[105]F. Verstraete, J. Dehaene, B. De Moor, and H. Verschelde, "Four qubits can be entangled in nine different ways," Phys. Rev. A **65**, 052112 (2002).
[106]R. H. Dicke, "Coherence in spontaneous radiation processes," Phys. Rev. **93**, 99–110 (1954).
[107]J. K. Stockton, J. M. Geremia, A. C. Doherty, and H. Mabuchi, "Characterizing the entanglement of symmetric many-particle spin-1/2 systems," Phys. Rev. A **67**, 022112 (2003).
[108]S. Köcher, T. Heydenreich, Y. Zhang, G. N. Reddy, S. Caldarelli, H. Yuan, and S. J. Glaser, "Time-optimal excitation of maximum quantum coherence: Physical limits and pulse sequences," J. Chem. Phys. **144**, 164103 (2016).
[109]Hermitian operators lead to positive and negative values, which are shown in red (dark gray) and green (light gray).
[110]S. J. Glaser, U. Boscain, T. Calarco, C. P. Koch, W. Köckenberger, R. Kosloff, I. Kuprov, B. Luy, S. Schirmer, T. Schulte-Herbüggen, D. Sugny, and F. K. Wilhelm, "Training Schrödinger's Cat: Quantum Optimal Control," Eur. Phys. J. D **69**, 279 (2015).
[111]N. J. Glaser, M. Tesch, and S. J. Glaser, "SpinDrops (Version 1.2.2) [Mobile application]," (2015), itunes.apple.com.
[112]M. Tesch, N. J. Glaser, and S. J. Glaser, "Spindrops 2.0," (2018), https://spindrops.org.
[113]B. Luy and S. J. Glaser, "Negative polarization transfer between a spin 1/2 and a spin 1," Chem. Phys. Lett. **323**, 377–381 (2000).
[114]R. A. Horn and C. R. Johnson, *Topics in Matrix Analysis* (Cambridge University Press, Cambridge, 1991).
[115]H. V. Henderson and S. R. Searle, "The Vec-Permutation Matrix, the Vec Operator, and Kronecker Products: A Review," Lin. Multilin. Alg. **9**, 271–288 (1981).
[116]P. A. Fuhrmann, *A Polynomial Approach to Linear Algebra*, 2nd ed. (Springer, New York, 2012).
[117]J. Huizenga, "Necessary and sufficient conditions for a sum of idempotents to be idempotent," MathOverflow, `https://mathoverflow.net/q/115255` (2012-12-03).
[118]B. Simon, *Representations of Finite and Compact Groups* (Oxford University Press, Oxford, 1995).
[119]S. Keppeler and M. Sjödahl, "Hermitian Young operators," J. Math. Phys. **55**, 021702 (2014).
[120]J. Alcock-Zeilinger and H. Weigert, "Compact Hermitian Young projection operators," J. Math. Phys. **58**, 051702 (2017).
[121]J. Alcock-Zeilinger and H. Weigert, "Transition operators," J. Math. Phys. **58**, 051703 (2017).
[122]J. R. Stembridge, "Orthogonal sets of Young symmetrizers," Adv. Appl. Math. **46**, 576–582 (2011).
[123]A. Acin, I. Bloch, H. Buhrman, T. Calarco, C. Eichler, J. Eisert, D. Esteve, N. Gisin, S. J. Glaser, F. Jelezko, S. Kuhr, M. Lewenstein, M. F. Riedel, P. O. Schmidt, R. Thew, A. Wallraff, I. Walmsley, and F. K. Wilhelm, "The quantum technologies roadmap: a European community view," New J. Phys. **20**, 080201 (2018).
[124]W. Bosma, J. J. Cannon, and C. Playoust, "The MAGMA Algebra System I: The User Language," J. Symbolic Comput. **24**, 235–265 (1997).
[125]The MathWorks Inc., *MATLAB, version 9.2 (R2017a)*, Natick, Massachusetts (2017).
[126]The Sage Developers, *SageMath, the Sage Mathematics Software System (Version 8.3)* (2018), `http://www.sagemath.org`.
[127]N. Khaneja and S. J. Glaser, "Efficient Transfer of Coherence through Ising Spin Chains," Phys. Rev. A **66**, 060301(R) (2002).
[128]B. Luy, O. Schedletzky, and S. J. Glaser, "Analytical polarization transfer functions for four coupled spins 1/2 under isotropic mixing conditions," J. Magn. Reson. **138**, 19–27 (1999).
[129]J. P. Elliott, J. Hope, and H. A. Jahn, "Theoretical studies in nuclear structure IV. Wave functions for the nuclear p-shell Part B. $\langle p^n|p^{n-2}p^2\rangle$ fractional parentage coefficients," Philos. Trans. Royal Soc. A **246**, 241–279 (1953).

D Linking the rotation of a rigid body to the Schrödinger equation

Bibliography:

Title: Linking the rotation of a rigid body to the Schrödinger equation: The quantum tennis racket effect and beyond

Authors: L. van Damme, D. Leiner, P. Mardešić, S. J. Glaser, and D. Sugny

Journal: Scientific Reports

Volume: 7

Issue: 1

Page: 3998

Published: 21.06.2017

DOI: 10.1038/s41598-017-04174-x

URL: https://doi.org/10.1038/s41598-017-04174-x

Summary and contribution to this manuscript:

In this work, we study the free rotation of a rigid body to obtain new geometric control schemes for quantum systems. In particular a geometric property known as the Tennis Racket Effect (TRE), which frequently occurs in such classical rotations, is analyzed. It is named after the characteristic behavior of a tennis racket, which is thrown in the air so that the handle makes a 2π rotation while simultaneously the head flips around π. A remarkable feature of this effect is its reproducibility for various rigid bodies and for an extensive set of initial conditions, corresponding to the initial inclination and velocity of the head of the racket, and showing its robustness, inherent to its geometric character. The TRE and more generally the free rotation of a rigid body is described by integrable functions whose solutions are trajectories which are obtained analytically by applying Jacobi elliptic functions. This description can be transferred to find notable control strategies of two-level quantum systems. If the applied control fields of the quantum systems are exactly equal to the angular velocities of the classical rigid body then a one-to-one mapping can be obtained between the trajectories of the classical and quantum object and the moments of inertia in the classical system can be seen as additional degrees of freedom used for the control fields. By exploiting these correspondence, first, a new family of control fields is introduced, which is established on the TRE and which allows for a robust manipulation of the quantum state of a spin system with respect to some experimental uncertainties. These controls rely on a variable choice of two parameters which can be adjusted to alter the duration, the efficiency and the robustness of the control process. Experimental

demonstrations on a spin 1/2 using techniques of nuclear magnetic resonance were done by David Leiner to show the feasibility of the TRE-based control strategy. As a model system, the ^{1}H spins of HDO with D_2O as a solvent was used. Simulations were also carried out by David Leiner to compare the experimental data with the theory. Second, the dynamics of a rigid body enables control fields to implement one-qubit quantum gates, in particular non-adiabatic geometric quantum phase gates based on the Montgomery phase. Its robustness is discussed. The paragraph containing the experimental description with the corresponding figure (Fig. 5) was done by David Leiner and revised by Steffen Glaser.

SCIENTIFIC REPORTS

OPEN

Linking the rotation of a rigid body to the Schrödinger equation: The quantum tennis racket effect and beyond

Received: 16 December 2016
Accepted: 10 May 2017
Published online: 21 June 2017

L. Van Damme[3], D. Leiner[2], P. Mardešić[1], S. J. Glaser[2] & D. Sugny[3,4]

The design of efficient and robust pulse sequences is a fundamental requirement in quantum control. Numerical methods can be used for this purpose, but with relatively little insight into the control mechanism. Here, we show that the free rotation of a classical rigid body plays a fundamental role in the control of two-level quantum systems by means of external electromagnetic pulses. For a state to state transfer, we derive a family of control fields depending upon two free parameters, which allow us to adjust the efficiency, the time and the robustness of the control process. As an illustrative example, we consider the quantum analog of the tennis racket effect, which is a geometric property of any classical rigid body. This effect is demonstrated experimentally for the control of a spin 1/2 particle by using techniques of Nuclear Magnetic Resonance. We also show that the dynamics of a rigid body can be used to implement one-qubit quantum gates. In particular, non-adiabatic geometric quantum phase gates can be realized based on the Montgomery phase of a rigid body. The robustness issue of the gates is discussed.

Quantum control is aimed at manipulating dynamical processes at microscopic scales by means of external electromagnetic fields[1–6]. Its successful experimental implementation requires robustness against parameter fluctuations and uncertainties, but also high efficiency in a sufficiently short time to avoid parasitic phenomena such as relaxation. These objectives can be viewed as a crucial prerequisite for a wide range of applications of such techniques in the emerging domain of quantum technologies[1]. In this setting, numerical algorithms based on optimal control theory[7] have been developed to realize a given task, while minimizing the control time and accounting for experimental constraints and imperfections[8]. In spite of its efficiency, this approach does not give a clear insight into the control mechanism, which makes it system-dependent and prevents its generalization. The physical understanding of a control process can be extracted from a geometric analysis of the dynamics[9–13]. The geometric properties of the corresponding physical effect will ensure its robustness against experimental errors and thus its usefulness[14,15]. The richness of this geometric approach is illustrated by the Berry phase in quantum mechanics[16,17]. The discovery of the Berry phase led to an impressive amount of studies both in quantum physics and chemistry. Geometric control protocols, resilient to certain types of experimental uncertainties, were developed in quantum computing from this effect[18,19]. In this work, we propose to use the study of the free rotation of a rigid body to develop new geometric quantum control strategies. A geometric property, known as the Tennis Racket Effect (TRE)[20,21], will be used as an illustrative example to describe this method. This phenomenon occurs in the free rotation of any three-dimensional rigid body[22–24]. It can be easily observed with a tennis racket through the following experimental protocol. We first mark the different faces of the head of the racket. We then take the racket by the handle and throw it in the air so that the handle makes a 2π rotation. After catching the handle, we observe that the head of the tennis racket has made a flip of π. This effect can be reproduced for many different

[1]Institut de Mathématiques de Bourgogne, UMR 5584 CNRS-Université de Bourgogne Franche-Comté, 9 Av. A. Savary, BP 47870, 21078, Dijon Cedex, France. [2]Department of Chemistry, Technical University of Munich, Lichtenbergstrasse 4, D-85747, Garching, Germany. [3]Laboratoire Interdisciplinaire Carnot de Bourgogne (ICB), UMR 5209 CNRS-Université Bourgogne Franche Comté, 9 Av. A. Savary, BP 47 870, F-21078, Dijon Cedex, France. [4]Institute for Advanced Study, Technical University of Munich, Lichtenbergstrasse 2 a, D-85748, Garching, Germany. Correspondence and requests for materials should be addressed to S.J.G. (email: glaser@tum.de) or D.S. (email: dominique.sugny@u-bourgogne.fr)

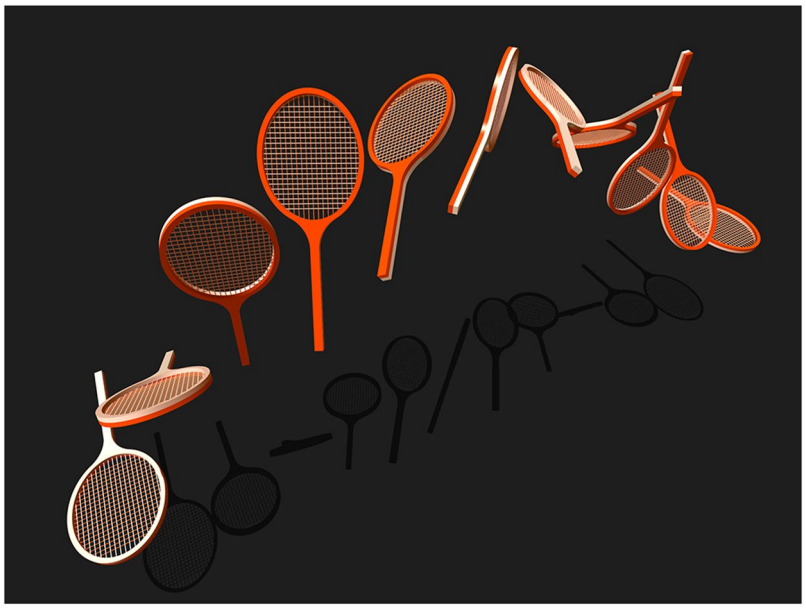

Figure 1. The tennis racket effect. Illustration of the motion of the tennis racket. Note the flip of the head when the handle makes a 2π rotation.

rigid bodies and a large range of initial conditions, corresponding to the initial inclination and velocity of the head of the racket, showing thus its robustness, inherent to its geometric character. An illustration of TRE is given in Fig. 1. A complete mathematical description of TRE was given in a series of papers[20,21,24]. These analyses are based on the fact that the free rotation of a rigid body[24] is an integrable system whose trajectories can be derived analytically by using Jacobi elliptic functions[23]. Here, we show that the TRE, and more generally the dynamics of a rigid body, find remarkable applications in the control of two-level quantum systems[1,2]. We first obtain a family of control fields based on the TRE which allows us to manipulate the state of the system in a robust manner with respect to some experimental uncertainties. Such fields depend on two parameters that can be adjusted to change the time, the efficiency and the robustness of the control process. We introduce the concept of a quantum TRE, which is the analog of the classical motion at the quantum level and we point out its specific quantum properties. The TRE control strategy is demonstrated experimentally on a spin 1/2 particle by using techniques of Nuclear Magnetic Resonance[25]. We also show that the dynamics of a rigid body allows us to design control fields to realize one-qubit quantum gates. In particular, we focus on the Montgomery phase[26], a geometric feature of the free rotation of a rigid body, which leads to quantum geometric phase gates[18] in the non-adiabatic regime.

A formal equivalence can be established between the free rotation of a rigid body and the dynamics of a spin 1/2 particle, which are governed respectively by the Euler and the Bloch equations. The two systems of differential equations have a similar mathematical structure of the form $\dot{\vec{X}} = H(t)\vec{X}$ where the matrix $H(t)$ can be written as follows:

$$H(t) = \begin{pmatrix} 0 & -\Omega_3 & \Omega_2 \\ \Omega_3 & 0 & -\Omega_1 \\ -\Omega_2 & \Omega_1 & 0 \end{pmatrix}. \tag{1}$$

The state of the system is described by the vector $\vec{X}(t)$ and the Ω_is denote the angular velocities along the i-direction, $i = 1, 2, 3$. We refer the reader to Supp. Sec. I or to textbook references for technical details[22,23,25]. The vector $\vec{X}$ can be identified with the angular momentum $\vec{L}$ of the rigid body (in the frame attached to the racket) or with the Bloch vector $\vec{M}$ of the spin (in a given rotating frame[25]). In the classical system, the components of $\vec{L} = (L_1, L_2, L_3)$ can be expressed in terms of the Ω_is through the principal moments of inertia I_i, $L_i = I_i\Omega_i$ (in the principal axis system of the inertia tensor), while in the quantum case, the angular velocities refer to external control fields applied along a given direction. The classical system admits two constants of motion making it Liouville integrable, namely the energy $E = \frac{L_1^2}{2I_1} + \frac{L_2^2}{2I_2} + \frac{L_3^2}{2I_3}$ and the norm of the angular momentum, $L_1^2 + L_2^2 + L_3^2$, which can be set to 1. If the control fields applied to the spin are exactly equal to the angular velocities of the rigid body then a one-to-one mapping can be defined between the trajectories of the classical and quantum objects. As shown below, the moments of inertia can be viewed as additional degrees of freedom used to design control fields with specific properties. In some experimental applications, only two external fields are available. In this limiting case, an ideal rigid body for which one of the moments of inertia goes to infinity can be considered. Note that the different geometric features of a rigid body are not modified in this limit. In the rest of the paper, we will assume that the three moments of inertia are equal to 1, $1/k^2$ with $k \in [0, 1]$, and $+\infty$.

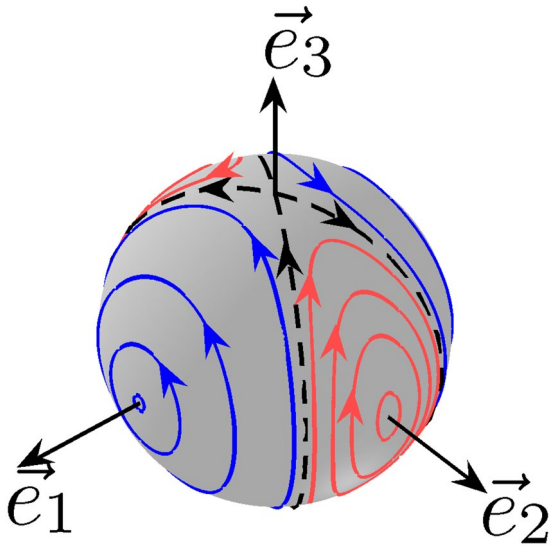

Figure 2. Dynamics of the angular momentum of a three-dimensional rigid body. Trajectories of the angular momentum $\vec{L}$ of a three-dimensional rigid body in the body-fixed frame $(\vec{e}_1, \vec{e}_2, \vec{e}_3)$. The blue (dark gray) and red (light gray) lines depict respectively the rotating and oscillating trajectories of the angular momentum. The dashed line represents the separatrix. The parameter k is set to 0.5. In the case of a corresponding two-level quantum system, the trajectories represent the dynamics of the Bloch vector in the rotating frame.

Classical and quantum tennis racket effects. Returning back to the dynamical behavior of the tennis racket, two fundamental motions can be considered.

The first motion is associated with the angular momentum $\vec{L}$ in the reference frame of the racket. During the rotation of the racket, the angular momentum is brought from its initial position to the diametrically opposite one. The different trajectories that can be followed by $\vec{L}$ are displayed in Fig. 2. The classical phase space has a simple structure made of a separatrix which is the boundary between two families of trajectories: the rotating and the oscillating ones, each distributed around a stable fixed point[23]. In the example of Fig. 2 where $\Omega_2(t) = 0, I_1 = 1$ and $I_3 = 1/k^2$, the north and the south poles are unstable equilibrium points. All the trajectories are periodic, except for the separatrix, which connects the two unstable points in an infinite time. In Fig. 2, a transfer from the north pole $(\vec{e}_3)$ to the south pole $(-\vec{e}_3)$ can be achieved on the Bloch sphere by following the separatrix. In the quantum mechanical setting, this control process requires an infinite time to be performed and corresponds to an Allen-Eberly type pulse sequence of the form ref. 27:

$$\Omega_1(t) = \frac{\pm 1}{\sqrt{1-k^2}}\,\mathrm{sech}(t+t_0); \quad \Omega_3(t) = \frac{\pm k}{\sqrt{1-k^2}}\tanh(t+t_0), \tag{2}$$

where t_0 is an arbitrary constant time.

The formal equivalence used in this work leads therefore to an insightful geometric interpretation of the Allen-Eberly solution as a singular trajectory, i.e. a separatrix, of a classical rigid body. In addition to this control strategy, two families of control fields can be derived from TRE. Such solutions, called TRE pulses, correspond to the oscillating or rotating trajectories close to the separatrix, which bring approximately the system from the north to the south pole of the Bloch sphere. Each element of the two sets can be characterized by the parameter k and a small positive constant ϵ, which describes the distance of the trajectory to the separatrix. The two parameters can be chosen to adjust the efficiency, the robustness and the time of the control process. More generally, we show in Supp. Sec. II by considering the whole range of variations of ϵ and k that a smooth transition can be established between π pulses of constant phase and Allen-Eberly solutions. In the case of Fig. 2, the rotation axis of the π pulse is associated with one of the two stable fixed points and the Allen-Eberly control with the separatrix. All the other trajectories, and in particular the TRE pulses, represent a compromise between the two solutions.

To evaluate the robust character of the TRE pulse, we consider the control of an ensemble of spins with different offset frequencies δ and scaling factors α of the amplitude of the control field, the two parameters belonging to intervals fixed by the experimental setup. This description reproduces the standard experimental uncertainties due to the field inhomogeneities that can be encountered in NMR[25] or in quantum information processing[28]. In the numerical simulations, we replace in Eq. (1) the three angular velocities by $(1+\alpha)\Omega_1, (1+\alpha)\Omega_2$ and $\Omega_3 + \delta$. We denote by t_f and $J_3 = -M_3(t_f)$, the control time and the figure of merit of the process, respectively. The initial state is the north pole of the Bloch sphere. Figure 3 shows the efficiency of the TRE pulse. We observe that the robustness of the process changes with the parameter k. It can be verified that this property does not depend on ϵ, for ϵ sufficiently small. The parameter ϵ affects predominantly the fidelity and the control time of the process. The analytical computations reveal that this time has a logarithmic divergence when ϵ goes to 0 (see Supp. Sec. II).

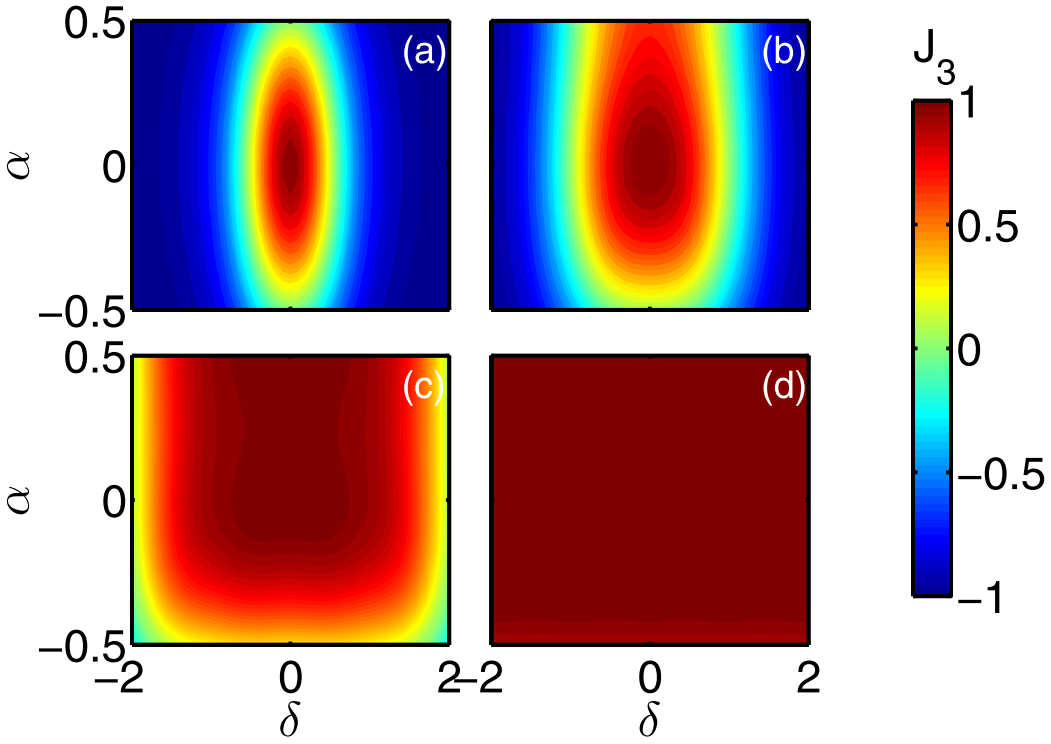

Figure 3. Efficiency and robustness of the Tennis Racket Effect pulses. The figure of merit J_3 is plotted as a function of the α and δ parameters. In the panels (**a–d**), k is respectively fixed to 0.2, 0.6, 0.9 and 0.99. The parameter ϵ is set to 0.01 (see Supplementary Sec. II for details).

A second relevant dynamical process is associated with the motion of the frame attached to the racket with respect to the laboratory frame (x, y, z). Denoting by $R(t) \in SO(3)$, the corresponding rotation matrix at a time t, whose dynamics is ruled by the equation $\dot{R}(t) = H(t)R(t)$, the final position of the racket is characterized in the ideal case by:

$$R_f = \begin{pmatrix} 1 & 0 & 0 \\ 0 & -1 & 0 \\ 0 & 0 & -1 \end{pmatrix}. \tag{3}$$

This analogy can be interpreted as a first step towards the implementation of quantum gates, here a NOT gate. However, this transformation is less robust than the one of the angular momentum because the total time of the process has to be perfectly adjusted in order to realize the 2π rotation of the handle (see below). Note that the racket exactly goes back to its initial position after 2 TREs. This geometric phenomenon can be extended to a purely quantum property by using the standard mapping between $SO(3)$ and $SU(2)$. A quantum TRE is then defined from the solution of the Schrödinger equation $i\frac{d}{dt}U(t) = \mathcal{H}(t)U(t)$ where $U(t) \in SU(2)$ and $\mathcal{H}$ is the 2×2-Hamiltonian matrix with complex entries corresponding to the Hamiltonian $H(t)$ of Eq. (1), which is defined by:

$$\mathcal{H} = \frac{1}{2}\begin{pmatrix} -\Omega_3 & \Omega_1 - i\Omega_2 \\ \Omega_1 + i\Omega_2 & \Omega_3 \end{pmatrix}. \tag{4}$$

We observe that after one TRE, the rotation matrix is given by

$$U_f = (-i)\begin{pmatrix} 0 & 1 \\ 1 & 0 \end{pmatrix}, \tag{5}$$

so that four TREs are needed for the quantum racket to come back to its initial state. A description of this quantum motion is displayed in Fig. 4 by using the DROPS representation of the propagator $U(t)$[29], illustrating the orientation of the effective rotation axis. While in the conventional experiment, this orientation is constant (along the x-axis), it follows in the TRE case a twisted trajectory from the y-via z- to the x-axes between $t = 0$ and $t = T_R$.

Experimental implementation. We now show by using NMR techniques the experimental performance of a TRE pulse to realize a state to state transfer from (0, 1, 0) to (0, −1, 0).

The experiments were performed on a Bruker Avance 600 MHz spectrometer. We used the ^{1}H spins of HDO with D_2O (99.9%) as a solvent in a Shigemi tube. The offset of the irradiation frequency was set to 2824 Hz and the maximum amplitude to 1115.6 Hz. At room temperature (298 K), the spin-lattice relaxation time is $T_1 = 1.82$ s and

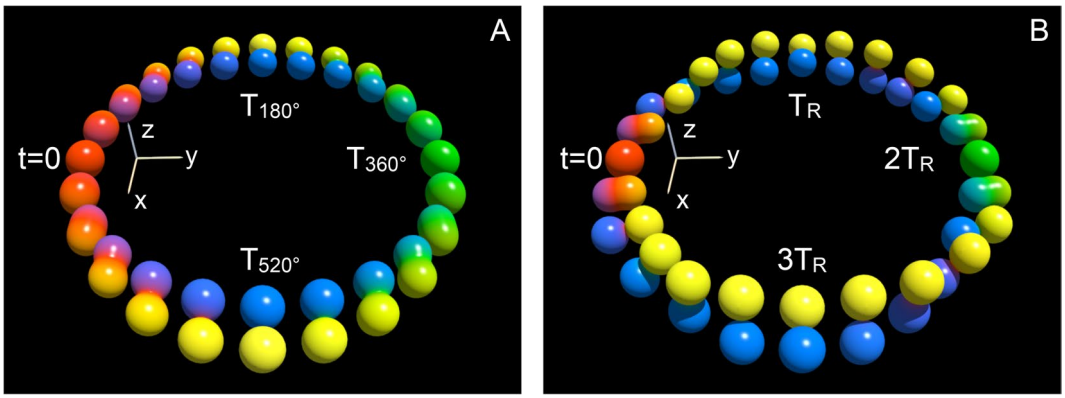

Figure 4. Drops representation of the propagators. Trajectories of the propagators $U(t)$ for standard rectangular pulses of constant amplitude and phase (**A**) and by TRE pulses (**B**) as a function of time. In panels (A,B), T_{180} and T_R are pulse durations corresponding to a 180°-rotation around the x-axis. In the DROPS representation[29], operators are depicted by complex spherical functions $f(\theta, \phi) = |f(\theta, \phi)|e^{i\eta}$, where for given azimuthal and polar angles θ and ϕ, the absolute value $|f(\theta, \phi)|$ is represented by the distance from the origin and the phase angle is color coded ($\eta = 0$: red, $\eta = \frac{\pi}{2}$: yellow, $\eta = \pi$: green, $\eta = \frac{3\pi}{2}$: blue). At $t = 0$, the propagator is the identity operator **1** (represented by red spheres), while at (**A**) $t = T_{360°} = 2T_{180°}$ and (**B**) $t = 2T_R$ the propagator is $-\mathbf{1}$ (represented by green spheres). In panels (A,B), the identity operator is created again at $t = 4T_{180°} = T_{720°}$ and $t = 4T_R$, respectively.

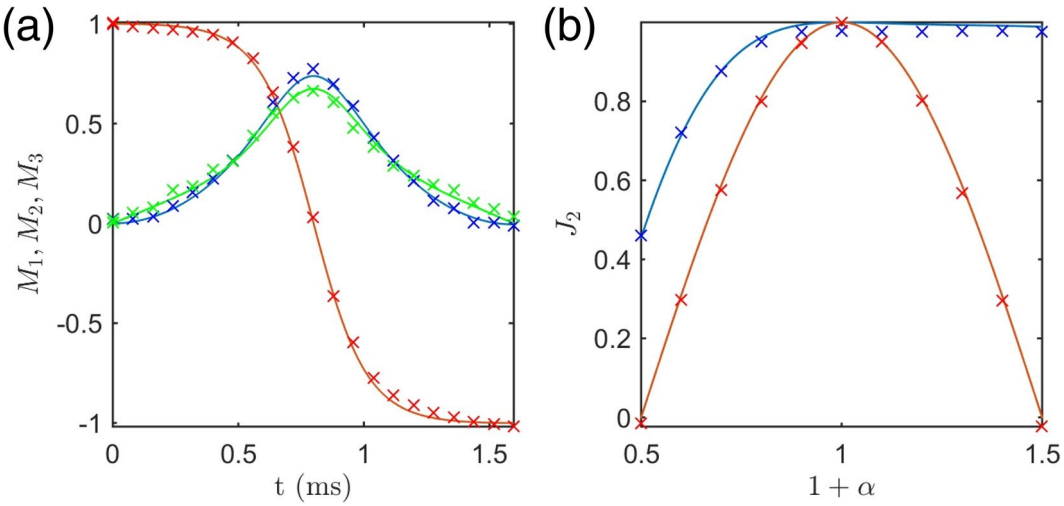

Figure 5. Experimental implementation of the TRE pulse. The panels (**a,b**) represent respectively the trajectories of the components of the Bloch vector (2: red or dark gray, 3: blue or black, 1: green or light gray) and the robustness of J_2 with respect to the α- parameter. A rectangular π pulse is used in panel (**b**) for comparison (red or dark gray). The experimentally measured points and the simulated trajectories are represented by crosses and solid lines, respectively. Experimental details can be found in the main text.

thus negligible since orders of magnitude larger than the pulse duration. The trajectory measurements were made by interrupting the control pulse at different times t. The x- and y-components of the Bloch vector were directly acquired. For the z-coordinate, the experiments were repeated with an additional $\frac{\pi}{2}$ pulse along the x-direction before the acquisition in order to flip the z-component of the magnetization vector to the transverse plane. The TRE pulse duration was set to 1.5965 ms and the parameters k and E to 0.7 and 0.2457, respectively. The π pulse is defined as a rectangular shaped pulse with the same amplitude and with 1000 intervals to be consistent with the digitization of the TRE pulse.

The evolution of the Bloch vector and the robustness of the shaped pulse with respect to the scaling factor α are displayed in Fig. 5. For the robustness experiments, we scaled the amplitude with factors ranging from $\alpha = -0.5$ to $\alpha = 0.5$ in 11 steps. The figure of merit J_2 is here defined by $J_2 = -M_2(t_f)$. In the experimentally measured trajectories, each data point corresponds to the average of 16 scans in order to increase the signal-to-noise ratio of the experimental spectra. Small but finite sources of systematic errors[30], in the NMR experiments are (a) relaxation losses during the pulses, (b) B_0 inhomogeneity, (c) non-linear effects due to radiation damping[31], (d) pulse shape distortions due to the amplifiers and the finite bandwidth of the resonator[32] and (e) partial saturation

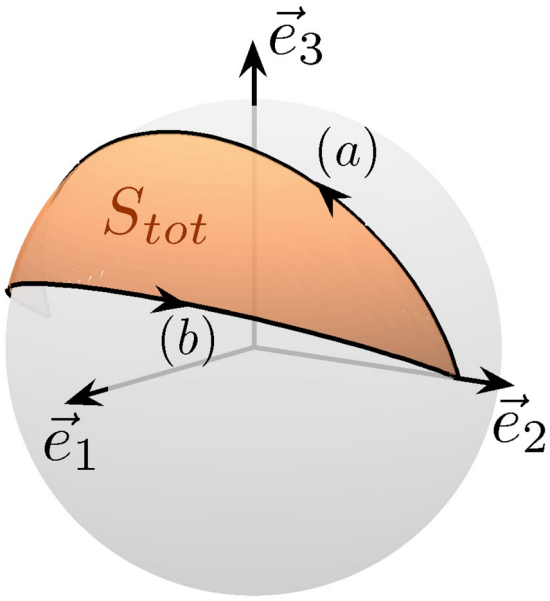

Figure 6. Quantum gate based on the Montgomery phase. Cyclic process on the Bloch sphere for implementing a $\pi/2$ phase gate. The loop is the concatenation of the trajectories (**a**,**b**) which are defined by different values of k (see the main text). The brown (gray) surface is the total geometric phase at the end of the process i.e. $S_{tot} = \pi/2$.

of the signal due to finite relaxation period between scans. Each of these sources of errors was minimized within the limits of the experimental setting and a reasonable match was found between the experimental results and simulations.

Implementation of one-qubit gates. The correspondence between the free rotation of a rigid body and the dynamics of a spin 1/2 particle also provides novel control strategies in quantum computing[28]. In Supp. Sec. V, we show how to implement the Hadamard gate, and more generally any one-qubit quantum gate. Here, we focus on the case of the geometric quantum phase gates[33], that can be realized by using a geometric feature of the free rotation of a rigid body, namely the Montgomery phase[26]. This phase can be defined by considering one period of the time evolution of the angular momentum $\vec{L}$ in the body-fixed frame. During this motion, the laboratory frame rotates about $\vec{L}$ by an angle, the Montgomery phase. This phase, $\Delta\psi$ can be expressed as the sum of a dynamical and a geometric contribution[16]:

$$\Delta\psi = \frac{2ET}{M} - S, \tag{6}$$

where M is the norm of the angular momentum, T the period of the motion of $\vec{M}$ and S the solid angle swept out by $\vec{M}$. One of the main difficulties to realize geometric phase gates is to find a way to cancel the dynamical contribution of the phase in order to obtain a robust control protocol. Different techniques have been proposed up to date[18,33]. Geometric phase gates can be implemented in the adiabatic regime[18], but it is possible to generalize this process to consider non-adiabatic cyclic evolution[34,35], which is crucial to avoid decoherence effects. Only very simple motions, such as a circle on the Bloch sphere, were proposed. Using the Montgomery phase and the dynamics of a rigid body, this idea can be considerably extended. The method can be described as follows. To simplify the discussion, we assume here that the system follows trajectories along the separatrices. We first make a transfer from the point $(0, 1, 0)$ to the point $(0, -1, 0)$ with a finite time T_a and a fixed parameter k_a. The system is brought in a second step from $(0, -1, 0)$ to $(0, 1, 0)$ with a different value of the parameter $k_b \neq k_a$. We choose the time T_b of the second process so that the two dynamical phases cancel each other. The global process is displayed in Fig. 6. A straightforward computation derived in Supp. Sec. V shows that:

$$T_b = \frac{k_a\sqrt{1-k_b^2}}{k_b\sqrt{1-k_a^2}}T_a, \tag{7}$$

which leads to a purely geometric phase given by:

$$\Delta\psi = 2[\arcsin(\sqrt{1-k_a^2}) - \arcsin(\sqrt{1-k_b^2})]. \tag{8}$$

Using this approach, any geometric phase gate can be implemented in the non-adiabatic regime. More generally, the dynamical phase is also at the origin of the relatively low robustness of the one-qubit quantum gates based on the dynamics of a rigid body. This property can be greatly improved by considering a generalization of the BIR-pulses used in NMR[36,37]. This control strategy consists in the concatenation of two (or more) pulses chosen so that

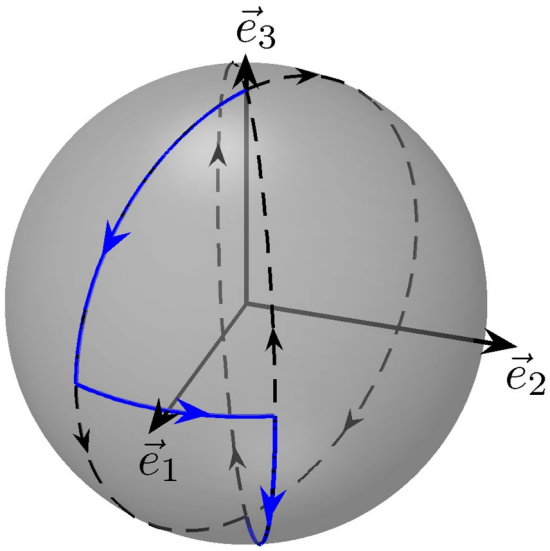

Figure 7. A robust NOT gate. Trajectory used to realized a robust NOT-gate (solid blue line). The dashed lines represent the separatrices. The black arrows indicate the direction of the dynamics of the classical angular momentum.

the global dynamical phase is cancelled. As an illustrative example, we consider here a NOT gate (see also Supp. Sec. V for technical details). The trajectory used to realized a robust NOT-gate is depicted in Fig. 7. We first follow a separatrix from the north pole to the equatorial plane of the sphere. The system is then brought to another separatrix followed in the opposite direction. The two separatrices are connected with a constant pulse Δ about $\vec{e}_3$ so that the global phase is cancelled. It can be shown that $\Delta = 2 \arccos k$.

Conclusion

By using the formal analogy between the free rotation of a rigid body and the dynamics of a spin 1/2 particle, we have derived a new family of control fields able to realize either a state to state transfer or a specific unitary transformation in a two-level quantum system. As demonstrated in this paper, the derived pulses have an explicit and relatively simple form, which is therefore easily implementable experimentally. Note that a Matlab code computing the trajectories of a rigid body and of the corresponding Bloch vector is provided in Supp. Sec. VI.

The results of this work pave the way to other analyses using the same kind of equivalence. The applicability of this analogy beyond simple two-level quantum systems, such as in a chain of three coupled spins[38,39], shows the general interest of this approach. Following the method proposed in ref. 38, the control fields derived from the dynamics of a rigid body could also be used as a building block to realize a CNOT gate in this system. Another possible direction is the generalization of this study to $SO(n)$, with $n > 3$, for instance in the integrable case of the Manakov top[40].

References

1. Glaser, S. J. *et al.* Training Schrödinger's cat: Quantum optimal control. *Eur. Phys. J. D* **69**, 279 (2015).
2. Brif, C., Chakrabarti, R. & Rabitz, H. Control of quantum phenomena: Past, present and future. *New J. Phys.* **12**, 075008 (2010).
3. Bason, M. G. *et al.* High-fidelity quantum driving. *Nature Phys.* **8**, 147 (2012).
4. Leibfried, D. *et al.* Experimental demonstration of a robust, high-fidelity geometric two ion-qubit phase gate. *Nature* **422**, 412 (2003).
5. Sorensen, J. *et al.* Exploring the Quantum Speed Limit with Computer Games. *Nature* **532**, 210 (2016).
6. Nöbauer, T. *et al.* Smooth Optimal Quantum Control for Robust Solid-State Spin Magnetometry. *Phys. Rev. Lett.* **115**, 190801 (2015).
7. Pontryagin, L. S., Bol'tanskii, V. G., Gamkrelidze, R. S. & Mischenko, E. F. *The Mathematical Theory of Optimal Processes* (ed. Pergamon Press, New York, 1964).
8. Khaneja, N., Reiss, T., Kehlet, C., Schulte-Herbrüggen, T. & Glaser, S. J. Optimal control of coupled spin dynamics: design of NMR pulse sequences by gradient ascent algorithms. *J. Magn. Reson.* **172**, 296 (2005).
9. Khaneja, N., Brockett, R. & Glaser, S. J. Time optimal control in spin systems. *Phys. Rev. A* **63**, 032308 (2001).
10. Lapert, M., Zhang, Y., Braun, M., Glaser, S. J. & Sugny, D. Singular Extremals for the Time-Optimal Control of Dissipative Spin 1/2 Particles. *Phys. Rev. Lett.* **104**, 083001 (2010).
11. Chen, X., Lizuain, I., Ruschhaupt, A., Guéry-Odelin, D. & Muga, J. G. Shortcut to Adiabatic Passage in Two- and Three-Level Atoms. *Phys. Rev. Lett.* **105**, 123003 (2010).
12. Garon, A., Glaser, S. J. & Sugny, D. Time optimal control of SU(2) quantum operations. *Phys. Rev. A* **88**, 043422 (2013).
13. Silver, M. S., Joseph, R. I., Chen, C.-N., Sank, V. J. & Hoult, D. I. Selective population inversion in NMR. *Nature* **310**, 681 (1984).
14. Ruschhaupt, A., Chen, X., Alonso, D. & Muga, J. G. Optimally robust shortcuts to population inversion in two-level quantum systems. *New J. Phys.* **14**, 093040 (2012).
15. Daems, D., Ruschhaupt, A., Sugny, D. & Guérin, S. Robust quantum control by a single-shot shaped pulse. *Phys. Rev. Lett.* **111**, 050404 (2013).
16. Bohm, A., Mostafazadeh, H., Koizumi, Q. & Zwanziger, J. *The geometric phase in quantum systems*. (ed. Springer, Berlin, 2003).
17. Nakahara, M. *Geometry, topology and physics*. (ed. Institute of physics publishing, Bristol and Philadelphia, 1990).

18. Jones, J. A., Vedral, V., Ekert, A. & Castagnoli, G. Geometric quantum computation using Nuclear Magnetic Resonance. *Nature* **43**, 869 (2000).
19. Abdumalikov, A. A. *et al*. Experimental realization of non-Abelian non-adiabatic geometric gates. *Nature* **496**, 482 (2013).
20. Ashbaugh, M. S., Chiconce, C. C. & Cushman, R. H. The twisting tennis racket. *J. Dyn. Diff. Eq.* **3**, 67 (1991).
21. Van Damme, L., Mardesic, P. & Sugny, D. The tennis racket effect in a three-dimensional rigid body. *Physica D* **338**, 17 (2017).
22. Arnold, V. I. *Mathematical methods of classical mechanics* (ed. Springer-Verlag, New York, 1989).
23. Goldstein, H. *Classical mechanics* (ed. Addison-Wesley, Reading, MA, 1950).
24. Cushman, R. H. *Global aspects of classical integrable systems* (ed. Birkhäuser, Berlin, 1997).
25. Levitt, M. H. *Spin Dynamics*: *Basics of Nuclear Magnetic Resonance* (ed. Wiley, New York, 2008).
26. Montgomery, R. How much does the rigid body rotate? A Berry's phase from the 18th century. *Am. J. Phys.* **59**, 394 (1991).
27. Allen, L. & Eberly, J. H. *Optical resonance and two-level atoms* (ed. Wiley, New York, 1975).
28. Nielsen, M. A. & Chuang, I. L. *Quantum computation and quantum information* (ed. Cambridge University Press, Cambridge, 2000).
29. Garon, A., Zeier, R. & Glaser, S. J. Visualizing Operators of Coupled Spins Systems. *Phys. Rev. A* **91**, 042122 (2015).
30. Ernst, R. R., Bodenhausen, G. & Wokaun, A. *Principles of Nuclear Magnetic Resonance in One and Two Dimensions*. (Oxford Science Publications, Oxford, 2004).
31. Augustine, M. P. & Hahn, E. L. Radiation Damping with Inhomogeneous Broadening: Limitations of the Single Bloch Vector Model. *Concepts Magn. Reson.* **13**, 1 (2001).
32. Tabuchi, Y., Negoro, M., Takeda, K. & Kitagawa, M. Total compensation of pulse transients inside a resonator. *J. Magn. Reson.* **204**, 327 (2010).
33. Sjöqvist, E. A new phase in quantum computation. *Physics* **1**, 35 (2008).
34. Xiang-Bin, W. & Keiji, M. Nonadiabatic conditional geometric phase shift with NMR. *Phys. Rev. Lett.* **87**, 097901 (2001).
35. Zhu, S.-L. & Wang, Z. D. Implementation of univeral quantum gates based on nonadiabatic geometric phases. *Phys. Rev. Lett.* **89**, 097902 (2002).
36. Tannus, A. & Garwood, M. Adiabatic pulses. *NMR Biomed.* **10**, 423 (1997).
37. Garwood, M. & Ke, Y. Symmetric pulses to induce arbitrary flip angles with compensation for RF inhomogeneity and resonance offsets. *J. Magn. Reson.* **94**, 511 (1991).
38. Khaneja, N. *et al*. Shortest paths for efficient control of indirectly coupled qubits. *Phys. Rev. A* **75**, 012322 (2007).
39. Van Damme, L., Zeier, R., Glaser, S. J. & Sugny, D. Application of the Pontryagin maximum principle to the time-optimal control in a chain of three spins with unequal couplings. *Phys. Rev. A* **90**, 013409 (2014).
40. Perelomov, A. M. Motion of four-dimensional rigid body around a fixed point: An elementary approach. *J. Phys. A* **38**, 801 (2005).

Acknowledgements

S. J. Glaser acknowledges support from the DFG (Gl 203/7-2). D. Sugny and S. J. Glaser acknowledge support from the ANR-DFG research program Explosys (ANR-14-CE35-0013-01; Gl203/9-1). D. Sugny acknowledges support from the ANR-DFG research program COQS and from the PICS CNRS program on the control of open quantum systems. This work has been done with the support of the Technische Universität München Institute for Advanced Study, funded by the German Excellence Initiative and the European Union Seventh Framework Programme under grant agreement 291763. Experiments were performed at the Bavarian NMR center at TU München. P. Mardešić acknowledges support from LAISLA (project funded by FONCICYT) and the PREI project (funded by UNAM DGAPA). D. Leiner acknowledges support from the Elite Network of Bavaria program ExQM.

Author Contributions

All authors contributed to the design and interpretation of the presented work. Numerical computations have been done by L.V.D., the construction of the experiment and the acquisition of the data were performed by D.L. and S.J.G.

Additional Information

Supplementary information accompanies this paper at doi:10.1038/s41598-017-04174-x

Competing Interests: The authors declare that they have no competing interests.

Publisher's note: Springer Nature remains neutral with regard to jurisdictional claims in published maps and institutional affiliations.